Ultrafast Dynamics and Nonlinear Photonics of Perovskites and Doped Semiconductor Nanocrystals

विद्या वाचस्पति की
उपाधि की अपेक्षाओं की आंशिक पूर्ति में प्रस्तुत शोध प्रबंध

A thesis submitted in partial fulfilment of the requirements of the degree of Doctor of Philosophy

द्वारा / By
अमन चतुर्वेदी / Aman Chaturvedi

पंजीकरण सं. २०१७३५३८ / Registration No.: 20173538

शोध प्रबंध पर्यवेक्षक / Thesis Supervisor
प्रो.पंकज मंडल/ Prof. Pankaj Mandal

भारतीय विज्ञान शिक्षा एवं अनुसंधान संस्थान पुणे
INDIAN INSTITUTE OF SCIENCE EDUCATION AND RESEARCH PUNE

2025

Dedicated to My Father

Mr. Dheeraj Kumar Chaturvedi

CERTIFICATE

Certified that the work incorporated in the thesis entitled "**Ultrafast Dynamics and Nonlinear Photonics of Perovskites and Doped Semiconductor Nanocrystals**" Submitted by **Mr. Aman Chaturvedi** was carried out by the candidate, under my supervision. The work presented here or any part of it has not been included in any other thesis submitted previously for the award of any degree or diploma from any other University or institution.

Prof. Pankaj Mandal

(Research Supervisor)

Date: 15/01/2025

Declaration by Student

Name of Student: Aman Chaturvedi

Reg. No.: 20173538

Thesis Supervisor: Prof. Pankaj Mandal

Department: Chemistry

Date of joining program: 01/08/2017

Date of Pre-Synopsis Seminar: 30/12/2024

Title of Thesis: Ultrafast Dynamics and Nonlinear Photonics of Perovskites and Doped Semiconductor Nanocrystals

I declare that this written submission represents my idea in my own words and where others' ideas have been included; I have adequately cited and referenced the original sources. I declare that I have acknowledged collaborative work and discussions wherever such work has been included. I also declare that I have adhered to all principles of academic honesty and integrity and have not misrepresented or fabricated or falsified any idea/data/fact/source in my submission. I understand that violation of the above will be cause for disciplinary action by the Institute and can also evoke penal action from the sources which have thus not been properly cited or from whom proper permission has not been taken when needed.

The work reported in this thesis is the original work done by me under the guidance of

Prof. Pankaj Mandal.

Date: 01/15/2025

Signature of the student

Acknowledgements

First and foremost, I would like to express my heartfelt gratitude to my thesis supervisor, Prof. Pankaj Mandal, for his invaluable guidance and unwavering support throughout my PhD journey. I have learned immensely from his exemplary scientific temperament and the patience required to manage such a complex laboratory. The excellent research environment he cultivated, coupled with the freedom he provided to explore new techniques and design innovative projects, has been instrumental in shaping my work. His consistent presence and critical scientific insights at every stage of the experiments have been invaluable in achieving meaningful research outcomes. Over the course of my PhD, the lab experienced several challenges, including prolonged laser breakdowns, the COVID-19 pandemic, and even a fire incident. Through it all, his ability to handle such difficult situations without ever losing his calm, finding solutions, and consistently working ethically is a quality I deeply admire and aspire to follow in my life.

I would also like to thank my research advisory committee members, Dr. Sayan Bagchi and Dr. Pramod Pillai, for their constant support, insightful discussions, and valuable suggestions during the annual RAC meetings.

A special note of appreciation goes to the individuals who played a significant role in completing this thesis-my collaborators. I am deeply grateful to Dr. Angshuman Nag and Prof. H.N. Ghosh for their support and collaboration. I would also like to thank Mr Parikshit Kumar Rajput and Dr Bharat Tandon from Dr Angshuman Nag's group at IISER Pune, as well as Dr Gurpreet Kaur from Prof. H.N. Ghosh's group at INST Mohali. They have been excellent collaborators and were always available for scientific discussions, which greatly enriched this work.

I am also grateful to IISER Pune for providing state-of-the-art facilities, a safe and encouraging work environment, and, most importantly, the fellowship that supported research. I would like to sincerely thank the Director of IISER Pune, the Chair of the Department of Chemistry, and the non-teaching and technical staff of IISER Pune. A special mention goes to Mr Nilesh Dumbre, Mr Mayuresh Kulkarni, and Mr Tushar for their support throughout this journey.

I would also like to express my gratitude to a key contributor whose occasional yet vital presence played an important role in this journey- Mr Morrison, our laser engineer. Nothing was more uplifting than his visits to the lab, ensuring the laser ran smoothly once again. Spending time with him during those troubleshooting sessions was a truly enriching and valuable learning experience.

I wish to express my heartfelt gratitude to my lab members, both past and present, Dr Sohini Sarkar, Dr Y. G. Reddy, Dr Sneha Banerjee, Dr Avinash Warankar, Dr Shabnum Maqbool, Rapti, Riteeka, Ziyad, Garvit, Nandana, and Sakshi for fostering a positive work environment. A loud shoutout goes to my incredible seniors-YGR, Sneha, and Avinash, who have always been there to help and support me in every possible way. Despite being busy with their lives now, they are still just a call away, and I am truly grateful for their constant encouragement. The countless memories shared with my labmates, not just in the lab but also during lab parties and trips, will always be cherished.

Now, for the most essential part of this journey, my friends at IISER Pune. Beyond this PhD degree, one of the most valuable gifts IISER Pune has given me is the lifelong friendship of these incredible people. Through the ups and downs, especially during difficult times, they were always there to support me, helping to keep me refreshed and away from the frustration of PhD life. I am deeply grateful to Manjeet Singh, Lakshmi, Vikas, Nilanjana, Pranjal, Pragalbh, and my two special seniors, Sneha and Avinash, who are also part of this cherished group. The endless memories we created together and the drive full of photographs will forever remind me of these beautiful times.

I want to express my gratitude to all my teachers, from school to university, who have played a pivotal role in shaping my academic journey. A special thanks goes to Prof. N.K. Awasthi from the University of Lucknow, thank you for your guidance. I am incredibly grateful to Mrs. Soni Shukla, whose teaching made chemistry so important in my life. She laid a strong foundation by clarifying the basics at the school level and turning chemistry into my favourite subject.

Last but certainly not least, I would like to express my deepest gratitude to my family, especially my parents, brother, and wife, Soumya. Without their unwavering support, patience, and belief in me, I wouldn't have reached this point. Their encouragement provided me with the strength to complete this journey. I am incredibly thankful to Soumya for her endless patience and support through every situation. Also, the short time we spent together at IISER Pune, sharing challenges and joyful moments, will always be a cherished memory.

List of Abbreviations

0D: Zero dimensional

1D: One dimensional

2D: Two dimensional

2-MPD: 2-methylpiperidine

3D: Three dimensional

ABCD: Air-biased coherent detection

AFM: Atomic force microscopy

ATC: Asymmetric transient current

BA: Butylammonium

BBO: Beta barium borate

BZ: Brillouin zone

CA: Close aperture

CB: Conduction Band

CBM: Conduction band minimum

$CsPbBr_3$: Cesium lead bromide

DFPT: Density functional perturbation theory

DFT: Density functional theory

DS: Drude-Smith

EMA/T: Effective medium approach/theory

EO: Electro-optic

EQE: External quantum efficiency

FA: Formamidium

FE: Free exciton

fs: femtosecond

FWM: Four wave mixing

FWHM: Full width at half maximum

GGA: Generalized gradient approximation

HMN: 2,2,4,4,6,8,8-heptamethyl nonane

HOIP: Hybrid organic inorganic perovskite

HVM: High voltage modulator

HTL: Hole transporting layer

IR: Infrared

IRF: Instrument response function

KE: Kinetic energy

LASER: Light amplification by stimulated emission of radiation

LD: Lower dimensional

LED: Light-emitting diode

LHP: Lead halide perovskite

LIDT: Laser induced damage threshold

LS: Light source

MA: Methylammonium

MBA: Methylbenzylammonium

meV: milli electron volt

mm: millimeter

MPA: 1-Phenylpropan-1-amine

MPEA: Methylphenethylamine

ms: millisecond

NCs: Nanocrystals

NIR: near-infrared

ns: nanosecond

OA: Open aperture

OD: Optical density

List of Abbreviations

OKE: Optical Kerr effect

OPA: Optical parametric amplifier

OPTP: Optical pump THz probe

OR: Optical rectification

PC: Photoconductivity

PCA: Photoconductive antenna

PCE: Power conversion efficiency

PEA: Phenethylammonium

PL: Photoluminescence

PLE: Photoluminescence excitation

PMT: Photomultiplier tube

PS: Polystyrene

ps: picosecond

PXRD: Powder X-ray diffraction

QY: Quantum yield

SCXRD: Single crystal X-ray diffraction

SFG: Sum frequency generation

SHG: Second harmonic generation

STE: Self-trapped exciton

STE: Self-trapped exciton

TAS: Transient absorption spectroscopy

TFISH: THz field induced second harmonic

THG: Third harmonic generation

THz: Terahertz

THz-TDS: Terahertz time-domain spectroscopy

TPA: Two photon absorption

TR-OKE: Time resolved optical Kerr effect

TRPL: Time resolved photoluminescence

TRTS: Time-resolved terahertz spectroscopy

UV-vis: Ultraviolet-visible

VB: Valence Band

VBM: Valence band maximum

μm: micrometer

μs: microsecond

Synopsis

Halide perovskites have gained significant attention for their versatile applications in photovoltaics, lasers, light-emitting diodes, photocatalysis, and photodetectors. This is attributed to their exceptional optoelectronic properties, ease of solution-based processing, and highly flexible crystal structures. Remarkably, when the size of perovskite crystals is reduced to the nanoscale, they exhibit extraordinary photophysical properties. In the ABX_3 perovskite structure, the dimensionality can be tuned from 3D to 0D by carefully selecting the A-site cations. Recently, lower-dimensional perovskites have gained attention as promising candidates for nonlinear optical applications. However, achieving even-order nonlinear responses, such as second-harmonic generation (SHG), is challenging due to the typically centrosymmetric nature of perovskite lattices. A breakthrough lies in hybrid perovskites, where introducing chirality into the inorganic sublattice using chiral A-site cations breaks the symmetry, paving the way for even-order nonlinear responses in these materials.

Doped transparent conducting oxides (TCOs) with crystallite sizes in the nanometer regime exhibit intriguing properties, including localized surface plasmon resonance (LSPR) behaviour similar to that of metal nanocrystals. Unlike metals, however, the free carrier density in doped TCO nanocrystals (NCs) can be precisely tuned by adjusting the dopant ion concentration, which directly influences the energy of the LSPR band. Studies suggest that co-doping with different cations can significantly alter the physical properties of the nanocrystals, such as their size. These changes, in turn, directly impact the quality factor (Q-factor) of the LSPR band. The LSPR Q-factor can be fine-tuned with precision by carefully selecting dopant cations. Despite these advancements, the exact mechanisms by which dopant ions influence the LSPR Q-factor and the underlying physical processes involved remain intriguing and open to further investigation.

In this thesis, we employed a range of ultrafast spectroscopic techniques to investigate the fundamental physical mechanisms in perovskites and doped semiconductor nanocrystals. Additionally, we explored the nonlinear optical properties of lead-free 0D chiral halides. Our study focused on charge carrier dynamics in $CsPbBr_3$ nanocrystals interfaced with inorganic hole-transporting layers, specifically CuI and Cu_2O. Furthermore, we examined the impact of co-doping Cr with Sn in In_2O_3 nanocrystals, analyzing how this modification influenced the system's physical properties, which led to an increase in the LSPR Q-factor.

Chapter 1: Introduction

In this chapter, we introduce the systems studied in this thesis and a brief overview of the spectroscopy techniques employed. The discussion begins with the role of inorganic hole transport layers (HTLs) in perovskite solar cells. These highly stable and cost-effective p-type inorganic materials have emerged as promising alternatives to conventional organic HTLs. Their incorporation into perovskite-based devices enhances both stability and cost efficiency, paving the way for potential commercialization. Beyond device architecture and materials, charge carrier dynamics play a pivotal role in determining device efficiency. Early-stage processes such as charge generation, interfacial transfer, and recombination mechanisms significantly influence performance. We highlight the importance of these processes and how ultrafast spectroscopic techniques, such as time-resolved terahertz (THz) spectroscopy and transient absorption spectroscopy, provide valuable insights into these critical early-time events.

Additionally, we explore the co-doping of Cr with Sn in In_2O_3 nanocrystals and its effect on the localized surface plasmon resonance (LSPR) Q-factor. THz time-domain spectroscopy offers direct evidence of changes in the material's dielectric constant with increasing Cr doping. Furthermore, Optical Kerr effect spectroscopy reveals how heavy Cr doping modifies optical phonon modes and tunes Kerr nonlinearity within the system. Lastly, we discuss low-dimensional chiral hybrid halides and their potential applications in nonlinear optics, emphasizing their relevance to emerging fields of research and technology.

Chapter 2: Experimental Methods and Data Analysis

In Chapter Two, we provide a detailed discussion of the spectroscopic techniques employed in this thesis and the data analysis procedures involved. All the spectroscopy setups were home-built, and custom LabVIEW programs were developed for data acquisition and analysis. The techniques covered include time-resolved terahertz spectroscopy (TRTS), Optical Kerr Effect (OKE) spectroscopy, terahertz time-domain spectroscopy (THz-TDS), the Z-scan technique, and nonlinear optical measurements (e.g., second-harmonic generation, SHG, and third-harmonic generation, THG).

We discussed the generation and detection of terahertz electromagnetic radiation using air plasma and how it can be utilized to study charge carrier dynamics in materials. For OKE spectroscopy,

the Fourier transform deconvolution technique is explained in detail, required for data analysis. Additionally, we provided the methodologies for both open and closed-aperture Z-scan techniques, which are used to measure the nonlinear absorption coefficient (β) and nonlinear refractive index (n_2).

Chapter 3: Ultrafast Hole Injection Dynamics in $CsPbBr_3$ Nanocrystals with Inorganic Hole Transporting Layers

This chapter explores the charge carrier dynamics in $CsPbBr_3$ nanocrystal (NC) films paired with copper-based inorganic hole-transporting materials (HTMs) such as CuI and Cu_2O. Using time-resolved techniques like time-resolved photoluminescence (PL), terahertz (THz) spectroscopy, and femtosecond transient absorption spectroscopy, we observed ultrafast hole injection from $CsPbBr_3$ NCs to the HTMs, occurring within a sub-picosecond timeframe. This process also includes the transfer of hot carriers. While both CuI and Cu_2O serve effectively as HTLs for $CsPbBr_3$ NCs, Cu_2O demonstrates significantly higher rates of hole transfer and overall efficiency. Its excellent stability, solution processability, cost-efficiency, and superior hole extraction capability make these inorganic materials a standout candidate for HTL applications.

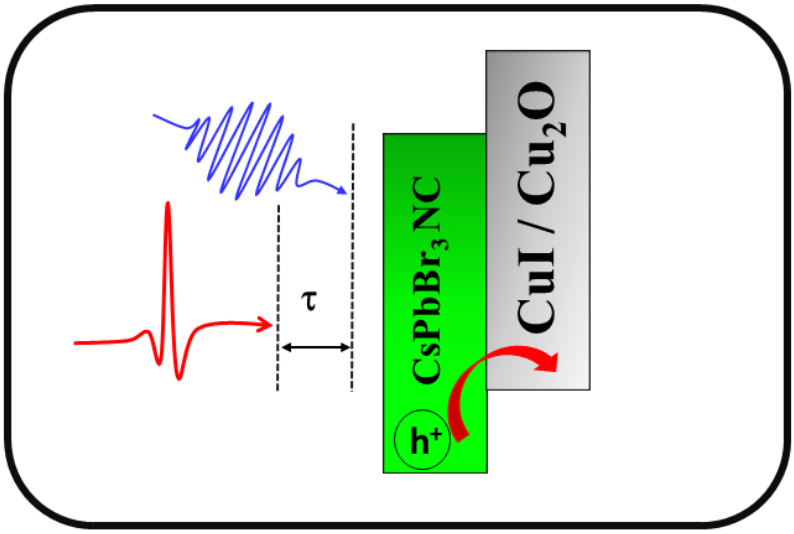

Chapter 4: Effect of Cr co-doping on Dielectric Constant and Kerr Nonlinearity in Sn-doped In_2O_3 Nanocrystals.

In this chapter, we examined how Cr co-doping with Sn in In_2O_3 nanocrystals (NCs) influences the dielectric constant of the medium. Terahertz time-domain spectroscopy (TH-TDS) revealed an

increase in the dielectric constant, which could be the reason for reduced ionic impurity scattering, as a higher dielectric constant weakens Coulombic interactions between ionic dopants and free carriers. Kerr nonlinearity measurements showed the slowest decay in Kerr nonlinearity for samples with the highest Cr concentration, with relaxation times increasing as Cr doping levels rose. This characteristic highlights their potential for ultrafast optical switching applications. Additionally, spectral density analysis from optical Kerr effect (OKE) experiments indicated a shift in vibrational modes toward lower frequencies with Cr doping. A significant phonon mode in the GHz range was also observed in the Cr-Sn co-doped samples, further emphasizing their unique optical and electronic properties.

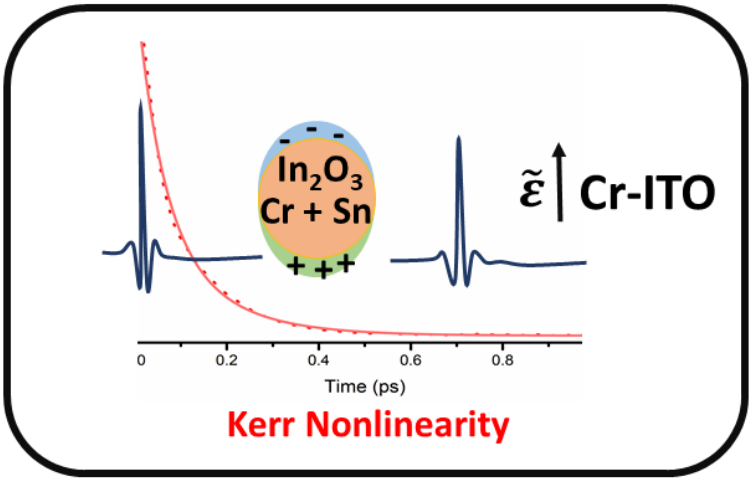

Chapter 5: Nonlinear Optical Properties of 0D Chiral Bismuth Iodides

In this chapter, we explored the second-and third-order nonlinear optical properties of 0D chiral hybrid perovskite derivatives (*R*-/*S*-MBA)$_4$Bi$_2$I$_{10}$, where MBA represents methyl benzyl ammonium, alongside their achiral counterpart (*Rac*-MBA)$_4$Bi$_2$I$_{10}$. The chiral derivatives (R-/S-(*R*-/*S*-MBA)$_4$Bi$_2$I$_{10}$ exhibit second-harmonic generation (SHG) and significantly stronger third-harmonic generation (THG) responses under femtosecond near-infrared (NIR) excitation in the 1360–1590 nm range. Notably, the achiral counterpart (*Rac*-MBA)$_4$Bi$_2$I$_{10}$ produces the highest THG intensity among the samples.

Z-scan measurements on thin films of these 0D perovskitoids, performed under femtosecond laser excitation at 800 nm, reveal exceptionally high nonlinear absorption coefficients (β) and nonlinear refractive indices (n_2), with the achiral (*Rac*-MBA)$_4$Bi$_2$I$_{10}$ exhibiting the highest values. The

combination of strong THG responses, large β and n_2 values, and excellent optical stability positions these materials as promising candidates for advanced nonlinear photonic applications.

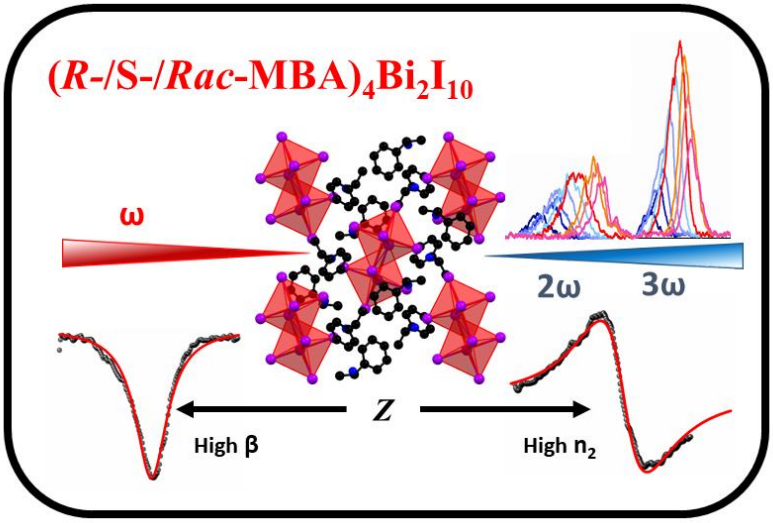

Table of Contents

Chapter 1

Introduction

1.1. Perovskite Solar Cell

The world is grappling with an energy crisis that poses a significant threat to both the environment and economic stability. This growing demand places immense pressure on limited fossil fuel resources such as coal, oil, and natural gas. As these resources become scarcer, the need for sustainable and renewable energy alternatives becomes more urgent. One of the most promising avenues for meeting future energy demands is the conversion of sunlight into electricity, a process that does not contribute to adverse climate change.[1] Currently, scientists aim to design photovoltaic devices that are highly efficient, low-cost, and suitable for large-scale production.[2] For solar cell technology to be successfully implemented on a global scale, significant improvements in materials and devices are needed to increase power conversion efficiency and lower production costs.[3]

In the last two decades, Perovskite solar cells (PSCs) have recently gained widespread recognition as a viable and cost-effective renewable energy technology, offering an alternative to traditional solar cells.[4] The field of perovskite solar cell research is progressing quickly, with continuous advancements in stability, scalability, and efficiency by optimizing material design, device architecture, and processing conditions.[5] In just a few years, there has been a remarkable increase in efficiency from 3.8% to 26.1%,[6] significantly surpassing the performance of many established commercial photovoltaic technologies, such as gallium arsenide (GaAs), cadmium telluride (CdTe) and silicon (Si) solar cells.[7]

The ABX_3 organometallic halide perovskite refers to a crystal structure where 'A' represents an inorganic or organic cation, such as Cs^+, methylammonium ($CH_3NH_3^+$) or formamidinium ($NH_2CHNH_2^+$) ion; 'B' stands for a metal ion like lead (Pb^{2+}), tin (Sn^{2+}), or cadmium (Cd^{2+}); and 'X' denotes a halogen ion, such as iodide (I^-), bromide (Br^-), or chloride (Cl^-). A three-dimensional network of corner-sharing BX_6 octahedra constitutes the structure, with the A ion positioned in the cuboctahedral spaces between them (Figure 1). The perovskite structure can vary from the ideal cubic lattice if a larger A cation is used.[8] Metal halide perovskites exhibit a broad absorption range that spans from the visible to the near-infrared spectrum (300–800 nm) and have a high extinction coefficient.[9] This results in efficient light absorption even in films with a few hundred nanometers thicknesses. Additionally, perovskites have a low exciton binding energy (20–30 meV), long and

relatively balanced carrier diffusion lengths, ambipolar carrier transport capability, and notable defect tolerance.[10-13] This facilitates efficient carrier dissociation, separation, and minimal loss during transport, making perovskites an excellent choice for photovoltaic applications.[14-17]

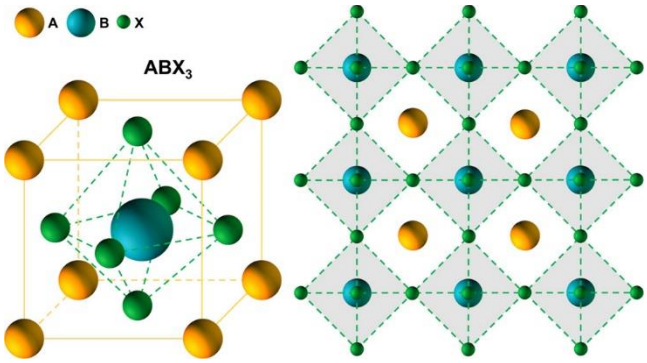

Figure 1. The cubic perovskite crystal structure consists of a network of corner-sharing BX_6 octahedra, with the A-site cations occupying the voids between these octahedral (reprinted with permission from ref. 17).

1.1.1. Inorganic Hole Transport Layers

Various device configurations have been developed for perovskite solar cells (PSCs). Figure 2 shows a typical cell structure involving an active perovskite absorber layer sandwiched between electron and hole transport layers (ETL and HTL).[18] These carrier-transporting layers enable efficient and irreversible separation of the photogenerated electrons and holes in the perovskite. Based on the arrangement of layers (Figure 3), PSCs can be categorized into two main architectures: n–i–p and p–i–n structures. In the n–i–p configuration, often referred to as the conventional structure, HTLs are on the top of the perovskite layers.[19] In contrast, the p–i–n structure, known as the inverted structure,[20] features the HTL-coated substrate where light enters the device. In this setup, the optical properties of HTL also play a crucial role in achieving high efficiency in PSC.[21-22]

Typically, transparent conducting oxides are used as electron transport layers (ETLs), while conducting organic materials like Spiro-OMeTAD,[23] PTAA,[24], and PEDOT[25] serve as hole transport layers (HTLs).[26] Although these organic HTLs are effective, but they are expensive and sensitive to humidity.[27] In response, several inorganic p-type materials, such as CuI, Cu_2O, NiO, and CuSCN, have emerged as alternatives to organic HTLs.[28] These inorganic HTLs offer a

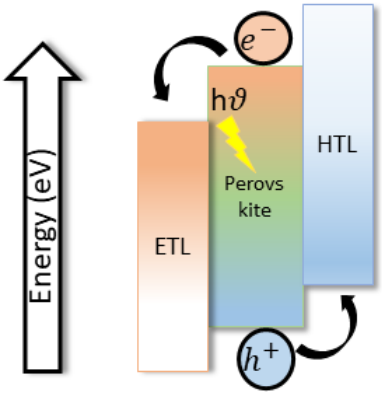

Figure 2. A typical PSC structure consists of an active perovskite absorber layer positioned between an electron transport layer (ETL) and a hole transport layer (HTL). With appropriate band alignment, these carrier-transporting layers provide the necessary thermodynamic driving force to facilitate efficient and irreversible separation of photoexcited electrons and holes within the perovskite layer.

compatible band gap, high carrier mobility, and long carrier lifetime, which ensure effective hole extraction and enhance solar cell efficiency.[29] Additionally, they are more cost-effective, visible light transparent and stable against heat, moisture, oxygen, and UV light compared to the organic

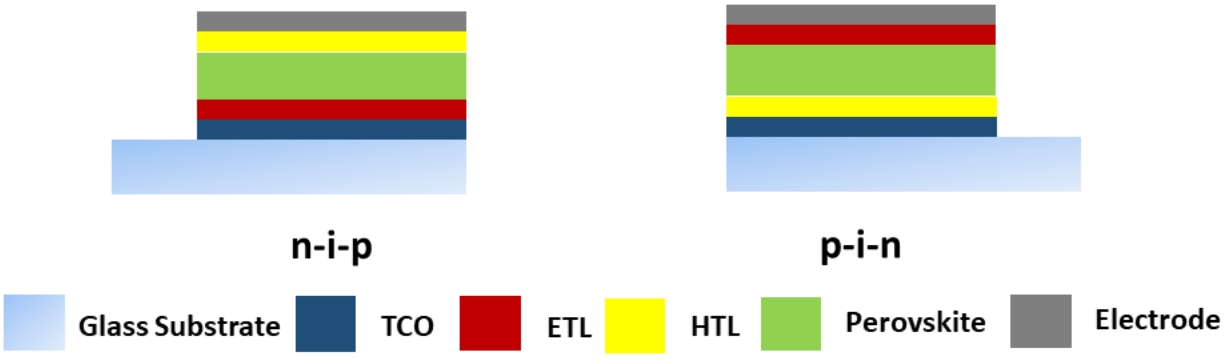

Figure 3. n-i-p and p-i-n design scheme of PSCs. Light illumination enters the device from the glass substrate side. In the n-i-p structure, it first passes through the electron transport layer (ETL) before reaching the perovskite absorber layer. In contrast, the p-i-n configuration directs light through the hole transport layer (HTL) before it encounters the perovskite layer. For optimal

performance in the p-i-n structure, the HTL must be transparent to visible light to ensure high device efficiency.

HTLs.[30] Even these inorganic HTLs can also provide stability to moisture-sensitive perovskite layers.[21, 31] As perovskite solar cells move towards commercialization, factors like material stability and processing costs become crucial, making inorganic HTLs a promising option for industrial applications.

1.1.2. Charge Carrier Dynamics in Perovskite Solar Cell

The outstanding performance of PSCs stems from both the unique optoelectronic characteristics of perovskite materials and extensive advancements in optimizing crystal quality, refining device architectures and interfaces, and unravelling the fundamental physics and chemistry involved.[32] This swift development in perovskite photovoltaic research further paves the way for investigating novel material systems and device theories. The direct conversion of solar energy into electricity in PV involves a series of charge processes occurring over timescales ranging from femtoseconds to seconds (Figure 4).[33] Unveiling these processes is crucial for developing effective design principles for PV materials and devices.

When a photon with energy equal to or greater than the bandgap energy (Eg) interacts with electrons in the valence band, it excites them, leading to the formation of excitons or free carriers.[34] In semiconductors like perovskites, where the exciton binding energy (E_b) is comparable to or lower than the thermal energy (26 meV), the rate of free carrier generation is typically high.[35] These photoexcited species are generated within a timescale ranging from femtoseconds to picoseconds. In solar cells, the type of photoexcited species—whether excitons or free carriers—plays a critical role in determining the device's working mechanism and design.[36] Free carriers are then transported through charge transport layers and ultimately collected at the electrodes. However, a portion of these carriers is lost due to bulk and interfacial recombination during the process. To achieve high photocurrent, ensuring a high carrier extraction rate, extended carrier lifetime, and minimal interfacial recombination is essential. The early-stage events, such as charge generation, relaxation, and interface transfer, occurring on a picosecond timescale [37] are crucial for governing the charge carrier dynamics and overall device performance.[38-40]

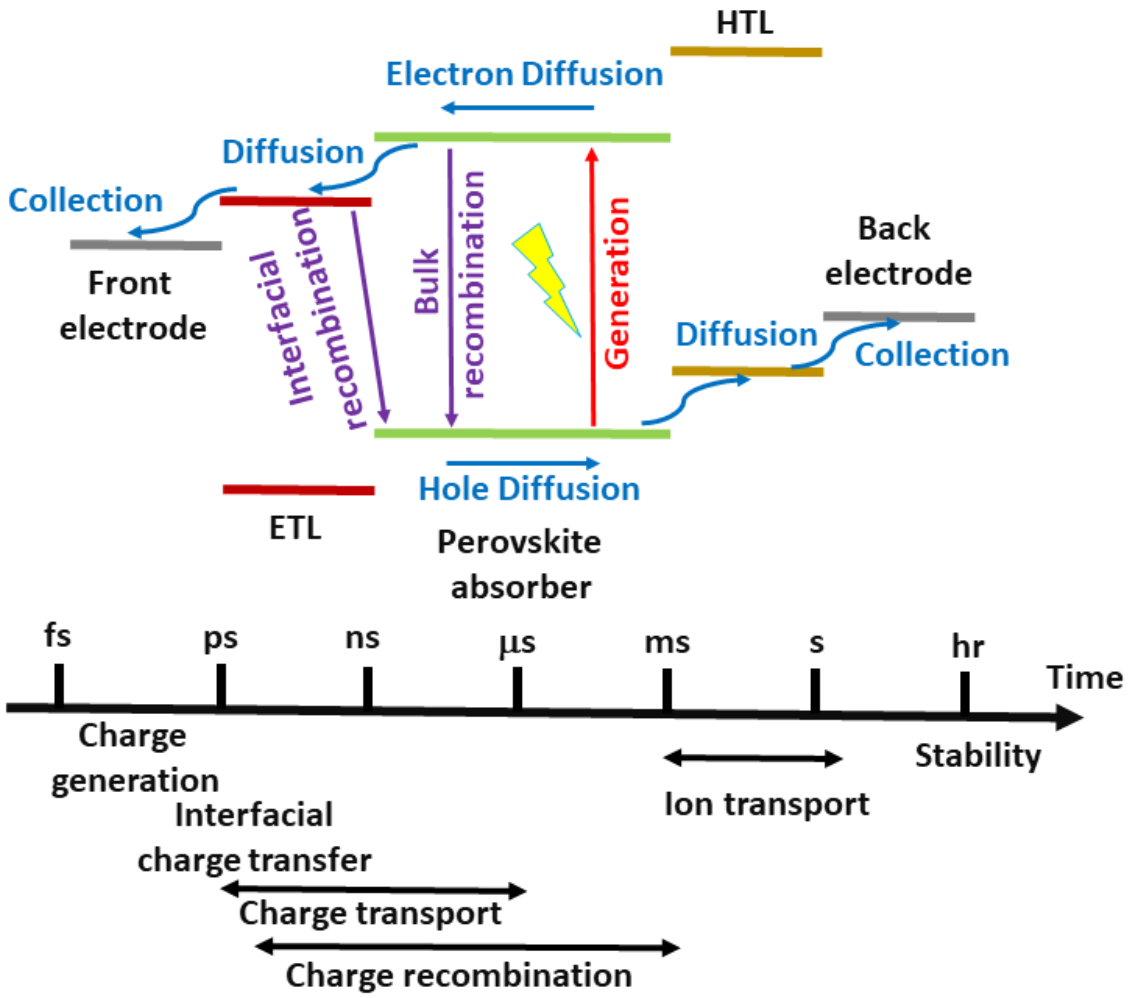

Figure 4. Possible processes in PSCs after photoexcitation and corresponding time scales.

Pump-probe spectroscopic techniques, which use femtosecond pulse lasers and optical delays, have been crucial in revealing these essential ultrafast charge processes in semiconductors.[41-43] Charge carrier dynamics in perovskite materials have been thoroughly investigated using different ultrafast pump-probe spectroscopy techniques, such as transient absorption spectroscopy[44-45] and time-resolved THz spectroscopy.[46-50]

1.1.3. Time-Resolved THz Spectroscopy

Spectroscopy using radiation in the terahertz (THz) frequency range is a powerful technique for examining charge carrier dynamics in semiconductors.[46, 51] The frequency of 1 THz is equivalent

to 1 picosecond (ps) in time and four milli-electron volts (meV) in energy. THz radiation can resonate with processes involving energies in the meV range, such as low-energy collective vibrational motions in condensed phases and biological systems, high-energy rotational motions in small molecules, and phonon vibrations in solids.[52-54] THz photons can also interact with free charge carriers or excitons produced after the photoexcitation of semiconductors. The presence of charge carriers significantly alters a medium's dielectric response in the low-frequency range, which induces changes in the phase and amplitude of the THz electric field.[38]

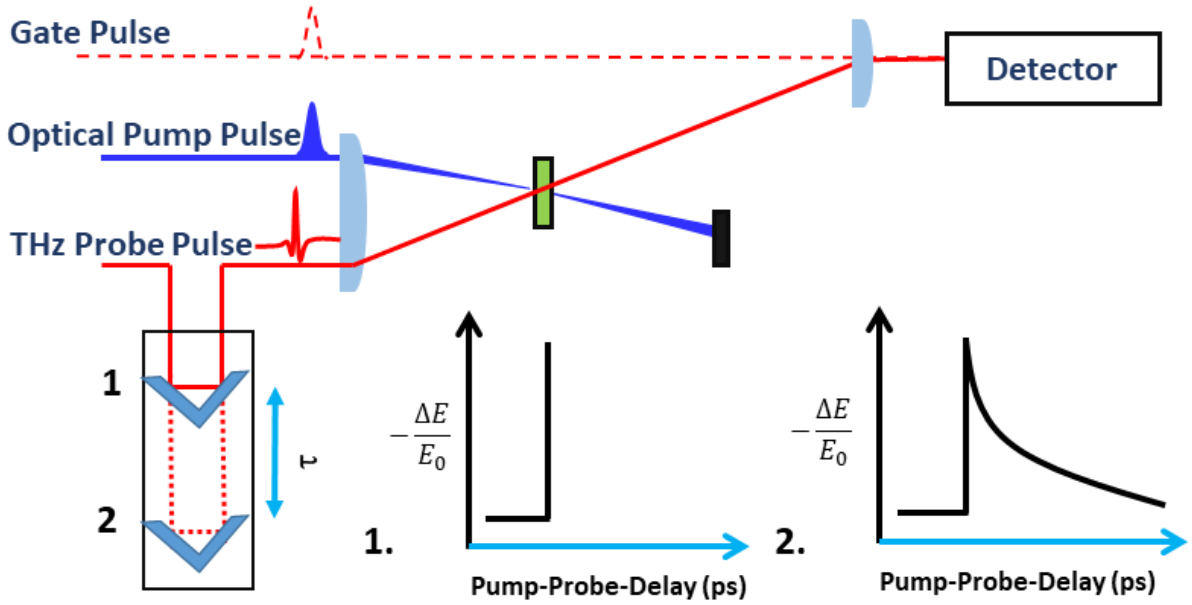

Figure 5. Schematic representation of Time-resolved THz spectroscopy (TRTS) technique. An optical pump pulse excites the sample, and then an optically delay probe pulse interrogates the excited sample, capturing the transient change in photoconductivity of the sample.

Time-resolved THz spectroscopy (TRTS) enables the tracking of time-dependent changes in the electric field amplitude of a single-cycle THz pulse transmitted through a sample, measured as a function of the time delay following optical excitation. A schematic of the TRTS setup is presented in Figure 5. As illustrated in Figure 5, the optical pump beam initially excites the sample. Following this, a THz probe beam passes through the sample via an optical delay stage. TRTS spectroscopy involves two types of experiments. In the first type, we monitor the photoinduced

change in peak amplitude of the THz electric field transmitted through the photoexcited sample. This experiment gives the frequency-averaged response of the sample. The optical pumping generates free charge carriers in the semiconductor, leading to a modulation in the amplitude and phase of the interacting THz electric field. This change in the THz electric field is recorded as a function of time delay between the optical pump pulse and THz probe pulse. The photoinduced change in photoconductivity of material is directly proportional to the modulation in the THz electric field amplitude ($-\Delta E/E_0$). The observed transients indicate changes in photoconductivity, defined as $\Delta\sigma = e\mu n$, where 'e' is the elementary charge, 'μ' is the charge-carrier mobility, and 'n' is the density of photo-induced charge carriers. As depicted in Figure 5, when the delay stage is at position 1, the probe beam reaches the sample immediately after photoexcitation (t = 0), resulting in a rise in transient photoconductivity, indicating an increase in charge carrier density and/or mobility. As the delay stage moves to position 2, a subsequent decrease in the photoconductivity signal is observed. This decrease in the photoconductivity signal is typically associated with charge-carrier dynamics, such as recombination or transfer across interfaces. By knowing the absorbed photon density and the photon-to-free carrier conversion ratio (ϕ), the charge-carrier mobility can be determined from the initial ($-\Delta E/E_0$) values without physical contact.[15, 47]

In the other part of the TRTS experiment, we scan the entire THz probe waveform in time-domain at several narrowly spaced pump-probe delay times. Subsequent Fourier transformation of this data provides frequency-resolved complex dielectric function of the excited state at different chosen pump-probe delays. We can derive other important excited state properties of the sample, such as absorption coefficient, refractive index, and complex conductivity. The experimental setup and details of the TRTS technique are given in Chapter 2.

1.1.4. Transient Absorption Spectroscopy

Femtosecond transient absorption spectroscopy (TAS) is a widely used time-resolved technique. This pump-probe technique delivers crucial insights into the transient dynamics of samples in their excited state.[55] A femtosecond pulsed laser output is divided into two beams with different energies using a beam splitter. One of these beams, a high-energy monochromatic pulse, serves as the pump to excite the sample. A weaker probe pulse (monochromatic or broadband white light continuum (WLC)), delayed by a time τ relative to the pump pulse, interrogates the excited sample (Figure

6). The detector measures the probe pulse intensity alternately from the excited sample (pump on, $I(\lambda)_{pump\text{-}on}$) and the unexcited sample (pump off, $I(\lambda)_{pump\text{-}off}$). The difference in absorbance ($\Delta A(\lambda) = -\log(I(\lambda)_{pump\text{-}on} / I(\lambda)_{pump\text{-}off})$) provides insights into the generation and evolution of transient products.[55] This technique can cover a probe wavelength span from the UV-visible to the infrared, and a study time range from a few femtoseconds to nanoseconds. The TAS data of optoelectronic functional materials can reveal information about ultrafast photophysical processes such as electron transitions, carrier relaxation, recombination, and charge transfer across interfaces.[39, 45, 56-57] TAS can investigate both radiative and nonradiative processes within a system and provide detailed information about the dynamics of the excited state.[58] TAS operates based on Lambert-Beer's law, necessitating good photon transmission for accurate analysis.

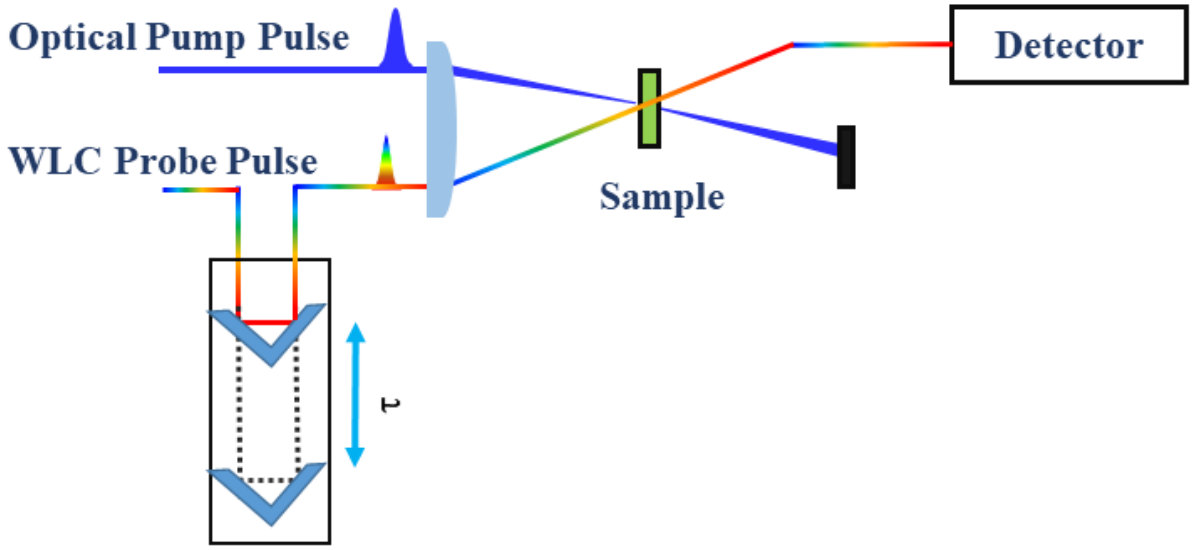

Figure 6. Schematic representation of Transient absorption spectroscopy technique.

1.2. Localized Surface Plasmon Resonance (LSPR) in Doped Conducting Oxide Nano Crystals

Transparent conducting oxides (TCOs) are specialized materials that exhibit the rare combination of high electrical conductivity and transparency to visible light.[59-60] This dual functionality makes

TCOs essential in the optoelectronic industry, where they are used as transparent electrodes in applications such as solar cells, light-emitting diodes, and flat-panel displays. These TCOs display intriguing properties when their crystallite size is reduced to a few nanometers. Nanocrystals (NCs) of doped metal oxides, such as In-doped CdO, Sn-doped In_2O_3 (ITO), Al-doped ZnO and other materials, exhibit Localized Surface Plasmon Resonance (LSPR) in the near-infrared (NIR) to mid-infrared (MIR) range.[61] This resonance occurs when the free charge carriers in the nanocrystals oscillate in response to the frequency of the incident electromagnetic radiation. Like metal NCs, free-charge carriers generate LSPR in TCO NCs. However, there are significant differences between the two.[62] In TCOs, the free electron density can be adjusted by varying the dopant concentration, allowing for LSPR bands that can be tuned across the near-infrared (NIR) to mid-infrared (MIR) range (approximately 1300 to 4000 nm).[60]

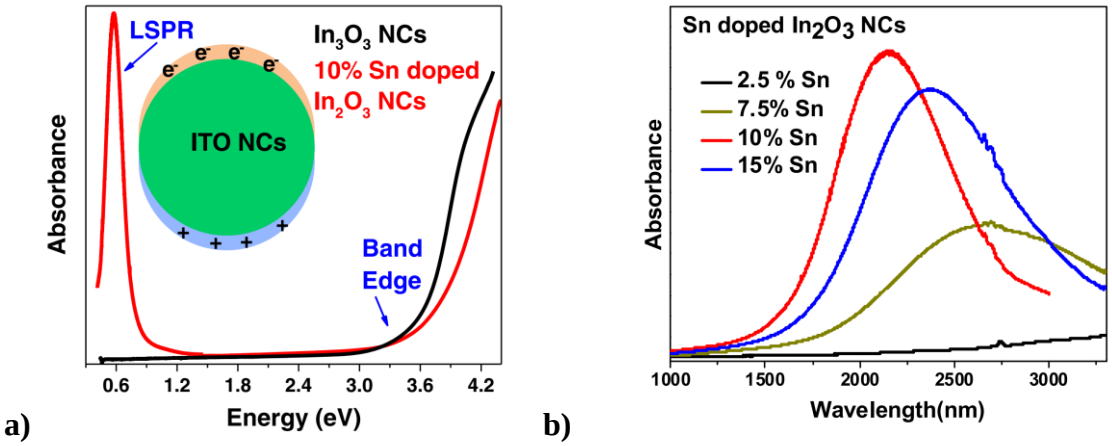

Figure 7. (a) 10 % Sn-doped In_2O_3 NCs showing LSPR band in NIR region (red), no LSPR band in undoped In_2O_3 NCs (black). **(b)** Change in LSPR Q factor (FWHM and peak energy) of Sn-doped In_2O_3 NCs with the increase in dopant concentration (reprinted with permission from ref [63]).

This level of tuning is not feasible with metal NCs.[62] Additionally, TCOs can be co-doped; for example, in Fe–Sn co-doped In_2O_3 NCs, free electrons from Sn^{4+} interact with magnetic spins from Fe^{3+}, resulting in unique magnetoelectric and magneto-optic properties not seen in metal NCs.[64] Metal NCs typically exhibit strong LSPR bands in the visible spectrum, whereas TCO NCs are transparent to visible light. Thus, the NIR and MIR LSPR from TCO NCs can complement the visible LSPR of metal NCs, making them suitable for applications that span a different and broader range of electromagnetic spectrum.

1.2.1. Cr-Sn co-doped In_2O_3 Nanocrystals

Bharat *et al.* designed colloidal Cr-Sn co-doped In_2O_3 NCs that exhibit a record LSPR Q factor.[65] The Q factor is defined as the ratio of the LSPR band's peak energy to its full width at half maximum (FWHM). A higher Q-factor signifies lower electronic damping, extended plasmon lifetimes, and enhanced near-field effects.[66-67] This makes the material particularly advantageous for advanced applications such as photovoltaics and sensing.[68-69] The LSPR band's peak energy depends directly on the free charge carrier density, and FWHM increases with free carrier scattering. However, the dopant ions which increase the free charge carrier density also act as electron scattering centres.[70] In this case, Sn^{4+} dopants increase the free charge carrier density but also act as electron scattering centres by forming complexes with interstitial oxygen, leading to an increased FWHM and a decreased Q factor.

High LSPR Q factors typically require high peak energy and minimal carrier scattering. These properties are often mutually exclusive, resulting in lower Q factors for doped semiconductor and metal oxide NCs. However, Cr^{3+} codoping with Sn^{4+} in In_2O_3 NCs significantly enhances the Q factor. The observed reduction in FWHM and increased LSPR peak energy with higher Cr^{3+} doping concentrations indicate increased carrier density and reduced carrier scattering. While Cr^{3+} doping does not introduce extra electrons, it increases the nanocrystal size.

In this thesis, to further investigate Cr-Sn co-doped In_2O_3 nanocrystals (NCs) and to explore the factors contributing to the significant increase in the LSPR Q factor beyond the observed increase in nanocrystal size, Terahertz Time Domain spectroscopy (THz-TDS) was employed. Also, given that indium tin oxide (ITO) exhibits high optical nonlinearity, optical Kerr effect (OKE) spectroscopy was used to examine how charge carrier density affects Kerr nonlinearity.

1.2.2. THz Time Domain Spectroscopy (THz-TDS)

Terahertz time-domain spectroscopy (THz-TDS) is a versatile technique widely used for material characterization and process control.[71] It enables non-destructive analysis of samples across various fields, including chemistry,[72] materials science,[73] engineering,[74] and medicine.[75-76] THz-

TDS, a steady-state spectroscopy method that can be performed in either transmission or reflection mode. The technique involves generating and detecting single-cycle pulses of radiation. In our home-built setup, THz electromagnetic radiation is generated by focusing 45 fs, 800 nm-centered pulses and their second harmonic in ambient air. This radiation interacts with the sample before reaching the detector. Unlike classical spectroscopy, which measures the intensity of electromagnetic waves, THz-TDS captures the time-dependent electric field waveform of the THz pulse after sample interaction. This approach enables simultaneous determination of the refractive index and absorption coefficient, providing complex refractive indices and conductivity values for the sample.[71] As a result, THz-TDS serves as a contact-free method for measuring conductivity in materials such as metals, semiconductors, 2D materials, and superconductors.[77-78] Detailed descriptions of the setup and methodology are provided in Chapter 2.

Figure 8. The change in the THz electric field waveform after interaction with the sample (green). Alterations in both the amplitude and phase relative to the reference THz waveform (shown in red). The change in the phase and amplitude of the THz electric field provides direct information about the sample's absorption coefficient (α) and refractive index (n). Using these parameters, other properties such as the extinction coefficient (k), complex refractive index (n̂), complex dielectric function (ε̂), and complex conductivity (σ̂) can be determined.

1.2.3. Optical Kerr Effect (OKE) Spectroscopy

Since it was first demonstrated in 1969,[79] optical Kerr effect (OKE) spectroscopy has become a popular method for investigating ultrafast dynamics in transparent fluids.[80] OKE spectroscopy has significantly enhanced our understanding of the microscopic behaviour of fluids, including simple

liquids. This technique offers direct insights through time-resolved observations of collective orientational diffusion and the dynamics of Raman-active intramolecular and intermolecular modes.[81]

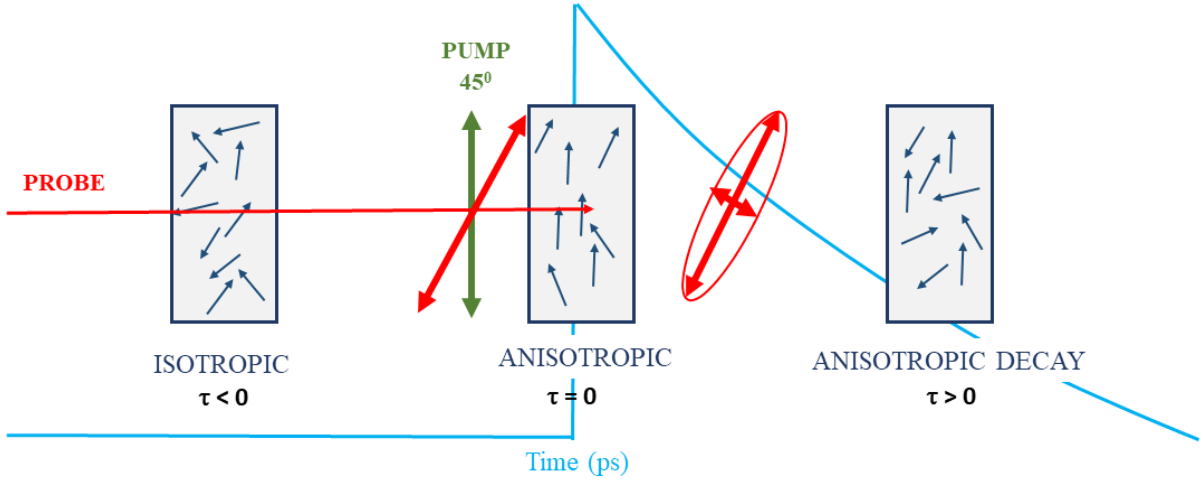

Figure 9. Schematic representation of Optical Kerr Effect in the medium. An intense laser pump pulse creates transient birefringence in an isotropic medium, and the probe pulse polarization is modulated by laser-induced anisotropy in the medium.

OKE spectroscopy is a pump-probe technique where a pump pulse, polarized at 45 degrees, excites an isotropic sample. The intense laser pump pulse induces birefringence in the sample as the electric field interacts with molecular dipole moments, causing some degree of net alignment (Figure 9). A probe pulse, with a variable time delay relative to the pump pulse and polarized vertically, enters the now anisotropic excited sample. The induced birefringence causes depolarization of the probe pulse. By varying the delay between the two pulses, the time-dependent birefringence can be measured, revealing information about the microscopic dynamics of the sample.[81-82] Detailed descriptions of the setup and data analysis are provided in Chapter 2.

1.3. Chiral Hybrid Metal Halide Perovskites

An object is considered chiral if it cannot be superimposed on its mirror image. A substance is chiral in chemistry if its molecules cannot align with their mirror images. This chirality arises from the lack of an improper axis of rotation (S_n), typically found in molecules with non-

centrosymmetric structures. Molecules and their non-superimposable mirror images are known as enantiomers, which can differentiate between left and right circularly polarized light. These materials exhibit unique properties, such as circular dichroism (CD), ferroelectricity, circularly polarized photoluminescence (PL), and nonlinear optical effects (NLO). Such characteristics make them valuable for applications in biology, chemistry, medicine, optics, and spintronic devices.[83]

As previously mentioned, halide perovskites have established themselves as significant optoelectronic materials with various applications, including light-emitting diodes, photonic lasers, solar cells, and photodetectors. In addition to their excellent optoelectronic properties, these

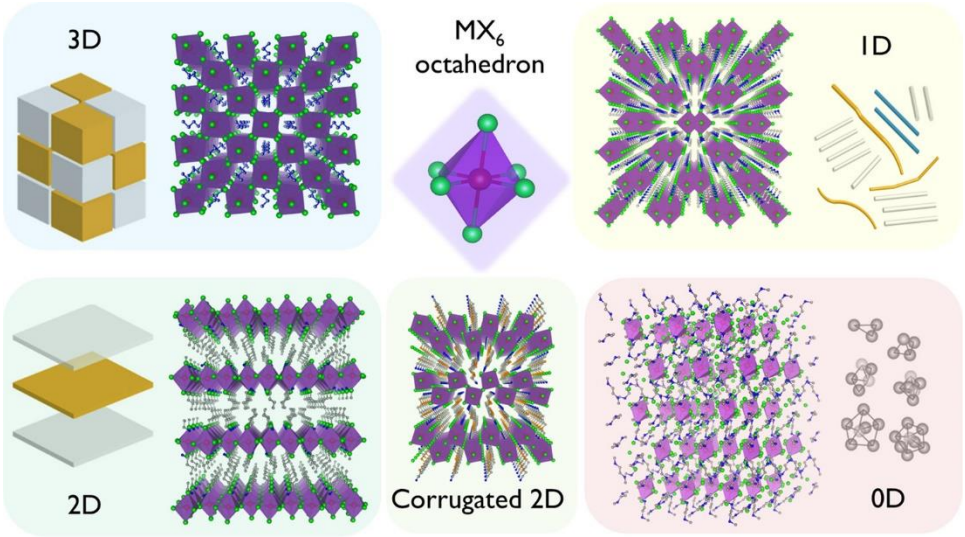

Figure 10. Typical 3D, 2D, 1D and 0D perovskite structures were synthesized with different combinations of A and B cations (reprinted with permission from ref. 79).

materials possess flexible structures. In cubic halide perovskite ABX_3, the B site is surrounded by six nearest neighbour anions (X), while the A cation is surrounded by twelve nearest neighbours. If a larger cation is placed at the A site, disrupting the tolerance factor, the cubic structure will distort, reducing crystal symmetry. Researchers have synthesized lower-dimensional perovskites by incorporating larger A cations, such as long-chain alkyl amine anions. By selecting appropriate A cations, the dimensionality can be precisely adjusted from 3D to lower dimensions, including 2D, 1D, and 0D (Figure 10).[84] The BX_6 octahedra form the inorganic sublattice, primarily

influencing the optical and electronic properties. However, these inorganic sublattices are always centrosymmetric and achiral.

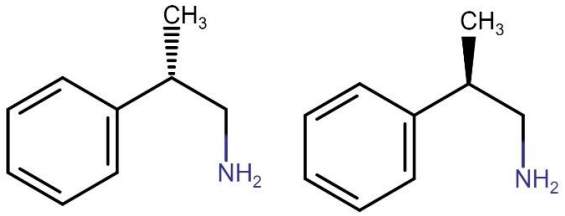

Figure 11. Chiral organic amines enantiomers R-MBA and S-MBA, where MBA refers to methylbenzylammonium.

Recently, researchers have discovered methods to introduce chirality into the inorganic sublattice, resulting in a chiral perovskite structure.[85] One approach uses a chiral organic A cation (like R-MBA and S-MBA in Figure 11), which interacts asymmetrically with the inorganic sublattice, distorting the BX_6 octahedron.[86-87] This deliberate introduction of chirality in perovskites combines the excellent properties of perovskites with the unique characteristics of chirality.[88] Chiral perovskites show potential for applications in chiral ferroelectrics,[89] circularly polarized photodetectors,[90] circularly polarized light emitters,[91-92] and nonlinear optical effects.[93-96] The first chiral halide perovskites were reported by Billing *et al.*[97], while the chiroptical properties were first investigated by Ahn *et al.* in 2017.[98] The research and exploration of chiral perovskites and their chiroptical properties are still in the early stages.

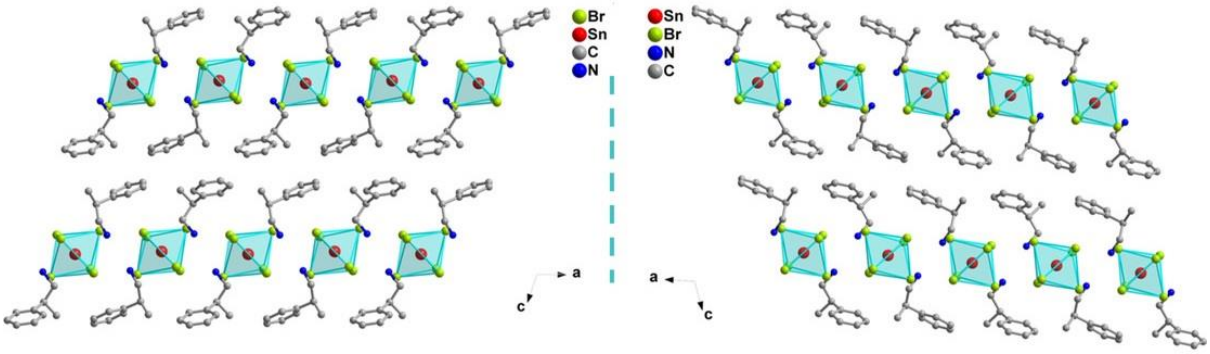

Figure 12. Crystal structures of chiral perovskites enantiomers (R-MPEA)$_2$SnBr$_6$ and (S-MPEA)$_2$SnBr$_6$ along b axis showing mirror symmetry. Here, MPEA refers to methylphenylethylamine, a chiral organic amine cation that introduces chirality into the inorganic sublattice, thereby making the perovskite structure itself chiral (reprinted with permission from ref. 102).

1.3.2. Nonlinear Optical (NLO) Effects

Nonlinear optical effects occur when high-intensity laser radiation interacts with matter in a nonlinear manner.[99] When an optical field is applied to a material, it induces polarization within the material. In the linear regime, the induced polarization (P) is directly proportional to the strength of the applied electric field (E). This induced polarization, defined as the net average dipole moment per unit volume, can be expressed as:

$$P = \varepsilon_0 \chi E$$

where ε_0 is the permittivity of free space, and χ is the optical susceptibility. However, when intense monochromatic laser beams with electric field strengths comparable to atomic fields are applied, the relationship between induced polarization P and electric field E becomes nonlinear. This nonlinear interaction alters the optical properties of the material, leading to phenomena such as higher harmonic generation, the Kerr effect, sum frequency generation, and difference frequency generation. In the nonlinear regime, the induced polarization changes nonlinearly with the applied electric field strength, as described by the equation:

$$P = \varepsilon_0 \left[\chi^{(1)} E + \chi^{(2)} E^2 + \chi^{(3)} E^3 + \chi^{(4)} E^4 \ldots \right]$$

Here, $\chi^{(1)}$ is the linear susceptibility, $\chi^{(2)}, \chi^{(3)}, \chi^{(4)}$, and so on, are the second, third, and fourth-order nonlinear susceptibilities, respectively. At higher intensities, these higher-order terms ($\varepsilon_0 \chi^{(n)} E^n$(n>1)) become significant and produce nonlinear polarization. According to Maxwell's electromagnetic equations, this nonlinear polarization modulates light propagation in dielectrics, leading to the generation of light fields with new frequencies and direct changes to the incident light field. The various nonlinear optical (NLO) effects resulting from this interaction have

versatile applications, including photon energy up-conversion, electro-optical (EO) modulation, and ultrafast all-optical switching.[100]

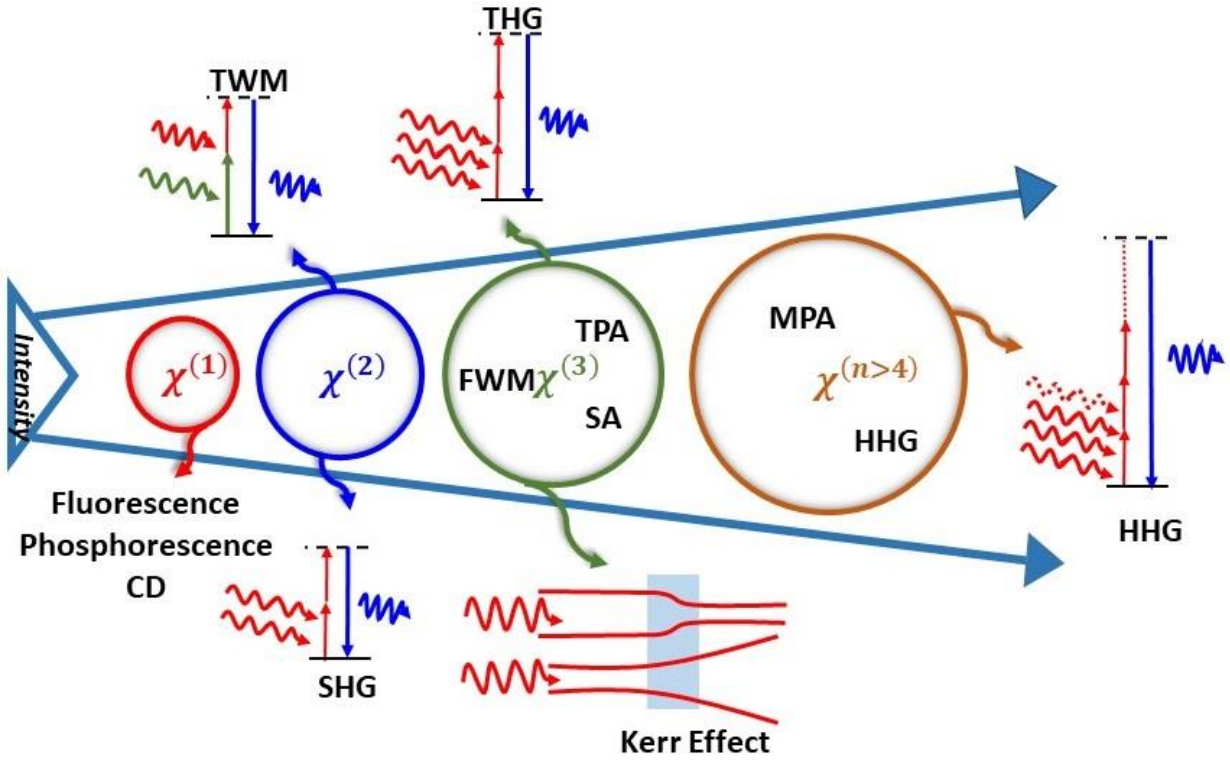

Figure 13. Schematic representation of various nonlinear optical processes associated with second and higher-order nonlinear susceptibilities.

Exploring high-quality nonlinear optical (NLO) materials is quite challenging. However, recent advancements have highlighted halide perovskites as promising candidates for NLO device applications, thanks to their tunable bandgap and large optical oscillator strength.[101-102] Notably, low-dimensional hybrid metal halide perovskites exhibit strong quantum confinement and have demonstrated exceptional NLO effects.[84, 103]

1.3.3. NLO Properties in Chiral Hybrid Metal Halide Perovskites

Non-centrosymmetric crystal structures are essential for nonlinear optical effects associated with even order susceptibilities, such as Second Harmonic Generation (SHG). However, halide perovskites typically have centrosymmetric structures, making it challenging to achieve an SHG response. Introducing chirality into perovskites addresses this issue and provides asymmetric crystal structure. Recent studies of chiral perovskites have shown that their non-centrosymmetric chemical structures, combined with tunable bandgaps, large NLO coefficients, and significant exciton binding energies, position them as promising candidates for NLO applications.[93-94, 104-108]

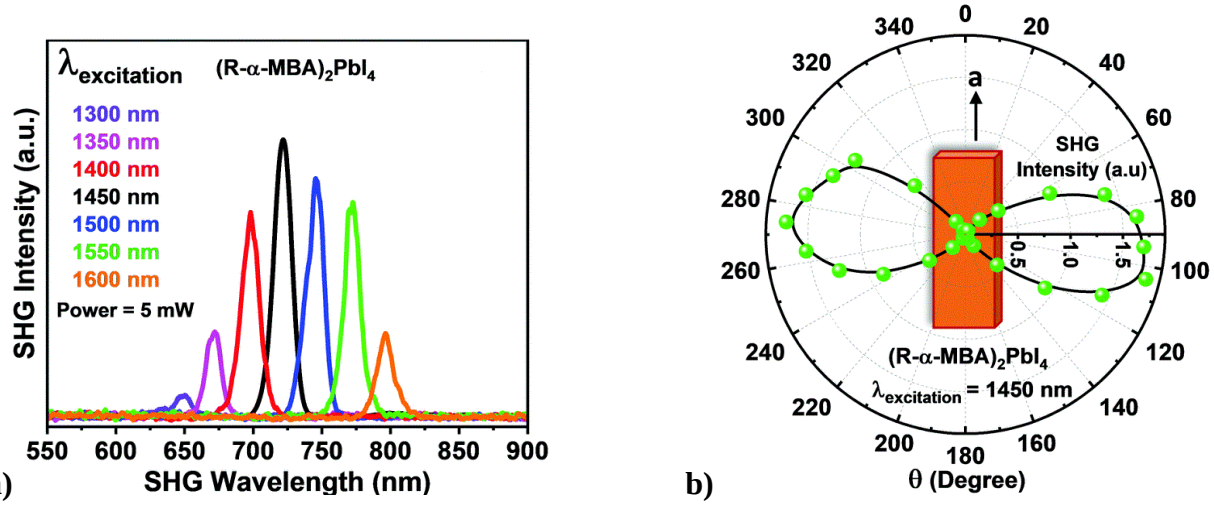

Figure 14. a) Second harmonic generation in chiral perovskite (R-MBA)$_2$PbI$_4$. (b) Variation in SHG intensity with polarization of incident pump light (reprinted with permission from ref [88]).

1.4. Scope and Organization of Thesis

As previously discussed, metal halide perovskites have become a game-changer in the field of optoelectronics. These versatile materials have also garnered significant attention in recent years for their remarkable nonlinear optical properties. Considerable effort has been dedicated to controlling and designing new materials for various applications. This rapid development also offers an opportunity to explore new materials and understand the essential mechanisms involved in these perovskite systems.

Besides perovskites, we have also discussed doped semiconductor metal nanocrystals (NCs) and their unique property of exhibiting localized surface plasmon resonance (LSPR). Bharat et al. developed a strategy involving the codoping of chromium (Cr) and tin (Sn) into indium oxide (In_2O_3) NCs, resulting in a high LSPR quality (Q) factor. They discovered that Cr doping increases the NCs' size, contributing to reduced carrier scattering and a narrower FWHM of the LSPR band. However, the underlying mechanism behind this dramatic improvement remains an intriguing open question for further exploration.

In this thesis, we have employed various ultrafast spectroscopy techniques to probe the fundamental physical mechanisms in perovskites and doped semiconductors. **Chapter Two** provides detailed descriptions of the spectroscopy techniques used in this research. All the spectroscopy setups were home-built, with our amplified femtosecond laser system as the primary source (except for the transient absorption spectroscopy, measurements performed at Prof. H. N. Ghosh's lab at IISER Mohali). The data acquisition interface software was developed using LabVIEW. Complete details of the setups and data analysis procedures are discussed in Chapter Two.

In Chapter Three, we investigated the charge carrier dynamics in $CsPbBr_3$ nanocrystal (NC) composites with two copper-based inorganic hole-transporting layers. Our group has extensively studied $CsPbBr_3$ NCs. First, Yettapu *et al*. reported charge carrier dynamics in colloidal $CsPbBr_3$ NCs using time-resolved THz spectroscopy, highlighting high charge carrier mobility and longer diffusion lengths. Additionally, Sarkar *et al*. explored ultrafast hot electron and hole transfer from colloidal $CsPbBr_3$ NCs to benzoquinone (BQ) and phenothiazine (PTZ) as electron and hole acceptors.

To build on this research and better understand the system, we examined charge carrier dynamics in $CsPbBr_3$ NC thin films with Cu_2O and CuI hole-transporting layers (HTLs). This study enhances our understanding of the NC/HTL interface, which is similar to its application in photovoltaic devices. As discussed previously, we chose inorganic HTLs due to their advantages over conventional organic HTLs, including greater stability, easier solution processability, and cost-effectiveness.

Using time-resolved THz and transient absorption spectroscopy, we demonstrated sub-picosecond hole injection from all-inorganic $CsPbBr_3$ perovskite NCs to Cu-based inorganic HTLs. This finding suggests the potential for cheaper and more stable photovoltaic devices. The hole transfer to the acceptor layer occurred on a sub-300 fs timescale, limited by our instrument response function (IRF). The effective performance of the solution-processed copper-based inorganic HTLs indicates they are a cost-effective and stable alternative to traditional organic HTLs.

In Chapter Four, we have investigated Cr-Sn co-doped In_2O_3 nanocrystals. Using time-domain THz spectroscopy, we gained valuable insights into their complex dielectric function and observed changes with increasing Cr concentration. This variation might be a contributing factor to reduced carrier scattering, possibly due to a decrease in Coulombic interactions between charge carriers and ionized dopants.

Indium tin oxide (ITO) exhibits high optical nonlinearity, which is influenced by carrier concentration. To examine how Kerr nonlinearity changes with Cr doping concentration, we employed Optical Kerr Effect (OKE) spectroscopy. Our time-resolved OKE measurements showed that the recovery time of the OKE signal was the longest for samples with the highest Cr doping.

In Chapter Five, we have investigated the second and third-order nonlinear optical properties of the 0D Pb-free perovskite [(*R*-/*S*-MBA)$_4$Bi$_2$I$_{10}$], where MBA refers to methylbenzylammonium. The chiral R-MBA and S-MBA cations introduce chirality into the Bi-I inorganic sublattice, making the perovskite chiral. In contrast, the achiral *Rac*-MBA cation results in a lack of chirality in both the organic and inorganic sublattices of [(*Rac*-MBA)$_4$Bi$_2$I$_{10}$].

The polarization-dependent second harmonic signal confirms the non-centrosymmetric nature of the perovskite crystals containing chiral cations *R*-MBA and *S*-MBA. In contrast, both chiral [(*R*-/*S*-MBA)$_4$Bi$_2$I$_{10}$]and achiral [(*Rac*-MBA)$_4$Bi$_2$I$_{10}$] crystals exhibit a strong third harmonic signal. To explore the third-order nonlinear behaviour in detail, we performed Z-scan measurements at a non-resonant wavelength (800 nm) using a 65 fs pulses. We observed a large two-photon absorption (2PA) cross-section and nonlinear refractive index in chiral [(*R*-/*S*-MBA)$_4$Bi$_2$I$_{10}$] perovskites, with these properties decreasing with increasing excitation intensity. Notably, the

nonlinear refractive index sign is opposite for the two enantiomers. The achiral [(Rac-MBA)$_4$Bi$_2$I$_{10}$] exhibits stronger third-order nonlinear optical (NLO) effects, including higher third-harmonic generation (THG), β, and n_2 values, compared to its chiral counterparts [(R-/S-MBA)$_4$Bi$_2$I$_{10}$]. This enhanced response is attributed to greater structural distortion in [(Rac-MBA)$_4$Bi$_2$I$_{10}$] relative to [(R-/S-MBA)$_4$Bi$_2$I$_{10}$]. This increased distortion likely amplifies the material's polarizability anisotropy, resulting in a stronger third-order NLO response.

1.5. References

1. Guney, M. S., Solar power and application methods. *Renewable and Sustainable Energy Reviews* **2016,** *57*, 776-785.

2. Rong, Y.; Hu, Y.; Mei, A.; Tan, H.; Saidaminov, M. I.; Seok, S. I.; McGehee, M. D.; Sargent, E. H.; Han, H., Challenges for commercializing perovskite solar cells. *Science* **2018,** *361* (6408), eaat8235.

3. Hayat, M. B.; Ali, D.; Monyake, K. C.; Alagha, L.; Ahmed, N., Solar energy—A look into power generation, challenges, and a solar-powered future. *International Journal of Energy Research* **2019,** *43* (3), 1049-1067.

4. Snaith, H. J., Perovskites: The Emergence of a New Era for Low-Cost, High-Efficiency Solar Cells. *The Journal of Physical Chemistry Letters* **2013,** *4* (21), 3623-3630.

5. Yang, C.; Hu, W.; Liu, J.; Han, C.; Gao, Q.; Mei, A.; Zhou, Y.; Guo, F.; Han, H., Achievements, challenges, and future prospects for industrialization of perovskite solar cells. *Light: Science & Applications* **2024,** *13* (1), 227.

6. Tandon, B.; Ghosh, S.; Milliron, D. J., Dopant selection strategy for high-quality factor localized surface plasmon resonance from doped metal oxide nanocrystals. *Chemistry of Materials* **2019,** *31* (18), 7752-7760.

7. Lee, S.-W.; Bae, S.; Kim, D.; Lee, H.-S., Historical Analysis of High-Efficiency, Large-Area Solar Cells: Toward Upscaling of Perovskite Solar Cells. *Advanced Materials* **2020,** *32* (51), 2002202.

8. Jin, S., Can We Find the Perfect A-Cations for Halide Perovskites? *ACS Energy Letters* **2021,** *6* (9), 3386-3389.

9. Palik, E. D., Chapter 14 - Optical Parameters for the Materials in HOC I and HOC II. In *Handbook of Optical Constants of Solids*, Palik, E. D., Ed. Academic Press: Boston, 1998; pp 313-335.

10. Xiao, Z.; Song, Z.; Yan, Y., From Lead Halide Perovskites to Lead-Free Metal Halide Perovskites and Perovskite Derivatives. *Advanced Materials* **2019,** *31* (47), 1803792.

11. Yin, W.-J.; Shi, T.; Yan, Y., Unique Properties of Halide Perovskites as Possible Origins of the Superior Solar Cell Performance. *Advanced Materials* **2014,** *26* (27), 4653-4658.

12. Tanaka, K.; Takahashi, T.; Ban, T.; Kondo, T.; Uchida, K.; Miura, N., Comparative study on the excitons in lead-halide-based perovskite-type crystals CH3NH3PbBr3 CH3NH3PbI3. *Solid State Communications* **2003,** *127* (9), 619-623.

13. Umari, P.; Mosconi, E.; De Angelis, F., Relativistic GW calculations on CH3NH3PbI3 and CH3NH3SnI3 Perovskites for Solar Cell Applications. *Scientific Reports* **2014,** *4* (1), 4467.

14. Qiu, C.; Wagner, L.; Liu, J.; Zhang, W.; Du, J.; Wang, Q.; Hu, Y.; Han, H., Probing charge carrier dynamics in metal halide perovskite solar cells. *EcoMat* **2023,** *5* (1), e12268.

15. Herz, L. M., Charge-Carrier Dynamics in Organic-Inorganic Metal Halide Perovskites. *Annual Review of Physical Chemistry* **2016,** *67* (Volume 67, 2016), 65-89.

16. Huang, J.; Yuan, Y.; Shao, Y.; Yan, Y., Understanding the physical properties of hybrid perovskites for photovoltaic applications. *Nature Reviews Materials* **2017,** *2* (7), 17042.

17. Romano, V.; Agresti, A.; Verduci, R.; D'Angelo, G., Advances in Perovskites for Photovoltaic Applications in Space. *ACS Energy Letters* **2022,** *7* (8), 2490-2514.

18. Kung, P.-K.; Li, M.-H.; Lin, P.-Y.; Chiang, Y.-H.; Chan, C.-R.; Guo, T.-F.; Chen, P., A Review of Inorganic Hole Transport Materials for Perovskite Solar Cells. *Advanced Materials Interfaces* **2018,** *5* (22), 1800882.

19. Liu, M.; Johnston, M. B.; Snaith, H. J., Efficient planar heterojunction perovskite solar cells by vapour deposition. *Nature* **2013,** *501* (7467), 395-398.

20. Meng, L.; You, J.; Guo, T.-F.; Yang, Y., Recent Advances in the Inverted Planar Structure of Perovskite Solar Cells. *Accounts of Chemical Research* **2016,** *49* (1), 155-165.

21. Kim, J. H.; Liang, P.-W.; Williams, S. T.; Cho, N.; Chueh, C.-C.; Glaz, M. S.; Ginger, D. S.; Jen, A. K.-Y., High-Performance and Environmentally Stable Planar Heterojunction Perovskite Solar Cells Based on a Solution-Processed Copper-Doped Nickel Oxide Hole-Transporting Layer. *Advanced Materials* **2015,** *27* (4), 695-701.

22. Wang, K.-C.; Jeng, J.-Y.; Shen, P.-S.; Chang, Y.-C.; Diau, E. W.-G.; Tsai, C.-H.; Chao, T.-Y.; Hsu, H.-C.; Lin, P.-Y.; Chen, P.; Guo, T.-F.; Wen, T.-C., p-type Mesoscopic Nickel Oxide/Organometallic Perovskite Heterojunction Solar Cells. *Scientific Reports* **2014,** *4* (1), 4756.

23. Jeon, N. J.; Lee, H. G.; Kim, Y. C.; Seo, J.; Noh, J. H.; Lee, J.; Seok, S. I., o-Methoxy Substituents in Spiro-OMeTAD for Efficient Inorganic–Organic Hybrid Perovskite Solar Cells. *Journal of the American Chemical Society* **2014,** *136* (22), 7837-7840.

24. Yang, W. S.; Park, B.-W.; Jung, E. H.; Jeon, N. J.; Kim, Y. C.; Lee, D. U.; Shin, S. S.; Seo, J.; Kim, E. K.; Noh, J. H.; Seok, S. I., Iodide management in formamidinium-lead-halide–based perovskite layers for efficient solar cells. *Science* **2017,** *356* (6345), 1376-1379.

25. Neophytou, M.; Griffiths, J.; Fraser, J.; Kirkus, M.; Chen, H.; Nielsen, C. B.; McCulloch, I., High mobility, hole transport materials for highly efficient PEDOT:PSS replacement in inverted perovskite solar cells. *Journal of Materials Chemistry C* **2017,** *5* (20), 4940-4945.

26. Zhao, X.; Wang, M., Organic hole-transporting materials for efficient perovskite solar cells. *Materials Today Energy* **2018,** *7*, 208-220.

27. Rong, Y.; Liu, L.; Mei, A.; Li, X.; Han, H., Beyond Efficiency: the Challenge of Stability in Mesoscopic Perovskite Solar Cells. *Advanced Energy Materials* **2015,** *5* (20), 1501066.

28. Yu, Z.; Sun, L., Inorganic Hole-Transporting Materials for Perovskite Solar Cells. *Small Methods* **2018,** *2* (2), 1700280.

29. Wang, Q.; Lin, Z.; Su, J.; Hu, Z.; Chang, J.; Hao, Y., Recent progress of inorganic hole transport materials for efficient and stable perovskite solar cells. *Nano Select* **2021,** *2* (6), 1055-1080.

30. Abate, A.; Correa-Baena, J.-P.; Saliba, M.; Su'ait, M. S.; Bella, F., Perovskite Solar Cells: From the Laboratory to the Assembly Line. *Chemistry – A European Journal* **2018,** *24* (13), 3083-3100.

31. You, J.; Meng, L.; Song, T.-B.; Guo, T.-F.; Yang, Y.; Chang, W.-H.; Hong, Z.; Chen, H.; Zhou, H.; Chen, Q.; Liu, Y.; De Marco, N.; Yang, Y., Improved air stability of perovskite solar cells via solution-processed metal oxide transport layers. *Nature Nanotechnology* **2016,** *11* (1), 75-81.

32. Shi, J.; Li, Y.; Li, Y.; Li, D.; Luo, Y.; Wu, H.; Meng, Q., From Ultrafast to Ultraslow: Charge-Carrier Dynamics of Perovskite Solar Cells. *Joule* **2018,** *2* (5), 879-901.

33. Sze, S. M.; Li, Y.; Ng, K. K., *Physics of semiconductor devices*. John wiley & sons: 2021.

34. Wannier, G. H., The structure of electronic excitation levels in insulating crystals. *Physical Review* **1937,** *52* (3), 191.

35. Stranks, S. D.; Burlakov, V. M.; Leijtens, T.; Ball, J. M.; Goriely, A.; Snaith, H. J., Recombination kinetics in organic-inorganic perovskites: excitons, free charge, and subgap states. *Physical Review Applied* **2014,** *2* (3), 034007.

36. D'innocenzo, V.; Grancini, G.; Alcocer, M. J.; Kandada, A. R. S.; Stranks, S. D.; Lee, M. M.; Lanzani, G.; Snaith, H. J.; Petrozza, A., Excitons versus free charges in organo-lead tri-halide perovskites. *Nature communications* **2014,** *5* (1), 3586.

37. Shah, J., *Ultrafast spectroscopy of semiconductors and semiconductor nanostructures*. Springer Science & Business Media: 2013; Vol. 115.

38. Johnston, M. B.; Herz, L. M., Hybrid perovskites for photovoltaics: charge-carrier recombination, diffusion, and radiative efficiencies. *Accounts of chemical research* **2016,** *49* (1), 146-154.

39. Sum, T. C.; Mathews, N.; Xing, G.; Lim, S. S.; Chong, W. K.; Giovanni, D.; Dewi, H. A., Spectral Features and Charge Dynamics of Lead Halide Perovskites: Origins and Interpretations. *Accounts of Chemical Research* **2016,** *49* (2), 294-302.

40. Sum, T. C.; Mathews, N., Advancements in perovskite solar cells: photophysics behind the photovoltaics. *Energy & Environmental Science* **2014,** *7* (8), 2518-2534.

41. Alfano, R. R., *Semiconductors Probed by Ultrafast Laser Spectroscopy Pt II*. Elsevier: 2012.

42. Othonos, A., Probing ultrafast carrier and phonon dynamics in semiconductors. *Journal of applied physics* **1998,** *83* (4), 1789-1830.

43. Tisdale, W. A.; Williams, K. J.; Timp, B. A.; Norris, D. J.; Aydil, E. S.; Zhu, X.-Y., Hot-electron transfer from semiconductor nanocrystals. *Science* **2010,** *328* (5985), 1543-1547.

44. Yang, G.; Tu, Y.; Ye, J.; Liu, R.; Zang, Y.; Zhang, L.; Wang, Y.; Li, G.; Zhou, Q.; Chu, L.; Yan, W., Study on carrier dynamics of perovskite solar cells via transient absorption. *Journal of Alloys and Compounds* **2023,** *952*, 170051.

45. Serpetzoglou, E.; Konidakis, I.; Kakavelakis, G.; Maksudov, T.; Kymakis, E.; Stratakis, E., Improved Carrier Transport in Perovskite Solar Cells Probed by Femtosecond Transient Absorption Spectroscopy. *ACS Applied Materials & Interfaces* **2017,** *9* (50), 43910-43919.

46. Ulbricht, R.; Hendry, E.; Shan, J.; Heinz, T. F.; Bonn, M., Carrier dynamics in semiconductors studied with time-resolved terahertz spectroscopy. *Reviews of Modern Physics* **2011,** *83* (2), 543-586.

47. Schmuttenmaer, C. A., Exploring dynamics in the far-infrared with terahertz spectroscopy. *Chemical reviews* **2004,** *104* (4), 1759-1780.

48. Wehrenfennig, C.; Liu, M.; Snaith, H. J.; Johnston, M. B.; Herz, L. M., Charge-carrier dynamics in vapour-deposited films of the organolead halide perovskite CH 3 NH 3 PbI 3− x Cl x. *Energy & Environmental Science* **2014,** *7* (7), 2269-2275.

49. Valverde-Chávez, D. A.; Ponseca, C. S.; Stoumpos, C. C.; Yartsev, A.; Kanatzidis, M. G.; Sundström, V.; Cooke, D. G., Intrinsic femtosecond charge generation dynamics in single crystal CH 3 NH 3 PbI 3. *Energy & Environmental Science* **2015,** *8* (12), 3700-3707.

50. Yang, Y.; Ostrowski, D. P.; France, R. M.; Zhu, K.; Van De Lagemaat, J.; Luther, J. M.; Beard, M. C., Observation of a hot-phonon bottleneck in lead-iodide perovskites. *Nature Photonics* **2016,** *10* (1), 53-59.

51. Ponseca Jr, C. S.; Sundström, V., Revealing the ultrafast charge carrier dynamics in organo metal halide perovskite solar cell materials using time resolved THz spectroscopy. *Nanoscale* **2016,** *8* (12), 6249-6257.

52. Dexheimer, S. L., *Terahertz spectroscopy: principles and applications*. CRC press: 2017.

53. Baxter, J. B.; Guglietta, G. W., Terahertz Spectroscopy. *Analytical Chemistry* **2011,** *83* (12), 4342-4368.

54. Jepsen, P. U.; Cooke, D. G.; Koch, M., Terahertz spectroscopy and imaging – Modern techniques and applications. *Laser & Photonics Reviews* **2011,** *5* (1), 124-166.

55. Berera, R.; van Grondelle, R.; Kennis, J. T. M., Ultrafast transient absorption spectroscopy: principles and application to photosynthetic systems. *Photosynthesis Research* **2009,** *101* (2), 105-118.

56. Ishioka, K.; Barker, B. G., Jr.; Yanagida, M.; Shirai, Y.; Miyano, K., Direct Observation of Ultrafast Hole Injection from Lead Halide Perovskite by Differential Transient Transmission Spectroscopy. *The Journal of Physical Chemistry Letters* **2017,** *8* (16), 3902-3907.

57. Zhai, Y.; Sheng, C. X.; Zhang, C.; Vardeny, Z. V., Ultrafast Spectroscopy of Photoexcitations in Organometal Trihalide Perovskites. *Advanced Functional Materials* **2016,** *26* (10), 1617-1627.

58. Aneesh, J.; Swarnkar, A.; Kumar Ravi, V.; Sharma, R.; Nag, A.; Adarsh, K. V., Ultrafast Exciton Dynamics in Colloidal CsPbBr3 Perovskite Nanocrystals: Biexciton Effect and Auger Recombination. *The Journal of Physical Chemistry C* **2017,** *121* (8), 4734-4739.

59. Frank, G.; Köstlin, H., Electrical properties and defect model of tin-doped indium oxide layers. *Applied Physics A* **1982,** *27*, 197-206.

60. Nag, A.; Shireen, A., Search for new transparent conductors: Effect of Ge doping on the conductivity of Ga2O3, In2O3 and Ga1. 4In0. 6O3. *Solid state communications* **2010,** *150* (35-36), 1679-1682.

61. Gilstrap, R. A.; Capozzi, C. J.; Carson, C. G.; Gerhardt, R. A.; Summers, C. J., Synthesis of a nonagglomerated indium tin oxide nanoparticle dispersion. *Adv. Mater* **2008,** *20* (21), 4163-4166.

62. Wang, T.; Radovanovic, P. V., Free electron concentration in colloidal indium tin oxide nanocrystals determined by their size and structure. *The Journal of Physical Chemistry C* **2011,** *115* (2), 406-413.

63. Tandon, B.; Shanker, G. S.; Nag, A., Multifunctional Sn- and Fe-Codoped In2O3 Colloidal Nanocrystals: Plasmonics and Magnetism. *The Journal of Physical Chemistry Letters* **2014,** *5* (13), 2306-2311.

64. Shanker, G. S.; Tandon, B.; Shibata, T.; Chattopadhyay, S.; Nag, A., Doping controls plasmonics, electrical conductivity, and carrier-mediated magnetic coupling in Fe and Sn codoped In2O3 nanocrystals: local structure is the key. *Chemistry of Materials* **2015,** *27* (3), 892-900.

65. Tandon, B.; Yadav, A.; Khurana, D.; Reddy, P.; Santra, P. K.; Nag, A., Size-Induced Enhancement of Carrier Density, LSPR Quality Factor, and Carrier Mobility in Cr–Sn Doped In2O3 Nanocrystals. *Chemistry of Materials* **2017,** *29* (21), 9360-9368.

66. Lounis, S. D.; Runnerstrom, E. L.; Llordés, A.; Milliron, D. J., Defect Chemistry and Plasmon Physics of Colloidal Metal Oxide Nanocrystals. *The Journal of Physical Chemistry Letters* **2014,** *5* (9), 1564-1574.

67. Gordon, T. R.; Paik, T.; Klein, D. R.; Naik, G. V.; Caglayan, H.; Boltasseva, A.; Murray, C. B., Shape-Dependent Plasmonic Response and Directed Self-Assembly in a New Semiconductor Building Block, Indium-Doped Cadmium Oxide (ICO). *Nano Letters* **2013,** *13* (6), 2857-2863.

68. Sannomiya, T.; Hafner, C.; Voros, J., In situ Sensing of Single Binding Events by Localized Surface Plasmon Resonance. *Nano Letters* **2008,** *8* (10), 3450-3455.

69. Jain, P. K.; Huang, X.; El-Sayed, I. H.; El-Sayed, M. A., Noble Metals on the Nanoscale: Optical and Photothermal Properties and Some Applications in Imaging, Sensing, Biology, and Medicine. *Accounts of Chemical Research* **2008,** *41* (12), 1578-1586.

70. Zhang, D. H.; Ma, H. L., Scattering mechanisms of charge carriers in transparent conducting oxide films. *Applied Physics A* **1996,** *62* (5), 487-492.

71. Koch, M.; Mittleman, D. M.; Ornik, J.; Castro-Camus, E., Terahertz time-domain spectroscopy. *Nature Reviews Methods Primers* **2023,** *3* (1), 48.

72. Sarkar, S.; Saha, D.; Banerjee, S.; Mukherjee, A.; Mandal, P., Broadband terahertz dielectric spectroscopy of alcohols. *Chemical Physics Letters* **2017,** *678*, 65-71.

73. Zhao, D.; Skelton, J. M.; Hu, H.; La-o-Vorakiat, C.; Zhu, J.-X.; Marcus, R. A.; Michel-Beyerle, M.-E.; Lam, Y. M.; Walsh, A.; Chia, E. E., Low-frequency optical phonon modes and carrier mobility in the halide perovskite CH3NH3PbBr3 using terahertz time-domain spectroscopy. *Applied Physics Letters* **2017,** *111* (20).

74. Kleine-Ostmann, T.; Nagatsuma, T., A Review on Terahertz Communications Research. *Journal of Infrared, Millimeter, and Terahertz Waves* **2011,** *32* (2), 143-171.

75. Abouelsayed, A.; El-Bahy, G. S.; Abdelrazzak, A. B., Terahertz Time-Domain Spectroscopic (THz-TDS) Insights into Protein Deformation. *Brazilian Journal of Physics* **2024,** *54* (2), 54.

76. Wilmink, G. J.; Ibey, B. L.; Tongue, T.; Schulkin, B.; Laman, N.; Peralta, X. G.; Roth, C. C.; Cerna, C. Z.; Rivest, B. D.; Grundt, J. E., Development of a compact terahertz time-domain spectrometer for the measurement of the optical properties of biological tissues. *Journal of biomedical optics* **2011,** *16* (4), 047006-047006-10.

77. Neu, J.; Schmuttenmaer, C. A., Tutorial: An introduction to terahertz time domain spectroscopy (THz-TDS). *Journal of Applied Physics* **2018,** *124* (23).

78. Lloyd-Hughes, J.; Jeon, T.-I., A Review of the Terahertz Conductivity of Bulk and Nano-Materials. *Journal of Infrared, Millimeter, and Terahertz Waves* **2012,** *33* (9), 871-925.

79. Duguay, M. A.; Hansen, J. W., AN ULTRAFAST LIGHT GATE. *Applied Physics Letters* **1969,** *15* (6), 192-194.

80. KINOSHITA, S.; KAI, Y.; ARIYOSHI, T.; SHIMADA, Y., LOW FREQUENCY MODES PROBED BY TIME-DOMAIN OPTICAL KERR EFFECT SPECTROSCOPY. *International Journal of Modern Physics B* **1996,** *10* (11), 1229-1272.

81. Zhong, Q.; Fourkas, J. T., Optical Kerr Effect Spectroscopy of Simple Liquids. *The Journal of Physical Chemistry B* **2008,** *112* (49), 15529-15539.

82. McMorrow, D.; Lotshaw, W. T., Intermolecular dynamics in acetonitrile probed with femtosecond Fourier-transform Raman spectroscopy. *The Journal of Physical Chemistry* **1991,** *95* (25), 10395-10406.

83. Long, G.; Sabatini, R.; Saidaminov, M. I.; Lakhwani, G.; Rasmita, A.; Liu, X.; Sargent, E. H.; Gao, W., Chiral-perovskite optoelectronics. *Nature Reviews Materials* **2020,** *5* (6), 423-439.

84. Lin, H.; Zhou, C.; Tian, Y.; Siegrist, T.; Ma, B., Low-Dimensional Organometal Halide Perovskites. *ACS Energy Letters* **2018,** *3* (1), 54-62.

85. Ahn, J.; Lee, E.; Tan, J.; Yang, W.; Kim, B.; Moon, J., A new class of chiral semiconductors: chiral-organic-molecule-incorporating organic–inorganic hybrid perovskites. *Materials Horizons* **2017,** *4* (5), 851-856.

86. Ma, J.; Wang, H.; Li, D., Recent Progress of Chiral Perovskites: Materials, Synthesis, and Properties. *Advanced Materials* **2021,** *33* (26), 2008785.

87. Billing, D. G.; Lemmerer, A., Synthesis and crystal structures of inorganic–organic hybrids incorporating an aromatic amine with a chiral functional group. *CrystEngComm* **2006,** *8* (9), 686-695.

88. Sheikh, T.; Maqbool, S.; Rajput, P. K.; Mandal, P.; Nag, A., Effect of chirality on the optical properties of layered hybrid perovskite R- and S-α-methylbenzylammonium lead iodide. *Chemical Communications* **2022,** *58* (55), 7650-7653.

89. Nayak, A.; Park, J.; De Mey, K.; Hu, X.; Duncan, T. V.; Beratan, D. N.; Clays, K.; Therien, M. J., Large Hyperpolarizabilities at Telecommunication-Relevant Wavelengths in Donor–Acceptor–Donor Nonlinear Optical Chromophores. *ACS Central Science* **2016,** *2* (12), 954-966.

90. Braune, M.; Maiwald, M.; Eppich, B.; Brox, O.; Ginolas, A.; Sumpf, B.; Trankle, G., Design and Realization of a Miniaturized DFB Diode Laser-Based SHG Light Source With a 2-nm Tunable Emission at 488should be a spacenm. *IEEE Transactions on Components, Packaging and Manufacturing Technology* **2017,** *PP*, 1-6.

91. Ye, W.; Zeuner, F.; Li, X.; Reineke, B.; He, S.; Qiu, C.-W.; Liu, J.; Wang, Y.; Zhang, S.; Zentgraf, T., Spin and wavelength multiplexed nonlinear metasurface holography. *Nature Communications* **2016,** *7* (1), 11930.

92. Kim, Y.-H.; Zhai, Y.; Lu, H.; Pan, X.; Xiao, C.; Gaulding, E. A.; Harvey, S. P.; Berry, J. J.; Vardeny, Z. V.; Luther, J. M.; Beard, M. C., Chiral-induced spin selectivity enables a room-temperature spin light-emitting diode. *Science* **2021,** *371* (6534), 1129-1133.

93. Zheng, Y.; Xu, J.; Bu, X.-H., 1D Chiral Lead Halide Perovskites with Superior Second-Order Optical Nonlinearity. *Advanced Optical Materials* **2022,** *10* (1), 2101545.

94. Fu, D.; Xin, J.; He, Y.; Wu, S.; Zhang, X.; Zhang, X.-M.; Luo, J., Chirality-Dependent Second-Order Nonlinear Optical Effect in 1D Organic–Inorganic Hybrid Perovskite Bulk Single Crystal. *Angewandte Chemie International Edition* **2021,** *60* (36), 20021-20026.

95. Dong, Y.; Zhang, Y.; Li, X.; Feng, Y.; Zhang, H.; Xu, J., Chiral Perovskites: Promising Materials toward Next-Generation Optoelectronics. *Small* **2019,** *15* (39), 1902237.

96. Yuan, C.; Li, X.; Semin, S.; Feng, Y.; Rasing, T.; Xu, J., Chiral Lead Halide Perovskite Nanowires for Second-Order Nonlinear Optics. *Nano Letters* **2018,** *18* (9), 5411-5417.

97. Billing, D. G.; Lemmerer, A., Bis-[(S)-β-phenethyl-ammonium] tri-bromo-plumbate(II). *Acta Crystallographica Section E* **2003,** *59* (6), m381-m383.

98. Dang, Y.; Liu, X.; Cao, B.; Tao, X., Chiral halide perovskite crystals for optoelectronic applications. *Matter* **2021,** *4* (3), 794-820.

99. Boyd, R. W., Chapter 1 - The Nonlinear Optical Susceptibility. In *Nonlinear Optics (Third Edition)*, Boyd, R. W., Ed. Academic Press: Burlington, 2008; pp 1-67.

100. Shen, W.; Chen, J.; Wu, J.; Li, X.; Zeng, H., Nonlinear Optics in Lead Halide Perovskites: Mechanisms and Applications. *ACS Photonics* **2021,** *8* (1), 113-124.

101. Xu, J.; Li, X.; Xiong, J.; Yuan, C.; Semin, S.; Rasing, T.; Bu, X.-H., Halide Perovskites for Nonlinear Optics. *Advanced Materials* **2020,** *32* (3), 1806736.

102. Zhang, R.; Fan, J.; Zhang, X.; Yu, H.; Zhang, H.; Mai, Y.; Xu, T.; Wang, J.; Snaith, H. J., Nonlinear Optical Response of Organic–Inorganic Halide Perovskites. *ACS Photonics* **2016,** *3* (3), 371-377.

103. Wang, G.; Mei, S.; Liao, J.; Wang, W.; Tang, Y.; Zhang, Q.; Tang, Z.; Wu, B.; Xing, G., Advances of Nonlinear Photonics in Low-Dimensional Halide Perovskites. *Small* **2021,** *17* (43), 2100809.

104. Jiang, S.; Zhao, P.; Xing, G.; Kang, H.; Li, X.; Zhao, T.; Li, B.; Zhang, T., Bismuth-Based Chiral Perovskite with Different Dimensions for Second-Order Nonlinear Optical Properties. *Advanced Optical Materials* **2023,** *11* (18), 2203078.

105. Tao, K.; Li, Q.; Yan, Q., 1D Tin(II)-Based Chiral Hybrid Perovskite Single Crystals with Extremely Distorted Inorganic Chains for Second Harmonic Generation. *Advanced Optical Materials* **2024,** *12* (17), 2400018.

106. Yao, L.; Zeng, Z.; Cai, C.; Xu, P.; Gu, H.; Gao, L.; Han, J.; Zhang, X.; Wang, X.; Wang, X.; Pan, A.; Wang, J.; Liang, W.; Liu, S.; Chen, C.; Tang, J., Strong Second- and Third-Harmonic Generation in 1D Chiral Hybrid Bismuth Halides. *Journal of the American Chemical Society* **2021,** *143* (39), 16095-16104.

107. Zhao, L.; Han, X.; Zheng, Y.; Yu, M.-H.; Xu, J., Tin-Based Chiral Perovskites with Second-Order Nonlinear Optical Properties. *Advanced Photonics Research* **2021,** *2* (11), 2100056.

108. Fu, X.; Zeng, Z.; Jiao, S.; Wang, X.; Wang, J.; Jiang, Y.; Zheng, W.; Zhang, D.; Tian, Z.; Li, Q.; Pan, A., Highly Anisotropic Second-Order Nonlinear Optical Effects in the Chiral Lead-Free Perovskite Spiral Microplates. *Nano Letters* **2023,** *23* (2), 606-613.

Chapter 2

Experimental Methods and Data Analysis

2.1. The Terahertz Spectrum and Spectroscopy

The terahertz (THz) region of the electromagnetic spectrum lies between the microwave and infrared regions, serving as a bridge between these two domains. THz radiation, with frequencies ranging from 0.1 to 20 THz, offers valuable insights into various physical phenomena. THz photon can resonate with low-energy excitations like collective vibrational or torsional modes in condensed-phase media, and molecular rotational and vibrational transitions.[1-4] In other units, 1 THz corresponds to 33.3 cm^{-1} (wavenumbers), 0.004 eV (photon energy), or a wavelength of 300 μm.

As discussed earlier in the thesis, terahertz time-domain spectroscopy (THz-TDS) offers static information about a sample's properties, which is useful for applications like molecular spectroscopy, biology, and quality control. On the other hand, time-resolved terahertz spectroscopy (TRTS) explores the dynamic and evolving properties of photo-excited materials in real time. Details about both techniques will be provided in subsequent sections. However, before moving to these techniques, will discuss the generation and detection of this unique part of the electromagnetic spectrum. The THz region has long been known as the "terahertz gap" due to the challenges associated with accessing it. Frequencies below the THz range can be generated using electronic circuits, while those above are accessible through optical methods. However, generating electromagnetic waves, specifically in the THz range, remained a significant challenge until the advent of ultrafast lasers, which revolutionized this field. The ultrafast lasers have enabled the generation of THz radiation, primarily through the excitation of materials using ultrashort laser pulses.[5]

Various mechanisms are employed to produce THz radiation, including photocarrier acceleration in photoconductive antennas, second-order nonlinear effects in electro-optic crystals, and nonlinear electronic transmission lines.[6-7] Photoconduction and optical rectification are the most common approaches for generating broadband pulsed THz beams. Despite these advancements, the efficiency of these methods remains low, and they often cover a limited THz bandwidth. Air plasma generation has emerged as a promising technique, offering high peak electric fields and ultrabroad bandwidth.[8] When ambient air or specific gases are excited with intense femtosecond laser pulses, they can efficiently generate and detect broadband THz radiation through nonlinear optical processes.

This thesis utilizes a custom-designed THz spectrometer that leverages ambient air to generate broadband THz radiation. Detection is performed using the air-biased coherent detection (ABCD) technique with the aid of a commercially available Zomega detector. The details of THz generation and detection processes are described in the subsequent sections.

2.1.1. Broadband THz generation by laser-induced gas plasma

The generation of THz waves from plasma was first demonstrated in the early 1990s, which was done by focusing a fundamental beam into gases.[9-10] However, achieving intense THz waves became feasible only when both the fundamental and second harmonic beams were focused into the air. This phenomenon is explained by the four-wave mixing (FWM) model, a third-order nonlinear optical process.[11-12] In this process, fundamental optical radiation (ω) interacts with its second harmonic (2ω), which is generated using a Type I β-barium borate (BBO) crystal with a thickness of 0.1 mm. Mathematically, the FWM process generates THz photon according to the following equation-

$$(2\omega + \omega_{THz}) - \omega - \omega = \omega_{THz} \quad (1)$$

In our Setup, we use ultrashort laser pulses centred at 800 nm with a pulse duration of 35 fs and a repetition rate of 1 kHz, generated by a regenerative amplifier. Each pulse delivers an average energy of 2 mJ, with a peak power sufficient to ionize air, generate plasma, and enhance the nonlinear perturbative effects, thereby producing intense THz radiation.

The amplitude of the generated THz field (E_{THz}) is directly proportional to the intensity of the fundamental beam (I_ω) and the square root of the intensity of the second harmonic beam ($\sqrt{I_{2\omega}}$), as described by the relation:

$$E_{THz} \propto \chi^{(3)} \sqrt{I_{2\omega}}\, I_\omega \cos(\varphi) \quad (2)$$

Here, φ represents the phase difference between the fundamental and second harmonic waves, and $\chi^{(3)}$ is the third-order nonlinear coefficient, which has a value of 1.68 x 10^{-25} (m/V) at 20^o C in air.

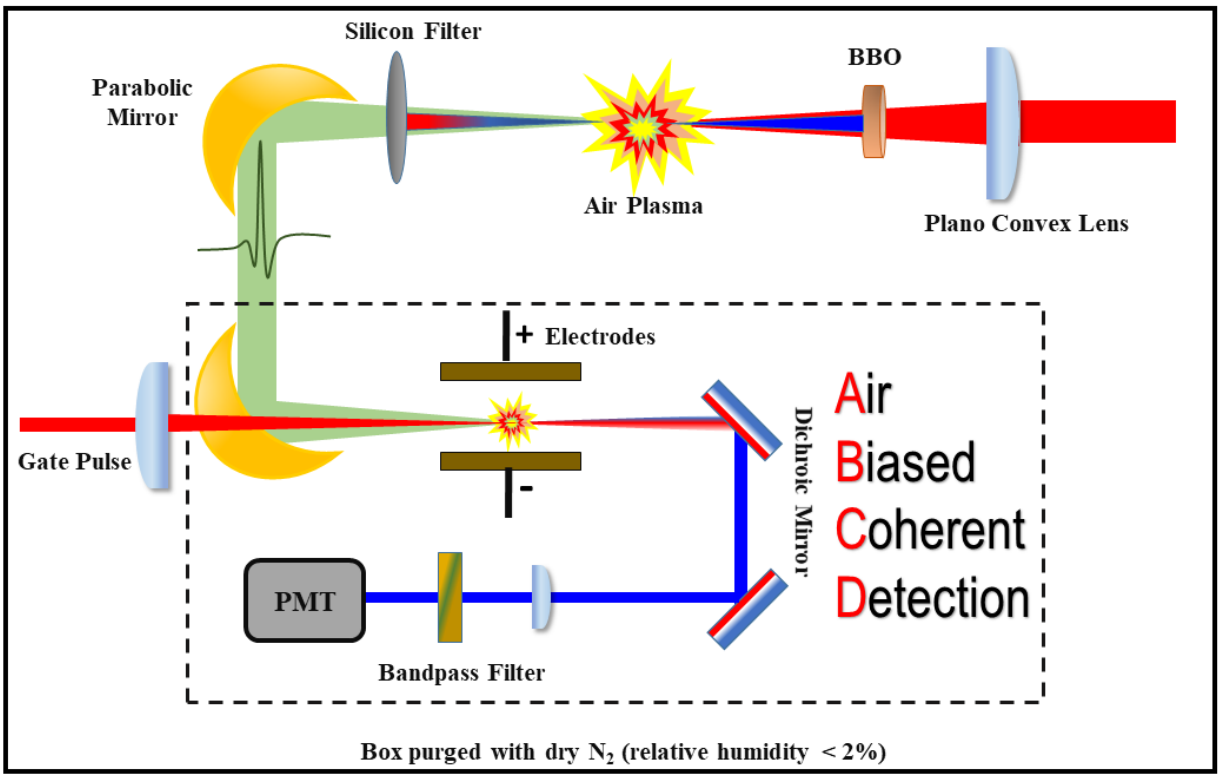

Figure 1. In the schematic representation of THz generation via laser-induced air plasma and detection using the air-biased coherent detection (ABCD) technique, fundamental (800 nm, red) and second harmonic (400 nm, blue) beams generated by a β-barium borate (BBO) crystal, are focused into ambient air, creating a plasma that emits THz radiation along with other electromagnetic waves. The THz radiation is isolated using a high-resistivity silicon wafer, which filters out unwanted components. For detection, the ABCD technique generates the second harmonic of a gate pulse (depicted as the blue beam in the dashed square box), and its intensity is measured, which is directly proportional to the amplitude of the THz electric field.

2.1.2. Air biased coherent detection (ABCD)

Broadband THz detection using air as the sensor relies on the THz Field-Induced Second Harmonic (TFISH) generation, a third-order nonlinear process.[13] In this technique, the interaction between the THz radiation and a gate beam occurs in the presence of a quasi-DC bias field, acting as a local oscillator (LO). This interaction generates the second harmonic of the gate beam from the plasma formed between electrodes, expressed as-

$$E_{2\omega} \propto \chi^{(3)} E_{\omega} E_{\omega} (E_{THz} + E_{LO}) \quad (3)$$

In terms of intensity, this can be written as:

$$I_{2\omega} \propto \left| E_{2\omega} \right|^2 \propto (\chi^{(3)})^2 I_{\omega}^2 (E_{THz}^2 + E_{LO}^2 + 2E_{THz}E_{LO}\cos(\varphi)) \quad (4)$$

The cross-term, $2E_{THz}E_{LO}\cos(\varphi)$, which is proportional to E_{THz}, plays a crucial role in enabling coherent detection. By modulating the quasi-DC bias field (LO) and employing a lock-in amplifier, the E_{LO}^2 term can be effectively removed, allowing the cross-term to dominate. This dominance occurs when the probe beam intensity exceeds the plasma threshold, making THz detection coherent. This method is referred to as air-biased coherent detection (ABCD).

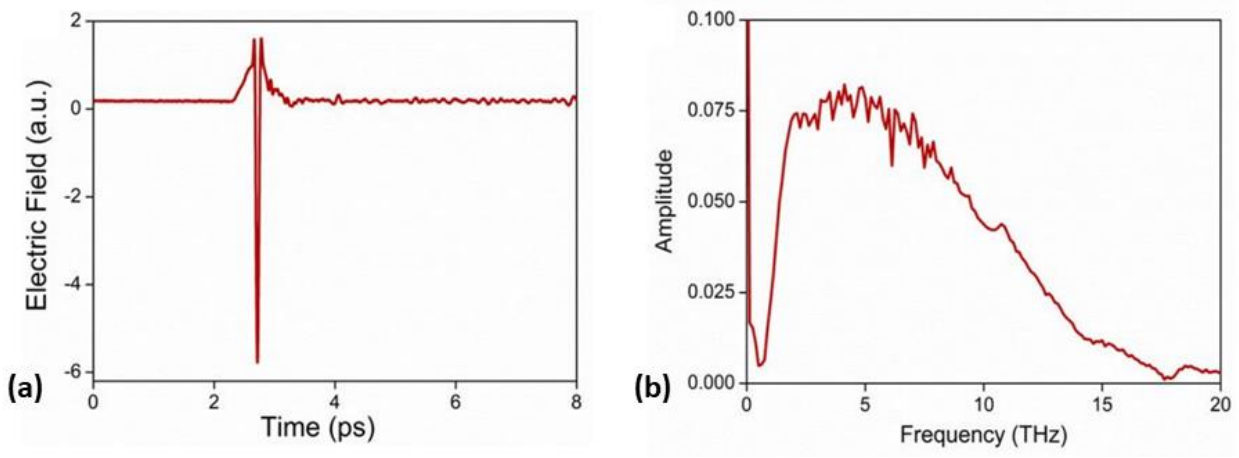

Figure 2. (a) The THz waveform in the time domain detected using the air-biased coherent detection (ABCD) technique. **(b)** The frequency domain amplitude spectrum obtained by Fourier's transformation of time domain data.

2.1.3. THz Time Domain spectroscopy

Figure 3 illustrates the schematic of the THz time-domain spectroscopy (THz-TDS) setup. The system employs a regenerative amplifier (Spitfire, Spectra-Physics), producing 800 nm-centered, 45 fs laser pulses with an average power of 2 mJ as the source. The beam is initially divided into two equal parts using a 50:50 ultrafast beam splitter. One portion is used to do the THz-TDS experiment encounters another beam splitter, which reflects 8% of the beam and transmits 92%. The reflected 8% serves as the gate beam for the air-biased coherent detection (ABCD) technique. The gate beam is directed through a retroreflector mounted on a computer-controlled 50 mm delay stage (delay 1) and then focused into the detector (Zomega) using a plano-convex lens, precisely

aligning it within the gap between two electrodes connected to a high-voltage modulator (HVM). An AC bias of 1.5 kV is applied to the electrodes. This AC electric field functions as the local oscillator for the coherent detection process.

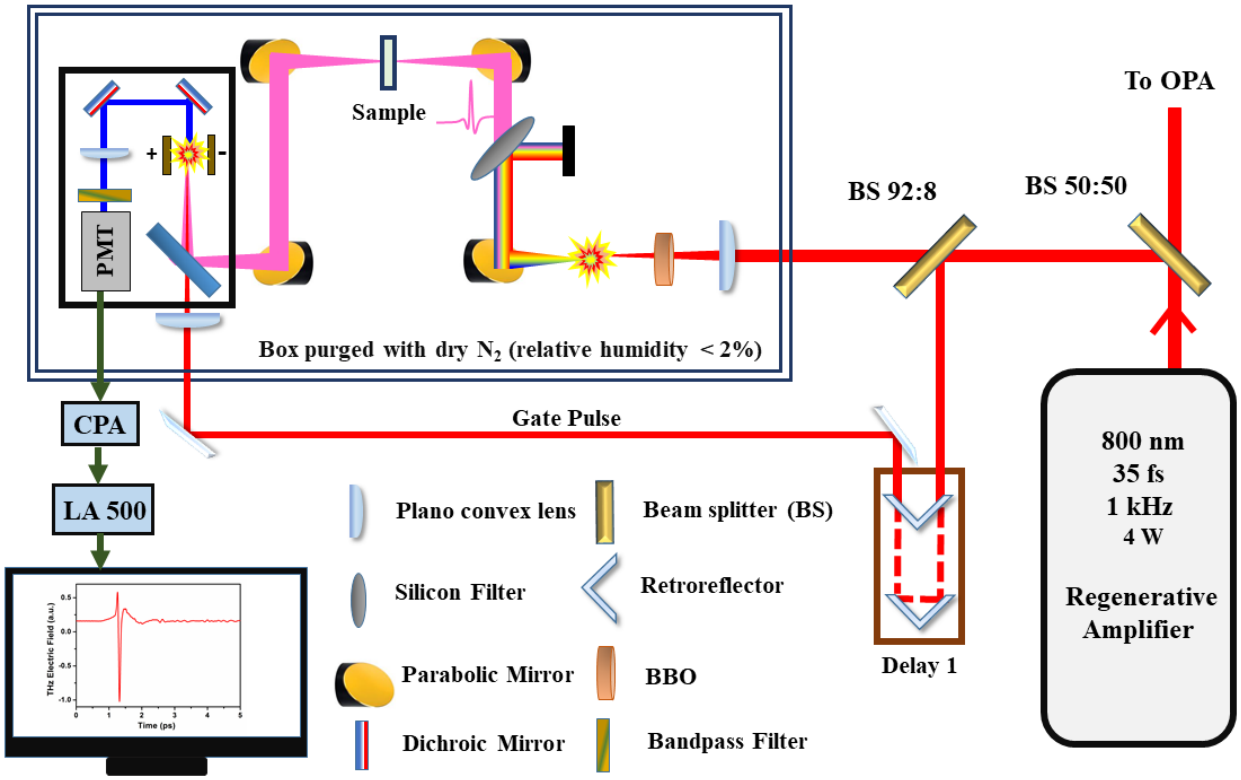

Figure 3. Schematic for experimental Setup of THz Time-domain Spectroscopy (THz-TDS).

The remaining 92% of the main beam is directed to generate THz radiation using air plasma. It is passed through a plano-convex lens and a β-barium borate (BBO) crystal to create the second harmonic. The fundamental and second harmonic frequencies meet at the focal point, forming air plasma and producing THz radiation. The THz beam is filtered through a high-resistivity silicon wafer and directed to the sample using a pair of off-axis parabolic mirrors. The parabolic mirror just before the sample focuses the THz beam onto the sample, while the next two parabolic mirrors, placed after the sample, collimate and then refocus the THz beam into the detector. The THz beam is aligned to converge at the same spot where the gate beam is focused, ensuring precise detection.

In the detector, the THz field interacts with the gate beam and generates its second harmonic, which is reflected through a pair of dichroic mirrors and then passes through a filter to remove the fundamental 800 nm component. The resulting signal is sent to a photomultiplier tube (PMT). The

PMT response is amplified using a signal pre-amplifier and then sent to a lock-in amplifier, synchronized with the high-voltage modulator operating at 500 Hz. The lock-in amplifier signal is recorded using a DAQ device (National Instruments) as the time delay between the gate and THz beams is varied by scanning the optical delay stage (delay1). This coherent detection technique enables the measurement of the transient THz electric field, including its amplitude and phase, rather than just its intensity.

The duration of the THz pulses is approximately 300 fs. When the THz electric field interacts with the sample, changes in amplitude and phase are analyzed to compute the sample's absorption coefficient and refractive index. These measurements allow the direct determination of the complex permittivity of the sample without requiring a Kramers-Kronig analysis. To prevent absorption of THz radiation by the ambient water vapour, the part of the Setup involving THz propagation is enclosed in a nitrogen-purged box, maintaining relative humidity below 2%.

2.1.4. Time-resolved THz spectroscopy (TRTS)

As discussed earlier, Time-Resolved THz Spectroscopy (TRTS) is a pump-probe technique that uses an optical pump and THz probe to study systems where the optical excitation induces changes in THz absorption/refraction properties on a sub-picosecond timescale. Figure 4 illustrates the schematic of the TRTS setup, which builds upon the steady-state THz-TDS setup (Figure 3) with some additional components. The key addition is an Optical Parametric Amplifier (OPA), powered by half of the laser output from the regenerative amplifier after the initial 50:50 beam splitter. The OPA generates a range of wavelengths (UV to NIR), which are used as the optical pump for the sample. The remaining reflected beam from the 50:50 beam splitter is directed toward THz generation, similar to the THz-TDS setup. However, in this configuration, the beam passes through a 600 mm delay stage (delay2) before reaching the 92:8 beam splitter. This delay stage introduces a controlled time delay between the optical pump and the THz probe beam, enabling time-resolved studies.

The pump beam (green), emerging from the OPA, passes through a mechanical chopper rotating at 333 Hz, allowing every third pulse to reach the sample. This beam is directed through a hole in the off-axis parabolic mirror just before the sample, ensuring it becomes collinear with the THz beam. The pump beam diameter, adjustable using a lens mounted on a translational stage, is set to ~3.0 mm at the sample, approximately 3.0 times larger than the THz beam diameter, ensuring

probing of uniformly excited sample. The beam diameters were precisely measured using the knife-edge technique. A black polyethene sheet (transparent to the THz probe) blocks any pump light transmitted through the sample to prevent interference with the photomultiplier tube (PMT).

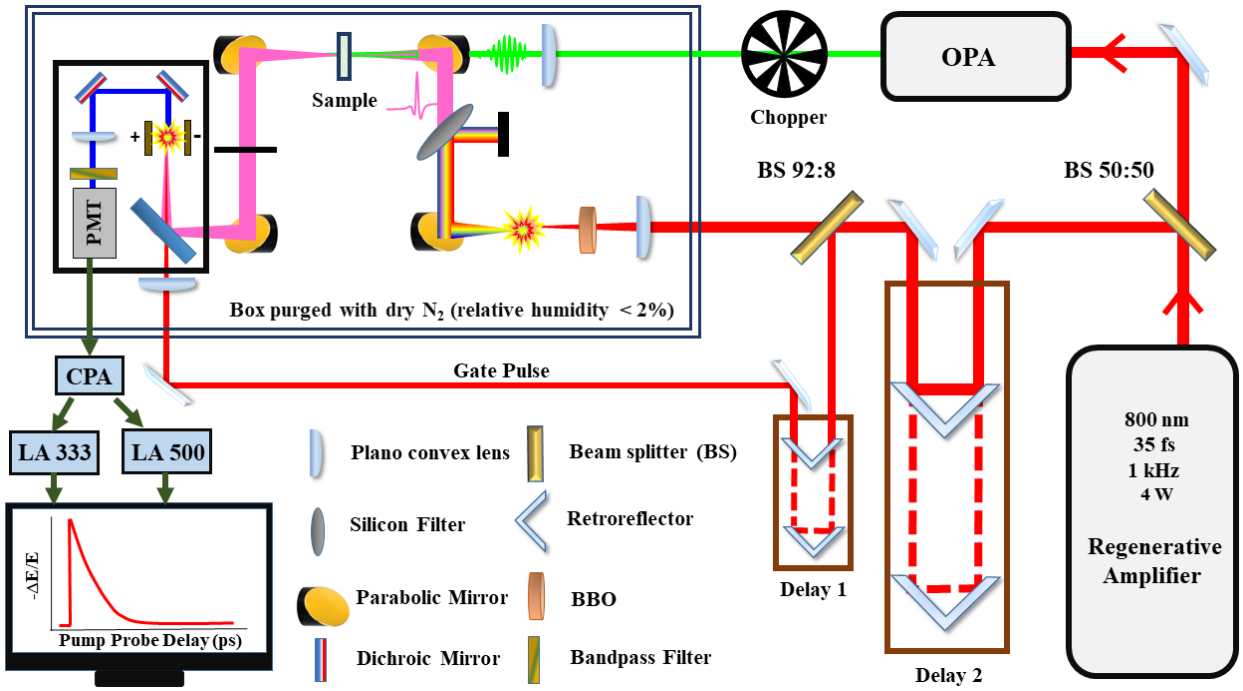

Figure 4. Schematic for experimental setup of Time-resolved THz Spectroscopy (TRTS).

In this Setup, the final output from the current preamplifier (CPA) is split and sent to two lock-in amplifiers. One lock-in amplifier is synchronized with the high-voltage modulator (HVM) at 500 Hz (half the laser repetition rate), while the other is synchronized with the mechanical chopper at 333 Hz. This dual lock-in detection technique minimizes the noise due to laser fluctuation by the simultaneous measurement of the THz electric field from the unexcited sample (E_{off}) and the pump-induced change in the THz electric field (ΔE) from the photoexcited sample.

2.1.4.1. Frequency-averaged experiments (Pump Scans)

Frequency-averaged scans (pump scans) are conducted by varying the delay between the optical pump and the THz probe beam using the 600 mm delay stage (Delay 2), while the 50 mm delay stage (Delay 1) is fixed at the peak of the THz field. The photoinduced change in THz field amplitude ($\Delta E = E_{on} - E_{off}$) is recorded as a function of the delay between the pump and probe pulses. This method captures the temporal evolution of the photoexcited sample.

2.1.4.2. Frequency-resolved experiments (Probe Scans)

Frequency-resolved scans (probe-scans) involve scanning the 50 mm delay stage (gate delay, Delay 1) to record the complete THz waveform at a fixed pump-probe delay set by Delay 2. This approach provides the pump-induced changes in the THz waveform (ΔE) at a specific pump-probe delay. A fast Fourier transformation (FFT) of the THz waveforms yields complex dielectric spectra of the photo-excited sample at chosen pump-probe delays.

2.1.5. Data Analysis

2.1.5.1. THz-TDS experiments

The time-dependent THz electric fields transmitted through the sample, and the reference are denoted as $E_s(t)$ and $E_r(t)$, respectively, and their corresponding Fourier transforms in the frequency domain are $E_s(\omega)$ and $E_r(\omega)$. The reference can be air or a non-conductive substrate such as high-resistivity silicon, high-density polyethene (HDPE) or polystyrene. The complex transmission function $\tilde{T}(\omega)$ is then defined as:

$$\tilde{T}(\omega) = \frac{\tilde{E}_s(\omega)}{\tilde{E}_r(\omega)} = \frac{E_s(\omega)}{E_r(\omega)} e^{i\varphi(\omega)} = T(\omega)e^{i\varphi(\omega)} \quad (5)$$

Here, $\varphi(\omega) = (\varphi_{sample} - \varphi_{ref})$ represents the phase shift between the sample and the reference. If the reference is air, the sample's refractive index can be determined from the phase information.[14] The relationship between the refractive index $n(\omega)$ and the phase shift $\varphi\,(\omega)$ is given by:

$$n(\omega) = 1 + \frac{c}{2\pi\omega d}\varphi\,(\omega) \quad (6)$$

where c is the speed of light in vacuum, ω is the angular frequency of the THz radiation, and d is the thickness of the sample. This formula assumes the reference medium (air) has a refractive index close to 1 and negligible absorption in the THz range.

The absorption coefficient $\alpha(\omega)$ can be calculated from the transmittance T(ω) using the following expression:

$$\alpha(\omega) = -\frac{1}{d}\ln\left(\frac{E_{ref}(\omega)}{E_{sample}(\omega)}\right)^2 \quad (7)$$

Extinction coefficient $k(\omega)$ can be calculated from absorption coefficient $\alpha(\omega)$ using the following relation:

$$k(\omega) = \frac{\lambda\alpha(\omega)}{4\pi} = \frac{c\alpha(\omega)}{2\omega} \quad (8)$$

With $n(\omega)$ and $k(\omega)$, we can get complex refractive index $\tilde{n}(\omega)$ by the relation:

$$\tilde{n}(\omega) = n(\omega) + ik(\omega) \quad (9)$$

The complex refractive index, $\tilde{n}(\omega)$, is directly related to the complex dielectric function, $\tilde{\varepsilon}(\omega)$, and from it, the complex conductivity, $\tilde{\sigma}(\omega)$, can be derived. The relationships are as follows:

$$\tilde{\varepsilon}(\omega) = \tilde{n}^2(\omega) \quad (10)$$

$$\tilde{\sigma}(\omega) = -2\pi\nu\varepsilon_0\tilde{\varepsilon}(\omega) \quad (11)$$

2.1.5.2. TRTS experiments

Thin films, nanoparticles in colloidal solutions, and materials with reasonably low absorption in the THz frequency range are typically studied using time-resolved THz spectroscopy (TRTS) in transmission mode. In TRTS, the optical pump-induced change in the THz probe pulses (ΔE) is collected, which is defined as:

$$\Delta E(t) = E_{on}(t) - E_{off}(t) \quad (12)$$

where $E_{on}(t)$ represents the THz field transmitted through the photoexcited sample (with the pump) and $E_{off}(t)$ represents the THz field transmitted through the unexcited sample (without the pump). Both $\Delta E(t)$ and $E_{off}(t)$ are measured simultaneously using a dual lock-in detection technique.[15-16] The ratio of Fourier transforms of these detected THz electric field $\Delta E(t)$ and $E_{off}(t)$ i.e., $\Delta E(\omega)/E_{off}(\omega)$, is directly proportional to the pump-induced change in photoconductivity $\Delta\sigma$ of the sample, and the relationship is expressed as:

$$\Delta\sigma = -\frac{(n_a+n_b)}{z_0\, d}\,\frac{\Delta E(\omega)}{E_{off}(\omega)} \quad (13)$$

In this context, n_a and n_b denote the refractive indices on either side of the thin film, while d represents the film thickness. The parameter z_0 is the free-space impedance, defined as $z_0 = \frac{1}{\varepsilon_0 c} \sim 377\ \Omega$.

2.1.5.3. THz peak conductivities and carrier mobilities

The initial carrier mobilities can be estimated by normalizing the peak conductivity $\Delta\sigma$ with the carrier density N_0.[17-18] In the linear excitation regime, assuming a photon-to-carrier conversion efficiency of φ = 1 (i.e., each absorbed photon generates one electron-hole pair), the mobility μ is calculated using:

$$\mu \cong \Delta\sigma / qN_0 \tag{14}$$

Where q is the elementary charge, and $N_0$is the total carrier density, given by:

$$N_0 = \varphi.\ 2N_{Ph} \tag{15}$$

However, since the photon-to-carrier conversion ratio φ is not precisely known, this approach yields effective mobility ($\varphi\mu$) rather than the actual mobility (μ). The absorbed photon density (N_{Ph}) is determined using the formula:

$$N_{Ph} = (F_l(1 - 10^{-OD_\lambda}))/\delta.h\nu \tag{16}$$

Where F_l is the incident photon flux, $(1 - 10^{-OD_\lambda})$ represents the fraction of pump light absorbed by the sample (based on the optical density OD_λ), δ is the penetration depth, and $h\nu$ is the energy of a single photon. This method provides an upper limit for N_{Ph}, as it neglects reflection and scattering losses of the pump during the experiments.

Complete THz waveforms are measured at multiple pump-probe delays to obtain the frequency-resolved conductivity spectra. The conductivity spectra are obtained using Equation 13, where $\Delta E(\omega)$ and $E_{off}(\omega)$ represent the Fourier transforms of the photoinduced change in the THz waveform and the reference THz waveform, respectively. The frequency resolved conductivity spectra, were analyzed with appropriate models to extract key parameters, such as carrier density (N_0) and mobility (μ), for each pump-probe delay.

2.1.5.4. Conductivity models for fitting probe scans

In TRTS experiments, materials exhibit distinct features in the frequency-resolved conductivity spectrum, influenced by contributions from free carriers, lattice vibrations, and other low-frequency excitations. By fitting this spectrum to appropriate conductivity models, it becomes possible to quantify both steady-state and photoconductivity. This analysis allows for the determination of critical material parameters, such as mobility and carrier density, as well as the temporal evolution of transport properties.

- **Drude model**

The behaviour of free charge carriers generated upon photoexcitation can be effectively explained using the Drude model, introduced by Paul Drude in 1900.[19-20] This model is primarily applicable to non-interacting electron gases in metals with extremely high carrier concentrations. When a semiconductor is photoexcited using an appropriate pump wavelength, the density of charge carriers increases significantly compared to the intrinsic carrier concentration. Under such conditions, these carriers in semiconductors can be approximated as free carriers, analogous to the electron gas in metals.

According to the Drude model, the complex conductivity of free carriers subjected to an external oscillating electric field with angular frequency ω is expressed as-

$$\tilde{\sigma}(\omega) = \frac{\sigma_{dc}}{(1-i\omega\tau)} \tag{17}$$

where,

$$\sigma_{dc} = \frac{ne^2\tau}{m^*} \tag{18}$$

Here, σ_{dc} represents the DC (or Drude) conductivity, and τ is the carrier momentum scattering time. The DC conductivity is directly related to the carrier concentration (n), scattering time (τ), and the effective mass (m^*) of the carriers.

- **Drude-Smith model**

In the case of nanomaterials, where the movement of charge carriers is restricted to small dimensions or in two-dimensional (2D) materials, the behaviour of carriers differs significantly from that in bulk systems. In these systems, carriers are primarily confined to a specific region and may be backscattered due to spatial constraints or surface effects. As a result, the standard Drude model, which assumes unrestricted carrier motion, requires modification to accurately describe the conductivity.

To address this, V. Smith introduced the Drude-Smith model, which incorporates backscattering parameters to account for the constrained motion of carriers. This modified model provides a more precise description of the conductivity in nanomaterials and 2D systems by extending the classical Drude framework to include these additional effects.[21]

$$\tilde{\sigma}(\omega) = \frac{\sigma_{dc}}{(1-i\omega\tau)}\left(1 + \frac{c}{(1-i\omega\tau)}\right) \quad (19)$$

In the Drude-Smith model, *c* represents the backscattering parameter, which quantifies the extent to which charge carriers are scattered back after interacting with defects, boundaries, or other obstacles. The value of *c* ranges from 0 to -1, where $c = 0$ corresponds to no backscattering (free carrier motion as in the standard Drude model), and $c = -1$ represents complete backscattering, indicating that carriers are entirely confined or reflected to their original direction. This parameter plays a crucial role in describing the modified conductivity in systems where localization effects are significant. The Drude-Smith model has been successfully applied to study the nature of conductivity in materials where charge carrier localization occurs due to defects, grain boundaries, or structural disorder. Examples include perovskite materials, where such effects significantly influence carrier dynamics.

- **Lorentz oscillator model**

The resonance features observed in the conductivity spectrum can arise from various phenomena and are often modelled using the Lorentz oscillator model. In semiconductors, absorption of THz frequencies occurs due to low-energy excitations in solids, such as phonon vibrations, exciton resonances, and other similar processes. These excitations manifest as distinct peaks in the real part of the complex conductivity spectrum.[22] The complex conductivity ($\tilde{\sigma}$) as described by the Lorentz model is given by the expression-

$$\tilde{\sigma}(\omega) = \sum_i \frac{\sigma_i \omega}{(\omega - i\tau_i)(\omega^2 - \omega_i^2)} \quad (20)$$

In the study of THz conductivity, it is common to use a superposition of different conductivity models to interpret the nature of the conductivity spectrum obtained from probe scans in the THz region. This approach helps capture the contributions of various mechanisms, such as free carrier motion, phonon resonances, or localized charge carrier effects, to the overall conductivity.

Similarly, photoconductivity transients measured during pump scans are typically analyzed using multiexponential models and kinetic models to describe the photoinduced recombination

processes. One effective approach is to model the normalized photoinduced THz transients using a multiexponential function convoluted with a Gaussian function. The Gaussian convolution accounts for the temporal resolution of the experimental Setup, ensuring a more accurate representation of the carrier dynamics. This method provides valuable insights into the recombination kinetics and the underlying processes contributing to the transient photoconductivity.[22]

$$y(t) = G(t - t_0) \otimes \frac{\sum_i^n a_i \, exp(t - t_0)}{t_i} \tag{21}$$

Here,

- $\sum_i^n a_i = 1$: This ensures that the sum of the amplitudes (a_i) corresponding to the i^{th}process is normalized. Each amplitude represents the contribution of a process with a characteristic time constant t_i.
- $G(t - t_0)$: This is the Gaussian function centred at t_0, representing the instrumental response function (IRF) with a full width at half maximum (FWHM) of approximately 300 fs.
- $\otimes$: This denotes the convolution operation, combining the multiexponential decay processes with the Gaussian IRF to account for the temporal resolution of the experimental setup.

We have applied these methods to analyze the data from THz spectroscopy experiments performed on $CsPbBr_3$ NCs composites with an inorganic hole transport layer, as detailed in Chapter 3. This approach provided a detailed understanding of the studied system's photoinduced carrier dynamics. Further details can be found in the chapter three.

2.2. Transient absorption spectroscopy

ump-probe spectroscopic techniques utilizing ultrashort pulse lasers allow researchers to observe ultrafast dynamic processes directly. Our understanding of ultrafast dynamics has significantly deepened as time resolution has improved, with pulse durations decreasing from nanoseconds to attoseconds. Crucial transient physical processes, such as carrier excitation, relaxation, recombination, and carrier transport, play a key role in determining the optoelectronic properties of semiconductors.[23-25] A thorough understanding of the physical mechanisms behind these

ultrafast processes is crucial for providing essential feedback for materials development and device optimization. Femtosecond Transient Absorption Spectroscopy (fs-TAS) is a key and well-established ultrafast technique capable of characterizing the excited states of samples and their decay dynamics.[23, 26] Today, commercial fs-TAS systems are widely available and have become a crucial part of the characterization toolkit in many materials laboratories.[27]

In fs-TAS, a pump pulse excites a fraction of the molecules to higher electronic states. Following this excitation, a weak probe pulse passes through the sample with a delay τ with respect to the pump pulse. A probe pulse is typically a broadband white light continuum (WLC) generated by the nonlinear interaction of ultrashort pulses with a nonlinear crystal such as sapphire or calcium fluoride. The low intensity of the probe pulse ensures that interactions with the sample remain linear, thereby avoiding the possibility of multiphoton processes during the probing. When the WLC probe pulse passes through the sample before the arrival of the pump pulse (negative delay), it provides the absorption spectrum of the sample in its ground state.

Conversely, when the probe pulse arrives after the pump pulse excitation, it reflects the absorption spectrum of the sample in its excited state. By measuring the intensity of the probe pulse with the pump on ($I(\lambda)_{pump\text{-}on}$) and with the pump off ($I(\lambda)_{pump\text{-}off}$) alternately, a difference absorption spectrum can be calculated. This difference absorption spectrum is given by:

$$\Delta A(\lambda) = -\log(I(\lambda)_{pump\text{-}on} / I(\lambda)_{pump\text{-}off}) \quad (22)$$

where $\Delta A(\lambda)$ represents the change in absorbance due to the pump pulse excitation.

By varying the time delays between the pump and probe pulses and recording a ΔA spectrum at each delay, a ΔA spectrum as a function of both time delay (τ) and wavelength (λ), denoted as $\Delta A(\lambda, \tau)$, is obtained. This ΔA profile provides insights into the generation and evolution of transient products. Time-resolved absorption spectroscopy offers the advantage of probing non-emissive and dark states, a capability not provided by time-resolved fluorescence. Generally, a ΔA spectrum includes contributions from the following processes:

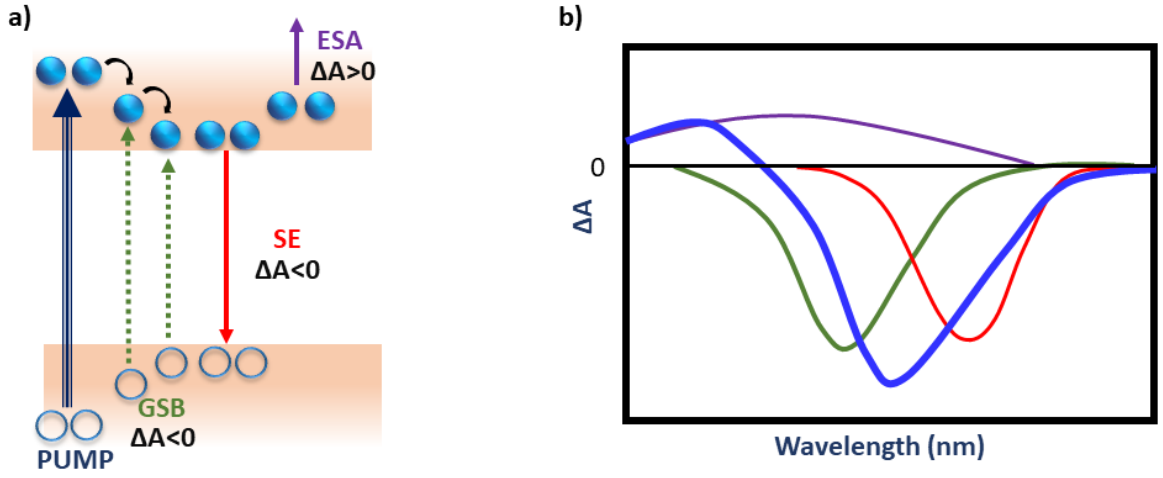

Figure 5. (a) A schematic illustrating various processes following photoexcitation, including ground state bleaching (GSB), excited state absorption (ESA), and stimulated emission (SE). **(b)** Contribution to a ΔA spectrum: GSB (green), ESA (violet), SE (red), the sum of these contributions (blue).

- **Ground-State Bleaching (GSB)**: When the pump pulse excites a fractions of the molecules to the excited states, the number of molecules in the ground state decreases (Figure 5a). This reduction in ground-state molecules leads to lower absorption and increased transmission of the probe light, resulting in a negative transient absorption signal known as the GSB signal. The GSB signal appears immediately after excitation and corresponds to the wavelength range of the characteristic peak observed in steady-state absorption spectroscopy of the sample, as illustrated schematically in Figure 5b (green line).
- **Excited State Absorption (ESA):** In this process, excited molecules absorb probe photons corresponding to optically allowed transitions, moving to even higher excited states. This absorption by excited state molecules can be viewed as absorption spectroscopy of the sample in its excited state. This absorption of the probe pulse by the excited molecules results in decreased transmittance, producing a positive ESA signal (purple line). The probe pulse's low intensity ensures that the population of excited states remains largely unaffected by the ESA process.

- **Stimulated Emission (SE):** In a two-level system, the Einstein coefficients for absorption from the ground state to the excited state (A_{12}) and for stimulated emission from the excited state to the ground state (A_{21}) are equal. When the pump pulse increases the excited state population, photons from the probe pulse induce stimulated emission to the ground state. This stimulated emission increases the detected light intensity, resulting in a negative ΔA signal, as schematically indicated in Fig. 1 (red line). Stimulated emission occurs only for optically allowed transitions. It usually corresponds to the wavelength region where the characteristic peak of the steady-state fluorescence spectrum appears. meaning it is Stokes shifted relative to the ground-state bleach. Since the excited particles must undergo some relaxation processes before interacting with the probe pulse photon to show stimulated radiative transitions, the SE signal generally does not appear immediately after the sample is excited.[26]

In addition to the above three possible contributions to the ΔA spectrum, changes in the ΔA signal can also occur due to photo-product absorption in the excited state. After the excitation of a photobiological or photochemical system, reactions may produce transient or long-lived molecular states, such as triplet states, isomerized states, etc. These transient products absorb the probe pulse, creating a positive signal in the ΔA spectrum. A ground-state bleach will be observed at the wavelengths where the reacting species, which forms the product state, has ground-state absorption.

2.2.1. Experimental setup for fs-Transient Absorption spectroscopy

The general schematic of the transient absorption setup is illustrated in Figure 6. A femtosecond amplified pulse from a regenerative amplifier serves as the primary light source. The beam is initially split into two parts: the majority is directed into an optical parametric amplifier (OPA) to generate tunable wavelengths for pumping the samples, while the remainder is routed to a sapphire crystal via a computer-controlled delay stage. With sufficient peak power, the ultrashort femtosecond pulse interacts nonlinearly with the sapphire crystal (or other nonlinear crystal), producing a white-light continuum. This continuum acts as a weak broadband probe to measure the sample's absorption. Its intensity is low enough to avoid significantly transferring the ground-state population to the excited state.[27]

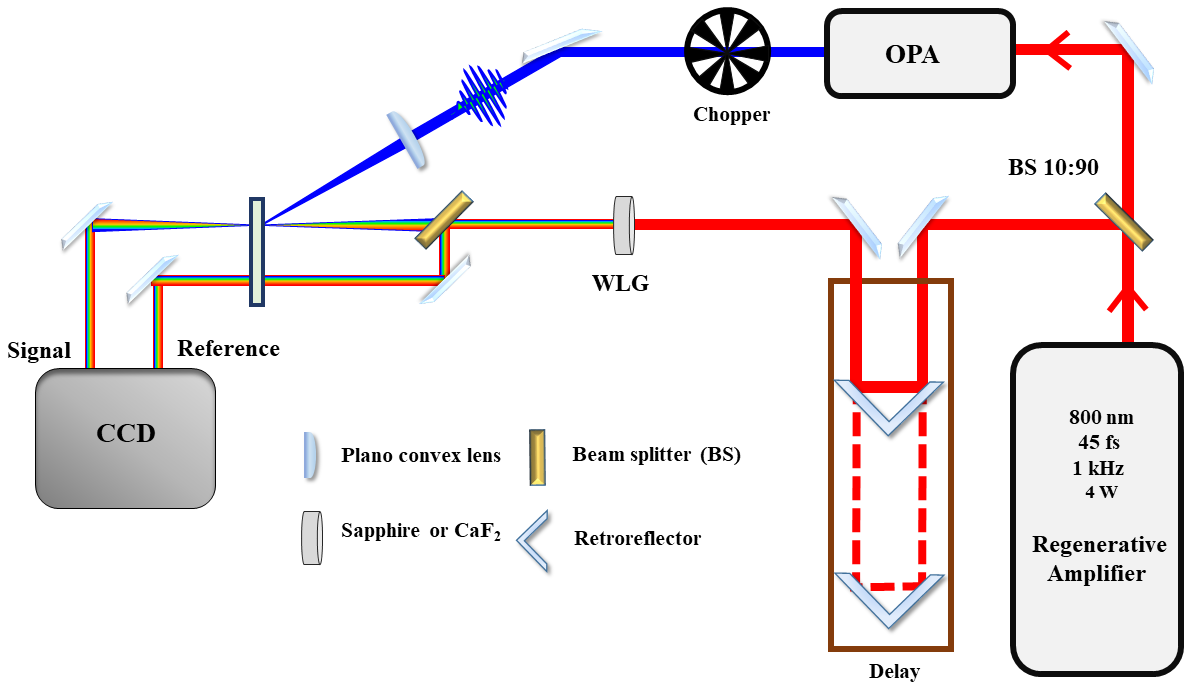

Figure 6. Schematic of a typical femtosecond transient absorption spectroscopy setup.

Before reaching the sample, the white-light continuum is divided into two beams: the probe and the reference. The probe beam is focused on the sample to a spot size slightly smaller than the pump, spatially overlapped with it, collimated, and then directed to a CCD detector to record the signal. On the other hand, the reference beam passes through a region of the sample not exposed to the pump pulse, ensuring it remains unaffected by excitation, and is also sent to the CCD for detection.

A mechanical chopper, synchronized with the laser repitition rate and operating at half the laser repetition rate, is positioned in the pump path before the sample to block every other pump pulse alternately. This results in consecutive probe pulses interacting with excited and unexcited sample regions. The transient absorbance is calculated as the ratio of these signals. Additionally, dividing the probe signal by the reference signal during data collection helps suppress intensity fluctuations in the white-light continuum, thereby improving the signal-to-noise ratio.[27]

The transient absorption data presented in this thesis (Chapter 3) was collected at Prof. H. N. Ghosh's laboratory at INST Mohali with the assistance of his student, Dr. Gurpreet Kaur. The measurements were performed using a Helios spectrometer (Ultrafast Systems LLC), with both pump and probe beams derived from a regeneratively amplified Ti:sapphire laser system (central

wavelength: 800 nm, pulse duration: 35 fs, pulse energy: 5 mJ, and repetition rate: 1 kHz). The pump pulses of various desired wavelengths were generated using a Optical Parametric Amplifier (Opera, Coherent). A white-light continuum (WLC) spanning 420 to 800 nm was produced by focusing the transmitted 800 nm pulses onto a sapphire window. The pump beam was modulated at 500 Hz using a synchronized optical chopper.[28] Data analysis was carried out using the Surface Explorer software.

2.3. Optical Kerr effect spectroscopy

In 1875, John Kerr applied a direct current (DC) electric field to a transparent, isotropic liquid medium. The interaction between the electric field and the molecular dipole moments caused a partial alignment of the molecules within the liquid. This alignment introduced anisotropy in the medium, resulting in different refractive indices parallel and perpendicular to the direction of the electric field. This phenomenon, where induced birefringence occurs due to an external electric field, came to be known as the Kerr effect, named in his honour.[29]

In contrast to the DC electric field used in the traditional Kerr effect, the optical Kerr effect (OKE) relies on an intense laser field to induce birefringence in a liquid. The oscillating electric field of the laser pulse generates induced dipoles within the liquid molecules. These induced dipoles interact with the laser field, causing the molecules to preferentially align their axis of maximum polarizability parallel to the laser polarization. This molecular alignment produces a transient birefringence in the liquid. In OKE spectroscopy, a second laser pulse probes this transient birefringence in real time. By analyzing its time-dependent behaviour, valuable insights into the microscopic dynamics of the medium can be obtained.

The first experimental demonstration of Optical Kerr Effect (OKE) spectroscopy was conducted by Duguay and Hansen in 1969.[30] Their work focused on investigating the orientational dynamics of carbon disulfide (CS_2) and nitrobenzene using ultrafast laser pulses with durations of a few picoseconds. Two major milestones have significantly advanced the development of OKE spectroscopy. The first was the incorporation of optical heterodyne detection by Ippen and Shank,[31] while the second was the development of the Fourier-transform deconvolution technique by McMorrow and Lotshaw.[32] These key innovations will be discussed in more detail in the following section.

2.3.1. Optically heterodyne detected optical Kerr effect (OHD-OKE) spectroscopy:

Figure 7 depicts the standard polarization geometry commonly employed in OKE spectroscopy. In this Setup, a pump pulse polarized at 45° relative to the probe pulse excites the sample. Following this, a probe pulse with a variable time delay is directed into the sample. An analyzer, positioned after the sample, is aligned with its axis perpendicular to the polarization of the probe pulse.

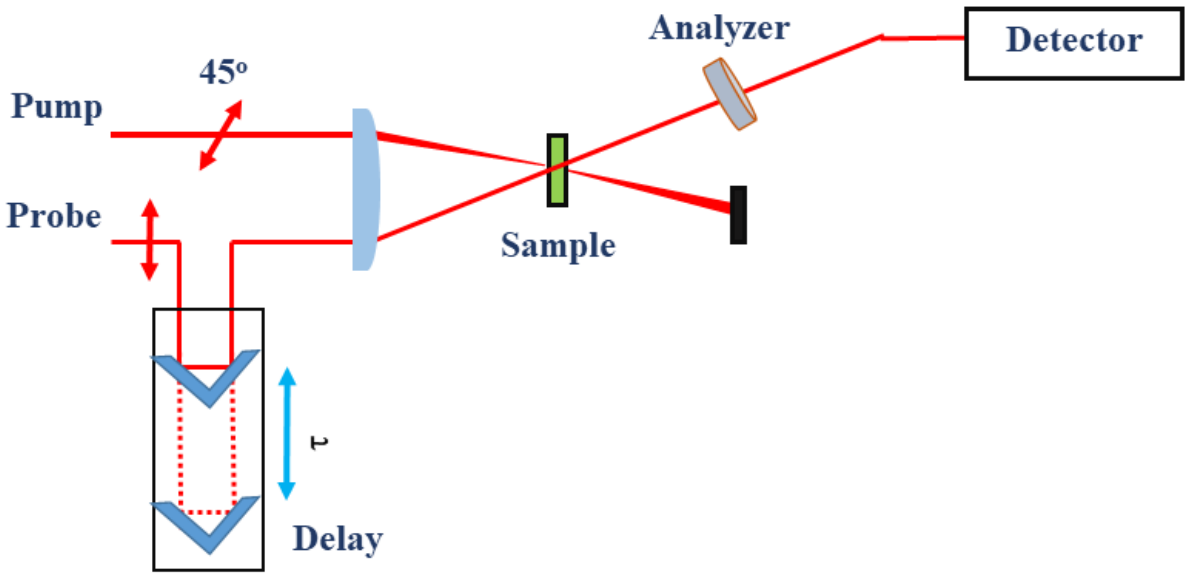

Figure 7. The schematic illustrates the layout for polarization spectroscopy implementation of the optical Kerr effect. The pump pulse is aligned at a 45° polarization angle in this configuration, while the probe pulse is set to vertical polarization. The analyzer polarizer is adjusted to transmit only horizontally polarized light, and the transmitted leakage is recorded as a function of the time delay between the pump and probe pulses. This represents the homodyne detection technique of the OKE signal.

In the absence of the pump pulse or at negative delays, the probe pulse interacts with an isotropic sample, resulting in no light passing through the analyzer. However, after pump excitation, the induced birefringence in the sample alters the polarization state of the probe pulse, causing depolarization. This depolarization allows some of the probe light to pass through the analyzer. The transmitted light intensity is linearly related to the degree of birefringence in the sample. By

varying the time delay between the pump and probe pulses, the time-dependent birefringence can be measured, providing insights into the dynamics of the sample.

This polarization spectroscopy configuration is designed to detect the difference between two components of the third-order response, $R^{(3)}_{xxxx}$(t) and $R^{(3)}_{xxyy}$(t). This difference is proportional to $R^{(3)}_{xyxy}$(t) in an isotropic medium and commonly referred to as the depolarized response.[33] Since the detected signal corresponds to the intensity in this experimental setup, it is proportional to the squared magnitude of the depolarized response. This detection approach is known as homodyne detection. The recorded homodyne signal is thus proportional to the square of the sample's nonlinear susceptibility. By varying the delay time τ, the time-dependent behaviour of the depolarized Kerr signal can be measured, providing insights into the medium's dynamics.

In heterodyne detection of the OKE signal, a quarter-wave plate is typically introduced into the probe beam path before the sample, with its fast axis aligned parallel to the probe beam's polarization plane. The probe beam's polarization is then slightly rotated (by about 1°) before passing through the quarter-wave plate. This slight rotation introduces an orthogonal polarization component, allowing a fraction of the probe light to pass through the analyzer polarizer. This orthogonal component acts as a local oscillator, introducing a heterodyne signal component that is linearly proportional to the nonlinear susceptibility of the sample, superimposed on a constant laser background. The constant background is electronically subtracted, and to eliminate any homodyne "contamination" in the signal, two sets of data are collected. In the second set, the probe beam's polarization is rotated by the same degree but in the opposite direction. By subtracting the two data sets, collected with opposite heterodyne angles, the homodyne contributions are effectively cancelled, isolating the pure heterodyne OKE signal. This method requires only a single photodiode paired with a lock-in amplifier, but it involves the complication of collecting two datasets for the heterodyne signal.[34]

In our Setup, we utilized an advanced approach to detect the OHD-OKE signal in a single shot. This approach utilizes a quarter-wave retardation plate combined with a Glan–Thompson polarizer before the detection stage. The detection process uses a pair of photodiodes configured for balanced detection. The linearly polarized probe beam, after passing through the sample, is converted to circularly polarized by the quarter-wave plate. The parallel and perpendicular

components of the beam are then separated by the Glan–Thompson polarizer and directed to the photodiodes, where the signals are electronically subtracted. This subtraction eliminates both the homodyne and background components, isolating the pure heterodyne signal in a single shot. Additionally, the balanced detection method minimizes the impact of random laser power fluctuations, significantly enhancing the signal-to-noise ratio. Before recording the OKE signal, the detector is balanced at a negative delay by rotating the quarter-wave plate and monitoring the signal from both photodiodes on an oscilloscope.

2.3.2. OKE experimental setup:

OKE spectroscopy features a relatively simple experimental setup compared to many other pump-probe techniques. Figure 8 illustrates the schematic of the home-built OHD-OKE spectroscopy system used in our lab. The Setup utilizes a Ti:Sapphire regenerative amplifier laser (Spitfire Pro XP, Spectra-Physics) seeded by an ultrafast Ti:Sapphire oscillator (Tsunami, Spectra-Physics). This laser system produces 800 nm, 45 fs pulses at a repetition rate of 1 kHz, serving as the primary light source.

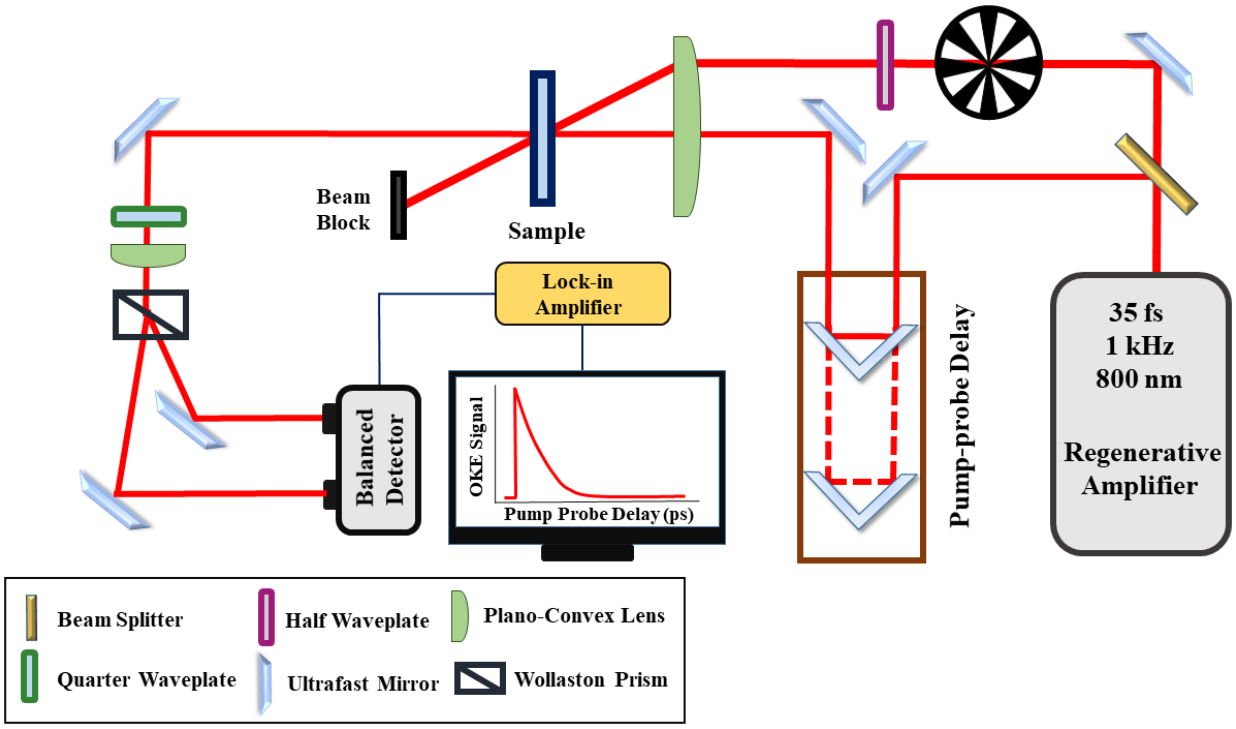

Figure 8. A schematic diagram illustrates the experimental setup for Optical Heterodyne-Detected Optical Kerr Effect (OHD-OKE) spectroscopy.

A portion of the amplifier output is split into two beams: the pump beam, carrying approximately 80% of the power (with pump power kept below 1 mW to prevent unwanted nonlinear processes in the sample), and the probe beam, which has lower power. The use of ultrashort pulses is crucial for achieving a broader spectral bandwidth, which is essential for effective OKE spectroscopy measurements.

The pump beam passes through a mechanical chopper and a half-wave plate, which aligns its polarization at 45° relative to the probe polarization. It is then routed and focused onto the sample. Meanwhile, the probe beam travels through a delay line, allowing precise control of the optical delay before reaching the sample. After interacting with the sample, the pump beam is blocked, while the probe beam continues through a quarter-wave plate, followed by a Wollaston prism, which is part of the heterodyne detection assembly.

The quarter-wave plate converts the linearly polarized probe light, altered by the anisotropy of the excited sample, into elliptically polarized light. The Wollaston prism then separates the light into its parallel and perpendicular polarization components, directing them to a balanced photodetector. This detector consists of a pair of photodiodes, which are balanced prior to the experiment in the absence of pump excitation. For accurate measurement, both the pump and probe beams are focused and spatially overlapped onto the sample. As the delay stage moves, the temporal overlap of the pump and probe pulses occurs at a specific point, generating a rise in the OKE signal, followed by transient birefringence. This signal is recorded as a function of the pump-probe delay.

As discussed earlier, the detection system automatically heterodynes the signal by electronically subtracting the horizontal and vertical components. The detector output is fed into a lock-in amplifier synchronized to the frequency of the chopper in the pump path. Data acquisition is managed through DAQ with custom LabVIEW software.

Figure 9 illustrates the heterodyne-detected OKE signal in the time domain for the first few picoseconds. The data includes the OKE signal for a CaF_2 crystal, used as an autocorrelation trace essential for data analysis and for a doped semiconductor nanocrystal. Around zero delay time, a sharp peak corresponding to the laser pulses is observed. This feature, known as the electronic response, arises due to the intense electric field of the laser pulse distorting the electron clouds in the sample molecules. It originates from the electronic hyperpolarizability of the material.

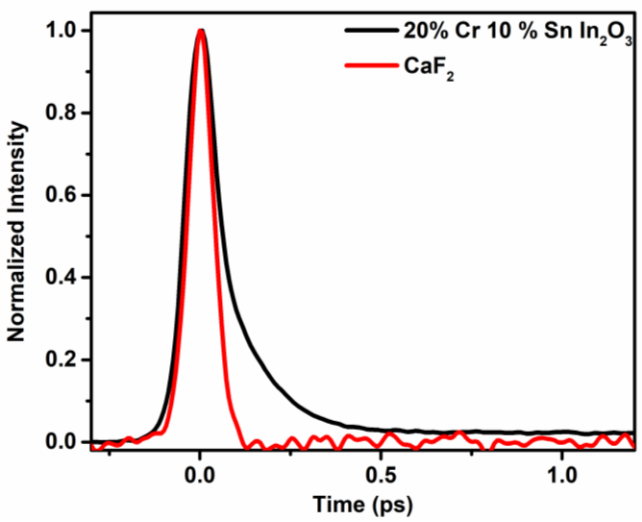

Figure 9. A typical OKE time domain signal of the CaF_2 and Sn-Cr co-doped ITO NCs.

The subsequent decay is referred to as the nuclear response, which has distinct components. In the initial few picoseconds, a gently decaying portion is observed, resulting from the coherent decay of Raman-active, collective intermolecular motions excited by the pump pulse. At longer times, the nuclear response exhibits a monotonically decaying tail, attributed to the collective orientational diffusion of liquid molecules.

Additionally, in some samples, oscillations in the nuclear response are visible, caused by low-frequency intramolecular vibrational modes coherently excited by the pump pulse. For these modes to appear in the OKE decay, they must be Raman-active and exhibit polarizability anisotropy, enabling their detection through the OKE technique.

After the pump excitation, spontaneous rotational diffusion begins to reorient the molecules back to their equilibrium positions. The process occurs on timescales related to rotational diffusion, which can be directly derived from the OKE data. The slowest component of the relaxation process is the timescale for orientational diffusion, typically exhibiting exponential decay behavior.

Also, Techniques such as Raman spectroscopy and NMR are sensitive to the orientational correlation functions of individual molecules. In contrast, OKE spectroscopy measures the collective orientational correlation function. The relationship between the collective orientational correlation time (τ_{coll}) and the single-molecule orientational correlation time (τ_{sm}) is expressed by the following equation-

$$\tau_{coll} = \frac{g_2}{j_2}\tau_{sm} \tag{23}$$

Here, g_2 and j_2 represent the static and dynamic pair orientational correlation parameters, respectively.[35] The parameter g_2 reflects the degree of parallel molecular ordering in a liquid, taking a value of 1 when there is no net ordering. For simple liquids, it is typically assumed that j_2 equals 1.

By comparing the orientational relaxation times obtained through OKE spectroscopy with the single-molecule relaxation times, valuable microscopic structural information about the liquid can be uncovered. This approach provides insights into the interplay between molecular dynamics and the liquid's structural organization.

2.3.3. Fourier transform deconvolution

One key advantage of the OKE experiment is its ability to analyze molecular dynamics in both the time and frequency domains using Fourier transform deconvolution, a technique first introduced by McMorrow and Lotshaw. This method enables the removal of the effects caused by the finite duration of laser pulses in OKE data. As a result, it allows for precise determination of Bose-Einstein-corrected spectral densities, providing more accurate insights into molecular and collective dynamics.[32]

The heterodyne-detected OKE signal, $S(t)$, is described by the equation:

$$S(t) \propto [I_{pump} \otimes I_{probe}] \otimes R^{(3)}_{xyxy} \tag{24}$$

Here, $\otimes$ denotes convolution, and the term in square brackets represents the instrument response, also referred to as the second-harmonic intensity autocorrelation trace, $G^{(2)}(t)$ which is given by-

$$G^{(2)}(t) = \int_{-\infty}^{\infty} I_{pump}(t') I_{probe}\,(t - t')dt' \tag{25}$$

This autocorrelation trace, $G^{(2)}(t)$, can be measured experimentally by performing cross-correlation between the pump and probe pulses with a CaF_2 crystal placed at the sample position.

Using the convolution theorem, the Fourier transform of $S(t)$ is expressed as:

$$\mathcal{F}[S(t)] = \mathcal{F}[G^{(2)}(t) \otimes R^{(3)}_{xyxy}] \tag{26}$$

By dividing the Fourier transform of $S(t)$ by that of $G^{(2)}(t)$, we obtain:

$$\mathcal{F}[R^{(3)}_{xyxy}] = \frac{\mathcal{F}[S(t)]}{\mathcal{F}[G^{(2)}(t)]} \tag{27}$$

The imaginary component of this Fourier transform, $Im\ \mathcal{F}[R^{(3)}_{xyxy}]$, is referred to as the spectral density. The electronic response appears as a delta function at zero time, contributing to the real part, $Re\ \mathcal{F}[R^{(3)}_{xyxy}]$. The nuclear response function can be extracted by applying the inverse Fourier transform to the spectral density.

To isolate specific dynamics, the diffusive orientational contribution is often subtracted from the spectral density. This results in the reduced spectral density (RSD), which is obtained by subtracting a function of the form

$$exp\left({}^{t}/_{\tau_{OKE}}\right)\left[1 - exp\left(-{}^{t}/_{\tau_{rise}}\right)\right] \tag{28}$$

Here, τ_{rise}, typically assumed to be 200 fs or less, represents the rise time. Its exact value has minimal impact on the shape of the RSD. The resulting nuclear response function is then Fourier transformed to derive the RSD, which provides detailed insights into the molecular and collective dynamics of the system.[36]

The reduced spectral density (RSD) is typically analyzed by fitting it to a sum of complex lineshapes, like the sum of antisymmetric Gaussians and Ohmic lineshapes. This approach allows for the characterization of the underlying dynamics in the system, as each lineshape corresponds to specific molecular or collective motions. By decomposing the RSD into these components, detailed insights into the relaxation processes, vibrational modes, and other dynamic behaviours of the system can be obtained.

An alternative approach to analyzing frequency-domain data is to consider the full spectral density across a wide range of frequencies, from GHz to THz. Instead of fitting the time-domain data to multiple exponential functions, this method fits the spectral density in the GHz-THz range using phenomenological models.

The Mode Coupling Theory (MCT) is one such model that captures both α and β relaxations. The α relaxation, which corresponds to long-time, collective molecular motions, is typically modelled using the Cole-Davidson function. In contrast, β relaxation, associated with more restricted or local

molecular motions, is described by the Cole-Cole function. Additionally, intermolecular modes, such as those arising from interactions between molecules, are often modelled by Brownian oscillators. This approach offers a more holistic view of molecular dynamics, capturing both fast and slow processes in the system without the need for multiple exponential fits, providing deeper insights into the relaxation and structural dynamics.[37]

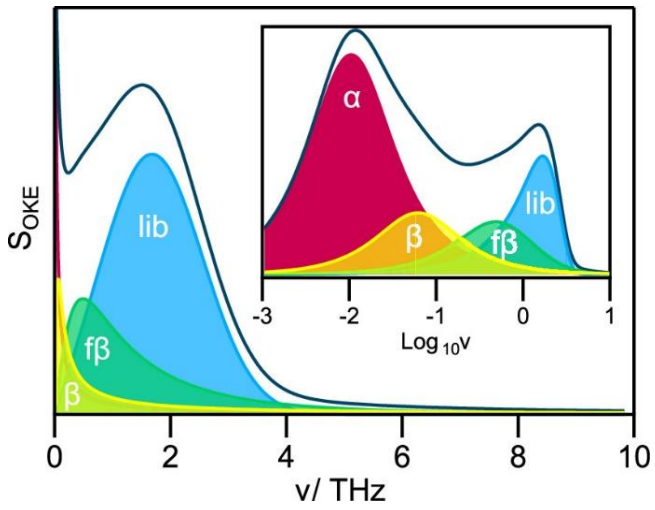

Figure 10. The general schematic of the low-frequency vibrational spectrum of a liquid includes several key contributions that characterize different molecular motions (reproduced with permission from reference 38). These contributions are as follows-

- α-relaxation: This corresponds to orientational relaxation, where molecules undergo large-scale reorientation over longer timescales, typically in the picosecond to nanosecond range.
- β-relaxation: This represents translational diffusion, where molecules undergo slower, more restricted motion compared to α-relaxation, often observed on the timescale of nanoseconds.
- Fast-β process (fβ) (cage-rattling): This fast process occurs on a femtosecond timescale, where molecules experience rapid, short-range motions as they move within their cages formed by neighbouring molecules.
- Librations (lib): A libration refers to a rocking motion of a molecule, where it oscillates back and forth around a fixed axis. This motion is typically caused by the constraints

imposed by the surrounding "cage" of nearest-neighbour molecules occurring in the terahertz range.

The inset version is on a logarithmic frequency axis is often used to better highlight the lowest frequency region, including the gigahertz and lower frequencies, which correspond to the slowest processes, such as α and β relaxations.[38]

2.4. Nonlinear optical properties measurements

Over the past two decades, metal halide perovskites (MHPs) have gained significant attention for their outstanding performance in solution-processed photovoltaic devices.[39] These organic/inorganic hybrid halide perovskites possess exceptional optoelectronic properties, leading to impressive results in various optoelectronic devices, including LEDs,[40] photodetectors,[41] and lasers.[42]

Recently, numerous studies have demonstrated a wide range of nonlinear optical (NLO) effects in MHPs. Their versatile chemical structures offer a tunable bandgap and high oscillator strength,[43] making them suitable for applications in NLO materials and devices.[44] Many reports highlight large two-photon absorption coefficients and efficient second, third, and higher-order NLO effects, especially from highly quantum-confined, lower-dimensional perovskite materials.[45]

In this thesis, we have explored the NLO properties of chiral 0D perovskite materials using two home-built setups. The first Setup is for the Z-scan spectroscopy technique, and the second is designed to collect upconverted photons from samples exhibiting second, third, or higher harmonic generation. The following sections will discuss the details of these setups and the data analysis involved in the experiments.

2.4.1. Z-Scan technique

The Z-scan technique is a precise single-beam method used to directly measure the nonlinear refractive index (n2) and the nonlinear absorption coefficient (β) of various materials. Introduced by Eric Van Stryland in 1990,[46] it has become the standard method for determining a material's third-order optical nonlinear parameters, β and n2. These measurements are directly linked to the

real and imaginary parts of the third-order nonlinear susceptibility $\chi^{(3)}$, offering crucial insights into the properties of materials.

In the Z-scan method, a sample is moved along a focused Gaussian beam, and its transmittance is recorded in the far field as a function of the sample's position relative to the focal plane. As illustrated in Figure 11, when the sample approaches the focal point f from the negative z direction, the incident intensity increases, reaching its peak at the focal point. The intense laser beam near the focal point interacts nonlinearly with the material, altering the sample's absorption coefficient and refractive index. These intensity-induced changes cause variations in both the intensity and phase of the beam passing through the sample. These nonlinear effects diminish as the sample moves past the focal point towards the positive z direction, where the incident intensity decreases.

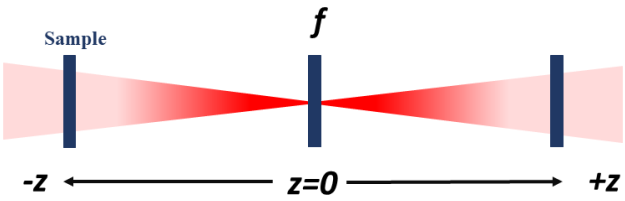

Figure 11. A figure illustrating the variation in laser fluence at the sample as it moves through the focal point, from the -z to +z direction, under a focused Gaussian beam.

In this technique, transmittance through the sample is measured in two different configurations. The "closed aperture" Z-scan includes an aperture before the photodiode detector in the far field, while the "open aperture" Z-scan does not use an aperture before the detector. Both configurations are detailed in the following sections, along with their respective setups.

2.4.2. Z-Scan Setup

Figure 12 shows the schematic of our Z-scan measurement setup. The Ti-sapphire regenerative amplifier (Spitfire Pro XP, Spectra-Physics), seeded by an oscillator (Tsunami, Spectra-Physics), produces ultrashort 35 fs pulses centred at 800 nm with a 1 kHz repetition rate, serving as the optical source for the experiment. Neutral density filters are used to adjust the laser power to the desired level.

The laser beam is initially divided into two portions using an ultrafast beam splitter. About 10% of the beam is sent to an optical autocorrelator (PulseScout, Spectra-Physics) to measure the pulse width, (the pulse width measured before the Z-scan setup was 65 fs) while the remaining 90% is utilized for the main experiment. A second beam splitter divides the main beam into two equal parts with a 50:50 ratio. One portion is directed to an amplified silicon photodiode (PD1) (PDA36A-EC, Thorlabs) for monitoring and minimizing laser fluctuations, while the other is focused onto the sample using a 200 mm plano-convex lens. Before the lens, the beam has a diameter of 2 mm and forms a focal spot with a size of around 70 μm ($\omega_0 = 31.25$ μm).

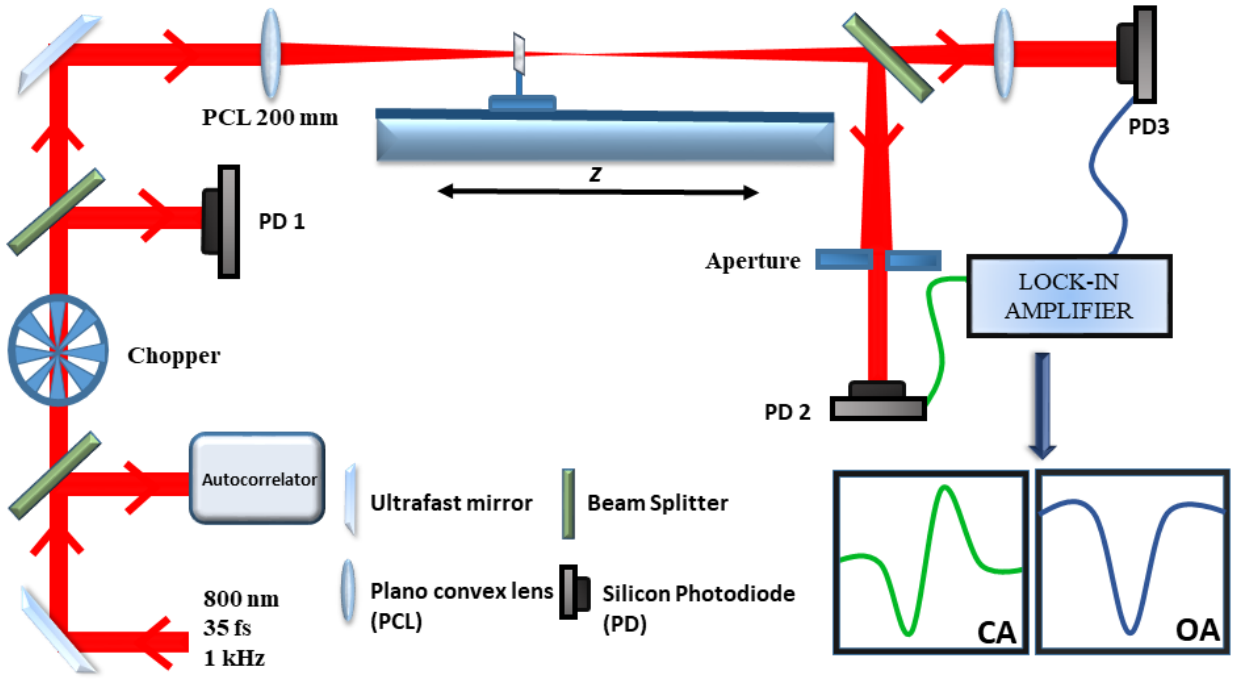

Figure 12. A schematic representation of the experimental Z-scan spectroscopy setup.

The sample is positioned on a 300 mm translation stage (PI M414.3PD) and systematically moved through the focal point. After interacting with the sample, the beam is again divided into two equal parts using another beam splitter. One portion is collimated by a lens and directed to photodiode PD3, while the other passes through an aperture before reaching photodiode PD2. The signals from both photodiodes are sent to a lock-in amplifier (SR830, Stanford Research Systems), which is synchronized with the 333 Hz frequency of an optical chopper in the laser path. Data acquisition

is then carried out using the lock-in amplifier output, processed through a data acquisition (DAQ) system (National Instruments) using a custom interface program developed in LabVIEW.

2.4.3. Open aperture (OA) Z-scan:

The voltage output from photodiode PD3, positioned without the aperture, captures intensity changes caused by nonlinear absorption and is used for open-aperture Z-scan measurements. The resulting Z-scan spectra are shown in Figure 13a and Figure 14a. A dip in intensity at the focal point, as observed in Figure 13a, indicates two-photon absorption (or multiphoton absorption). In this process, the sample transitions from the ground state to an excited state by simultaneously absorbing

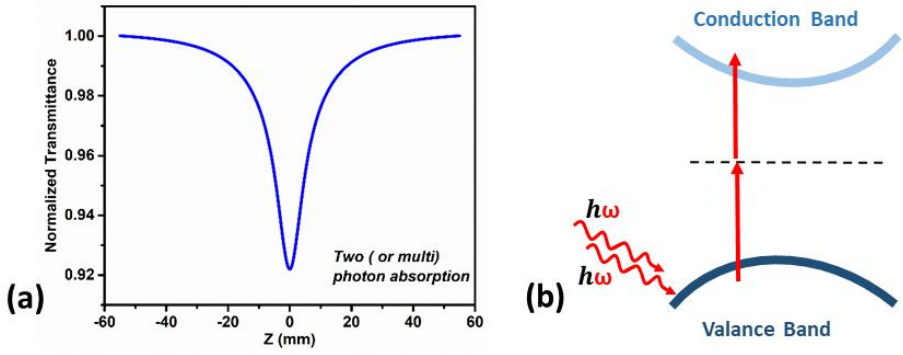

Figure 13. (a) A representation of a typical open-aperture Z-scan spectrum observed for nonlinear multiphoton absorption. **(b)** schematic representation of two-photon absorption via an intermediate virtual state.

two photons. During this transition, a virtual state (represented by the dotted line in Figure 13b) is temporarily formed between the real ground and excited states. This phenomenon is also referred to as reverse saturable absorption. Alternatively, a peak at the focal point can be observed, with the transmitted intensity increasing near the focal point due to saturable absorption, as shown in Figure 14. Saturable absorption is a property of materials where light absorption decreases as light intensity increases. At sufficiently high light intensities, the ground-state atoms in the material are excited at a rate so rapid that there is insufficient time for the excited atoms to return to the ground state. This depletion of the ground-state population leads to saturation of the material's absorption.

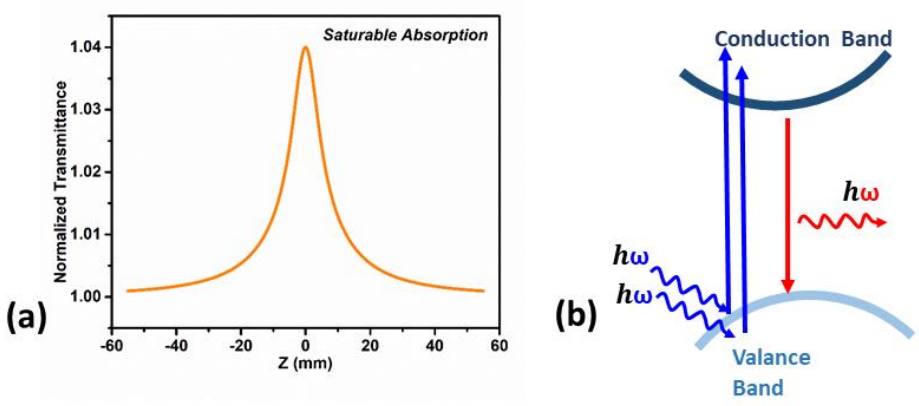

Figure 14. (a) A representation of a typical open-aperture Z-scan spectrum observed for saturable absorption (SA). **(b)** Schematic representation of saturation of absorption at high intensity.

To extract the two-photon absorption (TPA) coefficient (β), we have fitted the open aperture Z-scans to this equation-[47]

$$T(z) = 1 - \frac{1}{2\sqrt{2}}\left(\frac{Q}{1+{(z-z_0)^2}/{z_r^2}}\right) \tag{29}$$

where, $Q = \beta I_0 L_{eff}$

and, $L_{eff} = {1 - e^{-\alpha_0}L}/{\alpha_0}$

Q is the nonlinear absorption parameter, z_0 is the Focal point, β is the TPA coefficient, L_{eff} is the effective sample length and I_0 is the peak irradiance. z_r (= $\pi w_0^2/\lambda$) is the Rayleigh length, which is calculated to be 5.8 mm, where w_0 is the beam width at the focus is calculated to be 70.14 μm in our setup. The effective path length of the sample should be less than the Rayleigh range (z_r), to satisfy the thin film approximation, i.e. $L_{eff} << z_r$.[48]

2.4.4. Close aperture (CA) Z-scan

The photodiode PD2 monitors intensity changes caused by the nonlinear refractive index of the material. The refractive index under nonlinear conditions can be expressed as:

$$n = n_0 + n_2 I \tag{30}$$

Here, n_0 represents the linear refractive index, n_2 is the nonlinear optical constant that depends on the filed intensity, and I is the intensity of light. Depending on the sign of n_2, self-focusing or self-defocusing can occur due to the non-uniform refractive index. For a positive n_2, the material exhibits self-focusing, while a negative n_2 leads to self-defocusing. These effects alter the fraction of light passing through the aperture, thereby modulating the intensity detected by the photodiode PD2.

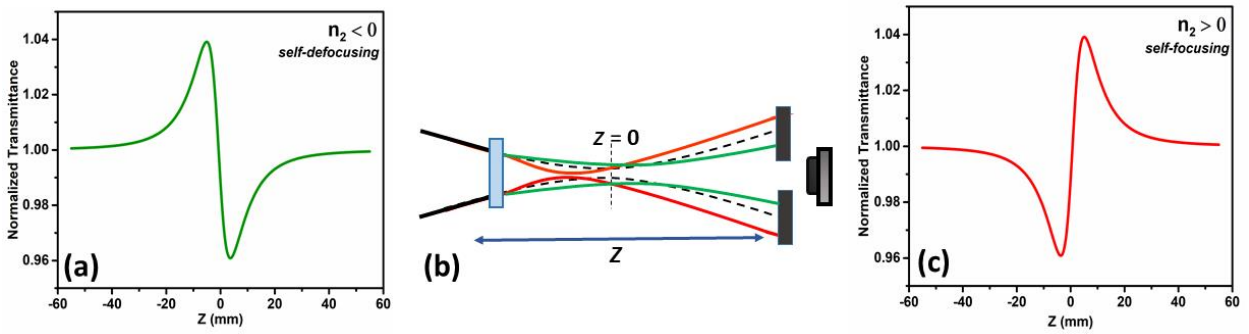

Figure 15. (a) A representation of a typical closed-aperture Z-scan spectrum for a material exhibiting self-defocusing behaviour ($n_2 < 0$), and **(c)** self-focusing behaviour ($n_2 > 0$) at high intensities. **(b)** A figure illustrating the collimation of the beam (green) leading to beam narrowing at the aperture and beam divergence (red) causing broadening before the aperture for samples with self-defocusing ($n_2 < 0$) and self-focusing ($n_2 > 0$) properties, respectively. These effects alter the amount of light transmitted through the aperture to the photodiode, resulting in a peak-valley spectrum for materials with a negative nonlinear refractive index and a valley-peak spectrum for those with a positive nonlinear refractive index.

A negative self-lensing effect (self-defocusing, $n_2<0$) prior to the focal point tends to collimate the beam, causing beam narrowing at the aperture (green line in Figure 15b). This results in an increase in measured transmittance. As the sample moves past the focal plane in the positive *z*-direction, the same self-defocusing effect increases beam divergence, leading to beam broadening at the aperture and a subsequent decrease in transmittance. This creates a characteristic Z-scan signature for negative nonlinear refraction: a prefocal transmittance peak followed by a postfocal transmittance valley, as illustrated in Figure 15(a).[48]

In contrast, a positive nonlinear refractive index (self-focusing, $n_2>0$) results in the opposite behaviour. Positive self-lensing focuses the beam before the actual focal point, causing the beam

to diverge at the aperture (red line in Figure 15b) and leading to a decrease in transmittance, forming a valley (Figure 15c). After the sample moves past the focal point in the positive z-direction, the beam is collimated, increasing transmittance and forming a peak. This valley-peak pattern is the hallmark of positive nonlinear refraction. An important feature of the Z-scan method is its ability to immediately indicate the sign of the nonlinear refractive index based on the data, making it a highly effective tool for characterizing nonlinear optical properties.[48]

If the sample exhibits purely refractive nonlinearity, with no contributions from absorptive nonlinearities (such as multiphoton absorption or saturation of absorption), only photodiode PD2 is used to perform the closed-aperture (CA) Z-scan. However, if both nonlinear absorption or saturation effects are present, they influence the transmittance recorded by PD2. Specifically, multiphoton absorption suppresses the peak and enhances the valley in the CA scan, while saturation of absorption has the opposite effect, enhancing the peak and suppressing the valley.

To isolate the refractive nonlinearity and eliminate the influence of absorptive effects, the output of photodiode PD2 is divided by that of photodiode PD3. The resulting PD2/PD3 ratio provides a closed-aperture scan that reflects only the refractive nonlinearity of the sample. As previously discussed, sensitivity to nonlinear refraction depends entirely on the presence of the aperture. Removing the aperture eliminates this effect altogether.

Additionally, the magnitude of this effect is influenced by the size of the aperture, quantified as *S*, which represents the fraction of light transmitted through the aperture. Adjusting *S* allows for control over the sensitivity of the Z-scan measurement to refractive nonlinearity.

To extract the values of n_2, the CA traces were fitted to the following equation-[48]

$$T(z)_{close} = 1 - \frac{4x}{(1+x^2)(9+x^2)}\Delta\phi_0 \tag{31}$$

$x = {}^{z}/_{z_r}$

$$\Delta\phi_0 = k\, n_2 I_0 L_{eff} \tag{32}$$

Where $\Delta\phi_0$is on axis nonlinear phase shift with the sample at focus (z=0), n_2 is the third-order nonlinear refractive index, and $k = {}^{2\pi}/_{\lambda}$ is wave vector.

Also,

$$\Delta T_{pv} \cong 0.406(1-S)^{0.25}|\Delta\phi| \quad (33)$$

$\Delta T_{pv} = T_p - T_v$, Change in transmittance between the peak and valley

S = fraction of light transmitted by the aperture

The equtaion 33 provides an alternative way to get $\Delta\phi_0$ from CA scans and then then n_2 can be calculated using equation 32.

Prior to recording data for perovskite samples, we optimized the Z-scan setup setup by measuring the nonlinear optical parameters of samples previously reported in the literature. As a benchmark, we measured the nonlinear refractive index (n_2) of carbon disulfide (CS_2) using a 1 mm quartz cuvette containing the liquid (Figure 16). The measured value of n_2, 5.8 x 10^{-6} cm²/GW at an input fluence (I_0) of 9 GW/cm², showed excellent agreement with the reported values in the literature.[49]

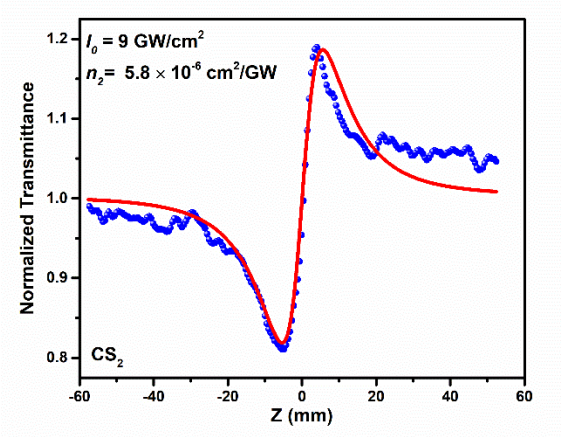

Figure 16. Close aperture (CA) Z-scan curve obtained at an excitation wavelength of 800 nm for CS_2 at 9.0 GW/cm².

Additionally, we performed both open-aperture (OA) and closed-aperture (CA) Z-scans on a solution of $CsPbBr_3$ nanocrystals (NCs) in hexane, also contained in a 1 mm quartz cuvette. The OA and CA scans for the $CsPbBr_3$ NCs solution, shown in Figure 17, provided for the TPA coefficient (β) and nonlinear refractive index (n_2) values consistent with literature reports.[50] These results validated the accuracy and reliability of our Z-scan setup. After ensuring the setup's performance, we proceeded to conduct experiments o n chiral perovskite samples, which are discussed in detail in Chapter 5 of this thesis.

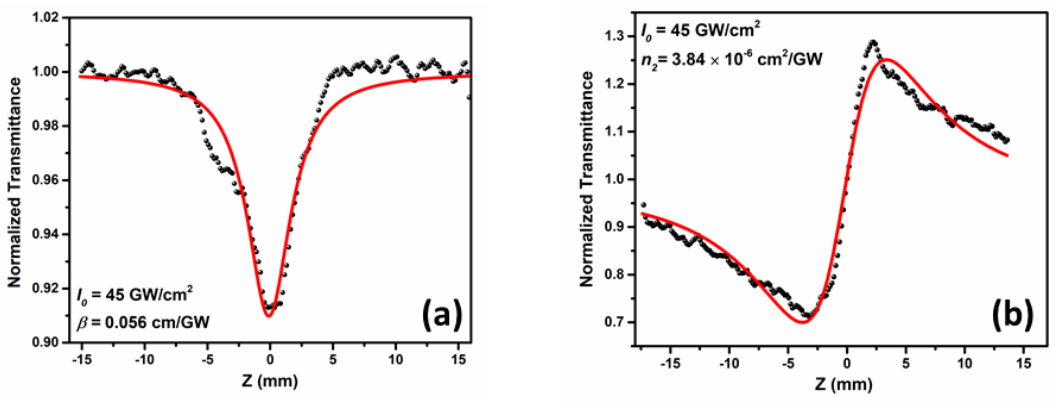

Figure 17. (a) Open and **(b)** closed aperture Z-scan curves obtained at an excitation wavelength of 800 nm for $CsPbBr_3$ NCs solution at 45 GW/cm². Open and closed aperture data are fitted to equations 5 and 6, respectively. The obtained value for the two-photon absorption coefficient (β) is 0.56 cm/GW, and the nonlinear refractive index (n_2) is 3.84 x 10^{-4} cm²/GW.[50-51]

2.5. SHG and THG measurement

We utilized a custom-built setup to collect upconverted photons from nonlinear samples, as schematically shown in Figure 18.[52] For SHG and THG measurement experiments, we employed near-infrared (NIR) light from an optical parametric amplifier (OPA, Light Conversion) as the excitation source. The OPA is pumped by the output of a regenerative amplifier (Spitfire X-Pro, Spectra Physics), delivering 800 nm pulses with a duration of 35 fs at a 1 kHz repetition rate. An 850 nm long-pass filter in the beam path ensured that only the desired NIR pump wavelengths reached the sample, while a neutral density (ND) filter was used to control the pump intensity.

The pump beam is focused onto the sample using a 200 mm plano-convex lens, with the sample positioned 135 mm away from the lens to avoid damage and to achieve a sufficiently large spot size for interaction. The sample crystals are sandwiched between two quartz microscope slides and mounted on a cage rotation mount (Thorlabs CRM1/M) for changing the crystal axis.

The SHG signal emitted by the sample is collimated using a 25 mm lens, passed through a 750 nm short-pass filter to block any residual pump wavelength, and coupled into a 400 µm optical fibre connected to a miniature spectrometer (USB4000, Ocean Optics) for analysis. To study polarization-dependent SHG, a Glan polarizer and half-wave plate assembly are incorporated to control the polarization of the pump beam.

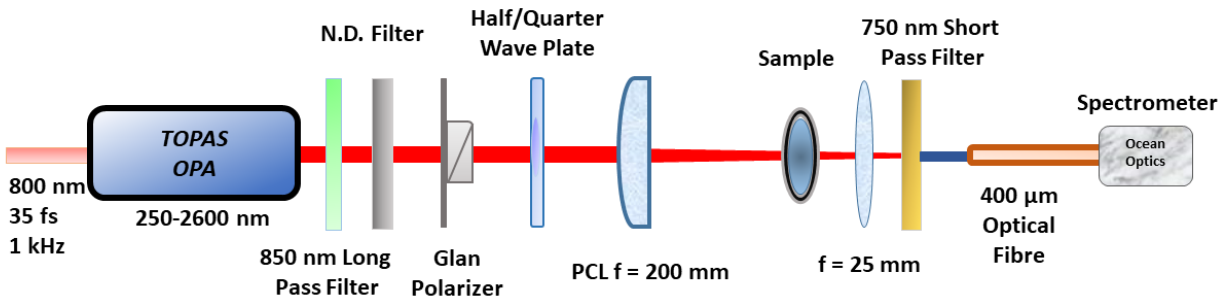

Figure 18. A schematic representation of the experimental Setup used for second-harmonic generation (SHG) and third-harmonic generation (THG) measurements.

For circular polarization-dependent measurements, the half-wave plate (λ/2) is replaced with a quarter-wave plate (λ/4) to generate circularly polarized excitation light. The λ/4 plate is continuously rotated from 0° to 360° to vary the pump beam polarization between linear, left-handed circular polarization (LCP), and right-handed circular polarization (RCP).

2.6. References

1. Baxter, J. B.; Guglietta, G. W., Terahertz Spectroscopy. *Analytical Chemistry* **2011,** *83* (12), 4342-4368.

2. Schmuttenmaer, C. A., Exploring Dynamics in the Far-Infrared with Terahertz Spectroscopy. *Chemical Reviews* **2004,** *104* (4), 1759-1780.

3. Siegel, P. H., Terahertz technology. *IEEE Transactions on Microwave Theory and Techniques* **2002,** *50* (3), 910-928.

4. Kimmitt, M. F., Restrahlen to T-Rays – 100 Years of Terahertz Radiation. *Journal of Biological Physics* **2003,** *29* (2), 77-85.

5. Ferguson, B.; Zhang, X.-C., Materials for terahertz science and technology. *Nature Materials* **2002,** *1* (1), 26-33.

6. Hashimshony, D.; Zigler, A.; Papadopoulos, K., Conversion of electrostatic to electromagnetic waves by superluminous ionization fronts. *Physical review letters* **2001,** *86* (13), 2806.

7. Mourou, G.; Stancampiano, C.; Antonetti, A.; Orszag, A., Picosecond microwave pulses generated with a subpicosecond laser-driven semiconductor switch. *Applied Physics Letters* **1981,** *39* (4), 295-296.

8. Dai, J.; Liu, J.; Zhang, X.-C., Terahertz wave air photonics: terahertz wave generation and detection with laser-induced gas plasma. *IEEE Journal of selected topics in Quantum Electronics* **2010,** *17* (1), 183-190.

9. Hamster, H.; Sullivan, A., s. Gordon, W. White, and RW Falcone. *Phys. Rev. Lett* **1993,** *71*, 2725.

10. Hamster, H.; Sullivan, A.; Gordon, S.; Falcone, R., Short-pulse terahertz radiation from high-intensity-laser-produced plasmas. *Physical Review E* **1994,** *49* (1), 671.

11. Cook, D.; Hochstrasser, R., Intense terahertz pulses by four-wave rectification in air. *Optics letters* **2000,** *25* (16), 1210-1212.

12. Bartel, T.; Gaal, P.; Reimann, K.; Woerner, M.; Elsaesser, T., Generation of single-cycle THz transients with high electric-field amplitudes. *Optics Letters* **2005,** *30* (20), 2805-2807.

13. Dai, J.; Xie, X.; Zhang, X.-C., Detection of broadband terahertz waves with a laser-induced plasma in gases. *Physical review letters* **2006,** *97* (10), 103903.

14. Cunningham, P. D., *Optical pump terahertz probe studies of semiconducting polymers*. University of Maryland, Baltimore County: 2010.

15. Iwaszczuk, K.; Cooke, D. G.; Fujiwara, M.; Hashimoto, H.; Jepsen, P. U., Simultaneous reference and differential waveform acquisition in time-resolved terahertz spectroscopy. *Optics Express* **2009,** *17* (24), 21969-21976.

16. D'Angelo, F.; Němec, H.; Parekh, S. H.; Kužel, P.; Bonn, M.; Turchinovich, D., Self-referenced ultra-broadband transient terahertz spectroscopy using air-photonics. *Optics Express* **2016,** *24* (9), 10157-10171.

17. Nienhuys, H.-K.; Sundström, V., Intrinsic complications in the analysis of optical-pump, terahertz probe experiments. *Physical Review B—Condensed Matter and Materials Physics* **2005,** *71* (23), 235110.

18. Jepsen, P. U.; Cooke, D. G.; Koch, M., Terahertz spectroscopy and imaging–Modern techniques and applications. *Laser & Photonics Reviews* **2011,** *5* (1), 124-166.

19. Ulbricht, R.; Hendry, E.; Shan, J.; Heinz, T. F.; Bonn, M., Carrier dynamics in semiconductors studied with time-resolved terahertz spectroscopy. *Reviews of Modern Physics* **2011,** *83* (2), 543-586.

20. Ashcroft, N. W.; Mermin, N., Solid State Physics: Cengage Learning. *Cengage Learning: Boston, MA, USA* **2011**.

21. Lloyd-Hughes, J.; Jeon, T.-I., A review of the terahertz conductivity of bulk and nano-materials. *Journal of Infrared, Millimeter, and Terahertz Waves* **2012,** *33*, 871-925.

22. Beard, M. C.; Turner, G. M.; Schmuttenmaer, C. A., Size-dependent photoconductivity in CdSe nanoparticles as measured by time-resolved terahertz spectroscopy. *Nano letters* **2002,** *2* (9), 983-987.

23. Yu, B.; Zhang, C.; Chen, L.; Qin, Z.; Huang, X.; Wang, X.; Xiao, M., Ultrafast dynamics of photoexcited carriers in perovskite semiconductor nanocrystals. *Nanophotonics* **2020,** *10* (8), 1943-1965.

24. Aneesh, J.; Swarnkar, A.; Kumar Ravi, V.; Sharma, R.; Nag, A.; Adarsh, K. V., Ultrafast Exciton Dynamics in Colloidal CsPbBr3 Perovskite Nanocrystals: Biexciton Effect and Auger Recombination. *The Journal of Physical Chemistry C* **2017,** *121* (8), 4734-4739.

25. Mondal, N.; De, A.; Das, S.; Paul, S.; Samanta, A., Ultrafast carrier dynamics of metal halide perovskite nanocrystals and perovskite-composites. *Nanoscale* **2019,** *11* (20), 9796-9818.

26. Sum, T. C.; Mathews, N.; Xing, G.; Lim, S. S.; Chong, W. K.; Giovanni, D.; Dewi, H. A., Spectral Features and Charge Dynamics of Lead Halide Perovskites: Origins and Interpretations. *Accounts of Chemical Research* **2016,** *49* (2), 294-302.

27. Berera, R.; van Grondelle, R.; Kennis, J. T. M., Ultrafast transient absorption spectroscopy: principles and application to photosynthetic systems. *Photosynthesis Research* **2009,** *101* (2), 105-118.

28. Kaur, A.; Goswami, T.; Babu, K. J.; Ghosh, H. N., Ultrafast Electron and Hole Transfer and Efficient Charge Separation in a Sb2Se3/CdS Thin Film p–n Heterojunction. *The Journal of Physical Chemistry Letters* **2024,** *15* (13), 3541-3548.

29. Zhong, Q.; Fourkas, J. T., Optical Kerr Effect Spectroscopy of Simple Liquids. *The Journal of Physical Chemistry B* **2008,** *112* (49), 15529-15539.

30. Duguay, M. A.; Hansen, J. W., AN ULTRAFAST LIGHT GATE. *Applied Physics Letters* **1969,** *15* (6), 192-194.

31. Ippen, E. P.; Shank, C. V., Picosecond response of a high−repetition−rate CS2 optical Kerr gate. *Applied Physics Letters* **1975,** *26* (3), 92-93.

32. McMorrow, D.; Lotshaw, W. T., Intermolecular dynamics in acetonitrile probed with femtosecond Fourier-transform Raman spectroscopy. *The Journal of Physical Chemistry* **1991,** *95* (25), 10395-10406.

33. Butcher, P. N.; Cotter, D., *The Elements of Nonlinear Optics*. Cambridge University Press: Cambridge, 1990.

34. Giraud, G.; Gordon, C. M.; Dunkin, I. R.; Wynne, K., The effects of anion and cation substitution on the ultrafast solvent dynamics of ionic liquids: A time-resolved optical Kerr-effect spectroscopic study. *The Journal of Chemical Physics* **2003,** *119* (1), 464-477.

35. Kivelson, D.; Madden, P. A., Light Scattering Studies of Molecular Liquids. *Annual Review of Physical Chemistry* **1980,** *31* (Volume 31), 523-558.

36. Murry, R. L.; Fourkas, J. T., Polarization selectivity of nonresonant spectroscopies in isotropic media. *The Journal of Chemical Physics* **1997,** *107* (23), 9726-9740.

37. Loughnane, B. J.; Scodinu, A.; Fourkas, J. T., Temperature-Dependent Optical Kerr Effect Spectroscopy of Aromatic Liquids. *The Journal of Physical Chemistry B* **2006,** *110* (11), 5708-5720.

38. Farrell, A. J.; González-Jiménez, M.; Ramakrishnan, G.; Wynne, K., Low-Frequency (Gigahertz to Terahertz) Depolarized Raman Scattering Off n-Alkanes, Cycloalkanes, and Six-Membered Rings: A Physical Interpretation. *The Journal of Physical Chemistry B* **2020,** *124* (35), 7611-7624.

39. Green, M. A.; Ho-Baillie, A.; Snaith, H. J., The emergence of perovskite solar cells. *Nature Photonics* **2014,** *8* (7), 506-514.

40. Stranks, S. D.; Hoye, R. L. Z.; Di, D.; Friend, R. H.; Deschler, F., The Physics of Light Emission in Halide Perovskite Devices. *Advanced Materials* **2019,** *31* (47), 1803336.

41. Liu, C.-K.; Tai, Q.; Wang, N.; Tang, G.; Loi, H.-L.; Yan, F. Sn-Based Perovskite for Highly Sensitive Photodetectors *Adv Sci (Weinh)* [Online], 2019, p. 1900751. PubMed. http://europepmc.org/abstract/MED/31508281

42. Wang, K.; Wang, S.; Xiao, S.; Song, Q., Recent Advances in Perovskite Micro- and Nanolasers. *Advanced Optical Materials* **2018,** *6* (18), 1800278.

43. Saparov, B.; Mitzi, D. B., Organic-Inorganic Perovskites: Structural Versatility for Functional Materials Design. *Chemical reviews* **2016,** *116* (7), 4558-96.

44. Xu, J.; Li, X.; Xiong, J.; Yuan, C.; Semin, S.; Rasing, T.; Bu, X.-H., Halide Perovskites for Nonlinear Optics. *Advanced Materials* **2020,** *32* (3), 1806736.

45. Wang, G.; Mei, S.; Liao, J.; Wang, W.; Tang, Y.; Zhang, Q.; Tang, Z.; Wu, B.; Xing, G., Advances of Nonlinear Photonics in Low-Dimensional Halide Perovskites. *Small* **2021,** *17* (43), 2100809.

46. Sheik-Bahae, M.; Said, A. A.; Wei, T. H.; Hagan, D. J.; Stryland, E. W. V., Sensitive measurement of optical nonlinearities using a single beam. *IEEE Journal of Quantum Electronics* **1990,** *26* (4), 760-769.

47. Krishnakanth, K. N.; Seth, S.; Samanta, A.; Venugopal Rao, S., Broadband ultrafast nonlinear optical studies revealing exciting multi-photon absorption coefficients in phase pure zero-dimensional Cs4PbBr6 perovskite films. *Nanoscale* **2019,** *11* (3), 945-954.

48. Sheik-Bahae, M.; Said, A. A.; Van Stryland, E. W., High-sensitivity, single-beam n2 measurements. *Opt. Lett.* **1989,** *14* (17), 955-957.

49. Couris, S.; Renard, M.; Faucher, O.; Lavorel, B.; Chaux, R.; Koudoumas, E.; Michaut, X., An experimental investigation of the nonlinear refractive index (n2) of carbon disulfide and toluene by spectral shearing interferometry and z-scan techniques. *Chemical Physics Letters* **2003,** *369* (3), 318-324.

50. Wang, Y.; Li, X.; Zhao, X.; Xiao, L.; Zeng, H.; Sun, H., Nonlinear Absorption and Low-Threshold Multiphoton Pumped Stimulated Emission from All-Inorganic Perovskite Nanocrystals. *Nano Letters* **2016,** *16* (1), 448-453.

51. Liu, S.; Chen, G.; Huang, Y.; Lin, S.; Zhang, Y.; He, M.; Xiang, W.; Liang, X., Tunable fluorescence and optical nonlinearities of all inorganic colloidal cesium lead halide perovskite nanocrystals. *Journal of Alloys and Compounds* **2017,** *724*, 889-896.

52. Maqbool, S.; Thekkayil, Z.; Mandal, P., 1D Diisopropylammonium Lead Iodide Perovskite Shows Exceptional Optical Stability and Third-Order Nonlinearity. *Advanced Optical Materials* **2023,** *11* (15), 2202942.

Chapter 3

Ultrafast Hole Injection Dynamics in $CsPbBr_3$ Nanocrystals with Inorganic Hole Transporting Layers

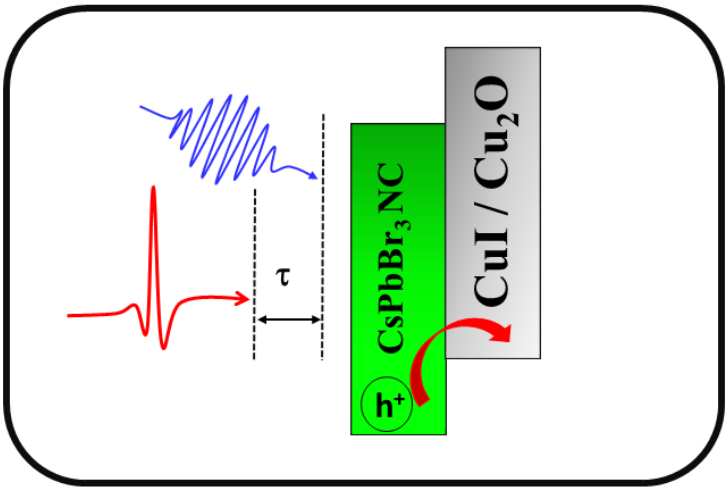

3.1 Introduction

With the growing focus on solar energy, the global demand for photovoltaic devices is steadily rising. There is an urgent need for cost-effective and highly efficient photovoltaic materials that can outperform conventional polycrystalline silicon devices and take a leading role in the commercial market. This challenge has become a key focus of cutting-edge research in the field. In recent decades, perovskite solar cells (PSCs) have emerged as a central focus in developing next-generation renewable energy technologies.[1-5] The power conversion efficiency (PCE) of PSCs has shown remarkable improvement, particularly in devices utilising hybrid organometallic halide perovskites such as $MAPbI_3$ and $FAPbI_3$, where organic cations occupy the A-site in the ABX_3 perovskite structure. These materials are highly efficient due to their exceptional optoelectronic properties, including a high absorption coefficient, excellent carrier mobility, long diffusion length, and low-cost production, making them strong contenders in the optoelectronics field.[6-8] However, a significant challenge to their commercial application is their inherent sensitivity to moisture, heat, and light, particularly due to the instability of the A-site cation.[9-10] This vulnerability compromises PSCs' structural, physical, and chemical integrity when exposed to moisture, oxygen, elevated temperatures, and prolonged illumination.[11-13]

Replacing the organic cation with inorganic Cs^+ to create an all-inorganic perovskite has proven to be an effective strategy for enhancing stability under common stress conditions.[14-15] The pioneering fabrication of Cesium lead iodide ($CsPbI_3$) perovskite solar cells (PSCs) by Snaith and coworkers in 2015 marked a significant milestone in this field, spurring rapid advancements.[1] Since then, the power conversion efficiency (PCE) of $CsPbI_3$ PSCs has surged from 2.9% to over 21% by 2023. Other Cesium lead halide perovskites, such as $CsPbI_2Br$, $CsPbIBr_2$, and $CsPbBr_3$, have also undergone substantial development. However, the highest PCE achieved for these $CsPbX_3$ PSCs remains at 21.8%, which is noticeably lower than that of organic-inorganic hybrid PSCs.[16-19]

Beyond photovoltaic applications, Cesium lead halide perovskites have garnered considerable attention for light-emitting applications, including light-emitting diodes (LEDs), single-photon emitters, and low-threshold lasing media.[19-23] Reducing the size of these perovskites from bulk to lower dimensions has unlocked remarkable photophysical properties. Colloidal perovskite

nanocrystals (NCs) have demonstrated exceptional performance compared to traditional semiconductor nanocrystals or quantum dots (e.g., CdSe, PbS, and InP) due to their superior defect tolerance, the ability to maintain favourable optical and electronic properties despite structural defects.[24-26]

Metal halide nanocrystals have also shown great promise in photovoltaic applications. Early breakthroughs achieved a record photovoltaic efficiency of approximately 13.43% using perovskite NCs, highlighting their potential.[27] Focusing specifically on $CsPbBr_3$ nanoparticle nanocrystals (NCs), their band gap is not ideal for optimal solar spectrum absorption, yet they demonstrate remarkable stability against moisture, prolonged light exposure, and thermal stress. This outstanding stability positions $CsPbBr_3$ NCs as a strong contender for commercial photovoltaic applications. To date, these NCs have been successfully employed in a variety of fields, including light-emitting devices, photovoltaics, and photocatalysis, highlighting their versatility and potential in next-generation technologies.[1, 21, 28-30]

In any photovoltaic device, the process begins with light absorption and the generation of free charge carriers. This is followed by the separation of electrons and holes, which are selectively collected by charge transport layers and subsequently transferred to the electrodes for further utilisation. Efficient and irreversible charge separation is crucial for enhancing device efficiency, which is achieved through charge transport layers.[31-33] As mentioned earlier in Chapter One, the structure of perovskite solar cells (PSCs) is typically classified into two main types: regular and inverted. Both configurations involve a perovskite absorber layer sandwiched between charge transport layers, comprising electron transport layers (ETLs) and hole transport layers (HTLs). These layers play a critical role in enabling charge separation and ensuring selective collection.[31, 34]

Focusing on HTLs, the most commonly used hole-transporting materials (HTMs) include poly(3,4-ethylenedioxythiophene):poly(styrenesulfonate) (PEDOT:PSS), spiro-MeOTAD, PTAA, and porphyrins.[35-42] However, the high cost and limited long-term stability of these materials pose significant challenges to device durability and cost-effectiveness. While many high-efficiency PSCs are based on a conventional structure employing organic HTMs, these materials often suffer from issues such as poor long-term UV and thermal stability. Additionally, their

hygroscopic nature further undermines the long-term stability of the devices, presenting a major obstacle to commercial scalability.[43-46]

To address the limitations of organic HTMs, a wide range of inorganic HTMs has been developed and integrated into PSCs. Common examples include carbon, vanadium(V) oxide (V_2O_5), molybdenum oxide (MoO_x), tungsten oxide (WO_x), spinel cobalt oxide (CoO_x), nickel oxide (NiO_x), Cu-based materials such as $CuAlO_2$, $CuGaO_2$, CuS, CuI, CuO_x, and CuSCN.[46-53] These inorganic HTMs offer several advantages, including excellent stability under humid and high-temperature conditions, favourable band alignment, UV-visible transparency, and high hole mobility, making them a promising alternative to their organic counterparts.[54-57]

Additionally, research has shown that inorganic HTMs can enhance perovskite materials' stability while being more cost-effective. This makes them particularly attractive for the commercialisation of PSCs, where the cost of materials and processing plays a critical role. Adopting inorganic HTLs represents a significant step toward the industrial-scale production and application of PSCs, ensuring both performance and economic viability.[58-60]

Design strategies and material development are critical aspects of advancing perovskite nanocrystal (NC) based photovoltaic and optoelectronic devices. The research community has made tremendous progress in enhancing the efficiency of these devices. Equally important, however, is gaining a deeper understanding of the intrinsic photophysics of these materials and the mechanisms of charge carrier transport across interfaces. Studying charge carrier dynamics and unravelling the fundamental photoinduced processes within perovskites and their interfaces is essential for further enhancing device performance.[61-64] Such insights not only help optimise existing devices but also guide the development of innovative strategies and materials for next-generation photovoltaic systems.[65]

In our research group, we have investigated the charge carrier dynamics in colloidal $CsPbBr_3$ nanocrystals (NCs) using time-resolved terahertz spectroscopy (TRTS). TRTS provides a non-contact AC probe for measuring photoconductivity, which is directly proportional to the number of charge carriers, regardless of their occupation states. With its sub-picosecond temporal resolution, this technique enables real-time monitoring of photoinduced charge carrier behaviour and recombination dynamics.[61, 66-68]

Gurivi *et al.* obtained remarkable results for colloidal $CsPbBr_3$ NCs, demonstrating that a free carrier–exiton equilibrium is established within 5–6 ps after photoexcitation. They found that charge carriers in these NCs exhibit exceptional mobility (~4500 $cm^2V^{-1}s^{-1}$) and long diffusion lengths (>9.2 μm). These values are orders of magnitude higher than those typically found in hybrid halide perovskite films and are comparable to single-crystalline bulk semiconductors.[69]

To further understand interfacial charge transfer, Sohini *et al.* investigated the charge carrier dynamics in $CsPbBr_3$ NCs in the presence of molecular electron and hole acceptors. Benzoquinone (BQ) and phenothiazine were used as electron and hole acceptors, respectively. They discovered that hot carriers are transferred to the molecular acceptors on an ultrafast timescale of less than 300 fs, which is limited by our instrument response function (IRF). Additionally, they observed a secondary transfer of thermalised electrons and holes with characteristic time constants of 30–50 ps and 196–250 ps, respectively.[70]

To build on these findings and better understand the dynamics in NC films and interfaces, as typically utilised in photovoltaic applications, we have now explored charge carrier dynamics in $CsPbBr_3$ NC films integrated with copper-based inorganic hole-transporting layers, such as CuI and Cu_2O. These inorganic HTLs exhibit proper band alignment with $CsPbBr_3$ nanocrystals (NCs), as reported in the literature.[57, 71] While numerous studies have explored ultrafast hole injection dynamics from perovskite active layers to organic HTLs,[72] there is limited research on inorganic HTLs. This motivated us to design this system, to investigate interfacial charge transfer efficiency and recombination mechanisms using ultrafast transient absorption and time-resolved terahertz spectroscopy (TRTS). We have especially explored the dynamics of the photo-induced hole transport from the active $CsPbBr_3$ layer to the inorganic hole-transport layer (CuI or Cu_2O). This work aims to provide deeper insights into interfacial processes and enhance the design of efficient photovoltaic devices.

3.2 Experimental Section

3.2.1 Synthesis and characterisation of $CsPbBr_3$ NCs

Following a previously reported procedure, we synthesised colloidal $CsPbBr_3$ nanocrystals (NCs) using the hot injection method.[25, 73] The process began with the preparation of a Cesium oleate

precursor. Specifically, 0.4 g of Cesium carbonate (Cs_2CO_3) was taken with 1.25 mL of oleic acid and 20 mL of octadecene in a 50 mL three-neck round-bottom flask. The mixture was dried under vacuum at 100°C for 1 hour using the Schlenk line setup. Then, under a nitrogen atmosphere, the temperature was increased to 150°C and maintained until a clear solution was obtained, indicating the complete reaction of Cs_2CO_3 with no remaining crystals.

In a separate round-bottom flask, 0.188 mmol of lead bromide ($PbBr_2$) was combined with 5 mL of octadecene and dried under vacuum for 1 hour. Following this, 0.5 mL each of oleylamine and oleic acid were added under a nitrogen atmosphere as ligands. The solution gradually turned clear after the addition of these ligands. The temperature was then increased to 190°C, and a pre-heated Cesium oleate solution (0.1 M, 0.4 mL) was rapidly injected into the reaction mixture. The reaction was quenched after 5 seconds by immersing the flask in an ice-water bath.

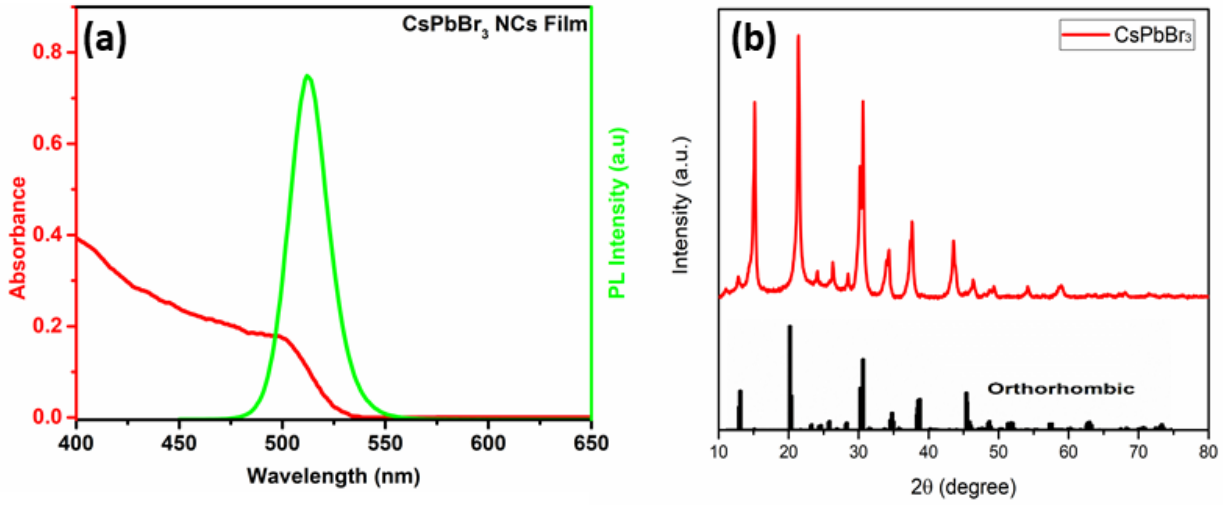

Figure 1. (a) UV-visible absorption spectrum and steady-state photoluminescence (PL) spectrum (excitation at 405 nm) of $CsPbBr_3$ NC Film. **(b)** Powder X-Ray diffraction (XRD) pattern of $CsPbBr_3$ NC film compared with simulated reference data.

The synthesised $CsPbBr_3$ nanocrystals were purified by washing with methyl acetate as an antisolvent and centrifugation at 7000 rpm for 10 minutes. The NCs were then redispersed in hexane to form a stable colloidal solution. For further experiments, NC films were prepared by spin-coating the colloidal solution onto glass substrates for transient absorption measurements and

polystyrene substrates for terahertz (THz) spectroscopy. Polystyrene was chosen due to its high transparency in the broad THz frequency range.

Figure 1a displays the UV-visible absorption spectrum (red) and steady-state photoluminescence (PL) spectrum (green) of the $CsPbBr_3$ Film. The absorption spectrum reveals the lowest-energy excitonic absorption peak at 500 nm, while the PL emission occurs at 512 nm. The UV-visible absorption spectrum was collected in transmission mode using a custom-built setup comprising a UV-visible light source (DH-2000, Ocean Optics) and a miniature spectrometer (USB4000, Ocean Optics) connected via optical fiber. Steady-state PL measurements of the NC film were performed using an FLS 980 spectrometer (Edinburgh Instruments). Figure 1b presents the powder X-ray diffraction (PXRD) data of the NC thin film, recorded with a Bruker D8 Advance diffractometer using Cu Kα radiation (λ = 1.54 Å). The PXRD peaks align well with previously reported data and reference patterns, confirming that the synthesised NCs crystallise in an orthorhombic crystal structure.[73]

3.2.2. Preparation of CuI and Cu_2O thin films

To investigate the ultrafast hole injection dynamics from $CsPbBr_3$ nanocrystals to inorganic hole-transporting materials, we selected two low-cost p-type semiconductors: copper iodide (CuI) and copper(I) oxide (Cu_2O). These materials have demonstrated potential as efficient HTMs in perovskite solar cells (PSCs) and exhibit excellent stability at room temperature.[49-50] All film fabrication processes were conducted at room temperature and under ambient conditions.

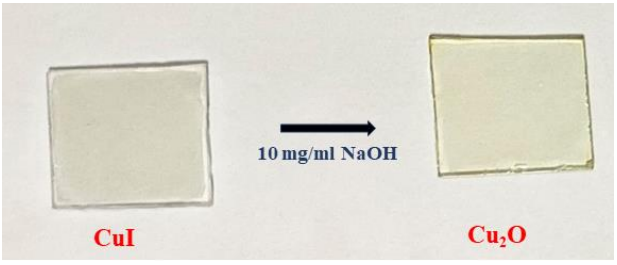

Figure 2. The CuI film was prepared by spin-coating CuI solution in acetonitrile onto a glass substrate. The Cu_2O film was then obtained from the CuI film through treatment with an aqueous NaOH solution.

To prepare the films of these HTMs, glass substrates were first cleaned using a soap solution, followed by sequential ultrasonic cleaning in deionised water, acetone, and isopropanol. Afterwards, the glass substrates were treated with plasma for 15 minutes. The CuI thin film was prepared by spin-coating a CuI solution in acetonitrile onto the glass substrate at 2000 rpm for 30 seconds. The CuI solution (30 mg/mL) was stirred overnight.

The Cu_2O film was obtained from the CuI film using a simple method reported by Zuo et al., involving aqueous NaOH solution.[48] The previously prepared CuI film, obtained through spin coating, was immersed in an aqueous NaOH solution (10 mg/mL) for 5 seconds. After immersion, the film was rinsed with distilled water and dried using nitrogen gas. Subsequently, the substrate was heated at 100°C for 10 minutes in an inert atmosphere to complete the transformation.

Figure 2a illustrates the glass substrate coated with a CuI film and the resulting Cu_2O film obtained after NaOH treatment. A slight colour change was observed, indicating the transformation. The conversion of CuI to Cu_2O was further confirmed by the change in the absorption spectrum of the film, which closely matches previously reported data, as shown in Figure 3a.

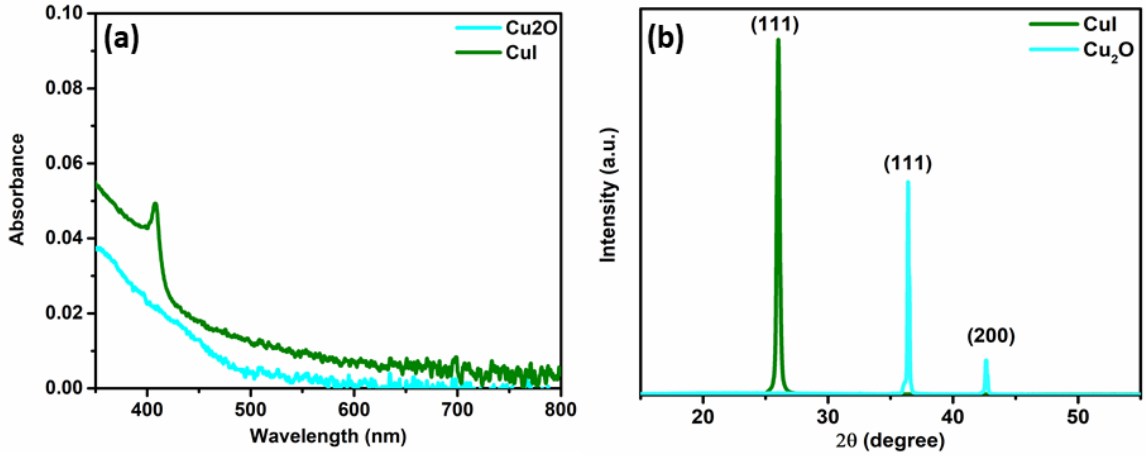

Figure 3. (a) The UV-visible absorption spectra and **(b)** PXRD patterns of CuI and Cu_2O thin films.

The PXRD patterns in Figure 3b provide additional evidence for the transformation. For the CuI thin film, a diffraction peak at 25.9° corresponds to the (111) plane of CuI crystals. This peak disappears in the Cu_2O film, whereas two new diffraction peaks emerge at 36.9° and 42.7°, corresponding to the (111) and (200) planes of Cu_2O, respectively. These PXRD patterns align

well with the reported literature, confirming the successful and complete conversion of CuI to Cu_2O.[74-75]

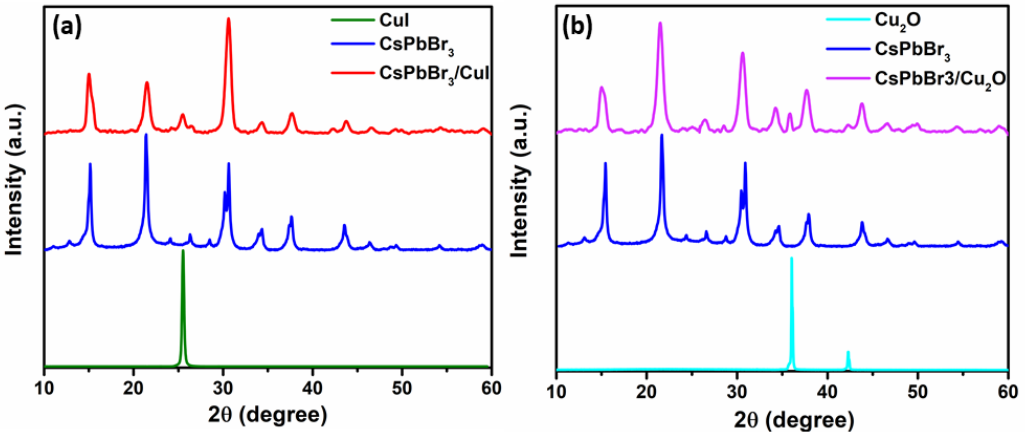

Figure 4. The powder XRD patterns are presented for **(a)** the $CsPbBr_3$/CuI composite film and **(b)** the $CsPbBr_3/Cu_2O$ composite film, alongside the XRD patterns of the pristine $CsPbBr_3$ NC film and the individual hole-transport materials, CuI and Cu_2O. In the $CsPbBr_3$/CuI composite film, characteristic diffraction peaks of both $CsPbBr_3$ NCs and CuI are observed, indicating the coexistence of these materials. Similarly, in the $CsPbBr_3/Cu_2O$ composite film, the XRD pattern shows peaks corresponding to both $CsPbBr_3$ NCs and Cu_2O, confirming the presence of both components in the composite structure. These results validate the integration of the HTMs with the $CsPbBr_3$ NCs.

The thickness of the CuI film can be adjusted by varying the concentration of the CuI solution in acetonitrile or by applying multiple spin-coating layers. The thickness of the resulting Cu_2O film, derived from the CuI film, is slightly less than that of the original CuI film. Therefore, marginally thicker CuI films were used to prepare the Cu_2O films. The concentration and thickness of the films were carefully optimised for this purpose.

The $CsPbBr_3$ NC film was spin-coated onto substrates already coated with an HTM (CuI or Cu_2O) layer. A solution of $CsPbBr_3$ NCs in hexane was spin-coated for 30 seconds at 1500 rpm, yielding a film with a thickness of approximately 200 nm, as measured by AFM (Figure 6). Figures 4a and 4b show the PXRD patterns of the $CsPbBr_3$ NC film on CuI and Cu_2O HTMs, respectively. In Figure 4a, the PXRD pattern of the $CsPbBr_3$/CuI film (red) includes the (111) peak of CuI

alongside the characteristic peaks of the $CsPbBr_3$ NCs, confirming the presence of both materials. Similarly, in Figure 4b, the PXRD pattern of the $CsPbBr_3/Cu_2O$ film (magenta) displays peaks corresponding to both $CsPbBr_3$ NCs and Cu_2O, verifying the coexistence of the two materials in the composite film.

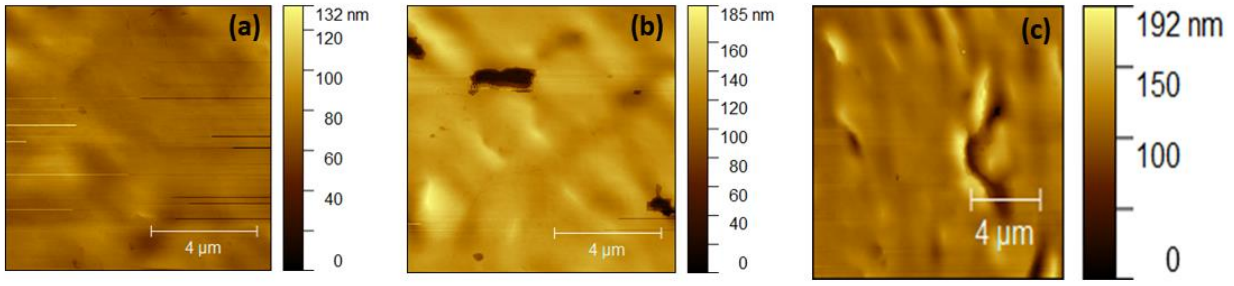

Figure 5. AFM images for **(a)** $CsPbBr_3$ NC film, **(b)** $CsPbBr_3$/CuI film and **(c)** $CsPbBr_3/Cu_2O$ film.

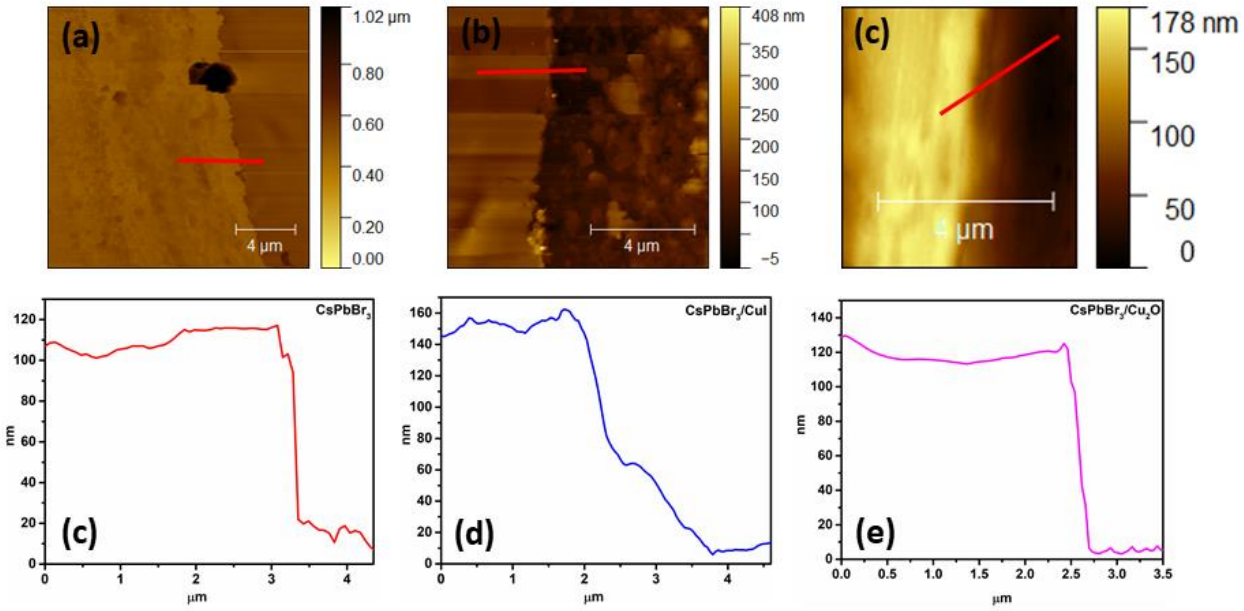

Figure 6. Thickness of **(a)** $CsPbBr_3$ NC film, **(b)** $CsPbBr_3$/CuI film and **(c)** $CsPbBr_3/Cu_2O$ film measured with AFM.

Figure 7 compares the absorption spectra of various films: a neat $CsPbBr_3$ film (blue), $CsPbBr_3$/CuI (red), $CsPbBr_3/Cu_2O$ (magenta), and individual HTM films of CuI (green) and Cu_2O (cyan). The absorbance spectra of the $CsPbBr_3$-based films are quite similar, indicating comparable film

thicknesses. Additionally, no significant shift in the excitonic peak at 500 nm was observed. The HTM films are relatively thin, resulting in much lower absorption compared to the $CsPbBr_3$ films, which exhibit a high extinction coefficient.

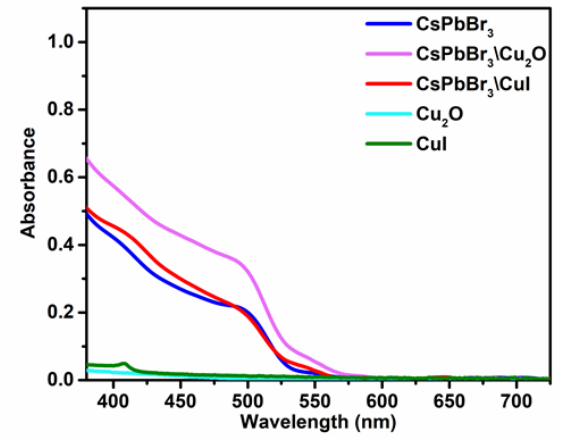

Figure 7. The absorption spectra include the neat $CsPbBr_3$ NC film (blue), $CsPbBr_3$/CuI composite film (red), $CsPbBr_3$/Cu_2O composite film (magenta), and thin films of the HTMs on glass substrates: CuI (green) and Cu_2O (cyan).

3.3. Photoluminescence (PL) spectra and PL decay lifetimes

To investigate the effect of HTMs on the $CsPbBr_3$ NC film, we measured the steady-state photoluminescence (PL) spectra and PL lifetimes. Figure 8a shows that all three samples exhibit PL emission near 512 nm. However, significant PL quenching was observed for the CuI/$CsPbBr_3$ (red) and Cu_2O/$CsPbBr_3$ (magenta) composite films compared to the pristine $CsPbBr_3$ NC film. Figure 8b illustrates the PL decay profiles for the three samples collected at respective PL peak wavelengths following excition at 405 nm. The PL decay is notably faster in the composite films, with the $CsPbBr_3$/Cu_2O sample showing the most pronounced steady-state PL quenching and the fastest PL decay. These results strongly suggest efficient hole transfer from $CsPbBr_3$ NCs to both HTMs, which is likely responsible for the observed quenching and rapid PL decay. This behaviour aligns with similar findings reported in the literature. The decay traces were fitted to a tri-exponential model, and the extracted parameters are summarised in Table 1.

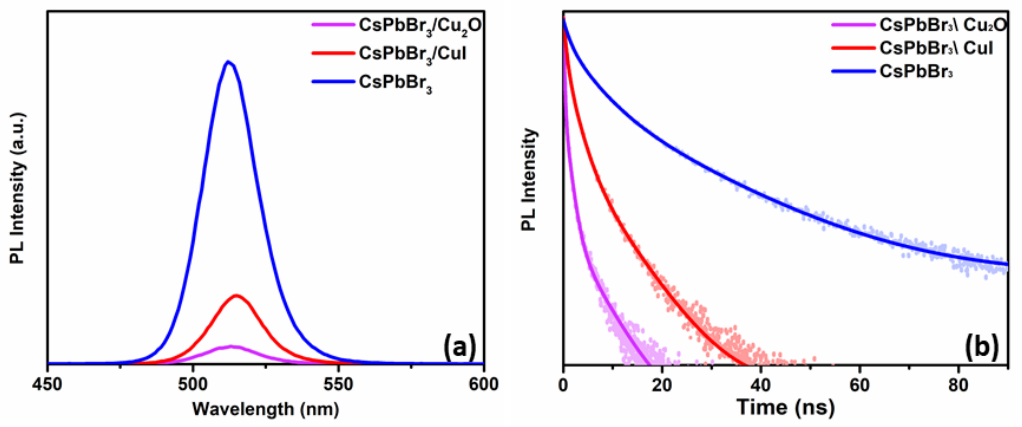

Figure 8. (a) Steady-state PL emission spectra upon 405 nm excitation for $CsPbBr_3$ NC film (blue), $CsPbBr_3$/CuI composite film (red), and $CsPbBr_3/Cu_2O$ composite film (magenta), showing significant PL quenching in the composite films. **(b)** PL decay profiles (at PL peak wavelength) of the pristine CsPbBr3 NC film and two NCs-HTM composite films excited at 405 nm. The solid lines are the fits to a triexponential function. The decay for the $CsPbBr_3$/CuI and $CsPbBr_3/Cu_2O$ composite films is significantly faster compared to the pristine $CsPbBr_3$ NC film indicating hole transfer from $CsPbBr_3$ to HTLs.

Table 1. Parameters obtained from fitting the PL decay profiles to a triexponential function.

	a_1	τ_1 (ns)	a_2	τ_2 (ns)	a_3	τ_3 (ns)	χ^2
$CsPbBr_3$	0.37	1.39	0.46	6.13	0.16	21.95	0.99
$CsPbBr_3$/CuI	0.55	0.56	0.40	1.95	0.05	6.75	0.99
$CsPbBr_3/Cu_2O$	0.87	0.18	0.13	1.03	0.01	5.53	0.99

The time scales and their contributions, obtained by fitting the PL decay profiles to a triexponential function, are summarised in Table 1. The average PL lifetime (τ_{avg}) was calculated using the formula:

$$\tau_{avg} = \sum_i \frac{a_i \tau_i^2}{a_i \tau_i} \quad (1)$$

For the pristine $CsPbBr_3$ NC film, τ_{avg} was found to be 14 ns. However, a significant reduction in τ_{avg} was observed in the case of $CsPbBr_3$ films with HTMs. For the $CsPbBr_3$/CuI composite, τ_{avg}

decreased to 2.8 ns, while for $CsPbBr_3/Cu_2O$, it further dropped to 1.3 ns. Additionally, the contributions of the fast decay components (τ_1 and τ_2) increased substantially in the presence of HTMs, indicating enhanced interaction between the HTM layers and $CsPbBr_3$ NCs.

These fast decay components are generally associated with charge transfer processes, providing evidence of significant charge transfer from $CsPbBr_3$ NCs to the HTMs. The ~80-90% quenching in PL intensity and the substantial reduction in average PL lifetime strongly support efficient charge transfer as one of the key mechanisms occurring between the $CsPbBr_3$ NCs and the HTM layers.

3.4. Transient absorption spectroscopy of $CsPbBr_3$ film and its composite film with HTMs CuI and Cu_2O

We employed femtosecond transient absorption spectroscopy (TAS) on these samples to investigate charge transfer on an ultrafast timescale. TAS provides insights into the charge transfer and hole injection dynamics from photoexcited $CsPbBr_3$ to the inorganic hole transport materials, CuI and Cu_2O.

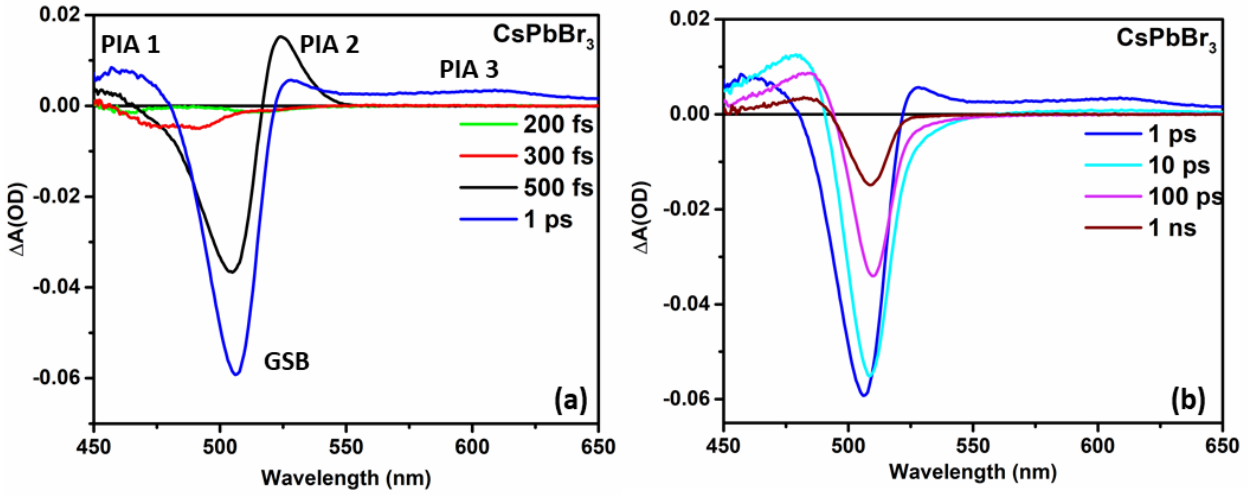

Figure 9. Transient absorption spectra of $CsPbBr_3$ NC film, ΔA (OD) vs wavelength plot at various time delays following photoexcitation at 400 nm. **(a)** Early delays from 200 fs to 1 ps represent the growth of the GSB peak. **(b)** At a delay time from 1 ps to 1 ns, the decay of the GSB peak is shown.

The measurements were performed on the same spin-coated samples on glass substrates at Prof. H. N. Ghosh's lab at INST Mohali. The setup employed a Helios Fire pump-probe spectrometer powered by a Ti:Sapphire femtosecond regenerative amplifier (800 nm, 35 fs, 1 kHz, 3 mJ), with detailed descriptions provided in Chapter Two. The samples were excited with a pump wavelength of 400 nm at a fluence of 100 μJ/cm². All films have similar thicknesses and showed comparable absorbance at 400 nm (Figure 7). The photon densities for the samples were calculated to be in the same order: 11.2×10^{17} cm^{-3} for $CsPbBr_3$ NCs films, 11.4×10^{17} for $CsPbBr_3$/CuI composite films, and 15.0×10^{17} for $CsPbBr_3/Cu_2O$ composite films. To enable comparison, the TAS spectra were normalised to the absorbed photon densities.

Figures 9a and 9b represent the transient absorption (TA) spectra for the $CsPbBr_3$ NC film, showing the pump-induced change in absorption (ΔA) as a function of wavelength at various pump-probe delays ranging from 200 fs to 1 ns after photoexcitation at 400 nm. The ΔA spectra in the 450–650 nm wavelength range reveal distinct features. Three positive ΔA signals, referred to as photoinduced absorption (PIA1, PIA2, and PIA3), are identified, along with a negative ΔA feature corresponding to ground-state bleaching (GSB). These features are labelled in Figure 9a and are discussed in detail in the following sections.

Figure 10 illustrates the TA spectra for $CsPbBr_3$/CuI and $CsPbBr_3/Cu_2O$ composite films. In the presence of the HTMs, the GSB peak intensity (-ΔA) decreases and the GSB recovery rate increases. By fitting the transient photoinduced bleaching to a multi-exponential function, we can extract the time scales for the charge carrier recombination dynamics in $CsPbBr_3$ NC layer and the charge transport processes between the $CsPbBr_3$ film and the inorganic HTM.

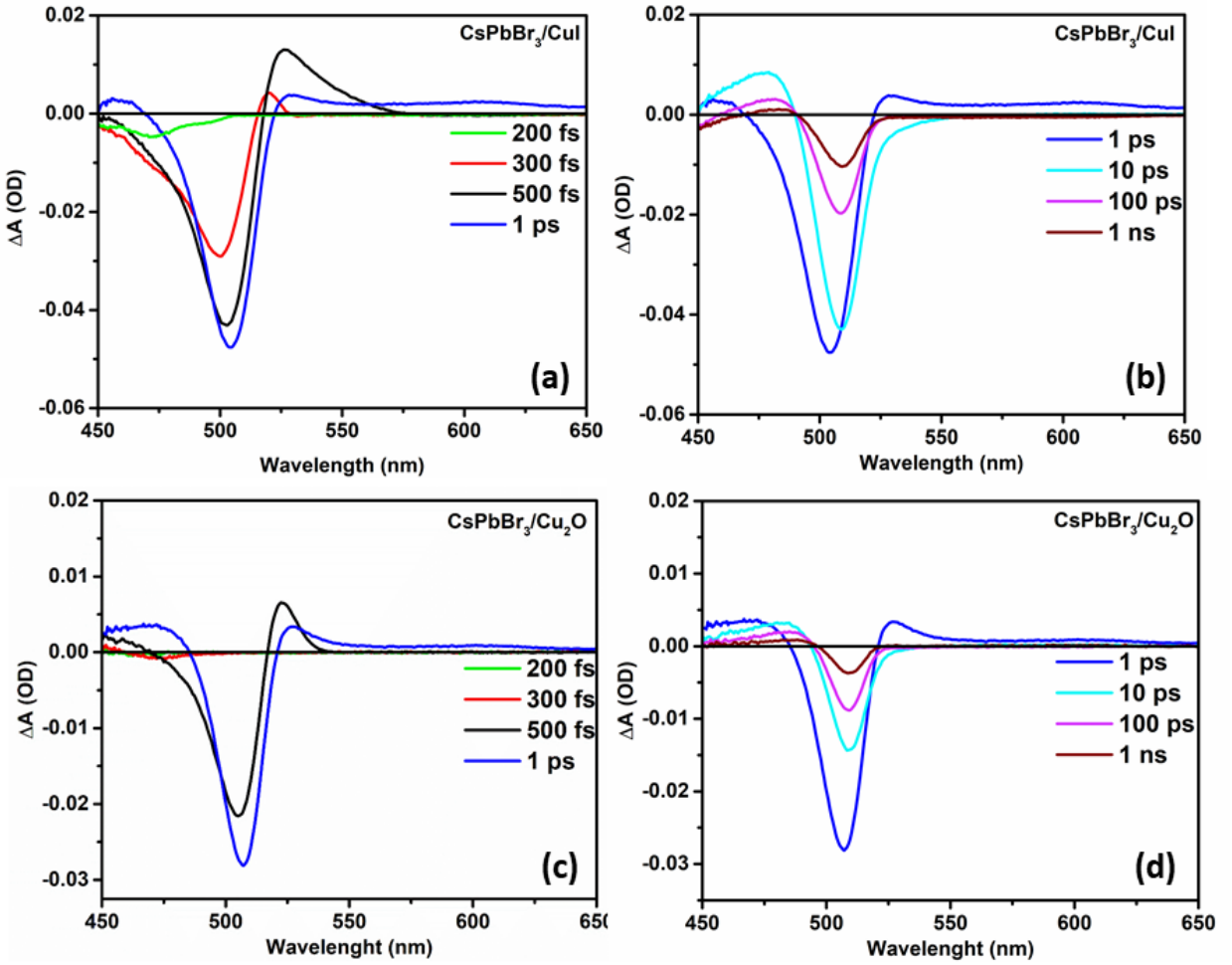

Figure 10. The ΔA (OD) vs wavelength plots at various time delays following photoexcitation at 400 nm are shown for composite films: **(a)** $CsPbBr_3$/CuI composite film at early time delays (200 fs to 1 ps), **(b)** $CsPbBr_3$/CuI composite film at later time delays (1 ps to 1 ns), **(c)** $CsPbBr_3/Cu_2O$ composite film at early time delays (200 fs to 1 ps), and **(d)** $CsPbBr_3/Cu_2O$ composite film at later time delays (1 ps to 1 ns).

Figure 11a-c show the PIA1 feature at different pump-probe delays for all three samples. Examining the kinetics of this PIA feature at 485 nm in Figure 11d reveals that the slowest rise and the highest ΔA value are observed for the pristine $CsPbBr_3$ NCs film. In contrast, both the rise and decay are fastest in the presence of HTM, with the $CsPbBr_3/Cu_2O$ composite film showing the most rapid dynamics.

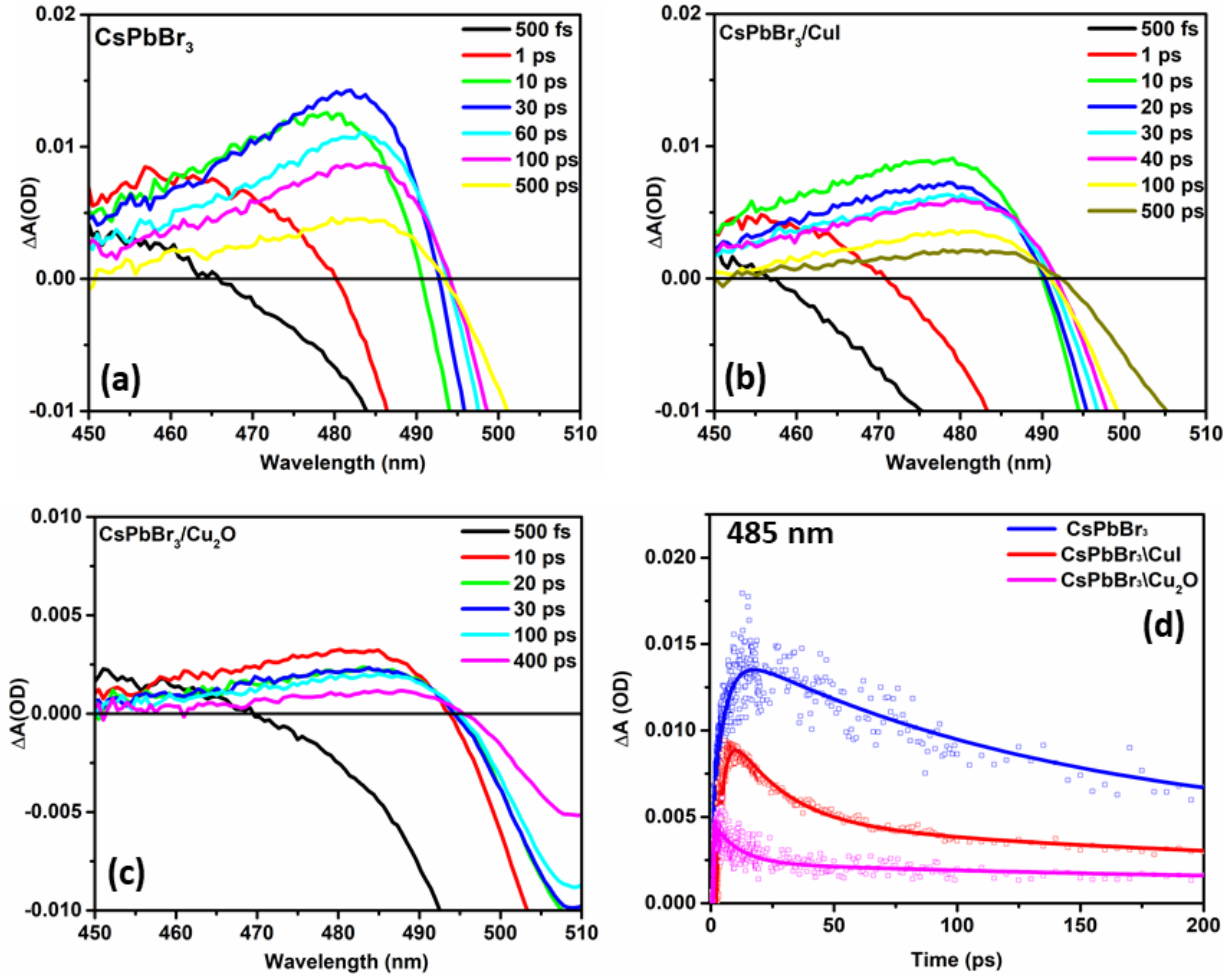

Figure 11. The ΔA (OD) vs wavelength plots at various time delays following photoexcitation at 400 nm are shown for composite films in the PIA 1 region for **(a)** CsPbBr3 NC film, **(b)** $CsPbBr_3$/CuI composite film, and **(c)** $CsPbBr_3/Cu_2O$ composite film. **(d)** Transient decay profiles of the photoinduced absorption signal (PIA 1) at 485 nm for $CsPbBr_3$ NC film (blue) and its composite film with HTM CuI (red) and Cu_2O (magenta). Points are experimental data, and the solid lines are bi-exponential fits for the data points.

The photoinduced absorption (PIA1) above the bandgap has been previously reported for $CsPbBr_3$ NCs. This phenomenon arises from the photoinduced activation of forbidden excitonic transitions due to the breaking of optical selection rules in $CsPbBr_3$ quantum dots (QDs). This results in photoinduced absorption in the wavelength range between two dipole-allowed excitonic transitions, a characteristic observed in strongly confined QDs.[76] Here, the confinement of excitons

within the same spatial region involves polaron formation. The interaction between photoexcited exciton and lattice gives access to the forbidden transition. This effect sustains throughout the exciton's lifetime. The faster rise and decay observed in the presence of HTM with $CsPbBr_3$ indicate quicker excitonic decay dynamics and faster excitonic dissociation.

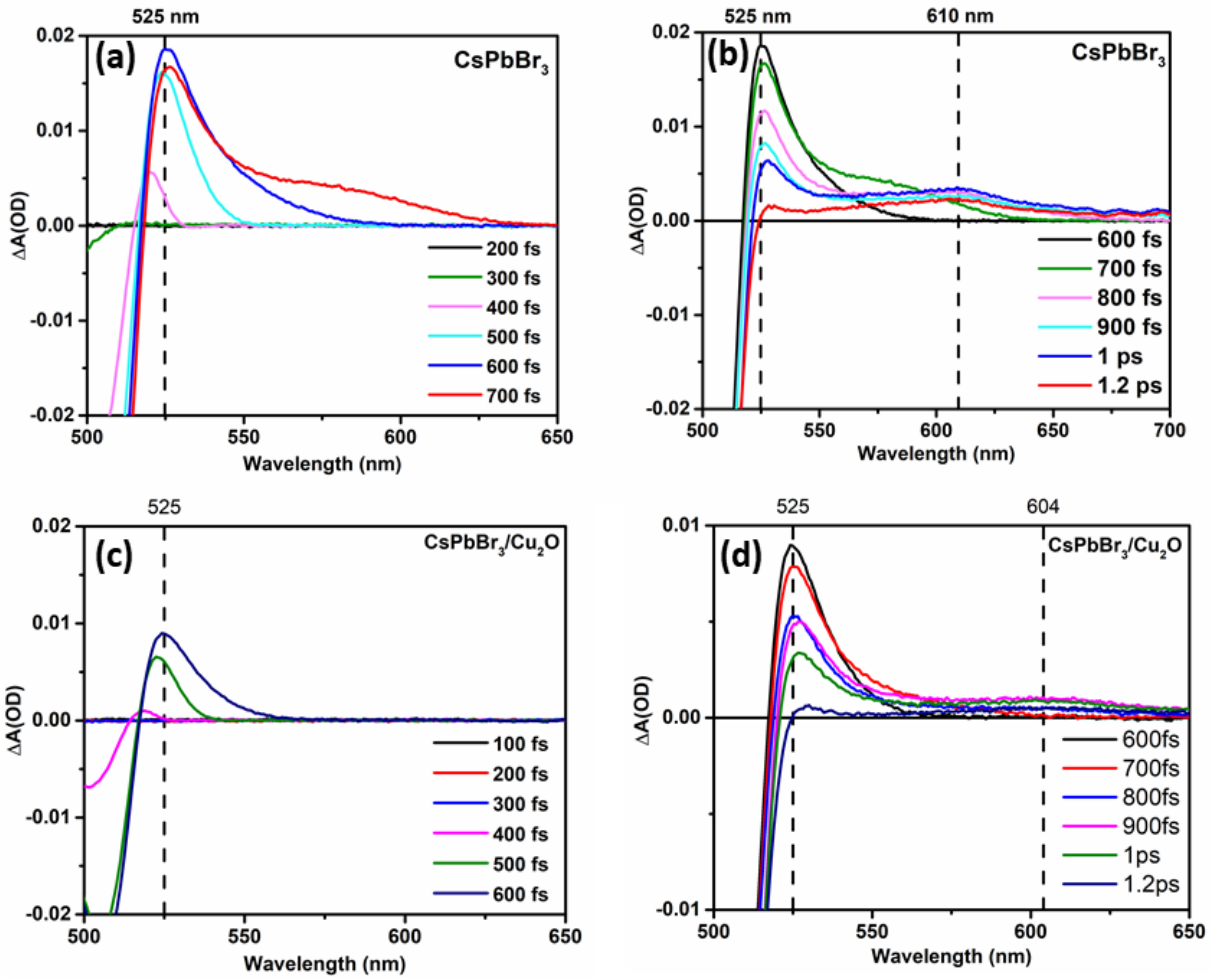

Figure 12. The ΔA vs wavelength plots at various time delays following photoexcitation at 400 nm are shown for composite films in the PIA 2 and PIA 3 region for $CsPbBr_3$ NC film **(a)** at early pump-probe delay till 600 fs showing rise of ΔA signal at 525 nm and **(b)** at time delays from 600 fs to 1.2 ps. The ΔA vs wavelength plots for $CsPbBr_3/Cu_2O$ composite film at **(c)** at early pump-probe delay till 600 fs and **(d)** at time delays from 600 fs to 1.2 ps.

The GSB peak exhibits a redshift in all three samples during the early timescales (less than one ps), accompanied by a derivative-like feature combining GSB and PIA2. Figure 12a shows that

the PIA2 intensity rises until approximately 700 fs before decaying in the 525 nm region, followed by an increase in signal intensity in the PIA3 region at 610 nm. In the presence of Cu_2O, the PIA2 signal at 525 nm is weaker and decays in a similar timescale of around 1.2 ps, as shown in Figure 12b.

The derivative-like feature (GSB with PIA2) and the observed redshift in both the GSB and PIA2 peaks in the differential absorption spectra immediately after photoexcitation can be attributed to the biexcitonic effect.[77] This effect occurs when the sample is excited with energy higher than the band edge, creating a hot exciton. The subsequent probe pulse generates a band-edge exciton and the Coulomb interaction between the hot exciton and the band-edge exciton results in an energy shift of the lowest optical transition.[78]

If E_g represents the energy of the lowest optical transition in the absence of a hot exciton, it becomes $E_g+\Delta_{xx}$ in the presence of a hot exciton, where Δ_{xx} is the biexciton binding energy (negative in value). Due to this negative binding energy, the lowest optical transition experiences a redshift. This effect is called the biexciton-induced stark effect. This explains the photoinduced absorption below the band-edge region (PIA2) and the redshift in the bleaching peak until the hot exciton relaxes to the band edge. After the hot exciton's relaxation, the PIA2 signal disappears, and a strong bleaching signal emerges near the band edge due to the state-filling effect (the GSB feature in Figure 9).[77]

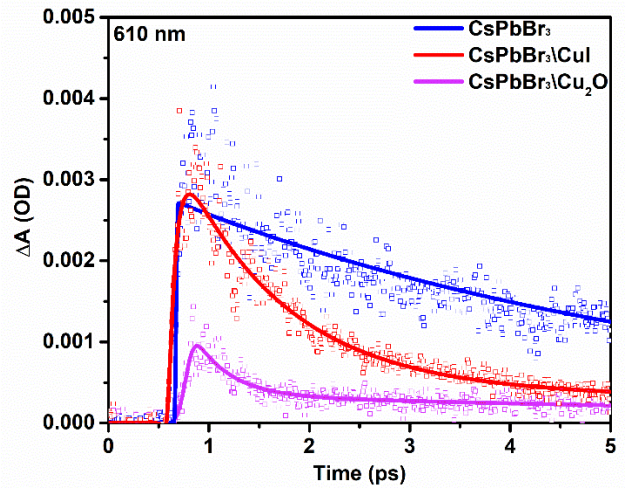

Figure 13. Transient decay profile for photoinduced absorption (ΔA) at 610 nm for $CsPbBr_3$ NC film (blue), $CsPbBr_3$/CuI composite film (red) and $CsPbBr_3$/Cu_2O composite film (magenta). The

solid lines are the fits to biexponential function. With <τ> obtained, 5.42 ps for pristine $CsPbBr_3$ Film, 1.83 ps for $CsPbBr_3$/CuI and 451 fs for $CsPbBr_3/Cu_2O$ composite film.

The photoinduced absorption in the higher wavelength region (PIA3) arises due to the absorption by excited-state species. Figures 12b and 12d show a rise in the PIA3 signal at 610 nm as the PIA2 signal decays. This indicates that PIA3 could partly originate from hot carriers, with its decay representing the cooling of these hot carriers. The decay kinetics at 610 nm, as depicted in Figure 13, shows the fastest decay for the $CsPbBr_3/Cu_2O$ sample. This faster decay is likely attributed to more efficient hot carrier cooling, which results from the transfer of hot carriers (holes) to the HTM and the faster dissociation of excitons.[79-81]

The decay kinetics of the transient photoinduced bleaching peak (GSB) were analysed and fitted to exponential functions to gain deeper insights into the ultrafast hole injection dynamics. Figure 14 illustrates the decay kinetics of the GSB signal for all three samples.

$$y = y_0 + A_1 exp\left(-{}^{x}/_{\tau_1}\right) + A_2 exp\left(-{}^{x}/_{\tau_2}\right) + A_3 exp\left(-{}^{x}/_{\tau_3}\right) \quad (2)$$

Table 2. The parameters obtained from fitting the GSB kinetics at 510 nm for the pristine $CsPbBr_3$ NC film, $CsPbBr_3$/CuI, and $CsPbBr_3/Cu_2O$ composite films.

	τ_{G1}	A_1	τ_1 (ps)	A_2	τ_2 (ps)	A_3	τ_3 (ps)
$CsPbBr_3$	487 fs (100%)	-39%	71	-45%	286	-15%	1100
$CsPbBr_3$/CuI	1.6 ps (100%)	-58%	6.4	-26%	54	-14%	1020
$CsPbBr_3/Cu_2O$	-	-47%	4.1	-28%	48	-23%	910

The rise of the excitonic bleach signal was fitted to a single exponential function for both the pristine $CsPbBr_3$ NC film and the $CsPbBr_3$/CuI composite film. However, for the $CsPbBr_3/Cu_2O$ composite film, the growth signal was extremely fast (<100 fs), making it difficult to extract a precise growth time component due to experimental limitations. The decay of the excitonic bleach

signal was fitted to a triexponential function (Equation 2) and the fitting parameters are summarised in Table 2.

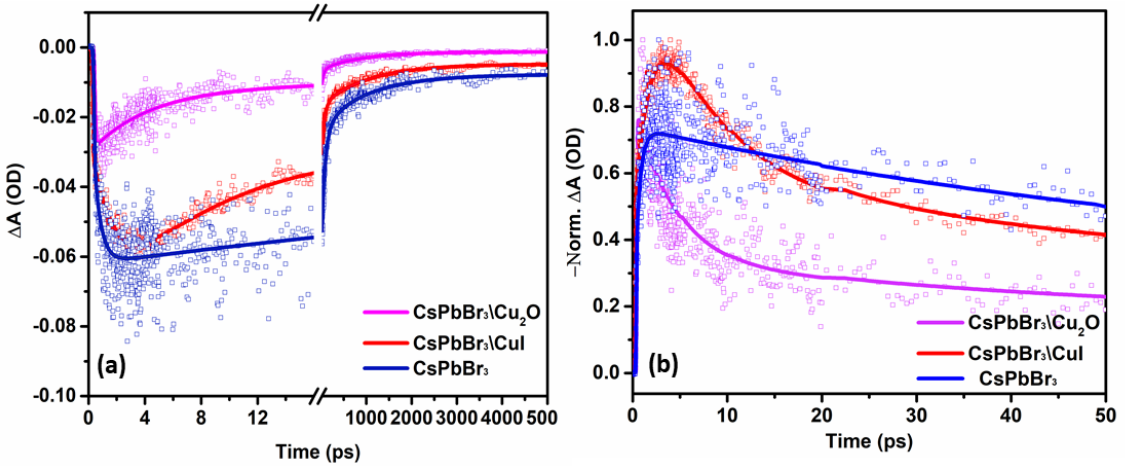

Figure 14. Formation and decay kinetics of the ground state bleach peak at 510 nm for $CsPbBr_3$ NC film (blue), $CsPbBr_3$/CuI composite film (red) and $CsPbBr_3$/Cu_2O composite film (magenta). Points are experimental data, and the solid lines are tri-exponential fits of the data points.

The ultrafast growth at the excitonic bleach position was observed for all three samples, with the fastest growth recorded for the $CsPbBr_3$/Cu_2O composite. This indicates the rapid cooling of electrons from higher excitonic states to the band-edge position. The bleach recovery process encompasses all mechanisms through which the system returns to its original ground state.

According to previous studies, the fast time component (τ_1) is associated with charge carrier trapping at perovskite grain boundaries and perovskite/HTL interfaces.[82] This time scale is faster for samples with HTM compared to the pristine $CsPbBr_3$ film, with the fastest value of 4.7 ps observed for Cu_2O. This time component represents the duration required for an excited electron to transition from the conduction band to trap states. A smaller τ_1 indicates quicker filling of trap states, allowing holes to be injected more efficiently into the HTL.[83]

The second time component (τ_2) is attributed to hole injection from the perovskite NC film into the inorganic hole transport material (HTL).[83-84] Like τ_1, τ_2 is faster in the presence of HTL, indicating ultrafast hole injection from the perovskite to the HTL. For Cu_2O as the HTL, τ_2 is even faster than for CuI, reflecting more efficient hole transport dynamics with Cu_2O. The faster τ_2 decay aligns with the photoluminescence (PL) characteristics, which show significant quenching

and faster PL decay in the presence of HTL, with Cu_2O exhibiting the strongest quenching and fastest decay. This demonstrates that Cu_2O is a superior HTM for $CsPbBr_3$ NCs, enabling faster hole extraction. Previous studies highlight that the τ_2 component plays a critical role in the device's electrical performance due to its influence on faster hole injection.[83]

Similar to τ_1 and τ_2, the τ_3 component is also found to be less in composite samples with HTL. Following photoexcitation, the fastest recombination process is exciton recombination, with typical lifetimes ranging from 10 ps to 10 ns, while slower recombination processes, such as trap-assisted recombination at grain boundaries and interfaces, are not detectable within the delay range used in this experiment. Here, τ_3 represents only the electron-hole recombination kinetics, which are similar across all three samples. However, in the presence of HTM, τ_3 is slowest for CuI and slightly faster for Cu_2O. Despite this, Cu_2O enables more efficient charge transfer, ultimately benefiting device performance more effectively.[83-86]

3.5. Time-Resolved THz spectroscopy of $CsPbBr_3$ film and its composite film with HTMs CuI and Cu_2O

To gain deeper insights into carrier transfer and recombination dynamics in $CsPbBr_3$ NC films in the presence of inorganic hole-transporting layers, we employed time-resolved terahertz (THz) spectroscopy. As outlined in previous chapters, TRTS is a powerful technique that directly probes the photoconductivity of materials, providing crucial information about charge carrier mobility and its temporal evolution. Upon photoexcitation, the change in the material's conductivity can be expressed as:

$$\Delta\sigma = \xi \times (\mu_e + \mu_h) \tag{3}$$

where ξ represents the quantum yield of charge generation, and μ_e and μ_h denote the mobilities of electrons and holes, respectively.[72] The temporal evolution of charge mobility and charge generation efficiency following photoexcitation shapes the THz photoconductivity spectra. Initially, photoconductivity rises due to charge generation and increased carrier mobility. Over time, if carrier mobility and density decline, the photoconductivity kinetics exhibit a decay. This decay may result from charge recombination or injection into other low-mobility materials.

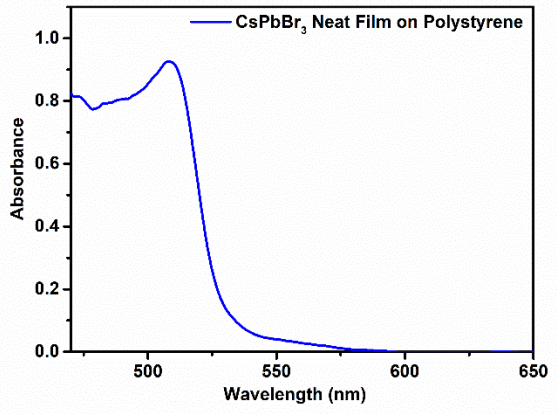

Figure 15. The absorption spectrum of the $CsPbBr_3$ NC film on a polystyrene substrate.

For the TRTS experiments, we utilised a polystyrene (PS) substrate chosen for its excellent transparency in the THz frequency range. The samples were prepared through spin coating, as described in the previous section. The thickness of the $CsPbBr_3$ films in all three samples was ~1 micron measured with AFM. Figure 15 presents the absorption spectrum of the $CsPbBr_3$ NC film on the polystyrene substrate, recorded in transmission mode, with the first excitonic peak observed at 508 nm. All THz measurements were conducted at room temperature (298 K) under a relative humidity of less than 1%. To mitigate thermal effects, the samples were slightly moved to new spots after a set of scans.

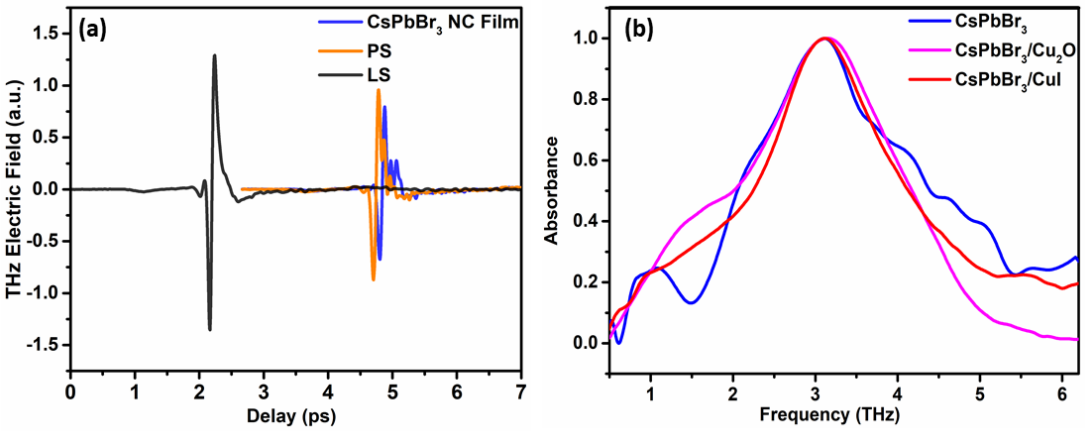

Figure 16. (a) THz-TDS waveforms transmitted through the air referred to as the light source (LS) (black), polystyrene (PS) substrate (orange) and through the $CsPbBr_3$ NC film on the PS substrate

(blue). **(b)** The normalised THz absorption spectrum of the $CsPbBr_3$ NC film (blue), $CsPbBr_3$/CuI composite film (red), and $CsPbBr_3/Cu_2O$ composite film (magenta).

We recorded the time-domain THz spectra for all three samples. Figure 16a shows the time-domain waveforms of the THz electric field without any sample (black), referred to as the light source (LS), after passing through the polystyrene (PS) substrate (orange), and the $CsPbBr_3$ NC film on the PS substrate (blue). The interaction with the substrate and the film induces changes in the electric field's amplitude and phase. The absorption spectrum of the $CsPbBr_3$ NC film was calculated from the negative logarithm of the amplitude ratios derived from the Fourier transform of the electric fields passing through the PS substrate and the $CsPbBr_3$ NC film on the PS substrate.

Figure 16b shows the THz absorption spectra for all three films: pristine $CsPbBr_3$ NC film, $CsPbBr_3$ NC film with HTM CuI, and $CsPbBr_3$ NC film with HTM Cu_2O, measured in the frequency range of 0.5 to 6 THz. All three samples exhibit a prominent absorption peak at ~3 THz, corresponding to IR-active phonon modes. However, a redshift of approximately 0.4 THz is observed compared to the strong peak seen in the $CsPbBr_3$ NC colloidal solution. In our previous work, using DFT calculations, this peak has been assigned to lattice vibrations (optical phonons) within the orthorhombic lattice of the NCs. The observed redshift may be due to the softening of phonon modes in the film compared to NCs in solution. The consistency of this peak across all samples also confirms the structural stability and similarity of the $CsPbBr_3$ material, whether in its neat film form or on a substrate with inorganic HTMs.[69]

3.5.1. Frequency Averaged Time Resolved THz Spectroscopy Experiment

We performed frequency-averaged time-resolved THz spectroscopy for all three samples. In this experiment, the gating delay (Delay 1, as shown in Figure 4 of Chapter 2) is fixed at the peak of the THz electric field (t_{max}). After photoexcitation, we measure the change in the peak THz electric field as a function of the pump-probe delay, controlled using Delay 2 (Figure 4, Chapter 2).

Using a lock-in amplifier and a mechanical chopper operating at 333 Hz, we recorded the THz peak electric field difference between the photoexcited and unexcited samples. This difference is

expressed as $E_{exc}(t_{max}) - E_0(t_{max})$, where $E_{exc}(t_{max})$ is the peak THz electric field of the excited sample, and $E_0(t_{max})$ is the corresponding field of the unexcited sample. The change in the THz electric field is recorded as a function of the pump-probe delay (t_p) and is represented as $\Delta E\left(t_p, t_{max}\right)$. This provides the temporal evolution of the sample's response following photoexcitation. The observed change in the THz electric field corresponds to a decrease in the transmission, as the presence of charge carriers in the excited sample leads to increased absorption compared to the unexcited sample. The normalised decrease in the THz transmission, given by (-$\Delta E\left(t_p\right)/ E_0\left(t_p\right)$) at a pump-probe delay t_p, is directly proportional to the change in the photoconductivity of the medium.[87]

$$\Delta\sigma = \frac{\varepsilon_0 c\,(n_a+n_b)}{d}\left(\frac{-\Delta E(\omega)}{E_{off}(\omega)}\right) \tag{4}$$

where d is the thickness of the photoexcited sample, $n_a$and n_b are the refractive indices of the media on either side of the sample. In our experiment, the media are air (n_a= 1) and the polystyrene substrate (n_b=1.52 as determined from our THz time-domain spectroscopy (TDS) measurements). Here, ε_0 is the permittivity of free space, and c is the speed of light.

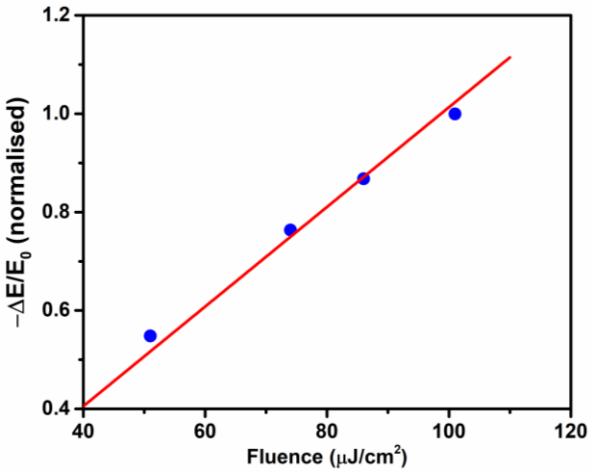

Figure 17. The negative differential transmission as a function of fluence used in the experiment fits well to a linear function.

For photoexcitation, we used a pump wavelength of 480 nm (photon energy: 2,58 eV). This wavelength was chosen because the HTM materials CuI and Cu_2O do not absorb in this range. For $CsPbBr_3$ NCs, however, this wavelength is slightly above the band gap, generating both hot charge carriers and excitons.

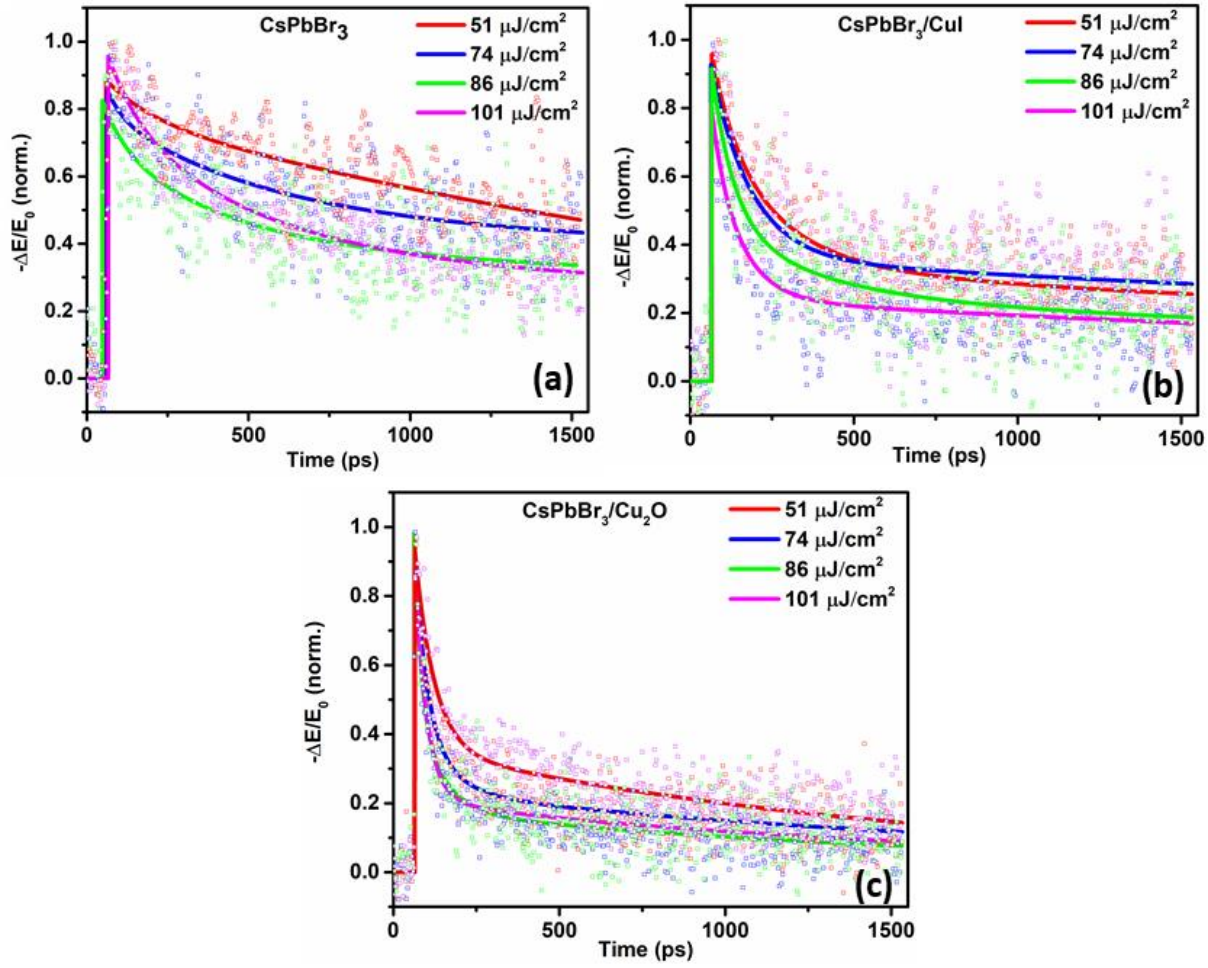

Figure 18. Normalised transient photoconductivity at different fluences following photoexcitation at 480 nm for **(a)** $CsPbBr_3$ NC film, **(b)** $CsPbBr_3$/CuI composite film, and **(c)** $CsPbBr_3/Cu_2O$ composite film. Points are experimental data, and the solid lines are tri-exponential fits for the data points.

Figure 18 shows the THz photoconductivity kinetics for all three samples after photoexcitation at 480 nm, measured at four different fluences. Figure 17 presents the peak negative differential

transmission ($-\Delta E(t_p)/ E_0(t_p)$) as a function of fluence, fitted well with the linear function, confirming that the experiments were conducted within the linear regime. The transient kinetics were analysed by fitting the data with a Gaussian-convoluted multi-exponential function:

$$y = G(t - t_0) \otimes \sum_i a_i exp\,[-(t - t_0)/\tau_i\,] \quad (5)$$

The parameters obtained from fitting all the transients are summarised in Tables 3, 4, and 5.

Table 3. The parameters obtained from fitting the normalised THz transients of the neat $CsPbBr_3$ NC film to Equation 5, following photoexcitation with a 480 nm pump wavelength.

Fluence ($\mu J/cm^2$)	a_1	τ_1 (ps)	a_2	τ_2 (ps)	a_3	τ_3 (ps)
51	0.476 (0.007)	8976 (35.0)	0.386 (0.004)	359.12 (3.8)	0.142 (0.006)	68.33 (0.6)
74	0.554 (0.009)	5024 (22.0)	0.342 (0.006)	462.25 (5.6)	0.086 (0.008)	47.25 (0.9)
86	0.434 (0.003)	8027 (29.5)	0.394 (0.005)	358.42 (3.1)	0.148 (0.004)	68.29 (0.5)
101	0.291 (0.005)	4041 (18.0)	0.473 (0.003)	447.53 (4.7)	0.193 (0.003)	96.65 (0.6)

The decay of photoconductivity is significantly faster in the presence of hole transport materials (HTMs) with $CsPbBr_3$ NC films, with the fastest decay observed for the Cu_2O composite. The parameters clearly indicate that the photoconductivity decay becomes even faster as the fluence increases. The slowest component, τ_1, generally corresponds to recombination processes with lifetimes extending up to ~10 ns. However, due to the limited temporal window of our experiment (1.5 ns), we cannot estimate τ_1 with high certainty. This limitation means our measurements primarily capture faster processes, such as excitonic recombination, rather than slower processes, like trap-assisted recombination. For pristine $CsPbBr_3$ NC film, τ_1 is in the range of ~ 4–9 ns. This lifetime decreases in the presence of HTMs, dropping to ~ 4–5 ns for $CsPbBr_3$/CuI and further reducing to ~ 1.8–2 ns for $CsPbBr_3/Cu_2O$. Additionally, the contribution of processes associated

Table 4. The parameters obtained from fitting the normalised THz transients of the neat $CsPbBr_3$/CuI composite film to Equation 5, following photo excitation with a 480 nm pump wavelength.

Fluence ($\mu J/cm^2$)	a_1	τ_1 (ps)	a_2	τ_2 (ps)	a_3	τ_3 (ps)
51	0.345 (0.003)	5586 (22.0)	0.38 (0.007)	215.8 (5.8)	0.263 (0.003)	77.7 (0.5)
74	0.353 (0.008)	5303 (38.0)	0.27 (0.009)	121 (7.2)	0.362 (0.007)	109.0 (0.9)
86	0.272 (0.006)	4873 (29.0)	0.24 (0.004)	309 (4.1)	0.481 (0.008)	66.3 (0.5)
101	0.295 (0.008)	4178 (33.0)	0.58 (0.006)	89.3 (2.8)	0.127 (0.007)	35.3 (0.4)

Table 5. The parameters obtained from fitting the normalised THz transients of the neat $CsPbBr_3/Cu_2O$ composite film to Equation 5, following photo excitation with a 480 nm pump wavelength.

Fluence ($\mu J/cm^2$)	a_1	τ_1 (ps)	a_2	τ_2 (ps)	a_3	τ_3 (ps)
51	0.181 (0.009)	2056 (27.0)	0.196 (0.007)	138 (4.7)	0.616 (0.008)	58.4 (0.8)
74	0.256 (0.006)	2160 (38.0)	0.175 (0.005)	108 (3.2)	0.575 (0.005)	40.2 (0.7)
86	0.171 (0.005)	1740 (19.0)	0.31 (0.003)	79 (6.2)	0.503 (0.003)	19.6 (0.5)
101	0.212 (0.007)	1871 (32.0)	0.032 (0.008)	194 (7.2)	0.752 (0.005)	34.7 (0.3)

with τ_1 decreases in the presence of HTMs, likely due to reduced carrier trapping. This reduction may result from alternative charge transfer pathways the HTM layers provide.

The intermediate decay component τ_2, becomes faster in the presence of HTMs. For $CsPbBr_3$, τ_2 ranges from ~ 350 to 460 ps. However, in the presence of CuI as the HTM, τ_2 decreases to ~ 89–215 ps, and with Cu_2O, it is further reduced to ~ 79–194 ps. We attribute τ_2 to the hole injection process from the perovskite to the hole transport layer. The fastest decay component, τ_3, also decreases significantly in the presence of HTMs. For pristine $CsPbBr_3$, τ_3 is ~ 68–96 ps, which reduces to ~ 35–77 ps for the $CsPbBr_3$/CuI composite and further to 34–58 ps for the $CsPbBr_3$ /Cu_2O composite. Similarly, the contributions of the processes associated with τ_2 and τ_3 also increase in the presence of HTM. We attribute τ_3 to the transfer process of thermalised holes to the HTM. However, τ_3 is also attributed to Auger recombination, which occurs at high fluence due to the presence of a high carrier density. This provides another possible explanation for the increased contribution of τ_3 -related processes at higher fluences.[69]

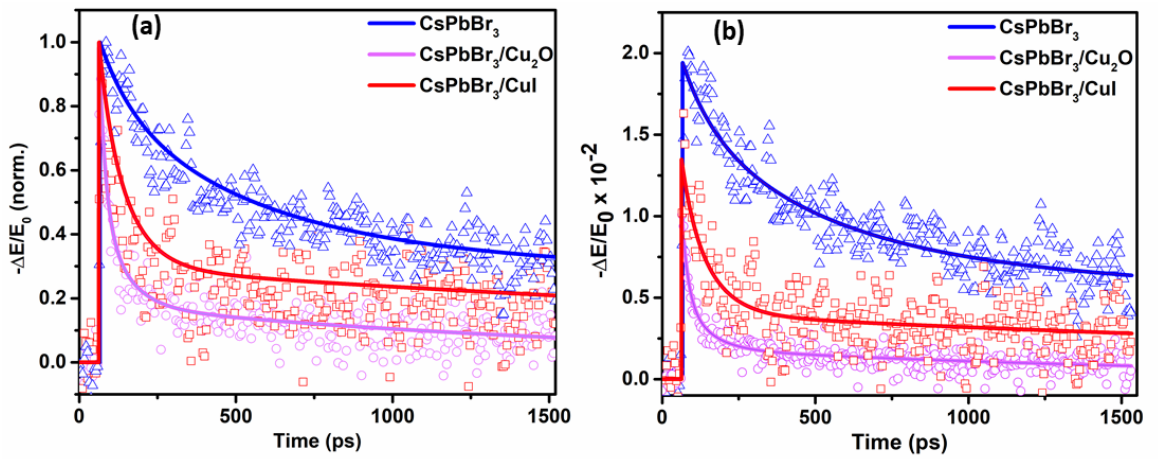

Figure 19. (a) Comparison of THz decay kinetics obtained for neat $CsPbBr_3$ NC film (blue), $CsPbBr_3$/CuI composite film (red) and $CsPbBr_3$/Cu_2O composite film (magenta) and **(b)** THz kinetics for neat $CsPbBr_3$ NC film (blue), $CsPbBr_3$/CuI composite film (red) and $CsPbBr_3$/Cu_2O composite film (magenta) normalised with respect to density of photon absorbed following photoexcitation with 480 nm pump wavelength at 51 μJ/cm^2 fluence.

3.5.2. Peak Conductivity and Effective Mobility

As shown in Figure 19a, the faster decay in ($-\Delta E(t_p)/E_0(t_p)$) value (photoconductivity) with pump-probe delay is observed in the presence of HTMs, demonstrating efficient charge transfer from the $CsPbBr_3$ NC film to the HTL. These findings are consistent with results from transient absorption (TA) spectroscopy, steady-state photoluminescence (PL) quenching, and time-resolved photoluminescence (TRPL) decay kinetics. They collectively confirm that hole transport is more efficient in the case of Cu_2O compared to CuI.

The peak conductivity of the samples can be determined from the peak value of the ($-\Delta E(t_p)/E_0(t_p)$), extracted from the kinetics using Equation 4. The conductivity values obtained at different fluences for $CsPbBr_3$ NC films are 121 to 163 S/m, for $CsPbBr_3$/CuI composite film are 72 to 105 S/m and for $CsPbBr_3/Cu_2O$ composite film are 60 to 91 S/m.[72]

Table 6. Peak conductivity obtained for neat $CsPbBr_3$ NC film. Decrease in peak conductivity in the presence of HTM CuI and Cu_2O with $CsPbBr_3$ NC film normalised with respect to initial carrier density.

Fluence ($\mu J/cm^2$)	N_0 ($\times 10^{18}$)	$CsPbBr_3$ S/m	Conductivity Quenching (%)	
			$CsPbBr_3$/CuI	$CsPbBr_3/Cu_2O$
51	1.6	121	40.5	50.1
74	2.4	133	38.3	48.0
86	2.8	151	37.8	46.5
101	3.2	163	39.5	47.23

These values clearly indicate significant quenching of conductivity in the presence of HTMs with $CsPbBr_3$ NC films. This effect is also evident in Figure 19b, which shows the pump-induced ($-\Delta E(t_p)/E_0(t_p)$) transients for all three samples, normalised with respect to absorbed photons.

The kinetics reveal a marked reduction in the peak values, which correspond to the peak conductivity. The conductivity quenching is nearly 50% for the $CsPbBr_3/Cu_2O$ composite and about 40% for the $CsPbBr_3$/CuI composite. Table 5 provides a detailed comparison of the conductivity quenching observed for the $CsPbBr_3$/HTM composites.

The observed quenching in initial peak conductivity indicates a substantial reduction in charge carrier density within the NCs on an ultrafast timescale. This suggests that hole transfer occurs on a timescale even faster than the instrument response function (~300 fs). The rapid carrier transfer is so fast that it raises the possibility of hot charge carrier transfer occurring before thermalisation. Similar findings have been reported in the literature. For example, Ponseca et al. demonstrated sub-200 fs hole transfer from $CH_3NH_3PbI_3$ to Spiro-OMeTAD, an organic hole acceptor.[88]

We calculated the initial effective mobilities (φμ) from the measured photoconductivity values using the equation:

$$\varphi\mu \cong \frac{\Delta\sigma}{qN_0} \tag{6}$$

where φμ is the effective mobility, q is the elementary charge, and N_0 is the number of carriers generated upon photoexcitation.

Here, φμ represents the photon-to-free-carrier conversion ratio, and we assume φ=1, meaning that every absorbed photon generates two charge carriers. Under this assumption, $N_0 = 2N_p$, where N_p is the number of absorbed photons. Np can be calculated using the equation-

$$N_p = F_l(1 - 10^{-OD_\lambda})/dh\nu \tag{7}$$

Where F_l is the fluence, $(1 - 10^{-OD_\lambda})$ is the fraction of photon absorbed of energy $h\nu$. Since we consider φ=1, the mobilities calculated represent a lower estimate. The calculated N_p values for the three samples at different fluences are in the range of 8.0×10^{17} to 1.9×10^{18} cm^{-3}. The mobility calculated for pristine $CsPbBr_3$ NCs film at lowest fluence is 4.54 $cm^2V^{-1}s^{-1}$. This mobility decreases to 1.9 $cm^2V^{-1}s^{-1}$ for $CsPbBr_3/Cu_2O$ composite film and for $CsPbBr_3/Cu_2O$ composite the mobility further reduces to 1.81 $cm^2V^{-1}s^{-1}$.

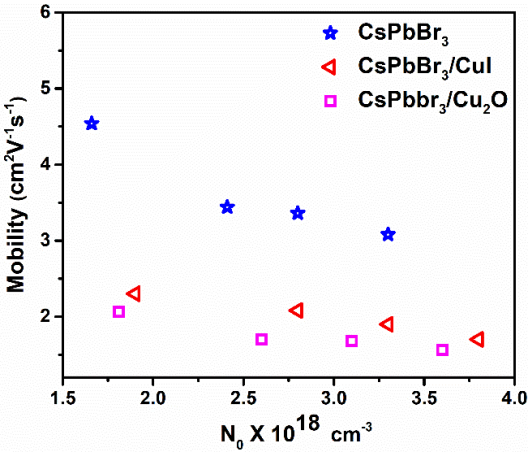

Figure 20. Initial effective mobility obtained for neat $CsPbBr_3$ NC film, $CsPbBr_3$/CuI and $CsPbBr_3/Cu_2O$ composite film as a function of initial carrier density.

Figure 20 presents the mobilities calculated from the peak conductivity for all three samples. A noticeable decrease in mobility is observed for the samples with HTL.[72] This drop in effective mobility can be attributed to the transfer of holes from $CsPbBr_3$ NCs to the inorganic hole-transporting layer.

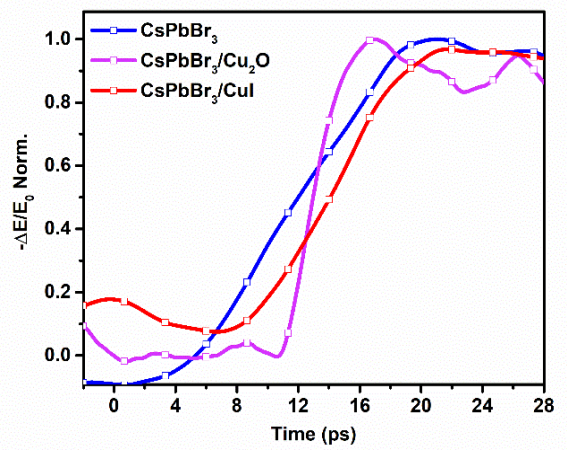

Figure 21. Normalised THz transient obtained at early pump-probe delay for neat $CsPbBr_3$ NC film (blue), $CsPbBr_3$/CuI composite film (red) and $CsPbBr_3/Cu_2O$ composite film (magenta) following photoexcitation with 480 nm pump wavelength at 51 μJ/cm^2 fluence.

In samples with HTMs, the observed decrease in measured peak mobility is unlikely to be caused by charge carrier relaxation, as relaxation does not occur on such a fast timescale (sub-picosecond). Instead, the ultrafast transfer of holes to the HTM is the primary reason for the mobility reduction. The measured mobility in the composite sample likely reflects only the electron mobility (μ_e).

An expanded view of the very early initial dynamics is presented in Figure 21. The initial rise reflects the generation of free charge carriers, while the subsequent curve at the peak represents the dissociation of loosely bound electron-hole pairs into free charges. For the neat $CsPbBr_3$ NC film, the conductivity rise is slower than the NC solution. This slower rise could be attributed to heterogeneity in the binding energy, which arises from an increased defect concentration in the film. A faster rise was observed for the sample with HTM. For the $CsPbBr_3$/CuI composite, only a single ultrafast, instrument-limited rise was observed. This behaviour aligns with previously reported results, where interfacial charge injection to charge transport layer occurs on a sub-picosecond timescale.[88-90]

These observations confirm that hole transport is more efficient and faster in the case of Cu_2O compared to CuI when used as a hole-transporting material (HTM). Proper band alignment is the primary factor influencing charge injection efficiency, which provides the driving force for charge transfer. Cu_2O, with a more favourable band alignment, extracts holes more efficiently than CuI.[57, 71]

3.6. Conclusion

In conclusion, we investigated the charge carrier dynamics in $CsPbBr_3$ NC films interfaced with two copper-based inorganic hole transport materials, CuI and Cu_2O, using time-resolved PL, time-resolved THz, and femtosecond transient absorption spectroscopy. In both cases, ultrafast hole injection from $CsPbBr_3$ NCs to the HTMs occurs on a sub-picosecond timescale, including the transfer of hot carriers. While both materials effectively function as HTLs for $CsPbBr_3$ NCs, the rate of hole transfer and overall efficiency are notably higher in the case of Cu_2O. The combination of stability, solution processability, cost-effectiveness, and superior hole extraction efficiency positions Cu_2O as a promising candidate for HTL applications.

3.7. References

1. Eperon, G. E.; Paternò, G. M.; Sutton, R. J.; Zampetti, A.; Haghighirad, A. A.; Cacialli, F.; Snaith, H. J., Inorganic caesium lead iodide perovskite solar cells. *Journal of Materials Chemistry A* **2015,** *3* (39), 19688-19695.

2. Jung, E. H.; Jeon, N. J.; Park, E. Y.; Moon, C. S.; Shin, T. J.; Yang, T.-Y.; Noh, J. H.; Seo, J., Efficient, stable and scalable perovskite solar cells using poly (3-hexylthiophene). *Nature* **2019,** *567* (7749), 511-515.

3. Saliba, M.; Matsui, T.; Domanski, K.; Seo, J.-Y.; Ummadisingu, A.; Zakeeruddin, S. M.; Correa-Baena, J.-P.; Tress, W. R.; Abate, A.; Hagfeldt, A., Incorporation of rubidium cations into perovskite solar cells improves photovoltaic performance. *Science* **2016,** *354* (6309), 206-209.

4. Burschka, J.; Pellet, N.; Moon, S.-J.; Humphry-Baker, R.; Gao, P.; Nazeeruddin, M. K.; Grätzel, M., Sequential deposition as a route to high-performance perovskite-sensitized solar cells. *Nature* **2013,** *499* (7458), 316-319.

5. Jiang, X.; Wang, D.; Yu, Z.; Ma, W.; Li, H. B.; Yang, X.; Liu, F.; Hagfeldt, A.; Sun, L., Molecular engineering of copper phthalocyanines: a strategy in developing dopant-free hole-transporting materials for efficient and ambient-stable perovskite solar cells. *Advanced Energy Materials* **2019,** *9* (4), 1803287.

6. Manser, J. S.; Christians, J. A.; Kamat, P. V., Intriguing Optoelectronic Properties of Metal Halide Perovskites. *Chemical Reviews* **2016,** *116* (21), 12956-13008.

7. Iftikhar, F. J.; Wali, Q.; Yang, S.; Iqbal, Y.; Jose, R.; Munir, S.; Gondal, I. A.; Khan, M. E., Structural and optoelectronic properties of hybrid halide perovskites for solar cells. *Organic Electronics* **2021,** *91*, 106077.

8. Conings, B.; Drijkoningen, J.; Gauquelin, N.; Babayigit, A.; D'Haen, J.; D'Olieslaeger, L.; Ethirajan, A.; Verbeeck, J.; Manca, J.; Mosconi, E., Intrinsic thermal instability of methylammonium lead trihalide perovskite. *Advanced Energy Materials* **2015,** *5* (15), 1500477.

9. Brunetti, B.; Cavallo, C.; Ciccioli, A.; Gigli, G.; Latini, A., On the thermal and thermodynamic (in) stability of methylammonium lead halide perovskites. Sci Rep 6: 31896. 2016.

10. Akbulatov, A. F.; Luchkin, S. Y.; Frolova, L. A.; Dremova, N. N.; Gerasimov, K. L.; Zhidkov, I. S.; Anokhin, D. V.; Kurmaev, E. Z.; Stevenson, K. J.; Troshin, P. A., Probing the

intrinsic thermal and photochemical stability of hybrid and inorganic lead halide perovskites. *The journal of physical chemistry letters* **2017,** *8* (6), 1211-1218.

11. Edri, E.; Kirmayer, S.; Henning, A.; Mukhopadhyay, S.; Gartsman, K.; Rosenwaks, Y.; Hodes, G.; Cahen, D., Why Lead Methylammonium Tri-Iodide Perovskite-Based Solar Cells Require a Mesoporous Electron Transporting Scaffold (but Not Necessarily a Hole Conductor). *Nano Letters* **2014,** *14* (2), 1000-1004.

12. Bryant, D.; Aristidou, N.; Pont, S.; Sanchez-Molina, I.; Chotchunangatchaval, T.; Wheeler, S.; Durrant, J. R.; Haque, S. A., Light and oxygen induced degradation limits the operational stability of methylammonium lead triiodide perovskite solar cells. *Energy & Environmental Science* **2016,** *9* (5), 1655-1660.

13. Juarez-Perez, E. J.; Ono, L. K.; Maeda, M.; Jiang, Y.; Hawash, Z.; Qi, Y., Photodecomposition and thermal decomposition in methylammonium halide lead perovskites and inferred design principles to increase photovoltaic device stability. *Journal of Materials Chemistry A* **2018,** *6* (20), 9604-9612.

14. Chen, H.; Xiang, S.; Li, W.; Liu, H.; Zhu, L.; Yang, S., Inorganic perovskite solar cells: a rapidly growing field. *Solar Rrl* **2018,** *2* (2), 1700188.

15. Sim, K. M.; Swarnkar, A.; Nag, A.; Chung, D. S., Phase Stabilized α-CsPbI3 Perovskite Nanocrystals for Photodiode Applications. *Laser & Photonics Reviews* **2018,** *12* (1), 1700209.

16. Wang, Y.; Zhang, T.; Kan, M.; Zhao, Y., Bifunctional Stabilization of All-Inorganic α-CsPbI3 Perovskite for 17% Efficiency Photovoltaics. *Journal of the American Chemical Society* **2018,** *140* (39), 12345-12348.

17. Wang, Y.; Dar, M. I.; Ono, L. K.; Zhang, T.; Kan, M.; Li, Y.; Zhang, L.; Wang, X.; Yang, Y.; Gao, X.; Qi, Y.; Grätzel, M.; Zhao, Y., Thermodynamically stabilized β-CsPbI₃–based perovskite solar cells with efficiencies >18%. *Science* **2019,** *365* (6453), 591-595.

18. Wang, Q.; Zhang, X.; Jin, Z.; Zhang, J.; Gao, Z.; Li, Y.; Liu, S. F., Energy-Down-Shift CsPbCl3:Mn Quantum Dots for Boosting the Efficiency and Stability of Perovskite Solar Cells. *ACS Energy Letters* **2017,** *2* (7), 1479-1486.

19. Liang, J.; Wang, C.; Wang, Y.; Xu, Z.; Lu, Z.; Ma, Y.; Zhu, H.; Hu, Y.; Xiao, C.; Yi, X.; Zhu, G.; Lv, H.; Ma, L.; Chen, T.; Tie, Z.; Jin, Z.; Liu, J., All-Inorganic Perovskite Solar Cells. *Journal of the American Chemical Society* **2016,** *138* (49), 15829-15832.

20. Sutton, R. J.; Eperon, G. E.; Miranda, L.; Parrott, E. S.; Kamino, B. A.; Patel, J. B.; Hörantner, M. T.; Johnston, M. B.; Haghighirad, A. A.; Moore, D. T.; Snaith, H. J., Bandgap-Tunable Cesium Lead Halide Perovskites with High Thermal Stability for Efficient Solar Cells. *Advanced Energy Materials* **2016,** *6* (8), 1502458.

21. Ramasamy, P.; Lim, D.-H.; Kim, B.; Lee, S.-H.; Lee, M.-S.; Lee, J.-S., All-inorganic cesium lead halide perovskite nanocrystals for photodetector applications. *Chemical Communications* **2016,** *52* (10), 2067-2070.

22. Lin, Y.; Zheng, X.; Shangguan, Z.; Chen, G.; Huang, W.; Guo, W.; Fan, X.; Yang, X.; Zhao, Z.; Wu, T.; Chen, Z., All-inorganic encapsulation for remarkably stable cesium lead halide perovskite nanocrystals: toward full-color display applications. *Journal of Materials Chemistry C* **2021,** *9* (36), 12303-12313.

23. Ullah, S.; Wang, J.; Yang, P.; Liu, L.; Yang, S.-E.; Xia, T.; Guo, H.; Chen, Y., All-inorganic CsPbBr3 perovskite: a promising choice for photovoltaics. *Materials Advances* **2021,** *2* (2), 646-683.

24. Yang, D.; Cao, M.; Zhong, Q.; Li, P.; Zhang, X.; Zhang, Q., All-inorganic cesium lead halide perovskite nanocrystals: synthesis, surface engineering and applications. *Journal of Materials Chemistry C* **2019,** *7* (4), 757-789.

25. Protesescu, L.; Yakunin, S.; Bodnarchuk, M. I.; Krieg, F.; Caputo, R.; Hendon, C. H.; Yang, R. X.; Walsh, A.; Kovalenko, M. V., Nanocrystals of Cesium Lead Halide Perovskites (CsPbX3, X = Cl, Br, and I): Novel Optoelectronic Materials Showing Bright Emission with Wide Color Gamut. *Nano Letters* **2015,** *15* (6), 3692-3696.

26. Shamsi, J.; Urban, A. S.; Imran, M.; De Trizio, L.; Manna, L., Metal Halide Perovskite Nanocrystals: Synthesis, Post-Synthesis Modifications, and Their Optical Properties. *Chemical Reviews* **2019,** *119* (5), 3296-3348.

27. Sanehira, E. M.; Marshall, A. R.; Christians, J. A.; Harvey, S. P.; Ciesielski, P. N.; Wheeler, L. M.; Schulz, P.; Lin, L. Y.; Beard, M. C.; Luther, J. M., Enhanced mobility CsPbI3 quantum dot

arrays for record-efficiency, high-voltage photovoltaic cells. *Science advances* **2017,** *3* (10), eaao4204.

28. Fang, F.; Chen, W.; Li, Y.; Liu, H.; Mei, M.; Zhang, R.; Hao, J.; Mikita, M.; Cao, W.; Pan, R.; Wang, K.; Sun, X. W., Employing Polar Solvent Controlled Ionization in Precursors for Synthesis of High-Quality Inorganic Perovskite Nanocrystals at Room Temperature. *Advanced Functional Materials* **2018,** *28* (10), 1706000.

29. Yu, H.; Xu, X.; Liu, H.; Wan, Y.; Cheng, X.; Chen, J.; Ye, Y.; Dai, L., Waterproof Cesium Lead Bromide Perovskite Lasers and Their Applications in Solution. *ACS Nano* **2020,** *14* (1), 552-558.

30. Zheng, W.; Wan, Q.; Liu, M.; Zhang, Q.; Zhang, C.; Yan, R.; Feng, X.; Kong, L.; Li, L., CsPbBr3 Nanocrystal Light-Emitting Diodes with Efficiency up to 13.4% Achieved by Careful Surface Engineering and Device Engineering. *The Journal of Physical Chemistry C* **2021,** *125* (5), 3110-3118.

31. Kung, P.-K.; Li, M.-H.; Lin, P.-Y.; Chiang, Y.-H.; Chan, C.-R.; Guo, T.-F.; Chen, P., A Review of Inorganic Hole Transport Materials for Perovskite Solar Cells. *Advanced Materials Interfaces* **2018,** *5* (22), 1800882.

32. Le Corre, V. M.; Stolterfoht, M.; Perdigón Toro, L.; Feuerstein, M.; Wolff, C.; Gil-Escrig, L.; Bolink, H. J.; Neher, D.; Koster, L. J. A., Charge Transport Layers Limiting the Efficiency of Perovskite Solar Cells: How To Optimize Conductivity, Doping, and Thickness. *ACS Applied Energy Materials* **2019,** *2* (9), 6280-6287.

33. Courtier, N. E.; Cave, J. M.; Foster, J. M.; Walker, A. B.; Richardson, G., How transport layer properties affect perovskite solar cell performance: insights from a coupled charge transport/ion migration model. *Energy & Environmental Science* **2019,** *12* (1), 396-409.

34. Jung, H. S.; Park, N.-G., Perovskite Solar Cells: From Materials to Devices. *Small* **2015,** *11* (1), 10-25.

35. Shen, Y.; Deng, K.; Li, L., Spiro-OMeTAD-Based Hole Transport Layer Engineering toward Stable Perovskite Solar Cells. *Small Methods* **2022,** *6* (11), 2200757.

36. Nie, W.; Tsai, H.; Asadpour, R.; Blancon, J.-C.; Neukirch, A. J.; Gupta, G.; Crochet, J. J.; Chhowalla, M.; Tretiak, S.; Alam, M. A., High-efficiency solution-processed perovskite solar cells with millimeter-scale grains. *Science* **2015,** *347* (6221), 522-525.

37. Zheng, X.; Chen, B.; Dai, J.; Fang, Y.; Bai, Y.; Lin, Y.; Wei, H.; Zeng, X. C.; Huang, J., Defect passivation in hybrid perovskite solar cells using quaternary ammonium halide anions and cations. *Nature Energy* **2017,** *2* (7), 1-9.

38. Xu, J.; Dai, J.; Dong, H.; Li, P.; Chen, J.; Zhu, X.; Wang, Z.; Jiao, B.; Hou, X.; Li, J., Surface-tension release in PTAA-based inverted perovskite solar cells. *Organic Electronics* **2022,** *100*, 106378.

39. Li, Y.; Wang, B.; Liu, T.; Zeng, Q.; Cao, D.; Pan, H.; Xing, G., Interfacial engineering of PTAA/perovskites for improved crystallinity and hole extraction in inverted perovskite solar cells. *ACS Applied Materials & Interfaces* **2022,** *14* (2), 3284-3292.

40. Zhao, D.; Sexton, M.; Park, H.-Y.; Baure, G.; Nino, J. C.; So, F., High-efficiency solution-processed planar perovskite solar cells with a polymer hole transport layer. *Adv. Energy Mater* **2015,** *5* (6), 1401855.

41. Kayser, L. V.; Lipomi, D. J., Stretchable conductive polymers and composites based on PEDOT and PEDOT: PSS. *Advanced Materials* **2019,** *31* (10), 1806133.

42. Yang, Y.; Zhu, C.; Lin, F.; Chen, T.; Pan, D.; Guo, X., Research progress of inverted perovskite solar cells. *Acta Chimica Sinica* **2019,** *77* (10), 964.

43. Dualeh, A.; Moehl, T.; Nazeeruddin, M. K.; Grätzel, M., Temperature dependence of transport properties of spiro-MeOTAD as a hole transport material in solid-state dye-sensitized solar cells. *Acs Nano* **2013,** *7* (3), 2292-2301.

44. Wang, S.; Huang, Z.; Wang, X.; Li, Y.; Günther, M.; Valenzuela, S.; Parikh, P.; Cabreros, A.; Xiong, W.; Meng, Y. S., Unveiling the role of tBP–LiTFSI complexes in perovskite solar cells. *Journal of the American Chemical Society* **2018,** *140* (48), 16720-16730.

45. Song, Z.; Abate, A.; Watthage, S. C.; Liyanage, G. K.; Phillips, A. B.; Steiner, U.; Graetzel, M.; Heben, M. J., Perovskite solar cell stability in humid air: partially reversible phase transitions in the PbI2-CH3NH3I-H2O system. *Advanced Energy Materials* **2016,** *6* (19), 1600846.

46. Gao, K.; Zhu, Z.; Xu, B.; Jo, S. B.; Kan, Y.; Peng, X.; Jen, A. K. Y., Highly efficient porphyrin-based OPV/perovskite hybrid solar cells with extended photoresponse and high fill factor. *Advanced Materials* **2017,** *29* (47), 1703980.

47. Li, E.; Guo, Y.; Liu, T.; Hu, W.; Wang, N.; He, H.; Lin, H., Preheating-assisted deposition of solution-processed perovskite layer for an efficiency-improved inverted planar composite heterojunction solar cell. *RSC advances* **2016,** *6* (37), 30978-30985.

48. Zuo, C.; Ding, L., Solution-Processed Cu2O and CuO as Hole Transport Materials for Efficient Perovskite Solar Cells. *Small (Weinheim an der Bergstrasse, Germany)* **2015,** *11* (41), 5528-5532.

49. Chatterjee, S.; Pal, A. J., Introducing Cu2O thin films as a hole-transport layer in efficient planar perovskite solar cell structures. *The Journal of Physical Chemistry C* **2016,** *120* (3), 1428-1437.

50. Wang, H.; Yu, Z.; Jiang, X.; Li, J.; Cai, B.; Yang, X.; Sun, L., Efficient and stable inverted planar perovskite solar cells employing CuI as hole-transporting layer prepared by solid–gas transformation. *Energy Technology* **2017,** *5* (10), 1836-1843.

51. Hong, J.; Kim, H.; Hwang, I., Aging-induced light-soaking effects and open-circuit voltage hysteretic behavior of inverted perovskite solar cells incorporating a hole transport metal halide layer via morphology-dependent inflow of iodide ions. *Journal of Materials Chemistry C* **2019,** *7* (5), 1173-1181.

52. Xi, Q.; Gao, G.; Zhou, H.; Zhao, Y.; Wu, C.; Wang, L.; Guo, P.; Xu, J., Highly efficient inverted solar cells based on perovskite grown nanostructures mediated by CuSCN. *Nanoscale* **2017,** *9* (18), 6136-6144.

53. Ye, S.; Sun, W.; Li, Y.; Yan, W.; Peng, H.; Bian, Z.; Liu, Z.; Huang, C., CuSCN-based inverted planar perovskite solar cell with an average PCE of 15.6%. *Nano letters* **2015,** *15* (6), 3723-3728.

54. Jeng, J.-Y.; Chen, K.-C.; Chiang, T.-Y.; Lin, P.-Y.; Tsai, T.-D.; Chang, Y.-C.; Guo, T.-F.; Chen, P.; Wen, T.-C.; Hsu, Y.-J., Nickel oxide electrode interlayer in CH3 NH3 PbI3 perovskite/PCBM planar-heterojunction hybrid solar cells. *Advanced Materials (Deerfield Beach, Fla.)* **2014,** *26* (24), 4107-4113.

55. Kung, P. K.; Li, M. H.; Lin, P. Y.; Chiang, Y. H.; Chan, C. R.; Guo, T. F.; Chen, P., A review of inorganic hole transport materials for perovskite solar cells. *Advanced Materials Interfaces* **2018,** *5* (22), 1800882.

56. Gil, B.; Yun, A. J.; Lee, Y.; Kim, J.; Lee, B.; Park, B., Recent progress in inorganic hole transport materials for efficient and stable perovskite solar cells. *Electronic Materials Letters* **2019,** *15*, 505-524.

57. Arumugam, G. M.; Karunakaran, S. K.; Liu, C.; Zhang, C.; Guo, F.; Wu, S.; Mai, Y., Inorganic hole transport layers in inverted perovskite solar cells: A review. *Nano Select* **2021,** *2* (6), 1081-1116.

58. Shaikh, J.; Shaikh, N.; Mishra, Y. K.; Kanjanaboos, P.; Shewale, P.; Sabale, S.; Praserthdam, S.; Lokhande, C., Low-cost Cu-based inorganic hole transporting materials in perovskite solar cells: Recent progress and state-of-art developments. *Materials Today Chemistry* **2021,** *20*, 100427.

59. Li, X.; Yang, J.; Jiang, Q.; Lai, H.; Li, S.; Tan, Y.; Chen, Y.; Li, S., Perovskite solar cells employing an eco-friendly and low-cost inorganic hole transport layer for enhanced photovoltaic performance and operational stability. *Journal of Materials Chemistry A* **2019,** *7* (12), 7065-7073.

60. Wu, Q.; Xue, C.; Li, Y.; Zhou, P.; Liu, W.; Zhu, J.; Dai, S.; Zhu, C.; Yang, S., Kesterite Cu2ZnSnS4 as a low-cost inorganic hole-transporting material for high-efficiency perovskite solar cells. *ACS applied materials & interfaces* **2015,** *7* (51), 28466-28473.

61. Ponseca Jr, C. S.; Savenije, T. J.; Abdellah, M.; Zheng, K.; Yartsev, A.; Pascher, T. r.; Harlang, T.; Chabera, P.; Pullerits, T.; Stepanov, A., Organometal halide perovskite solar cell materials rationalized: ultrafast charge generation, high and microsecond-long balanced mobilities, and slow recombination. *Journal of the American Chemical Society* **2014,** *136* (14), 5189-5192.

62. Luque, A.; Hegedus, S., *Handbook of photovoltaic science and engineering*. John Wiley & Sons: 2011.

63. Shi, J.; Xu, X.; Zhang, H.; Luo, Y.; Li, D.; Meng, Q., Intrinsic slow charge response in the perovskite solar cells: Electron and ion transport. *Applied Physics Letters* **2015,** *107* (16).

64. Dong, J.; Shi, J.; Li, D.; Luo, Y.; Meng, Q., Controlling the conduction band offset for highly efficient ZnO nanorods based perovskite solar cell. *Applied Physics Letters* **2015,** *107* (7).

65. Shi, J.; Li, Y.; Li, Y.; Li, D.; Luo, Y.; Wu, H.; Meng, Q., From Ultrafast to Ultraslow: Charge-Carrier Dynamics of Perovskite Solar Cells. *Joule* **2018,** *2* (5), 879-901.

66. Mondal, N.; De, A.; Das, S.; Paul, S.; Samanta, A., Ultrafast carrier dynamics of metal halide perovskite nanocrystals and perovskite-composites. *Nanoscale* **2019,** *11* (20), 9796-9818.

67. Ravali, V.; Ghosh, T., Charge carrier dynamics and transient spectral evolutions in lead halide perovskites. *Chemical Communications* **2023,** *59* (94), 13939-13950.

68. Liu, X.; Zeng, P.; Chen, S.; Smith, T. A.; Liu, M., Charge Transfer Dynamics at the Interface of CsPbX3 Perovskite Nanocrystal-Acceptor Complexes: A Femtosecond Transient Absorption Spectroscopy Study. *Laser & Photonics Reviews* **2022,** *16* (12), 2200280.

69. Yettapu, G. R.; Talukdar, D.; Sarkar, S.; Swarnkar, A.; Nag, A.; Ghosh, P.; Mandal, P., Terahertz Conductivity within Colloidal CsPbBr3 Perovskite Nanocrystals: Remarkably High Carrier Mobilities and Large Diffusion Lengths. *Nano Letters* **2016,** *16* (8), 4838-4848.

70. Sarkar, S.; Ravi, V. K.; Banerjee, S.; Yettapu, G. R.; Markad, G. B.; Nag, A.; Mandal, P., Terahertz Spectroscopic Probe of Hot Electron and Hole Transfer from Colloidal CsPbBr3 Perovskite Nanocrystals. *Nano Letters* **2017,** *17* (9), 5402-5407.

71. Wang, M.; Gao, L.; Yu, P.; Wang, Q.; Yu, C.; Zhang, X.; Wang, Y.; Zheng, W.; Zhang, J., Synergetic interfacial passivation, band alignment, and long-term stability with halide-optimized CsPbBrxI3−x nanocrystals for high-efficiency MAPbI3 solar cells. *Journal of Materials Chemistry C* **2022,** *10* (13), 5134-5140.

72. Ponseca Jr, C. S.; Sundström, V., Revealing the ultrafast charge carrier dynamics in organo metal halide perovskite solar cell materials using time resolved THz spectroscopy. *Nanoscale* **2016,** *8* (12), 6249-6257.

73. Swarnkar, A.; Chulliyil, R.; Ravi, V. K.; Irfanullah, M.; Chowdhury, A.; Nag, A., Colloidal CsPbBr3 Perovskite Nanocrystals: Luminescence beyond Traditional Quantum Dots. *Angewandte Chemie International Edition* **2015,** *54* (51), 15424-15428.

74. Wang, L.; Cheng, W.; Gong, H.; Wang, C.; Wang, D.; Tang, K.; Qian, Y., Facile synthesis of nanocrystalline-assembled bundle-like CuO nanostructure with high rate capacities and enhanced cycling stability as an anode material for lithium-ion batteries. *Journal of Materials Chemistry* **2012,** *22* (22), 11297-11302.

75. Liu, X.; Du, H.; Wang, P.; Lim, T.-T.; Sun, X. W., A high-performance UV/visible photodetector of Cu 2 O/ZnO hybrid nanofilms on SWNT-based flexible conducting substrates. *Journal of Materials Chemistry C* **2014,** *2* (44), 9536-9542.

76. Rossi, D.; Wang, H.; Dong, Y.; Qiao, T.; Qian, X.; Son, D. H., Light-Induced Activation of Forbidden Exciton Transition in Strongly Confined Perovskite Quantum Dots. *ACS Nano* **2018,** *12* (12), 12436-12443.

77. Yumoto, G.; Tahara, H.; Kawawaki, T.; Saruyama, M.; Sato, R.; Teranishi, T.; Kanemitsu, Y., Hot Biexciton Effect on Optical Gain in CsPbI3 Perovskite Nanocrystals. *The Journal of Physical Chemistry Letters* **2018,** *9* (9), 2222-2228.

78. Klimov, V. I., Spectral and Dynamical Properties of Multiexcitons in Semiconductor Nanocrystals. *Annual Review of Physical Chemistry* **2007,** *58* (Volume 58, 2007), 635-673.

79. Chung, H.; Jung, S. I.; Kim, H. J.; Cha, W.; Sim, E.; Kim, D.; Koh, W.-K.; Kim, J., Composition-Dependent Hot Carrier Relaxation Dynamics in Cesium Lead Halide (CsPbX3, X=Br and I) Perovskite Nanocrystals. *Angewandte Chemie International Edition* **2017,** *56* (15), 4160-4164.

80. Shen, Q.; Ripolles, T. S.; Even, J.; Ogomi, Y.; Nishinaka, K.; Izuishi, T.; Nakazawa, N.; Zhang, Y.; Ding, C.; Liu, F.; Toyoda, T.; Yoshino, K.; Minemoto, T.; Katayama, K.; Hayase, S., Slow hot carrier cooling in cesium lead iodide perovskites. *Applied Physics Letters* **2017,** *111* (15).

81. Mondal, N.; Samanta, A., Complete ultrafast charge carrier dynamics in photo-excited all-inorganic perovskite nanocrystals (CsPbX3). *Nanoscale* **2017,** *9* (5), 1878-1885.

82. Wang, L.; McCleese, C.; Kovalsky, A.; Zhao, Y.; Burda, C., Femtosecond Time-Resolved Transient Absorption Spectroscopy of CH3NH3PbI3 Perovskite Films: Evidence for Passivation Effect of PbI2. *Journal of the American Chemical Society* **2014,** *136* (35), 12205-12208.

83. Serpetzoglou, E.; Konidakis, I.; Kakavelakis, G.; Maksudov, T.; Kymakis, E.; Stratakis, E., Improved Carrier Transport in Perovskite Solar Cells Probed by Femtosecond Transient Absorption Spectroscopy. *ACS Applied Materials & Interfaces* **2017,** *9* (50), 43910-43919.

84. Zhu, Z.; Ma, J.; Wang, Z.; Mu, C.; Fan, Z.; Du, L.; Bai, Y.; Fan, L.; Yan, H.; Phillips, D. L.; Yang, S., Efficiency Enhancement of Perovskite Solar Cells through Fast Electron Extraction: The Role of Graphene Quantum Dots. *Journal of the American Chemical Society* **2014,** *136* (10), 3760-3763.

85. Piatkowski, P.; Cohen, B.; Ponseca, C. S., Jr.; Salado, M.; Kazim, S.; Ahmad, S.; Sundström, V.; Douhal, A., Unraveling Charge Carriers Generation, Diffusion, and

Recombination in Formamidinium Lead Triiodide Perovskite Polycrystalline Thin Film. *The Journal of Physical Chemistry Letters* **2016,** *7* (1), 204-210.

86. Bernardi, M.; Grossman, J. C., Computer calculations across time and length scales in photovoltaic solar cells. *Energy & Environmental Science* **2016,** *9* (7), 2197-2218.

87. Nienhuys, H.-K.; Sundström, V., Intrinsic complications in the analysis of optical-pump, terahertz probe experiments. *Physical Review B* **2005,** *71* (23), 235110.

88. Shen, Q.; Ogomi, Y.; Chang, J.; Tsukamoto, S.; Kukihara, K.; Oshima, T.; Osada, N.; Yoshino, K.; Katayama, K.; Toyoda, T.; Hayase, S., Charge transfer and recombination at the metal oxide/CH3NH3PbClI2/spiro-OMeTAD interfaces: uncovering the detailed mechanism behind high efficiency solar cells. *Physical Chemistry Chemical Physics* **2014,** *16* (37), 19984-19992.

89. Ponseca, C. S., Jr.; Savenije, T. J.; Abdellah, M.; Zheng, K.; Yartsev, A.; Pascher, T.; Harlang, T.; Chabera, P.; Pullerits, T.; Stepanov, A.; Wolf, J.-P.; Sundström, V., Organometal Halide Perovskite Solar Cell Materials Rationalized: Ultrafast Charge Generation, High and Microsecond-Long Balanced Mobilities, and Slow Recombination. *Journal of the American Chemical Society* **2014,** *136* (14), 5189-5192.

90. Hendry, E.; Koeberg, M.; O'Regan, B.; Bonn, M., Local Field Effects on Electron Transport in Nanostructured TiO2 Revealed by Terahertz Spectroscopy. *Nano Letters* **2006,** *6* (4), 755-759.

Chapter 4

Effect of Cr co-doping on Dielectric Constant and Kerr Nonlinearity in Sn-doped In_2O_3 Nanocrystals

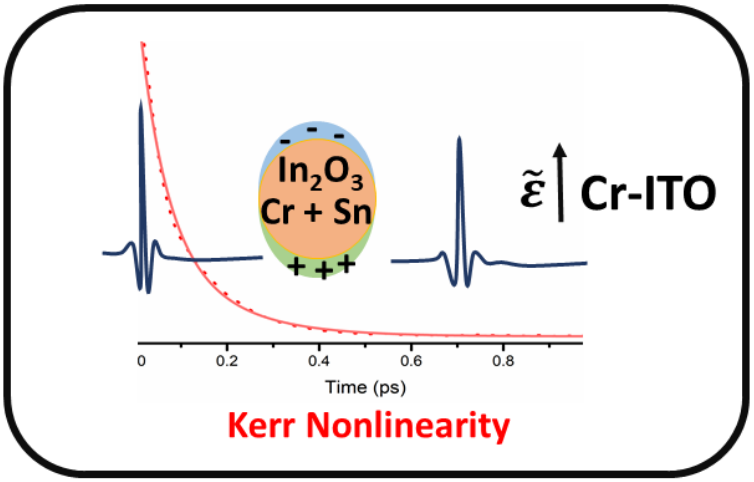

4.1 Introduction

Transparent conducting oxides (TCOs) are highly regarded in optoelectronics for their unique ability to combine electrical conductivity with transparency in the visible light spectrum—two properties that rarely coexist.[1-3] These materials are commonly used as transparent electrodes in devices like solar cells and LEDs. TCOs exhibit high charge density and metallic charge transport due to the abundance of free electrons in their conduction band when doped, such as with indium-doped tin oxide.[4-7]

When researchers synthesise nanocrystals (NCs) of doped TCOs, these NCs demonstrate localised surface plasmon resonance (LSPR), a property typically associated with metal nanocrystals. In TCO NCs, free electrons in the conduction band oscillate in response to specific frequencies of electromagnetic radiation, mimicking the behaviour of metal nanocrystals. However, the LSPR in doped TCO NCs has distinct features.[8-11]

First, the LSPR band can be tuned from the near-infrared (NIR) to the mid-infrared (mid-IR) region by adjusting the free electron density through changes in dopant concentration.[12] Second, co-doping introduces new functionalities, such as the magnetoelectric and magneto-optic properties observed in Fe-Sn co-doped NCs, which arise from interactions between free electrons from Sn^{4+} and magnetic spins from Fe^{3+}.[13] Unlike metal nanocrystals, TCO NCs possess both free electrons and bound excitons.[14] The free electrons, generated through doping, shield the Coulomb interaction between the bound electron-hole pairs (excitons), reducing excitonic features in the absorption spectrum as the dopant concentration increases.[13]

A defining characteristic of TCO NCs is their visible light transparency, which contrasts with metal nanocrystals that typically exhibit strong LSPR bands in the visible spectrum. Instead, TCO NCs exhibit LSPR in the NIR and mid-IR regions, enabling applications in these less-explored spectral ranges.[15-16]

Bharat *et al.* reported Cr-Sn co-doped In_2O_3 nanocrystals (NCs) with an impressive LSPR quality factor (Q-factor) of 7.2.[17] The Q-factor is a measure of LSPR performance, calculated as the ratio of the LSPR peak energy to the full width at half maximum (FWHM) of the band. A higher Q-factor indicates reduced electronic damping, longer plasmon lifetimes, and stronger near-field enhancement,[18-19] making the material highly suitable for applications in photovoltaics and sensing.[20-24]

The free carrier density and the degree of carrier scattering influence the Q-factor. An increase in free carrier density raises the LSPR peak energy, thereby enhancing the Q-factor. However, the FWHM of the LSPR band, which is determined by the level of carrier scattering, can also widen as free carrier density increases. This is because dopant ions, while contributing to higher carrier density, simultaneously act as scattering centres for the charge carriers. Achieving an optimal Q-factor requires balancing these opposing contributors. Enhancing carrier density through heterovalent doping must be carefully managed to minimise scattering effects caused by the dopant ions. This trade-off is crucial for maximising the potential of LSPR materials in advanced applications.[17]

When Cr^{3+} was co-doped with Sn^{4+} in In_2O_3 nanocrystals (NCs), an interesting increase was observed in the LSPR quality factor (Q-factor) with rising Cr^{3+} concentration while keeping Sn^{4+} concentration constant. This finding is intriguing because Cr^{3+} and In^{3+} are isovalent, meaning that substituting In^{3+} with Cr^{3+} should not alter the charge carrier density. Bharat *et al.* attributed the significant improvement in the LSPR Q-factor to changes in NC size. This conclusion was supported by powder X-ray diffraction (PXRD) patterns, which showed narrower peaks, and transmission electron microscopy (TEM) images, which confirmed larger NC sizes. The size increase enhanced the free carrier density while simultaneously reducing carrier scattering.

The observed increase in free carrier density was linked to a rise in the oxygen-tin complexes in the NC core. These complexes generate free electrons upon reduction. In smaller NCs, these complexes are more abundant on the surface, where they are less likely to undergo reduction and produce free electrons. Larger NCs, with more oxygen-tin complexes in their core, facilitate higher free carrier generation, which boosts the LSPR peak energy.[17, 25]

Additionally, a significant reduction in the FWHM of the LSPR band was noted with increased Cr^{3+} concentration, indicating decreased carrier scattering. However, the simultaneous increase in dopant ions in the NC core (enhancing carrier scattering) and the observed reduction in scattering appear contradictory, suggesting that further investigation is needed to explain these results fully.

One possible reason for the observed decrease in carrier scattering could be the change in the dielectric constant of the medium with increasing Cr^{3+} concentration.[26-28] Literature reports suggest that dopant ions can enhance the high-frequency dielectric constant of materials, which reduces the Coulombic interaction between charge carriers and ionised dopants, thereby

influencing the LSPR Q factor.[18-19, 29] A similar mechanism might be at play here, as Cr_2O_3 has a higher static dielectric constant compared to Sn-doped In_2O_3.[28] This increase in the lattice dielectric constant could lead to a reduction in ionic impurity scattering.

To better understand the increase in the LSPR Q factor with Cr^{3+} doping, we employed THz time-domain spectroscopy (THz-TDS). This technique allows direct measurement of the material's frequency-dependent complex dielectric response. We synthesised three samples for the experiments: one with only Sn-doped In_2O_3 and two with Cr-Sn co-doping, maintaining a constant Sn^{4+} concentration while varying the Cr^{3+} concentration. The results revealed an increase in the dielectric constant of the medium with higher Cr^{3+} doping levels, supporting our hypothesis that the enhanced dielectric constant contributes to the observed increase in the LSPR Q factor.

Several studies in the literature have reported the optical Kerr nonlinearity of indium tin oxide (ITO). Zhu and co-workers observed significant optical Kerr nonlinearity in tin-doped indium oxide, where the measured nonlinearity depended on the carrier concentration, increasing with higher free carrier density as Sn doping increased.[30] As discussed, Cr^{3+} doping causes a sharp rise in carrier density along with a notable reduction in carrier scattering. To investigate the impact of carrier density on optical nonlinearity, we conducted femtosecond time-resolved optical Kerr effect (OKE) spectroscopy on the samples. We determined the relaxation time of OKE in the time domain. Interestingly, the slowest relaxation in Kerr nonlinearity was observed in the sample with the highest Cr^{3+} concentration. Optical Kerr nonlinearity is directly relevant to the development of all-optical switching devices. The Kerr nonlinearity can be effectively tuned in these samples by adjusting the carrier concentration through controlled doping. This tunability is highly desirable for optoelectronic applications, particularly in the design of ultrafast all-optical switching devices.[31-32]

We obtained the spectral density from the OKE data using Fourier transform deconvolution,[33], as outlined in Chapter 2 of this thesis. The OKE spectral density, which corresponds to the Bose-Einstein-corrected Raman spectral density, provides insights into Raman-active phonon modes within the crystal lattice.[34] Changes in the spectral density were evident with increasing Cr^{3+} doping, likely due to alterations in the crystal lattice. These changes occur as smaller Cr^{3+} ions (effective ionic radius: 64 pm) replace the larger In^{3+} ions (effective ionic radius: 80 pm), resulting in a contraction of the unit cell. This contraction was confirmed by the shift of diffraction peaks to higher 2θ values with increasing Cr^{3+} concentration. A detailed line shape

analysis of the spectral density revealed the composition of vibrational modes, offering more profound insights into the underlying physics of the system.[35]

4.2 Experimental Section

Dr. Bharat Tandon from Prof. Angshuman Nag's research group at IISER Pune synthesised and characterised all three samples used in this experiment. The samples included one containing 10% Sn-doped In_2O_3 nanocrystals (NCs) and two co-doped samples with a fixed 10% Sn concentration: one with 10% Cr and 10% Sn, and the other with 20% Cr and 10% Sn. The synthesis followed a previously reported method using a standard Schlenk line setup.[17] Precursors of indium, chromium, and tin were measured in specific proportions to achieve the desired NC composition. For instance, to prepare 10% Cr and 10% Sn-doped In_2O_3 NCs, 1.2 mmol of indium(III) acetylacetonate, 0.15 mmol of tin(IV) bis(acetylacetonate) dichloride, and 0.15 mmol of chromium(III) acetylacetonate were combined in 10 mL of oleylamine. The mixture was degassed at 100°C under vacuum and then heated to 250°C under a nitrogen atmosphere. After maintaining the reaction at 250°C for 5 hours, the mixture was cooled to room temperature. The NCs were purified using methanol as an antisolvent, followed by centrifugation at 6,000 rpm for 7 minutes. Finally, the purified NCs were redispersed in nonpolar solvents such as tetrachloroethylene, hexane, or toluene.

Table 1. The elemental composition of Cr-Sn co-doped In_2O_3 NCs was obtained using energy-dispersive X-ray analysis (EDX) and inductively coupled plasma-optical emission spectroscopy (ICP-OES) compared with the precursor ratios used during synthesis.

Sample	**In:Sn:Cr**		
	Precursors Ratio	**EDAX Composition**	**ICP-OES Composition**
10 % Sn doped In_2O_3 NC	90 : 10 : 0	91.3 : 8.7 : 0	93.3 : 6.7 : 0
10 % Cr-10 % Sn doped In_2O_3 NC	80 : 10 : 10	88.9 : 8.8 : 8.8	84.0 : 6.6 : 9.4
20 % Cr-10 % Sn doped In_2O_3 NC	70 : 10 : 20	73 : 9.0 : 18.0	69.6 : 6.6 : 23.8

Figure 1 illustrates the XRD patterns of Cr-doped In_2O_3 NCs. As the Cr doping concentration increases, a noticeable shift in the diffraction peak toward higher 2θ values is observed (Figure 1b). This shift confirms successful lattice doping, as the Cr^{3+} ion (60 pm) replacing In^{3+} (80

pm) has a smaller effective ionic radius. Consequently, the reduction in unit cell size leads to the observed shift.

The final elemental composition of the NCs did not precisely match the precursor ratios used during synthesis. The actual composition was determined using energy-dispersive X-ray analysis (EDX) and inductively coupled plasma optical emission spectroscopy (ICP-OES). Table 1 provides the precursor ratios used and the measured compositions obtained from these techniques for all three samples. Despite the differences in elemental composition, we have used sample names based on the precursor ratios used during synthesis.

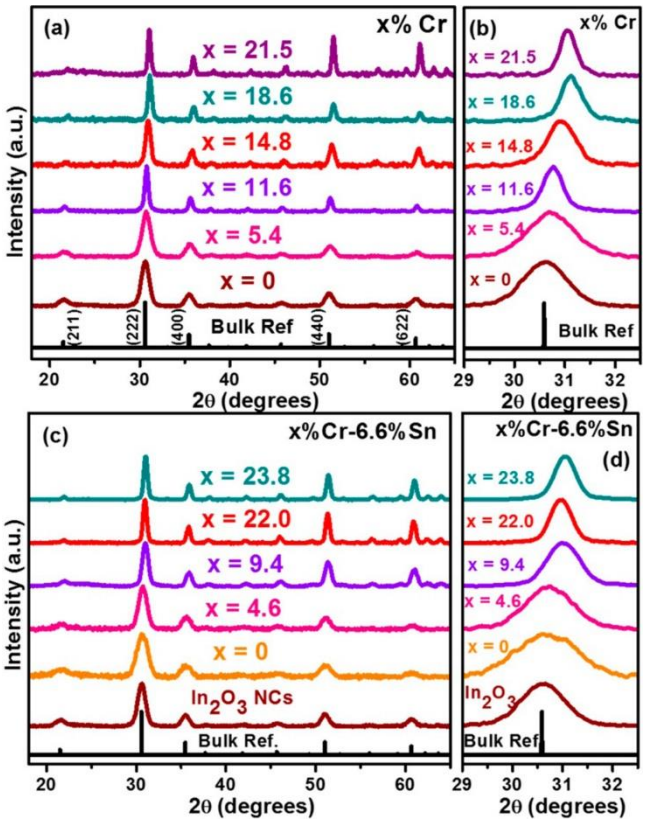

Figure 1. Powder XRD pattern for **(a, b)** Cr-doped In_2O_3 NCs and **(c, d)** Cr-Sn co-doped In_2O_3 NCs with reference pattern for bulk In_2O_3 cubic bixbyite structure. The figure is used with permission from ref 17.

Figure 1d showed the XRD patterns for Cr-Sn co-doped In_2O_3 NCs, which exhibited a shift in the diffraction peak at 30.6° (Figure 1d). Along with this shift, a reduction in the linewidth of the diffraction peak was observed, indicating an increase in NC size with higher Cr doping. The larger NC size resulted in more Sn atoms being incorporated into the core rather than the surface of the nanocrystals. Within the bulk, Sn atoms formed a neutral complex ($O_i^{2-}2Sn_{In}^{+}$)

which released free electrons upon reduction as described by the following equation 1.[25] In contrast, Sn atoms on the surface formed complexes with oxygen that were less likely to undergo reduction. As previously mentioned, the increase in the number of such Sn-O complexes within the bulk enhanced the carrier density.[25, 36-38]

$$(O_i^{2-}2Sn_{In}^{+})^{x} \rightarrow 2Sn_{In}^{+} + 2e' + \frac{1}{2}O_2 \quad (1)$$

Here ($O_i^{2-}2Sn_{In}^{+}$) represents the neutral complex formed by 2 Sn^{4+} ions by replacing the In^{3+} ion in the lattice of In_2O_3 with an interstitial oxygen. Sn_{In}^{+} represents the positive charge left when Sn^{4+} replaced the In^{3+} ion at the lattice site.

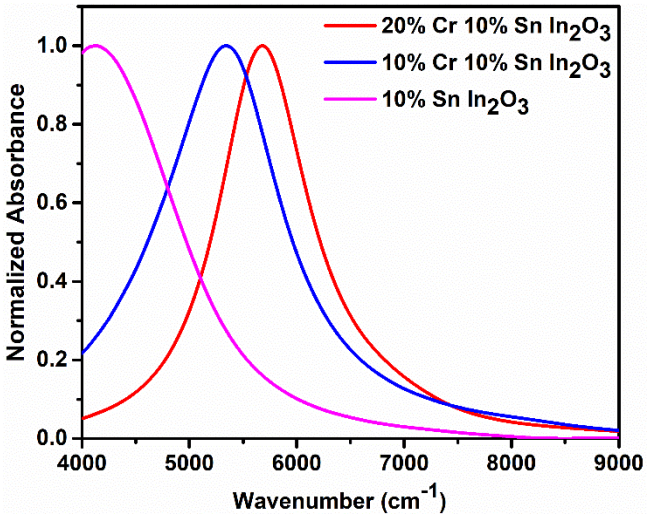

Figure 2. The normalized absorbance versus wavenumber plot represents the LSPR characteristics of 20% Cr 10% Sn In_2O_3 (red), 10% Cr 10% Sn In_2O_3 (blue), and 10% Sn In_2O_3 (magenta). The plot demonstrates the shift in the LSPR peak toward higher energy and decrease in FWHM with increasing Cr doping concentration.

Figure 2 displayed the normalized absorbance versus wavenumber for the three samples - 20% Cr 10% Sn In_2O_3, 10% Cr 10% Sn In_2O_3, and 10% Sn In_2O_3 in the NIR range. A shift in the LSPR peak position toward higher energy was observed with increased Cr concentration in the samples. This shift clearly indicated an increase in charge carrier density in the NCs with Cr doping. Additionally, a significant reduction in the FWHM was observed as Cr doping increased, highlighting a decrease in carrier scattering. As mentioned earlier, a change in the dielectric constant could be a possible factor contributing to this reduction in carrier scattering. THz time-domain spectroscopy (THz-TDS) was performed on these samples to investigate further.

4.3 THz Time-domain spectroscopy (THz-TDS) of Cr-Sn co-doped In_2O_3 NCs

The time-domain THz experiments were conducted in transmission mode on two Cr-Sn co-doped In_2O_3 nanoparticle nanocrystal samples. The NCs were dispersed in 2,2,4,4,6,8,8-Heptamethylnonane (HMN), an aliphatic hydrocarbon known for its transparency in the THz frequency range. These NC solutions were injected into a demountable liquid sample cell (Harrick Scientific Products, DLC-M25), as shown in Figure 3a. The cell was equipped with two high-resistivity silicon windows (2 mm thick, 1-inch diameter) separated by a 750-micron Teflon spacer. The concentrations of NCs in the solutions were specified as 38.04 mg/ml for 20% Cr 10% Sn In_2O_3 and 35.83 mg/ml for 10% Cr 10% Sn In_2O_3.

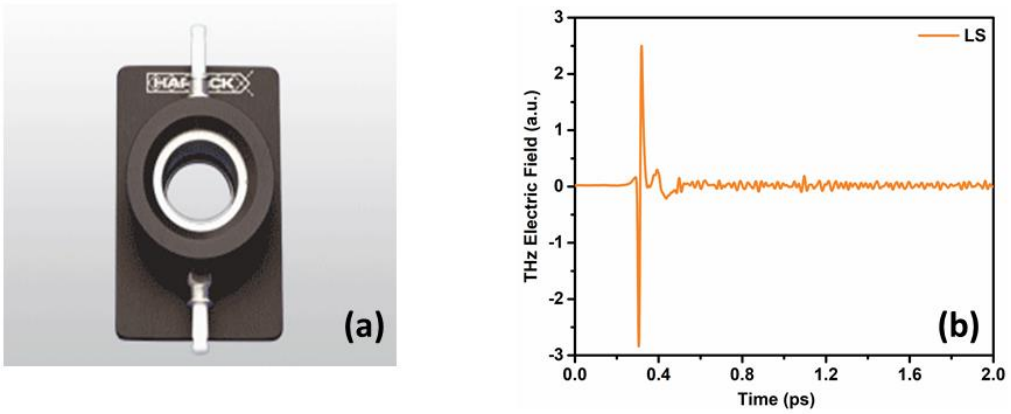

Figure 3. (a) Demountable liquid cell (Harrick Scientific Products, DLC-M25) used for the THz-TDS measurements of the solutions of all three samples in HMN. **(b)** Time-domain THz waveform transmitted through air, referred to as the light source (LS).

Figure 3b displays the time-domain THz waveform measured through air, which served as the light source for the experiment. The THz pulses were generated using air plasma and detected through the air-biased coherent detection method, as detailed in Chapter 2. During the experiments, the sample cell was positioned at the sample location between two parabolic mirrors (Figure 3, Chapter 2), precisely at the focal point of both parabolic mirrors.

First, the THz signal transmitted through the empty sample cell, referred to as the reference signal $E_{cell}(t)$ was recorded. Subsequently, the THz signal transmitted through the sample cell filled with the NC solution, $E_{sam}(t)$, was measured. The average of multiple such scans was

used for the final analysis to ensure a satisfactory signal-to-noise ratio. Figure 4a illustrates the THz electric field waveforms transmitted through the empty sample cell, the cell filled with HMN, and the cell filled with Cr-Sn co-doped NC solutions in HMN. Figure 4b shows the phase shift and amplitude change observed for the Cr-Sn co-doped In_2O_3 NC solution compared to HMN. Notably, the changes are more pronounced for the sample with a higher Cr doping concentration, specifically 20% Cr and 10% Sn in In_2O_3 NCs. By analysing the modulation of the THz electric field waveform caused by the interaction with the sample relative to the reference (empty sample cell), the sample's optical properties, such as the absorption coefficient and refractive index, can be determined.

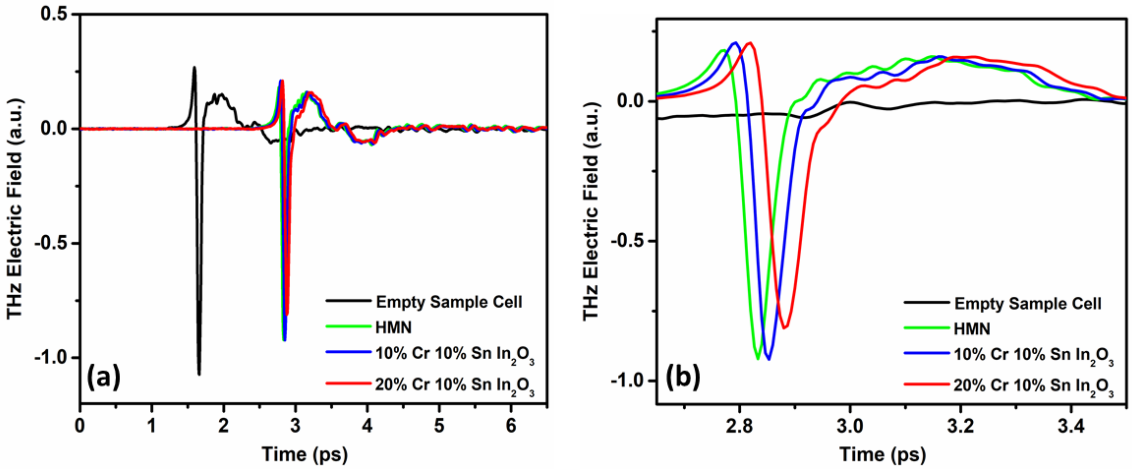

Figure 4. (a) The THz electric field waveforms transmitted through an empty sample cell (black), sample cell containing HMN (green), and sample cells containing solutions of 10% Cr 10% Sn (blue) and 20% Cr 10% Sn (red) co-doped In_2O_3 NCs in HMN. **(b)** A zoomed-in view highlights changes in the phase and amplitude of the THz electric field waveforms after interacting with the solutions of Cr-Sn co-doped In_2O_3 NCs.

The shape and amplitude of the THz electric field $E_{sam}(t)$, after interacting with the sample cell filled with HMN or NC solution, change relative to the electric field transmitted through the empty sample cell $E_{cell}(t)$. By calculating the ratio of the complex Fourier transforms of $E_{sam}(t)$ and $E_{cell}(t)$, the complex refractive index of the sample can be determined. The Exact Blackman windowing function was applied to the time-domain signal before performing the Fourier transformation.

$$\frac{fE_{sam}(t)}{fE_{cell}(t)} = \frac{\tilde{E}_{sam}(\omega)}{\tilde{E}_{cell}(\omega)} = \frac{E_s(\omega)}{E_r(\omega)} e^{i\varphi(\omega)} = \sqrt{T(\omega)} e^{i\varphi(\omega)} \quad (2)$$

The power transmittance $T(\omega)$ and the relative phase $\varphi(\omega)$ were used to determine the complex refractive index of the sample. This was achieved by applying an iterative method, as described in the work of Nashima et al. From this, we obtained the frequency-dependent complex dielectric functions of the sample using the following equations-

The complex refractive index $\tilde{n}(\omega)$ is defines as-

$$\tilde{n}(\omega) = n(\omega) + ik(\omega) \tag{3}$$

Where, $$n(\omega) = 1 + \frac{c}{2\pi\omega d}\varphi(\omega) \tag{4}$$

And, $$k(\omega) = \frac{\lambda\alpha(\omega)}{4\pi} = \frac{c\alpha(\omega)}{2\omega} \tag{5}$$

$$\alpha(\omega) = -\frac{1}{d}\ln\left(\frac{E_{ref}(\omega)}{E_{sample}(\omega)}\right)^2 \tag{6}$$

Here $k(\omega)$ is Extinction coefficient, $\alpha(\omega)$ is absorption coefficient, λ is the wavelength of light, and c is the speed of light in vacuum. The complex dielectric function is given as

$$\tilde{\varepsilon}(\omega) = \varepsilon'(\omega) + i\varepsilon''(\omega) \tag{7}$$

It is related to the complex refractive index as

$$\varepsilon'(\omega) = n^2(\omega) - k^2(\omega) \tag{8}$$

and, $$\varepsilon''(\omega) = 2n(\omega)\,k(\omega) \tag{9}$$

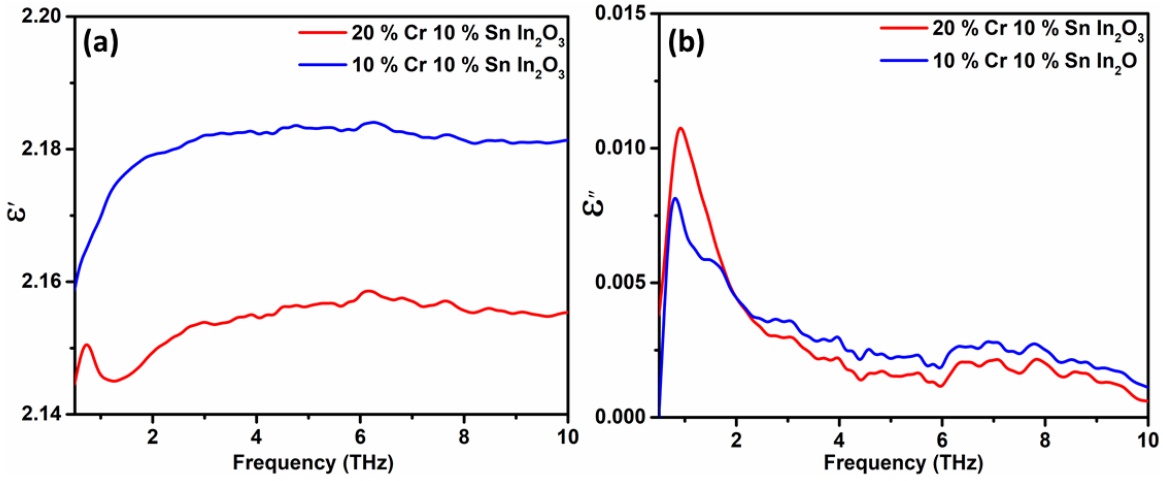

Figure 5. (a) Real and **(b)** imaginary parts of the frequency dependent dielectric functions of 10% Cr 10% Sn (blue) and 20% Cr 10% Sn (red) co-doped In_2O_3 NCs solutions in HMN.

Figures 5a and 5b show the real and imaginary components of the complex dielectric function, respectively, for the two Cr-Sn co-doped In_2O_3 NC solutions in HMN. However, these values represent the dielectric function of the composite system, i.e., NC particles embedded in the host material, which in this case is HMN. The simple linear effective medium theory was applied to extract the intrinsic dielectric response of the doped NC particles. This approach separates the contribution of the NCs from that of the host material. The dielectric response from the NCs was obtained using the relation-

$$\varepsilon = f\varepsilon_p + (1-f)\varepsilon_h \tag{10}$$

where f is the volume fraction, ε_p dielectric function of the NCs, and ε_h dielectric function of the host obtained from the THz-TDS experiment.

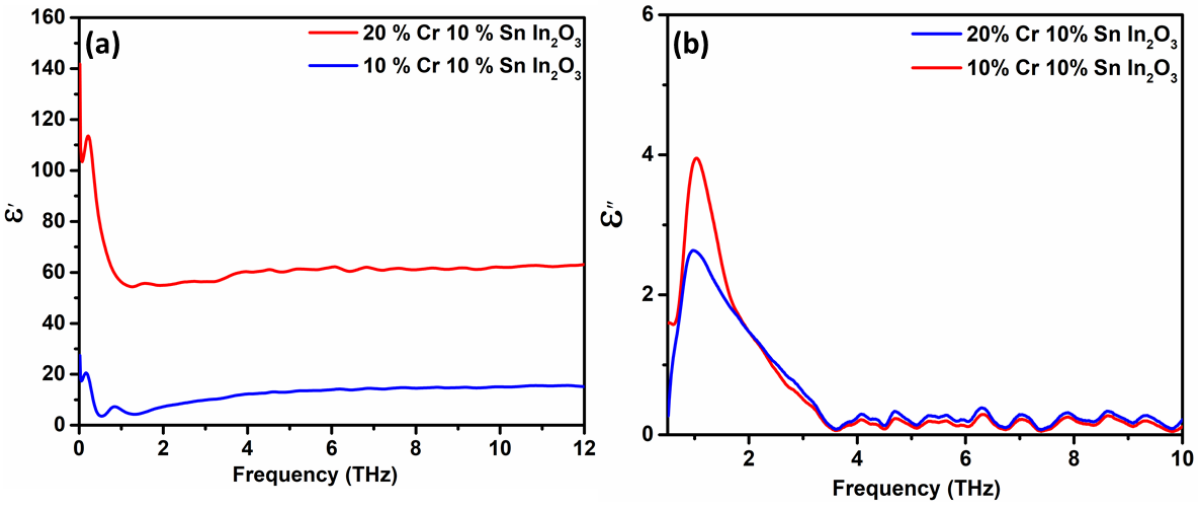

Figure 6. (a) Real and **(b)** imaginary parts of the frequency-dependent dielectric functions of 10% Cr 10% Sn (blue) and 20% Cr 10% Sn (red) co-doped In_2O_3 NCs obtained by applying simple effective medium theory.

Figures 6a and 6b illustrate the real and imaginary components of the complex dielectric function for the Cr-Sn co-doped In_2O_3 NCs, excluding the contributions from the host material. The results show a noticeable increase in the frequency-dependent real dielectric function with higher Cr doping levels. Specifically, the 20% Cr and 10% Sn co-doped In_2O_3 NCs exhibit a higher dielectric constant compared to the 10% Cr and 10% Sn co-doped In_2O_3 NCs. This increase in the dielectric constant may be attributed to reduced ionic impurity scattering with higher Cr doping, which could contribute to an improved Q-factor value for the material.

4.4 Optical Kerr effect (OKE) spectroscopy of Cr-Sn co-doped In_2O_3 NCs

Several studies in the literature have reported the optical Kerr nonlinearity in doped transparent metal oxides. For instance, Zhu et al. observed a carrier concentration-dependent optical Kerr nonlinearity in indium-doped tin oxide films, while a strong optical Kerr effect was reported for indium-doped ZnO nanowires. The ability to tailor Kerr nonlinearity through carrier concentration is highly desirable for ultrafast optical switching applications in optoelectronic devices.[39-40]

In this study, the Kerr nonlinearity of Cr-Sn co-doped In_2O_3 NCs was investigated following excitation with an 800 nm femtosecond pulse. The results showed that the decay of Kerr nonlinearity depended on the carrier concentration of the sample. Notably, the slowest decay was observed in the sample with the highest Cr concentration, specifically the 20% Cr and 10% Sn co-doped In_2O_3 NCs.

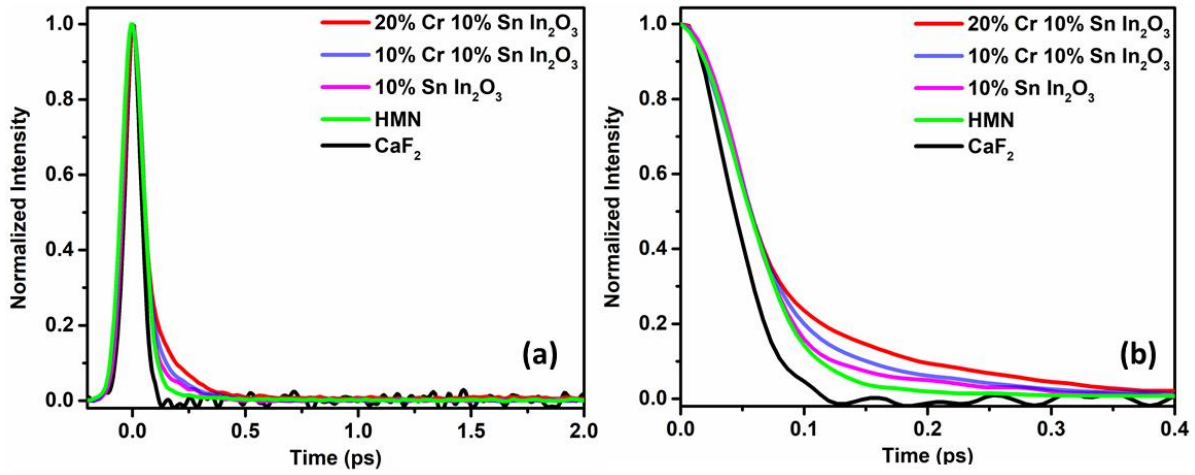

Figure 7. (a) OKE time transients obtained for 10% Cr 10% Sn (blue) and 20% Cr 10% Sn (red) co-doped In_2O_3 NC solution, 10 % Sn doped In_2O_3 NC solution (magenta), HMN (green) and CaF_2 (black) following 800 nm pump excitation. **(b)** OKE transients at early pump-probe delay highlighting the slowest decay for the sample with maximum Cr doping (red).

The Optical Kerr Effect (OKE) experiment was conducted on the samples using our custom-built setup, the details of which, along with the data analysis process, are provided in Chapter 2. A non-resonant 800 nm pump pulse with an average power of less than 1 mW was used to excite the samples. This pump induced transient birefringence in the samples, which was subsequently probed using an optically delayed probe pulse, polarized at 45° relative to the polarization of the pump pulse. Figure 7a shows the OKE time transients for all the samples,

highlighting the birefringence decay over time. Similar solutions of NCs dispersed in HMN were prepared and filled into a 1 mm thick quartz cuvette for the measurements. Figure 7b, with the early pump-probe delay, clearly demonstrates that the slowest decay was observed for the 20% Cr and 10% Sn co-doped In_2O_3 NCs. This indicates a significant influence of Cr concentration on the decay dynamics of birefringence.

The transient OKE signals were fitted using a bi-exponential function to analyze the dependence of cubic nonlinearity on Cr doping concentration and evaluate its relaxation time. Figure 8 illustrates the OKE transients along with their bi-exponential fits with R^2 value greater than 0.99 for all three samples. The fitting parameters for each sample are summarized in Table 2.

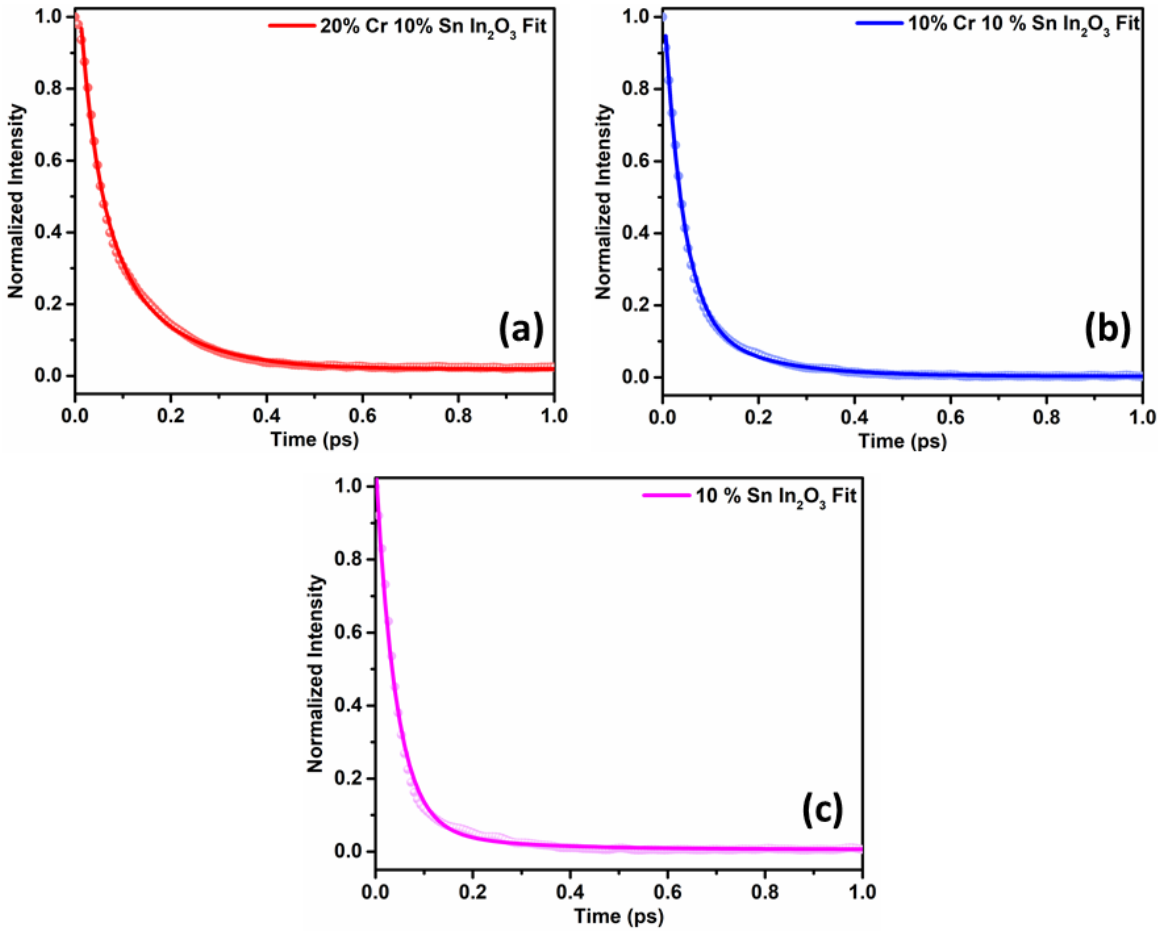

Figure 8. OKE transients as a function of pump-probe delay following 800 nm pump excitation fitted with bi-exponential function for **(a)** 20% Cr 10% Sn (red) and **(b)** 10% Cr 10% Sn (red) co-doped In_2O_3 NC solution and **(c)** 10 % Sn doped In_2O_3 NC solution (magenta) in HMN. The symbol represents experiment data points, and solid lines represent the bi-exponential fit.

The faster component, τ_1, is attributed to the autocorrelation of the laser pulse, while the slower component, τ_2, corresponds to the recovery time of the excited electrons in the sample. Among the three samples, the 20% Cr and 10% Sn co-doped In_2O_3 NCs exhibited the largest contribution to τ_2 with the longest Kerr nonlinearity decay time. This result highlights the significant influence of higher Cr doping on the material's relaxation dynamics and nonlinear optical response.

Table 2. Parameters obtained by fitting OKE transient to a bi-exponential function.

Sample	a_1	τ_1 (ps)	a_2	τ_2 (ps)	χ^2
20% Cr 10% Sn In_2O_3	0.445 (0.01)	0.354 (0.001)	0.563 (0.01)	0.126 (0.002)	0.997
10% Cr 10% Sn In_2O_3	0.836 (0.01)	0.0395 (0.002)	0.198 (0.01)	0.158 (0.002)	0.998
10% Sn In_2O_3	0.993 (0.002)	0.0414 (0.0005)	0.068 (0.01)	0.191 (0.02)	0.994

In the time domain, around zero delay time, a sharp peak corresponding to the laser pulses is observed. This feature, known as the electronic response, arises from the intense electric field of the laser pulse distorting the electron clouds in the sample molecules. It is attributed to the electronic hyperpolarizability of the material. Following this, the decay is referred to as the nuclear response, which comprises distinct components. In the first few picoseconds, a gently decaying portion originates from the coherent decay of Raman-active, collective intermolecular motions excited by the pump pulse.[34]

As discussed in Chapter 2, Fourier transform deconvolution can be used to extract Bose-Einstein-corrected Raman spectral densities for the samples.[33] The Raman spectral density provides comprehensive information about the structural dynamics of a given system. It encapsulates details about the vibrational modes, including intra- and intermolecular interactions, and offers insights into the collective motions of molecules within the material.[41]

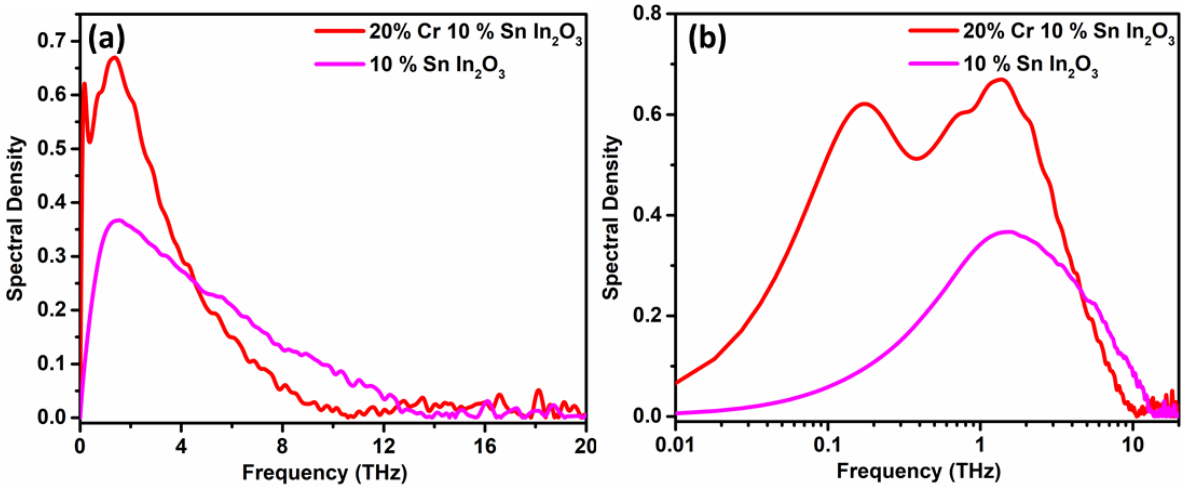

Figure 9. (a) Spectral density response for 20% Cr 10% Sn co-doped In_2O_3 NCs (red) and 10 % Sn doped In_2O_3 NC solution (magenta). **(b)** Spectral density response in the frequency range of 10 GHz to 10 THz highlighting the generation of new Raman active modes in low-frequency region with Cr codoping in the Sn-doped In_2O_3 NCs.

Figure 9a shows the spectral densities for the 20% Cr and 10% Sn co-doped In_2O_3 NCs and 10% Sn In_2O_3 NCs without Cr doping, within the frequency range of 0 to 20 THz. These results highlight the influence of Cr doping on the vibrational dynamics of the material. Figure 9b highlights a new mode emerging at a lower frequency of 170 GHz in the Cr-Sn co-doped sample. This mode is likely attributed to the generation of a new optical phonon mode in the medium due to Cr doping, as optical phonon modes typically resonate in this frequency range.

As discussed, the effective ionic radius of the Cr^{3+} ion is smaller than that of the In^{3+} ion, leading to a reduction in the unit cell size. High Cr doping levels (greater than 20%) are causing significant changes in the crystal lattice structure. These changes in the crystal lattice are further supported by the observed peak shifts in the XRD pattern with increasing Cr doping concentrations. While detailed theoretical calculations are necessary to precisely determine the origin of this new mode, it can be inferred that high Cr doping alters the crystal lattice, resulting in the appearance of this low-energy optical phonon mode. Furthermore, this phonon mode present in the co-doped sample could interact with free electrons in the system, potentially influencing the localised surface plasmon resonance (LSPR) quality factor of the sample.

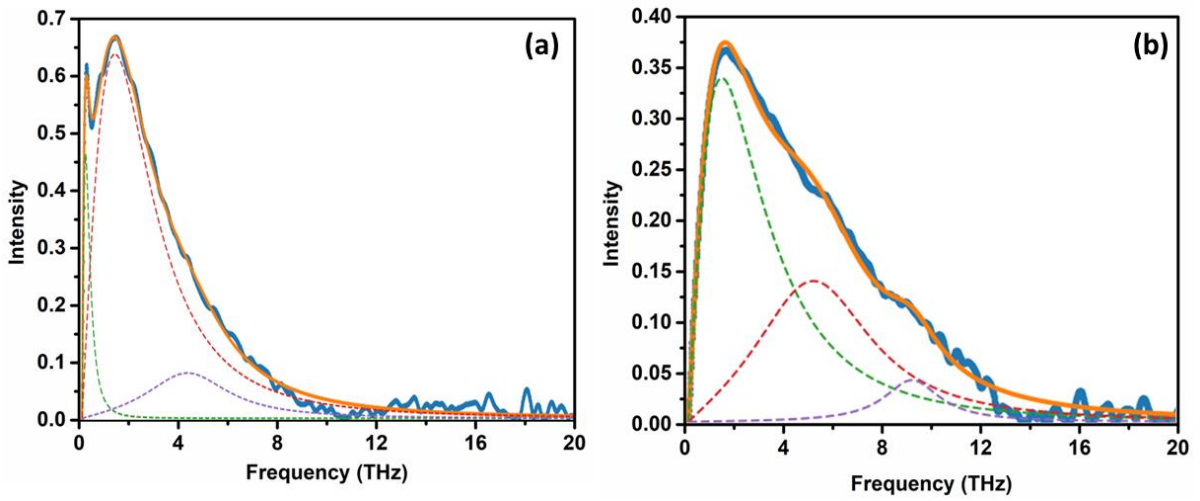

Figure 10. Spectral density in the range of 0 to 20 THz fitted with the sum of three Brownian oscillators for **(a)** 20% Cr 10% Sn co-doped In_2O_3 NCs and **(b)** 10 % Sn doped In_2O_3 NCs. The solid blue line represents the experimental data, the orange line represents the fit to the experimental data, and the dotted green, red, and purple lines show the contributions of the individual Brownian oscillators.

A detailed line shape analysis was performed to understand the vibrational mode compositions of the accessed frequencies. The spectral density was fitted with a sum of three Brownian oscillators, represented by the following equation:[35]

$$I_{BO} = \sum_i \left(\frac{A_{BO,i}\ \gamma_{BO,i}\ \omega}{(\omega_{BO,i}^2 - \omega^2)^2 + \gamma_{BO,i}^2 \omega^2} \right) \quad (11)$$

where $A_{BO,i}$, $\gamma_{BO,i}$ and $\omega_{BO,i}$are the amplitude, damping parameter, and characteristic frequency, respectively, of the ith Brownian oscillator. This model allows us to capture the contributions of different vibrational modes within the system by decomposing the spectral density into distinct oscillator components.

Table 3. Parameters obtained from fitting the spectral density obtained for 10% Sn doped In_2O_3 NCs with the sum of three Brownian oscillators. (R^2 = 0.994)

	B1	**B2**	**B3**
A_{BO}	26.9	27.25	2.93
ω_{BO} (THz)	2.76	5.88	9.29
γ_{BO}	6.35	5.96	2.77

Table 4. . Parameters obtained by fitting the spectral density obtained for 20% Cr 10% Sn doped In_2O_3 NCs with the sum of three Brownian oscillators. (R^2 = 0.996)

	B1	**B2**	**B3**
A_{BO}	0.03	27.98	6.11
ω_{BO} (THz)	0.26	2.38	4.74
γ_{BO}	0.58	4.91	4.12

Figure 10 presents the spectral density fitted with the sum of three Brownian oscillators for both the 10% Sn In_2O_3 NCs and 20% Cr 10% Sn In_2O_3 NCs. Brownian oscillators are typically employed in the line shape analysis to fit frequencies ranging from a few tens of GHz to a few THz.[42-43] For the 10% Sn In_2O_3 NCs, the spectral density was fitted with three oscillators corresponding to peaks at 2.7, 5.8, and 9.29 THz, assigned as B1, B2, and B3, respectively. Similarly, three oscillators were used for the Cr-Sn co-doped sample, corresponding to peaks at 0.26, 2.38, and 4.7 THz, also assigned as B1, B2, and B3.

The parameters associated with the Brownian oscillators for both samples are provided in Tables 3 and 4. The significant lattice changes induced by high Cr doping concentrations result in shifts in the vibrational modes to lower frequencies, most notably the appearance of a strong peak at 0.26 THz. These changes in vibrational modes could be associated with the generation of new phonon modes in the Cr-doped samples. The pronounced changes in vibrational dynamics caused by high Cr doping may directly impact the localized surface plasmon resonance (LSPR) properties of the sample, influencing its optical and electronic behaviour.

4.5 Conclusions

In conclusion, we investigated the changes in the complex dielectric function of Cr-Sn co-doped In_2O_3 NCs and observed that the sample with the highest Cr doping concentration exhibited the highest dielectric constant. This increase in the dielectric constant likely contributes to reduced ionic impurity scattering, as a higher dielectric constant decreases the Coulombic interaction between ionic dopants and free carriers.

The Kerr nonlinearity measurements revealed the slowest Kerr nonlinearity decay for the sample with the maximum Cr concentration, with the relaxation time increasing as the Cr doping concentration increased. This demonstrates that the Kerr nonlinearity in these materials can be tailored by adjusting the doping concentration, which effectively alters the carrier concentration. These properties make Cr-Sn co-doped In_2O_3 NCs a promising candidate for ultrafast optical switching applications, as the recovery time of the optical Kerr effect (OKE) for all samples was found to be less than one ps.

The spectral density derived from the OKE experiments indicated a shift of vibrational modes toward lower frequencies with the introduction of Cr doping. Furthermore, a pronounced phonon mode in the GHz range was identified in the Cr-Sn co-doped samples. The significant changes in vibrational dynamics, including the emergence of a low-energy optical phonon mode due to high Cr doping, may directly impact the localised surface plasmon resonance (LSPR) properties of the sample.

4.6. References

1. Afre, R. A.; Sharma, N.; Sharon, M.; Sharon, M., Transparent Conducting Oxide Films for Various Applications: A Review. *REVIEWS ON ADVANCED MATERIALS SCIENCE* **2018,** *53* (1), 79-89.

2. Liu, H.; Avrutin, V.; Izyumskaya, N.; Özgür, Ü.; Morkoç, H., Transparent conducting oxides for electrode applications in light emitting and absorbing devices. *Superlattices and Microstructures* **2010,** *48* (5), 458-484.

3. Morales-Masis, M.; De Wolf, S.; Woods-Robinson, R.; Ager, J. W.; Ballif, C., Transparent Electrodes for Efficient Optoelectronics. *Advanced Electronic Materials* **2017,** *3* (5), 1600529.

4. Habis, C.; Zaraket, J.; Aillerie, M. In *Transparent Conductive Oxides. Part I. General Review of Structural, Electrical and Optical Properties of TCOs Related to the Growth Techniques, Materials and Dopants*, Defect and Diffusion Forum, Trans Tech Publ: 2022; pp 243-256.

5. Dey, K. High mobility and highly transparent cerium doped indium oxide films deposited by magnetron sputtering for photovoltaic applications. National University of Singapore (Singapore), 2018.

6. Aliyu, K. I.; Ali, A. H.; Nayan, N., Indium tin oxide thin films: an ideal transparent and conductive oxides contact for solar cells application. **2020**.

7. Dixon, S. C.; Scanlon, D. O.; Carmalt, C. J.; Parkin, I. P., n-Type doped transparent conducting binary oxides: an overview. *Journal of Materials Chemistry C* **2016,** *4* (29), 6946-6961.

8. Agrawal, A.; Johns, R. W.; Milliron, D. J., Control of localized surface plasmon resonances in metal oxide nanocrystals. *Annual Review of Materials Research* **2017,** *47* (1), 1-31.

9. Tandon, B.; Agrawal, A.; Heo, S.; Milliron, D. J., Competition between depletion effects and coupling in the plasmon modulation of doped metal oxide nanocrystals. *Nano Letters* **2019,** *19* (3), 2012-2019.

10. Tandon, B.; Ghosh, S.; Milliron, D. J., Dopant selection strategy for high-quality factor localized surface plasmon resonance from doped metal oxide nanocrystals. *Chemistry of Materials* **2019,** *31* (18), 7752-7760.

11. Liu, X.; Swihart, M. T., Heavily-doped colloidal semiconductor and metal oxide nanocrystals: an emerging new class of plasmonic nanomaterials. *Chemical Society Reviews* **2014,** *43* (11), 3908-3920.

12. Wang, T.; Radovanovic, P. V., Free electron concentration in colloidal indium tin oxide nanocrystals determined by their size and structure. *The Journal of Physical Chemistry C* **2011,** *115* (2), 406-413.

13. Tandon, B.; Shanker, G. S.; Nag, A., Multifunctional Sn-and Fe-codoped In2O3 colloidal nanocrystals: plasmonics and magnetism. *The journal of physical chemistry letters* **2014,** *5* (13), 2306-2311.

14. Shanker, G. S.; Tandon, B.; Shibata, T.; Chattopadhyay, S.; Nag, A., Doping controls plasmonics, electrical conductivity, and carrier-mediated magnetic coupling in Fe and Sn codoped In2O3 nanocrystals: local structure is the key. *Chemistry of Materials* **2015,** *27* (3), 892-900.

15. Pradhan, N.; Das Adhikari, S.; Nag, A.; Sarma, D., Luminescence, plasmonic, and magnetic properties of doped semiconductor nanocrystals. *Angewandte Chemie International Edition* **2017,** *56* (25), 7038-7054.

16. Agrawal, A.; Cho, S. H.; Zandi, O.; Ghosh, S.; Johns, R. W.; Milliron, D. J., Localized Surface Plasmon Resonance in Semiconductor Nanocrystals. *Chemical Reviews* **2018,** *118* (6), 3121-3207.

17. Tandon, B.; Yadav, A.; Khurana, D.; Reddy, P.; Santra, P. K.; Nag, A., Size-Induced Enhancement of Carrier Density, LSPR Quality Factor, and Carrier Mobility in Cr–Sn Doped In2O3 Nanocrystals. *Chemistry of Materials* **2017,** *29* (21), 9360-9368.

18. Lounis, S. D.; Runnerstrom, E. L.; Llordés, A.; Milliron, D. J., Defect Chemistry and Plasmon Physics of Colloidal Metal Oxide Nanocrystals. *The Journal of Physical Chemistry Letters* **2014,** *5* (9), 1564-1574.

19. Gordon, T. R.; Paik, T.; Klein, D. R.; Naik, G. V.; Caglayan, H.; Boltasseva, A.; Murray, C. B., Shape-Dependent Plasmonic Response and Directed Self-Assembly in a New Semiconductor Building Block, Indium-Doped Cadmium Oxide (ICO). *Nano Letters* **2013,** *13* (6), 2857-2863.

20. Liu, X.; Lee, C.; Law, W.-C.; Zhu, D.; Liu, M.; Jeon, M.; Kim, J.; Prasad, P. N.; Kim, C.; Swihart, M. T., Au–Cu2–xSe Heterodimer Nanoparticles with Broad Localized Surface Plasmon Resonance as Contrast Agents for Deep Tissue Imaging. *Nano Letters* **2013,** *13* (9), 4333-4339.

21. Verellen, N.; Van Dorpe, P.; Huang, C.; Lodewijks, K.; Vandenbosch, G. A. E.; Lagae, L.; Moshchalkov, V. V., Plasmon Line Shaping Using Nanocrosses for High Sensitivity Localized Surface Plasmon Resonance Sensing. *Nano Letters* **2011,** *11* (2), 391-397.

22. Sannomiya, T.; Hafner, C.; Voros, J., In situ Sensing of Single Binding Events by Localized Surface Plasmon Resonance. *Nano Letters* **2008,** *8* (10), 3450-3455.

23. Jain, P. K.; Huang, X.; El-Sayed, I. H.; El-Sayed, M. A., Noble Metals on the Nanoscale: Optical and Photothermal Properties and Some Applications in Imaging, Sensing, Biology, and Medicine. *Accounts of Chemical Research* **2008,** *41* (12), 1578-1586.

24. Haes, A. J.; Hall, W. P.; Chang, L.; Klein, W. L.; Van Duyne, R. P., A Localized Surface Plasmon Resonance Biosensor: First Steps toward an Assay for Alzheimer's Disease. *Nano Letters* **2004,** *4* (6), 1029-1034.

25. Frank, G.; Köstlin, H., Electrical properties and defect model of tin-doped indium oxide layers. *Applied Physics A* **1982,** *27* (4), 197-206.

26. Abdullah, M. M.; Rajab, F. M.; Al-Abbas, S. M., Structural and optical characterization of Cr2O3 nanostructures: Evaluation of its dielectric properties. *AIP Advances* **2014,** *4* (2).

27. Gerfin, T.; Grätzel, M., Optical properties of tin-doped indium oxide determined by spectroscopic ellipsometry. *Journal of Applied Physics* **1996,** *79* (3), 1722-1729.

28. Fang, P. H.; Brower, W. S., Dielectric Constant of ${\mathrm{Cr}}_{2}$${\mathrm{O}}_{3}$ Crystals. *Physical Review* **1963,** *129* (4), 1561-1561.

29. Ye, X.; Fei, J.; Diroll, B. T.; Paik, T.; Murray, C. B., Expanding the Spectral Tunability of Plasmonic Resonances in Doped Metal-Oxide Nanocrystals through Cooperative Cation–Anion Codoping. *Journal of the American Chemical Society* **2014,** *136* (33), 11680-11686.

30. Elim, H. I.; Ji, W.; Zhu, F., Carrier concentration dependence of optical Kerr nonlinearity in indium tin oxide films. *Applied Physics B* **2006,** *82* (3), 439-442.

31. Singh, M. R.; Yastrebov, S., Switching and Sensing Using Kerr Nonlinearity in Quantum Dots Doped in Metallic Nanoshells. *The Journal of Physical Chemistry C* **2020,** *124* (22), 12065-12074.

32. Chai, Z.; Hu, X.; Wang, F.; Niu, X.; Xie, J.; Gong, Q., Ultrafast All-Optical Switching. *Advanced Optical Materials* **2017,** *5* (7), 1600665.

33. McMorrow, D.; Lotshaw, W. T., Intermolecular dynamics in acetonitrile probed with femtosecond Fourier-transform Raman spectroscopy. *The Journal of Physical Chemistry* **1991,** *95* (25), 10395-10406.

34. Zhong, Q.; Fourkas, J. T., Optical Kerr effect spectroscopy of simple liquids. *The Journal of Physical Chemistry B* **2008,** *112* (49), 15529-15539.

35. Shirota, H., Comparison of Low-Frequency Spectra between Aromatic and Nonaromatic Cation Based Ionic Liquids Using Femtosecond Raman-Induced Kerr Effect Spectroscopy. *ChemPhysChem* **2012,** *13* (7), 1638-1648.

36. González, G. B.; Mason, T. O.; Okasinski, J. S.; Buslaps, T.; Honkimäki, V., Determination of the Solubility of Tin in Indium Oxide Using In Situ and Ex Situ X-Ray Diffraction. *Journal of the American Ceramic Society* **2012,** *95* (2), 809-815.

37. Mason, T. O.; González, G. B.; Hwang, J. H.; Kammler, D. R., Point defects and related properties of highly co-doped bixbyite In2O3. *Physical Chemistry Chemical Physics* **2003,** *5* (11), 2183-2189.

38. Warschkow, O.; Ellis, D. E.; González, G. B.; Mason, T. O., Defect Cluster Aggregation and Nonreducibility in Tin-Doped Indium Oxide. *Journal of the American Ceramic Society* **2003,** *86* (10), 1707-1711.

39. Yan, X.-Y.; Zhang, K.-X.; Yao, C.-B.; Li, Q.-H., Ultrafast nonlinear optical properties and optical Kerr effect of In-doped ZnO nanowires. *Materials Letters* **2016,** *176*, 49-51.

40. Elim, H. I.; Ji, W.; Zhu, F., Carrier concentration dependence of optical Kerr nonlinearity in indium tin oxide films. *Applied Physics B* **2006,** *82*, 439-442.

41. Dhar, L.; Rogers, J. A.; Nelson, K. A., Time-resolved vibrational spectroscopy in the impulsive limit. *Chemical Reviews* **1994,** *94* (1), 157-193.

42. Tanimura, Y.; Mukamel, S., Two-dimensional femtosecond vibrational spectroscopy of liquids. *The Journal of chemical physics* **1993,** *99* (12), 9496-9511.

43. Nagata, Y.; Hasegawa, T.; Tanimura, Y., Analyzing atomic liquids and solids by means of two-dimensional Raman spectra in frequency domain. *The Journal of chemical physics* **2006,** *124* (19).

Chapter 5

Nonlinear Optical Properties of 0D Chiral Bismuth Iodides

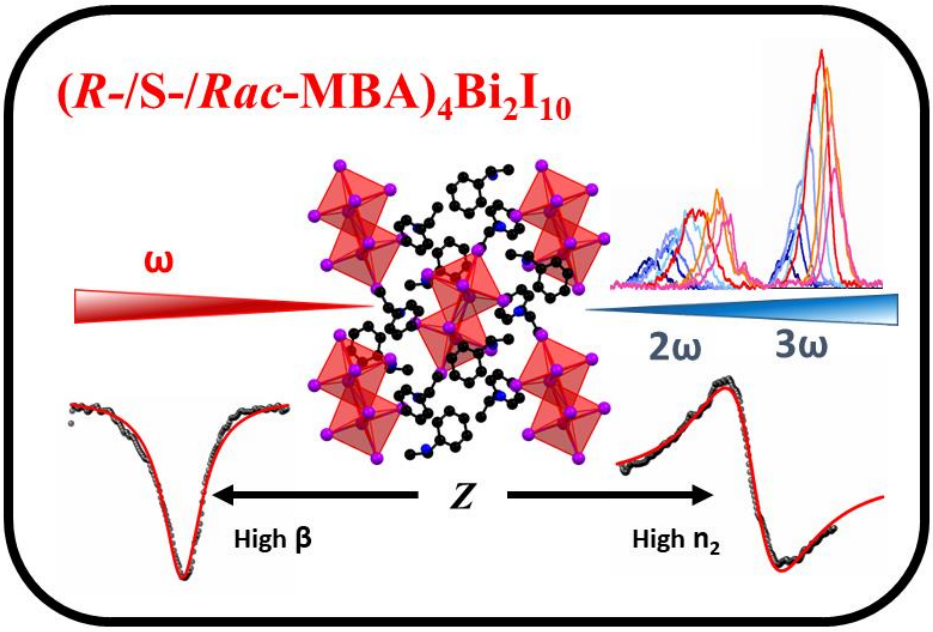

5.1. Introduction

Nonlinear optics is a specialized area of study that explores the interactions between intense light beams and various materials.[1] These nonlinear interactions give rise to secondary optical fields and alter the light's phase and frequency within nonlinear optical (NLO) materials. [2] This unique ability to manipulate photons is pivotal to cutting-edge technologies, such as optical communication systems, laser innovations, and advanced data processing.[3-6] As a result, researchers worldwide continue to actively seek highly efficient NLO materials to push the boundaries of modern science and technology.

Nonlinear optical processes like Second-Harmonic Generation (SHG) and Third-Harmonic Generation (THG), which involve photon energy up-conversion, are essential for advancements in laser manufacturing,[7] optical communication,[8] and related technologies. In SHG, two photons of frequency ω combine to generate a single coherent photon with twice the frequency (2ω). Similarly, THG combines three photons of frequency ω to produce a photon with triple the frequency (3ω). While SHG occurs exclusively in non-centrosymmetric materials or interfaces and is governed by the second-order nonlinear susceptibility, $\chi^{(2)}$, THG operates without structural symmetry constraints and depends on the third-order nonlinear susceptibility, $\chi^{(3)}$.[9] Additionally, $\chi^{(3)}$ also determines the efficiency of other nonlinear phenomena, including two-photon absorption (TPA), the optical Kerr effect, and saturable absorption. Materials exhibiting strong nonlinear absorption and high optical nonlinearity are vital for various applications, including optical switches,[10-11] data storage,[12] and laser technology.[13]

Organic-inorganic hybrid perovskites have gained attention as a promising class of nonlinear optical materials due to their remarkable photophysical properties, structural versatility, and scalable solution-based fabrication methods.[6, 14] However, their inherently high structural symmetry often limits Second-Harmonic Generation (SHG).[15] One approach to breaking this symmetry is the incorporation of enantiopure chiral organic molecules into the perovskite structure.[16-18] These chiral molecules disrupt the symmetry of the inorganic sub-lattice through asymmetric hydrogen bonding and effectively induce chirality in the perovskite structure.[17-19] This approach not only introduces unique chiroptical and chiral optoelectronic properties but also unlocks the potential of chiral perovskites for cutting-edge applications, including circularly polarized photodetectors, chiral ferroelectrics, and circularly polarized light-emitting devices.[20-24]

Chiral halide perovskites have attracted considerable interest for their nonlinear optical properties, with numerous studies demonstrating wavelength-tunable and polarization-dependent SHG in low-dimensional chiral hybrid perovskites.[25-27] However, the widespread use of toxic lead (Pb) in these materials has raised environmental concerns, driving efforts to develop lead-free alternatives.[28-29] Recent advancements have highlighted bismuth (Bi) and tin (Sn)-based chiral perovskites as promising substitutes for lead-based counterparts in nonlinear optical applications.[9, 29-31] Bismuth (Bi^{3+}), in particular has ionic radius being similar to that of lead (Pb^{2+}) and its analogous $6s^26p^0$ electronic configuration. Additionally, bismuth-based perovskites stand out for their high absorption coefficients and exceptional environmental stability, making them strong contenders for sustainable nonlinear optical technologies.[29, 32]

In this study, we present wavelength-tunable and polarization-dependent SHG and THG in the 0D chiral hybrid perovskite derivative (*R*-/*S*-MBA)$_4Bi_2I_{10}$, where MBA represents methyl benzyl ammonium, as well as its achiral counterpart (*Rac*-MBA)$_4Bi_2I_{10}$. The third-order nonlinear optical properties of these materials were further explored through open aperture (OA) and closed aperture (CA) Z-scan techniques in the femtosecond (fs) regime. Unlike previously reported bismuth-based chiral perovskites,[29] this material not only exhibits SHG but also demonstrates a significant THG response alongside excellent thermal stability. Furthermore, the thin films display remarkable third-order optical nonlinearity, characterized by a high nonlinear absorption coefficient (β) and nonlinear refractive index (n_2), underscoring their potential for advanced nonlinear optical applications.

5.2. Experimental section

5.2.1. Chemicals

Bismuth (III) oxide (Sigma Aldrich, 99.9%), hypophosphorous acid (Avra, 50% w/w H_2O), hydroiodic acid (Sigma Aldrich, 57% w/w in H_2O), *R*-(+)- α- methyl benzylamine (Sigma Aldrich, 99%), *S*- (-)-α-methyl benzylamine (Sigma Aldrich, 99%), *Rac*-methyl benzylamine (Sigma Aldrich, 98%). All chemicals were used without any further purification.

5.2.2. Synthesis and characterization of 0D (*R*-/*S*-/*Rac*-MBA)$_4Bi_2I_{10}$ crystals

The crystals of (*R*-/*S*-/*Rac*-MBA)$_4Bi_2I_{10}$ were prepared through a temperature-lowering crystallization method, following a previously reported reaction scheme.[33] The synthesis and

characterization of the samples were performed by Mr. Parikshit Kumar Rajput from Prof. Angshuman Nag's group at IISER Pune. First, one millimole of bismuth(III) oxide was dissolved in a mixture of 10 mL hydroiodic acid and 1 mL hypophosphorous acid at approximately 100 °C under continuous magnetic stirring. Once a clear and transparent solution was achieved, two millimoles of *R*-, *S*-, or *Rac*-methylbenzylamine were added. The mixture was stirred continuously for 30 minutes, after which heating and stirring were stopped. Crystals were obtained by gradually cooling the solution at a controlled rate of 5 °C per hour using the temperature-lowering crystallization technique. The solution was left undisturbed overnight, resulting in the formation of orange-red crystals of (*R*-/*S*-/*Rac*-MBA)$_4$Bi$_2$I$_{10}$ as shown in Figure 1.

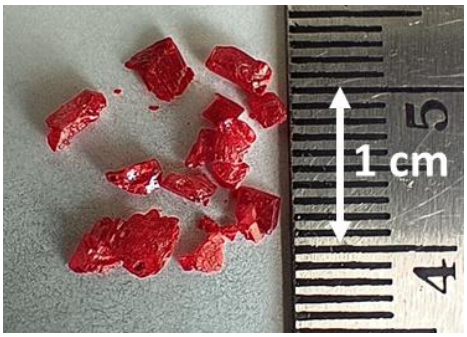

Figure 1. Digital photographs of (*Rac*-MBA)$_4$Bi$_2$I$_{10}$ crystals.

The crystals were characterized using powder X-ray diffraction (PXRD), which revealed sharp diffraction peaks, confirming the high phase purity of the (R-/S-MBA)$_4$Bi$_2$I$_{10}$ crystals. Powder X-ray Diffraction (PXRD) data were collected using a Bruker D8 Advanced X-ray diffractometer with Cu Kα radiation (λ = 1.54 Å). These peaks align well with both the simulated patterns and previously reported data (Figure 2).[33] The crystal structures of (*R*-/*S*-/*Rac*-MBA)$_4$Bi$_2$I$_{10}$ were drawn using CIF files from reference 33. The chiral (*R*-/*S*-MBA)$_4$Bi$_2$I$_{10}$ crystallizes in the monoclinic system with the chiral Sohncke space group P2$_1$, while the achiral (*Rac*-MBA)$_4$Bi$_2$I$_{10}$ crystallizes in the achiral space group P2$_1$/c. All three variants adopt a 0D perovskite derivative structure, as depicted in Figures 3a, 3b, and 3c.

Each unit of (*R*-/*S*-/*Rac*-MBA)$_4$Bi$_2$I$_{10}$ consists of four *R*-/*S*-/*Rac*-MBA cations and a $[Bi_2I_{10}]^{4-}$ inorganic anion, creating an overall charge-neutral structure. The $[Bi_2I_{10}]^{4-}$ anion is formed by two $[BiI_6]^{2-}$ octahedra linked through shared iodine (I) atoms, creating an edge-sharing dimer. The spaces between these dimers are occupied by four *R*-/*S*-/*Rac*-MBA cations, which isolate the

$[Bi_2I_{10}]^{4-}$ dimers into a 0D structure. It has been observed that chiral organic amines (MBA) transfer their chirality to the inorganic dimers through asymmetric hydrogen bonding (N-H···I) with the iodine atoms in the $[Bi_2I_{10}]^{4-}$ dimer. These interactions distort the inorganic sub-lattice, breaking inversion and mirror symmetry in the $[Bi_2I_{10}]^{4-}$ unit, and confer chirality to the (*R*-/*S*-/*Rac*-MBA)$_4Bi_2I_{10}$ structure. Conversely, in the case of *Rac*-MBA cations, the hydrogen bonding is symmetrical, preserving inversion symmetry in the inorganic sub-lattice. Consequently, the *Rac*-MBA system lacks chirality in both its organic and inorganic sub-lattices, resulting in an achiral hybrid lattice for (*Rac*-MBA)$_4Bi_2I_{10}$.[33]

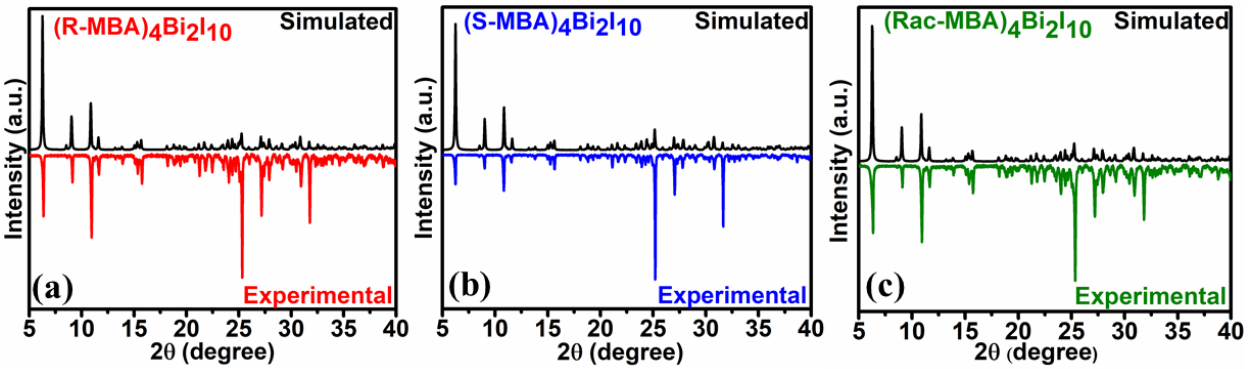

Figure 2. Powder XRD patterns of **(a)** (*R*-MBA)$_4Bi_2I_{10}$, **(b)** (*S*-MBA)$_4Bi_2I_{10}$, **(c)** (*Rac*-MBA)$_4Bi_2I_{10}$ crystals in finely powdered form, compared with simulated ones generated from CIF files of single crystal XRD analysis from the reported literature.

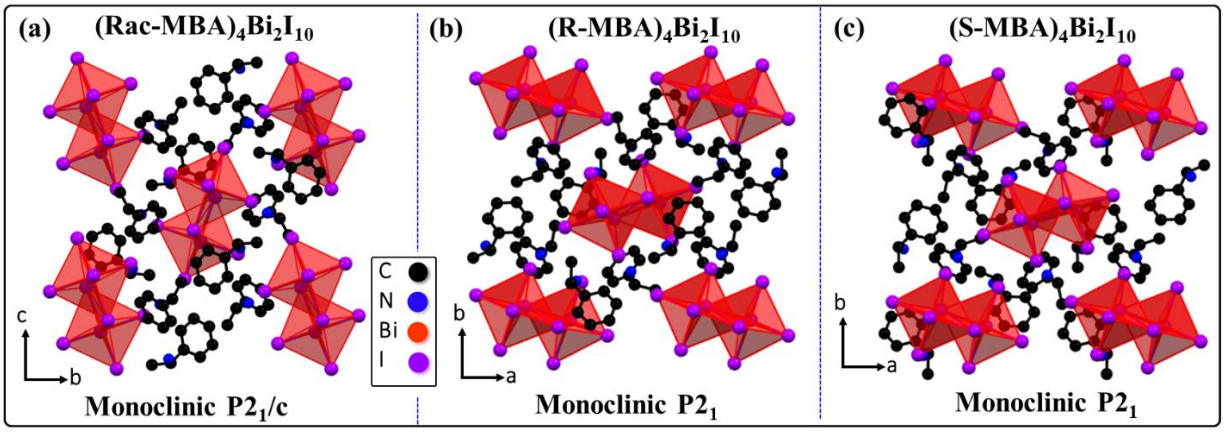

Figure 3. Crystal structure of **(a)** (*Rac*-MBA)$_4Bi_2I_{10}$, **(b)** (*R*-MBA)$_4Bi_2I_{10}$, and **(c)** (*S*-MBA)$_4Bi_2I_{10}$. as determined from single-crystal XRD at 296 K, are depicted based on CIFs from reference 33. For better visualization, hydrogen atoms have been omitted from the structures.

5.2.3. Preparation of thin films of (*R*-/*S*-/*Rac*-MBA)$_4$Bi$_2$I$_{10}$ crystals

Thin films of (*R*-/*S*-/*Rac*-MBA)$_4$Bi$_2$I$_{10}$ were prepared for circular dichroism (CD) and Z-scan measurements using the spin-coating method on glass substrates. The substrates were thoroughly cleaned by ultrasonic treatment in distilled water, acetone, and 2-propanol for 15 minutes in each solvent. The synthesized (*R*-/*S*-/*Rac*-MBA)$_4$Bi$_2$I$_{10}$ crystals were dissolved in dimethylformamide (DMF) to achieve a concentration of 0.069 M. The solution was spin-coated onto glass substrates at a speed of 3000 rpm for 30 seconds. Following the coating process, the films were annealed at 100 °C for 10 minutes to promote crystallization.

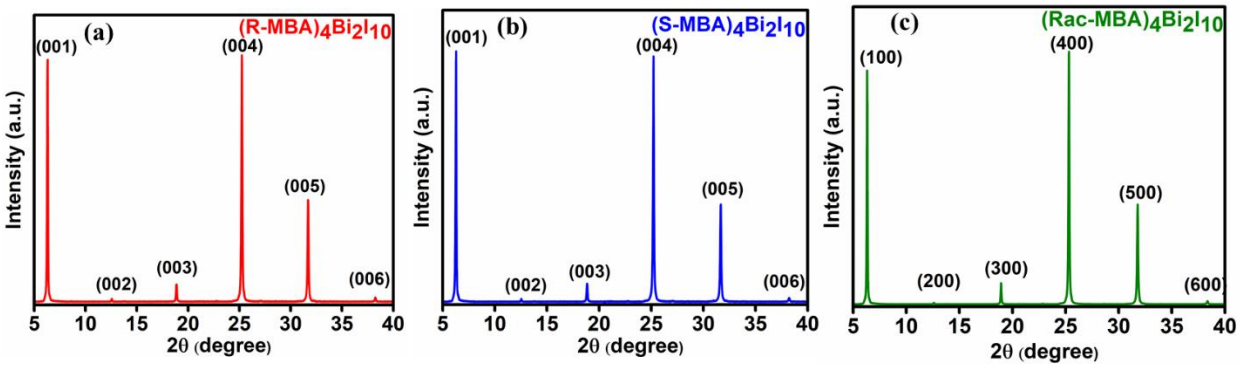

Figure 4. Powder XRD patterns of the thin film of **(a)** (*R*-MBA)$_4$Bi$_2$I$_{10}$, **(b)** (*S*-MBA)$_4$Bi$_2$I$_{10}$, **(c)** (*Rac*-MBA)$_4$Bi$_2$I$_{10}$ at room temperature.

The X-ray diffraction (XRD) patterns of the thin films for all three samples reveal sharp peaks, as illustrated in Figure 4, confirming their high crystallinity, even in film form. The prominent diffraction peaks align closely with those of the corresponding crystalline powders. Atomic force microscopy (AFM) images of the (*R*-/*S*-/*Rac*-MBA)$_4$Bi$_2$I$_{10}$ thin film presented in Figure 5 indicate a smooth surface. The average surface roughness of the thin films, as determined from AFM measurements, is presented in Figure 6. The R_a values were found to be 2.67 nm for (*R*-MBA)$_4$Bi$_2$I$_{10}$, 2.73 nm for (*S*-MBA)$_4$Bi$_2$I$_{10}$, and 15.72 nm for (*Rac*-MBA)$_4$Bi$_2$I$_{10}$ films. The thickness of the films for all three films, measured with AFM, falls within the range of 105 to 120 nm, as shown in Figure 7.

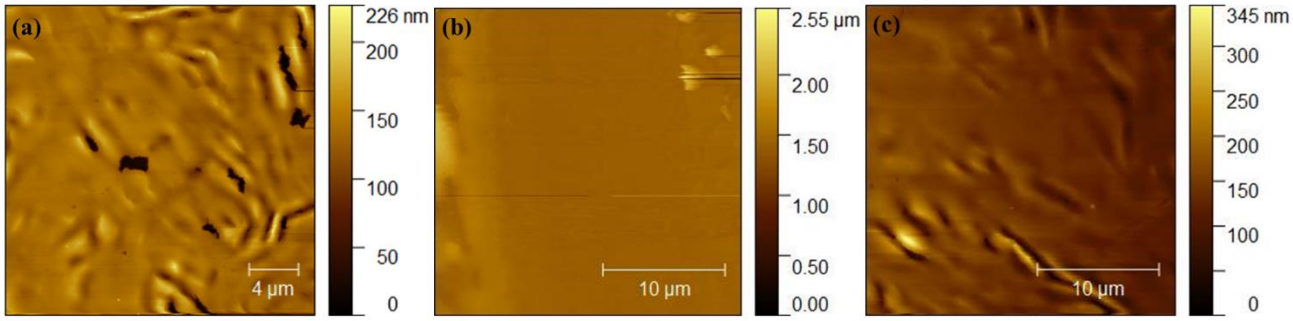

Figure 5. AFM images of thin films of (a) (*R*-MBA)$_4$Bi$_2$I$_{10}$, (b) (*S*-MBA)$_4$Bi$_2$I$_{10}$, and (c) (*Rac*-MBA)$_4$Bi$_2$I$_{10}$.

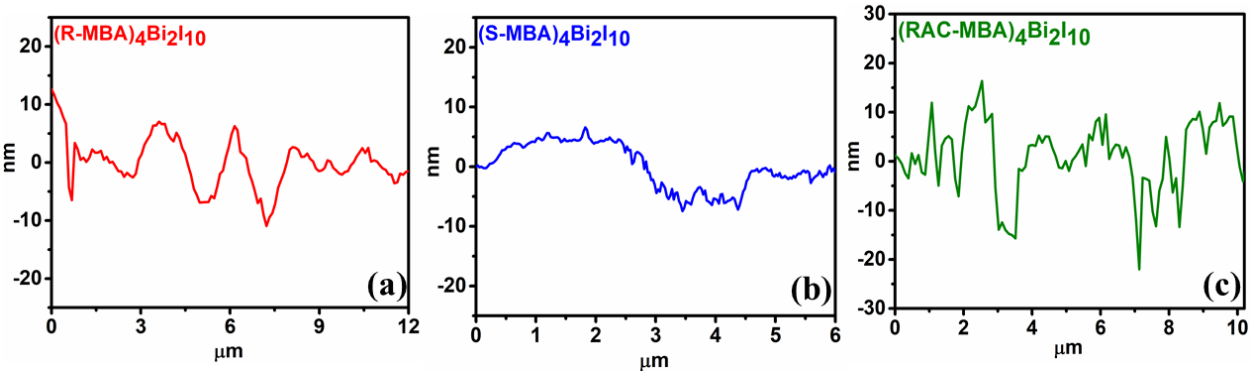

Figure 6. Roughness average (R$_a$) of film surface measured from AFM images of the thin films of **(a)** (*R*-MBA)$_4$Bi$_2$I$_{10}$: Ra = 2.67 nm, **(b)** (*S*-MBA)$_4$Bi$_2$I$_{10}$: R$_a$ = 2.73 nm, and **(c)** (*Rac*-MBA)$_4$Bi$_2$I$_{10}$: Ra =15.72 nm.

5.2.4. UV-visible absorption and Circular Dichroism (CD) spectra

The optical absorption spectra of the thin films were measured in transmission mode using a Cary series UV-visible spectrophotometer. Circular dichroism (CD) measurements were conducted with a JASCO J-815 spectropolarimeter, operated at a scan speed of 50 nm/min and a resolution of 0.5 nm. The UV-visible absorption spectra of all three thin films, shown in Figure 8b, display a sharp exciton absorption peak followed by a continuum band, suggesting that the structural chirality has almost no significant effect on the band gap. Circular dichroism (CD) spectra of the (*R*-/*S*-/*Rac*-MBA)$_4$Bi$_2$I$_{10}$ thin films were recorded in transmission mode. The CD spectra reveal distinct features with opposite signs for (*R*-/*S*-MBA)$_4$Bi$_2$I$_{10}$, while achiral (*Rac*-MBA)$_4$Bi$_2$I$_{10}$ shows no notable features across the entire wavelength range, as expected, as illustrated in Figure 8a.

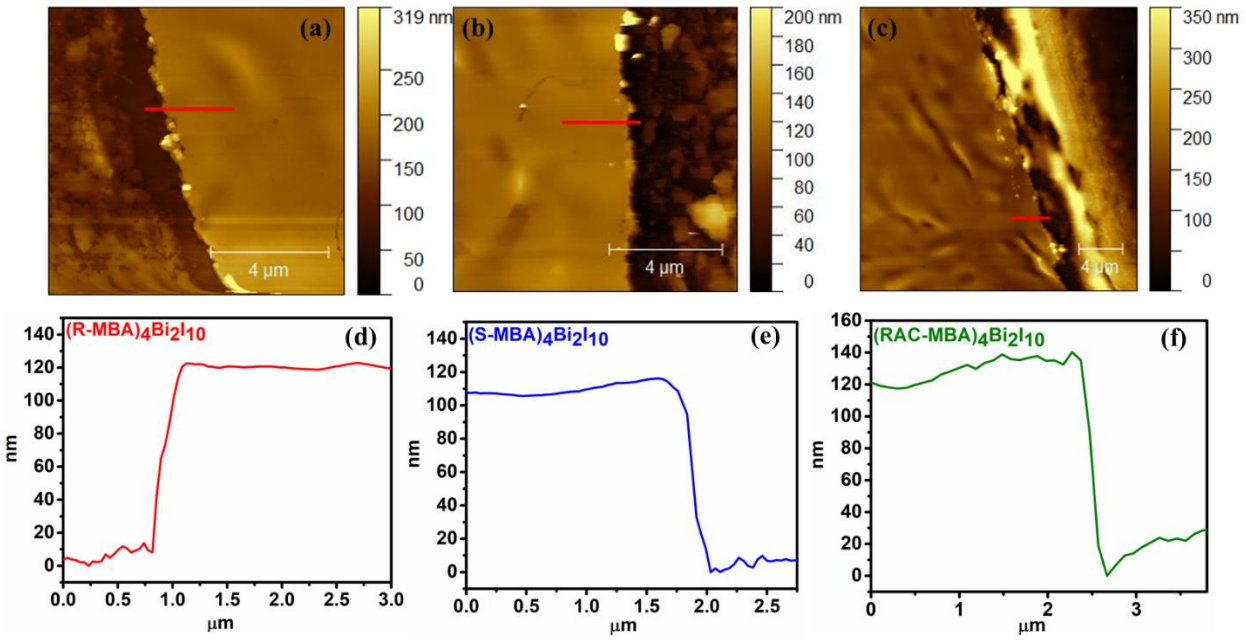

Figure 7. Film thickness measurement using atomic force microscopy (AFM) on sample films prepared on glass substrates for Z-scan measurements. AFM images of the films correspond to **(a)** (*R*-MBA)$_4$Bi$_2$I$_{10}$, **(b)** (*S*-MBA)$_4$Bi$_2$I$_{10}$, and **(c)** (*Rac*-MBA)$_4$Bi$_2$I$_{10}$. Height profiles along the red lines in the respective images are shown in **(d)**, **(e)**, and **(f)**. The measured film thicknesses were approximately ~120 nm for (*R*-MBA)$_4$Bi$_2$I$_{10}$ (d), ~115 nm for (*S*-MBA)$_4$Bi$_2$I$_{10}$ (e), and ~120 nm for (*Rac*-MBA)$_4$Bi$_2$I$_{10}$ (f).

As illustrated in Figure 8, when comparing the absorption spectra with the circular dichroism (CD) spectra, all three samples show a distinct excitonic absorption peak at 499 nm (2.48 eV). Notably, the CD spectra (Figure 2a) of (*R*-/*S*-MBA)$_4$Bi$_2$I$_{10}$ display a derivative-like positive and negative response, with a zero crossing at 499 nm. This behavior aligns with earlier findings, where the fundamental excitonic transition splits into two states (excitonic splitting) that are selectively excited by left- or right-circularly polarized light.[34-35] It is important to note that the organic cations, R-MBA and S-MBA, do not absorb in this wavelength range, suggesting that the observed CD signals originate from the inorganic sub-lattice.[25]

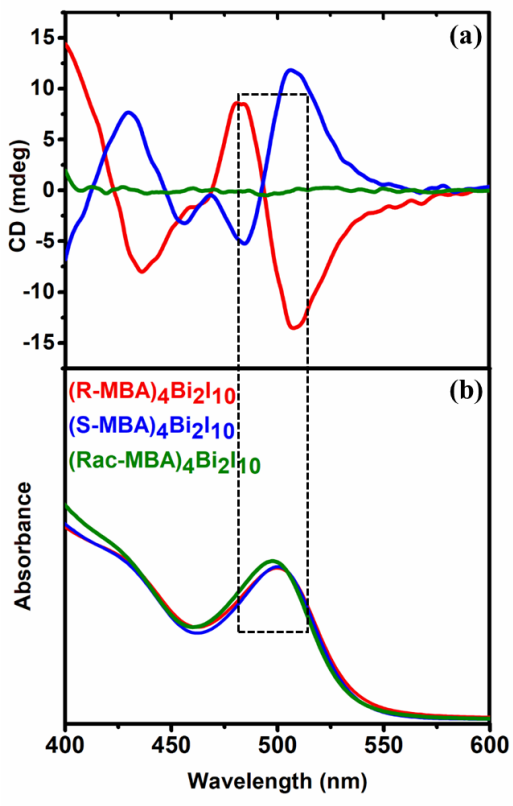

Figure 8. (a) Circular dichroism (CD) and **(b)** linear optical absorption spectra of (*R*-/*S*-/*Rac*-MBA)$_4$Bi$_2$I$_{10}$ thin films recorded in transmission mode.

5.3. SHG and THG in (*R*-/*S*-/*Rac*-MBA)$_4$Bi$_2$I$_{10}$

We explored the NLO properties of (*R*-/*S*-/*Rac*-MBA)$_4$Bi$_2$I$_{10}$ crystals, by exciting the samples using different pump wavelengths. The up-converted photons emitted were collected using a custom-built setup in transmission mode. The details of the setup are provided in the chapter 2. Briefly, the setup employed an optical parametric amplifier (OPA) driven by a regenerative amplifier (800 nm, 35 fs, 1 kHz) which provides near-infrared (NIR) pump pulses (1360–1590 nm, ~45 fs) for exciting the sample. To ensure precise wavelength and intensity control, an 850 nm long-pass filter and neutral density (ND) filters were employed. The pump beam was focused using a 200 mm plano-convex lens onto the sample crystals. To avoid damage and ensure a sufficiently large spot size, the sample was placed 135 mm away from the lens. The sample crystals were carefully sandwiched between two quartz microscope slides and securely mounted on a cage rotation mount (Thorlabs CRM1/M). The emitted SHG and THG signals were collimated with a lens, filtered through a 750 nm short-pass filter to eliminate the pump wavelength, and directed

into a spectrometer (USB4000, Ocean Optics) for detection. Polarization-dependent SHG and THG measurements utilized a Glan polarizer and a half-wave plate assembly to control the pump beam polarization. To produce circularly polarized light for SHG circular dichroism (CD) measurements, the half-wave plate was substituted with a quarter-wave plate.

The crystals were excited with wavelengths ranging from 1360 to 1590 nm at a fixed power of 0.75 mW. Under linearly polarized excitation, the NLO responses of (*R*-MBA)$_4$Bi$_2$I$_{10}$ and (*S*-MBA)$_4$Bi$_2$I$_{10}$ were similar. As shown in Figures 9a and 9b, each pump wavelength produced two distinct signals simultaneously. The central wavelengths of these signals corresponded to half and one-third of the pump wavelength, indicating second-harmonic generation (SHG) and third-harmonic generation (THG), respectively. The SHG signals in (*R*-/*S*-MBA)$_4$Bi$_2$I$_{10}$ indicated chirality and symmetry breaking within the inorganic sub-lattice, consistent with the SHG symmetry condition. As anticipated, no SHG signal was detected in the achiral (*Rac*-MBA)$_4$Bi$_2$I$_{10}$ (Figure 9c). However, all three compounds displayed significantly stronger THG signals, with similar THG intensities in the chiral (*R*-/*S*-MBA)$_4$Bi$_2$I$_{10}$ and an order of magnitude higher THG intensity in the achiral (*Rac*-MBA)$_4$Bi$_2$I$_{10}$.

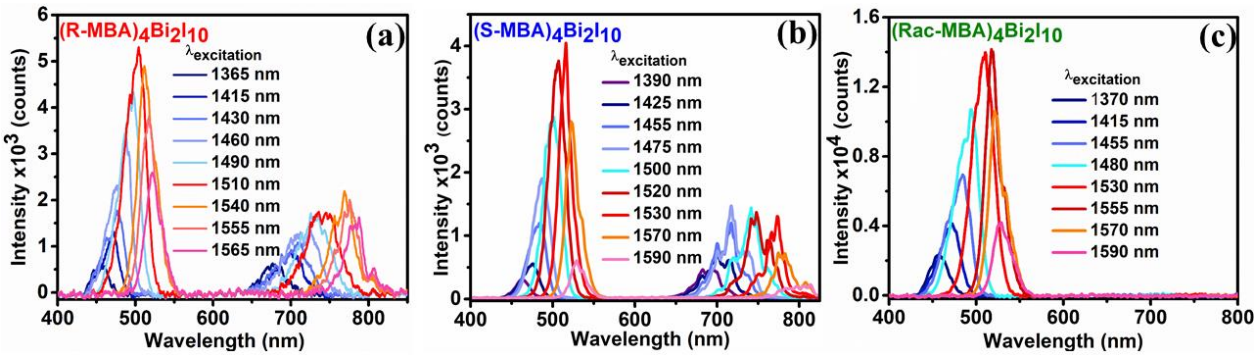

Figure 9. Wavelength-dependent SHG/THG response from **(a)** (*R*-MBA)$_4$Bi$_2$I$_{10}$, **(b)** (*S*-MBA)$_4$Bi$_2$I$_{10}$, and (*Rac*-MBA)$_4$Bi$_2$I$_{10}$ at a constant excitation power of 0.75 mW.

Figure 10 shows the variation in SHG and THG intensities of (*R*-/*S*-/*Rac*-MBA)$_4$Bi$_2$I$_{10}$ crystals with pump wavelength. The strongest SHG and THG signals are observed near a pump wavelength of 1510–1530 nm. Notably, the wavelength of the maximum THG response (~506 nm) aligns with the excitonic absorption peak of the (*R*-/*S*-/*Rac*-MBA)$_4$Bi$_2$I$_{10}$ crystals. This selective enhancement

of THG is attributed to excitonic resonance conditions and the localized amplification of the incident field.[36] Below 1510 nm, THG intensity drops sharply, likely due to self-absorption effects, whereas minimal self-absorption is anticipated near the absorption edge.[36]

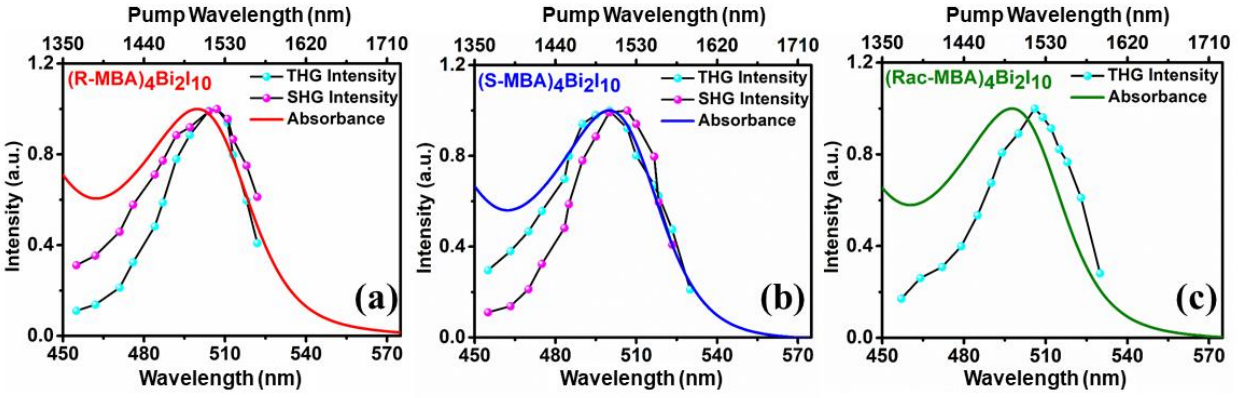

Figure 10. Wavelength-dependent THG and SHG intensity with absorbance of **(a)** (*R*-MBA)$_4$Bi$_2$I$_{10}$, **(b)** (*S*-MBA)$_4$Bi$_2$I$_{10}$, **(c)** (*Rac*-MBA)$_4$Bi$_2$I$_{10}$.

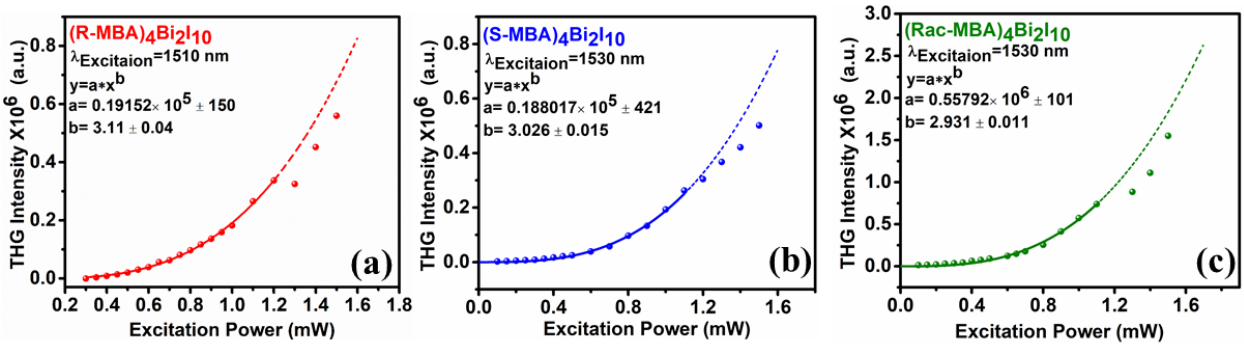

Figure 11. Excitation power dependent THG response of **(a)** (*R*-MBA)$_4$Bi$_2$I$_{10}$, **(b)** (*S*-MBA)$_4$Bi$_2$I$_{10}$, **(c)** (*Rac*-MBA)$_4$Bi$_2$I$_{10}$.

5.3.1. Laser-Induced Damage Threshold (LIDT) calculations for (*R*-/*S*-/*Rac*-MBA)$_4$Bi$_2$I$_{10}$

To validate the SHG and THG behavior in (*R*-/*S*-/*Rac*-MBA)$_4$Bi$_2$I$_{10}$ crystals and assess their laser-induced damage threshold (LIDT),[37] we measured the power-dependent SHG and THG responses at an excitation wavelength of 1510 nm for where the maximum nonlinear response was observed. As shown in Figure 11 and Figure 12, the THG intensity demonstrated a cubic dependence, while the SHG intensity displayed a quadratic dependence on pump power. However, at pump powers

above 1.2 mW, deviations from these trends were observed, likely due to saturation effects such as local heating and lattice relaxation, which reduce SHG and THG efficiencies.[38]

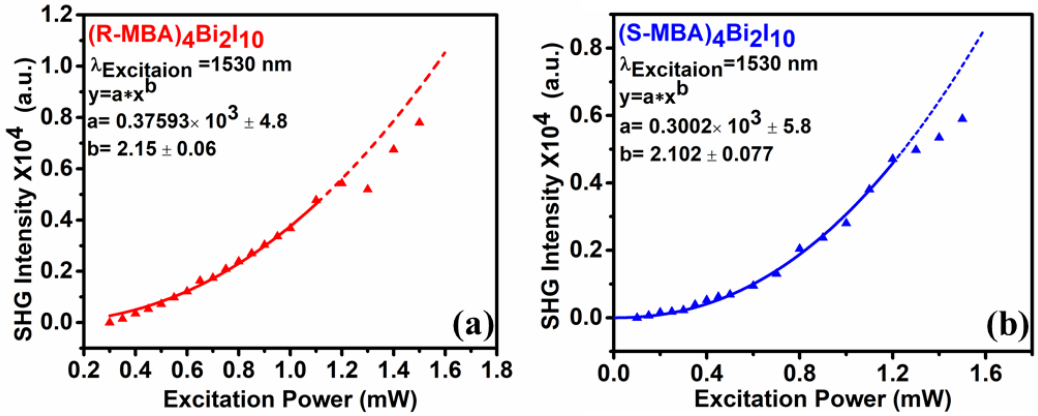

Figure 12. Excitation power-dependent SHG response of **(a)** (*R*-MBA)$_4$Bi$_2$I$_{10}$ and **(b)** (*S*-MBA)$_4$Bi$_2$I$_{10}$.

The LIDT serves as a measure of a material's optical stability, particularly its capacity to endure high-intensity laser exposure without degradation. It is determined based on the excitation pump power at which the second-harmonic generation (SHG) and third-harmonic generation (THG) responses begin to deviate from their characteristic quadratic and cubic dependencies, respectively.[38] The peak laser intensity at this critical pump power defines the LIDT of the material. The LIDT values for all three samples were calculated as follows:

$$Peak\ Intensity = \frac{Energy\ per\ pulse}{(Pulse\ width) \times (Effective\ spot\ area)}$$

$$Energy\ per\ pulse = \frac{Average\ Power}{Repetition\ Rate}$$

$$LIDT = Peak\ Intensity = \frac{Average\ power}{(Repetition\ rate) \times (Pulse\ width) \times (Effective\ spot\ area)}$$

For our setup, $Repetition\ rate = 1000\ Hz,\ Pulse\ width\ = 45 \times 10^{-15} s,\ Beam\ radius = 150 \times 10^{-6} m.$

Table 1: LIDT values of (R/S/rac-MBA)$_4$Bi$_2$I$_{10}$.

Sample	Average Power for SHG (mW)	LIDT (GW/cm^2)	Average Power for THG (mW)	LIDT (GW/cm^2)
(*R*-MBA)$_4$Bi$_2$I$_{10}$	1.2	37.68	1.2	37.68
(*S*-MBA)$_4$Bi$_2$I$_{10}$	1.2	37.68	1.1	34.54
(*Rac*-MBA)$_4$Bi$_2$I$_{10}$	-	-	1.1	34.54

The LIDT for (*R*-/*S*-/*Rac*-MBA)$_4$Bi$_2$I$_{10}$ crystals were found to range between 34.54 and 37.68 GW/cm^2. This high LIDT demonstrates outstanding thermal stability, which is a vital attribute for potential applications in nonlinear optics.

5.3.2. Determination of second-order ($\chi^{(2)}$) and third-order ($\chi^{(3)}$) NLO susceptibility

Nonlinear susceptibilities are critical for evaluating the performance of nonlinear optical (NLO) materials. The second-order ($\chi^{(2)}$) and third-order ($\chi^{(3)}$) NLO susceptibility values of the samples were determined using a relative method based on nonlinear Maxwell's equations.[39-40] Pyridinium-lead-iodide ($PyPbI_3$) crystals were employed as a reference for $\chi^{(3)}$ measurements,[41] while β-Barium Borate (BBO) crystals were used as the reference for $\chi^{(2)}$ measurements.[36, 42]

In the non-phase-matching condition, the third-order nonlinear susceptibility $\chi^{(3)}$ of two samples with nearly identical thicknesses and excited under similar conditions can be compared using their third-harmonic generation (THG) intensities. This comparison is expressed by the following equation 1.[39]

$$\chi_S^{(3)} = \chi_R^{(3)} \left[\frac{I_S(3\omega)}{I_R(3\omega)}\right]^{1/2} \quad (1)$$

Here, $I_S(3\omega)$ and $I_R(3\omega)$ are the relative THG intensities of the sample and reference; and, $\chi_S^{(3)}$ and $\chi_R^{(3)}$ are the third-order NLO susceptibilities of the sample and reference, respectively. When incorporating frequency dependence, the third-order nonlinear optical susceptibility $\chi^{(3)}$ can be calculated at the frequency where the sample exhibits its maximum response. The modified equation is given by.[57]

$$\chi^{(3)}_{\omega_1} = \chi^{(3)}_{\omega_2} \left(\frac{3\omega_2}{3\omega_1}\right) \left[\frac{I(3\omega_1)}{I(3\omega_2)}\right]^{1/2} \quad (2)$$

Similarly, the second-order nonlinear susceptibility $\chi^{(2)}$ can be calculated using a comparable equation to the one used for third-order susceptibility but adapted for second-harmonic generation (SHG). The relative intensity method compares the SHG intensities of the sample and reference under the same conditions. The modified equation is:

$$\chi^{(2)}_S = \chi^{(2)}_R \left[\frac{I_S(2\omega)}{I_S(2\omega)}\right]^{1/2} \quad (3)$$

After incorporating frequency dependence, the equation for the second-order nonlinear susceptibility $\chi^{(2)}$ becomes-

$$\chi^{(2)}_{\omega_1} = \chi^{(2)}_{\omega_2} \left(\frac{2\omega_2}{2\omega_1}\right) \left[\frac{I(2\omega_1)}{I(2\omega_2)}\right]^{1/2} \quad (4)$$

The $\chi^{(2)}$ and $\chi^{(3)}$ values obtained for (*R*-/*S*-/*Rac*-MBA)$_4$Bi$_2$I$_{10}$ are given in table 2.

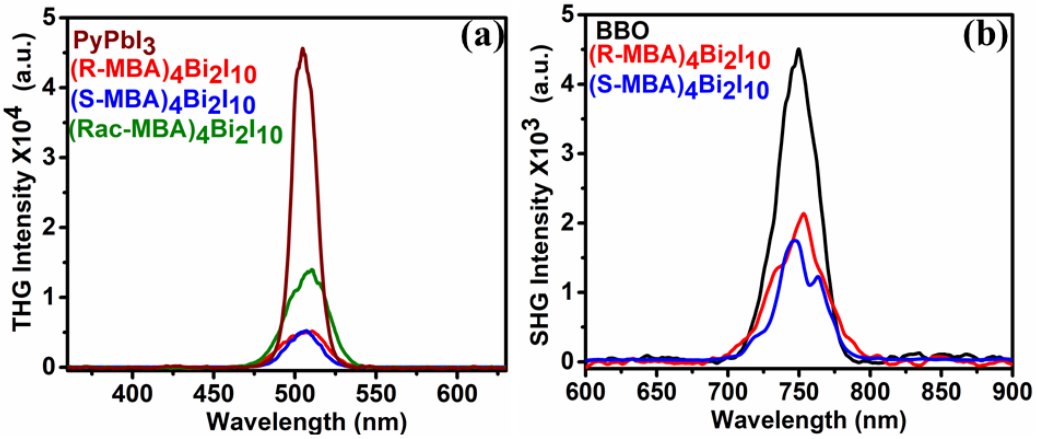

Figure 13. (a) Comparison of THG response of (*R*-/*S*-/*Rac*-MBA)$_4$Bi$_2$I$_{10}$ with pyridinium lead iodide (PyPbI$_3$) and **(b)** comparison of SHG response of (*R*/*S*-MBA)$_4$Bi$_2$I$_{10}$ with beta barium borate (BBO) crystal.

Table 2: Calculated $\chi^{(3)}$ values of (*R*/*S*/*Rac*-MBA)$_4$Bi$_2$I$_{10}$ and $\chi^{(2)}$ values of (*R*/*S*-MBA)$_4$Bi$_2$I$_{10}$

Sample	**$\chi^{(3)}$ at 1530 nm(m^2V^{-2})**	**$\chi^{(2)}$ at 1500 nm(pmV^{-1})**
(*R*-MBA)$_4$Bi$_2$I$_{10}$	0.66 x 10^{-18}	3.05
(*S*-MBA)$_4$Bi$_2$I$_{10}$	0.58 x 10^{-18}	2.63
(*Rac*-MBA)$_4$Bi$_2$I$_{10}$	1.05 x 10^{-18}	

The $\chi^{(3)}$ values for (*R*-MBA)$_4$Bi$_2$I$_{10}$ and (*S*-MBA)$_4$Bi$_2$I$_{10}$ were found to be 0.66 × 10^{-18} m^2V^{-2} and 0.58 × 10^{-18} m^2V^{-2}, respectively. However, the $\chi^{(3)}$ value for achiral (*Rac*-MBA)$_4$Bi$_2$I$_{10}$ was about twice that of the chiral counterparts (*R*-MBA)$_4$Bi$_2$I$_{10}$ and (*S*-MBA)$_4$Bi$_2$I$_{10}$, measured as 1.05 × 10^{-18} m^2V^{-2}. A comparative summary of $\chi^{(2)}$ and $\chi^{(3)}$ values for various chiral perovskites, as reported in the literature, is provided in Table 3.

Table 3. Effective SHG ($\chi^{(2)}$) and THG ($\chi^{(3)}$) susceptibilities of various chiral hybrid organic-inorganic metal halides.

Chiral hybrid metal halides	Form	Dimensionality	χ^2 (pmV^{-1})	χ^3 (pm^2V^{-2})	λ_{pump} (nm)	Ref.
(*R*-MPA)$_2$BiBr$_5$	crystal	1D	2.059	-	980	29
(*R*-MBA)$_4$Bi$_2$Br$_{10}$	crystal	0D	1.000	-	980	29
(*S*-2-MPD)PbBr$_3$	crystal	1D	29.9	-	980	26
(*R*-MPEA)$_2$SnBr$_6$	crystal	0D	0.33	-	980	31
(*R*-MBA)BiI$_4$	film	1D	130.5	9 x 10^6	1550	9
(*R*-MBA)$_4$Bi$_2$I$_{10}$	crystal	0D	3.05	6.6 x 10^5	1530	this work
(*S*-MBA)$_4$Bi$_2$I$_{10}$	crystal	0D	2.63	5.8 x 10^5	1530	this work
(*Rac*-MBA)$_4$Bi$_2$I$_{10}$	crystal	0D	-	1.0 x 10^6	1530	this work

The $\chi^{(2)}$ values for (*R*-MBA)$_4$Bi$_2$I$_{10}$ and (*S*-MBA)$_4$Bi$_2$I$_{10}$ were found to be comparable with previously reported data, as summarized in Table 3. It was observed that the $\chi^{(2)}$ values in 0D structures are lower compared to those in similar chiral systems with 1D structures. This difference

arises because, in 1D structures, the alignment of chiral organic amines along a defined axis creates a more rigid and ordered arrangement, inducing greater distortion in the inorganic lattice. In contrast, 0D crystals have more flexible frameworks, leading to only minor symmetry breaking.[29] Despite this, both (*R*-MBA)$_4$Bi$_2$I$_{10}$ and (*S*-MBA)$_4$Bi$_2$I$_{10}$ exhibit promising $\chi^{(2)}$ and $\chi^{(3)}$ values, highlighting their potential within the class of chiral perovskite materials.

The higher $\chi^{(3)}$ value observed for (*Rac*-MBA)$_4$Bi$_2$I$_{10}$ can be attributed to greater structural distortion in this material compared to (*R*-/*S*-MBA)$_4$Bi$_2$I$_{10}$.[33] This increased distortion likely enhances the polarizability anisotropy of the material, leading to a stronger third-order nonlinear optical (NLO) response. The N–H···I hydrogen bonds, formed between the hydrogen atoms of the chiral amine and the halogen atoms of the inorganic lattice, contribute to distortions in the regular octahedral structure. The extent of this distortion can be quantified using the bond length distortion index (D) and the bond angle variance (σ^2) of the individual octahedra, as defined by Equation 5 and Equation 6, respectively.

$$D = \frac{1}{6}\sum_{i=1}^{6}\frac{|d_i - d_0|}{d_0} \tag{5}$$

$$\sigma^2 = \frac{1}{11}\sum_{i=1}^{12}(\theta_i - 90)^2 \tag{6}$$

Here, d_i= individual Bi-I bond lengths, d_0= mean Bi-I bond distances, and θ_i= octahedral I-Bi-I bond angles. In the present case, the bond length distortion index (D) remains nearly identical for all samples, with values of 0.039 for (*Rac*-MBA)$_4$Bi$_2$I$_{10}$ and 0.040 for both (*R*/*S*-MBA)$_4$Bi$_2$I$_{10}$. However, the bond angle variance (σ^2) is slightly higher for (*Rac*-MBA)$_4$Bi$_2$I$_{10}$ (18.33) compared to (*R*-MBA)$_4$Bi$_2$I$_{10}$ and (*S*-MBA)$_4$Bi$_2$I$_{10}$ (17.33).[33] Although the distortion caused by hydrogen bonding in (*Rac*-MBA)$_4$Bi$_2$I$_{10}$ is symmetric, maintaining inversion symmetry within the crystal structure, the overall distortion is more pronounced in (*Rac*-MBA)$_4$Bi$_2$I$_{10}$. These values for bond angle variance and bond length distortion index were calculated using the deposited CIF files at room temperature, as detailed in reference 33.

5.3.3. Polarization-dependent THG and SHG response of (*R*-/*S*-/*Rac*-MBA)$_4$Bi$_2$I$_{10}$

Second-order ($\chi^{(2)}$) and third-order ($\chi^{(2)}$) susceptibilities, which describe the nonlinear polarization of a material in response to an applied electric field, are represented as third- and fourth-rank tensors, respectively.[43] Both $\chi^{(2)}$ and $\chi^{(3)}$ are influenced by the crystal symmetry, offering valuable insights into the structure-property relationships that govern nonlinear optical (NLO) effects.[9] To investigate the relationship between lattice symmetry and NLO properties in (*R*-/*S*-/*Rac*-MBA)$_4$Bi$_2$I$_{10}$, we measured the SHG and THG responses as a function of the polarization angle of the incident laser light. These results are depicted in Figure 14a and 14b for (*R*-MBA)$_4$Bi$_2$I$_{10}$, Figure 15a and 15b for (*S*-MBA)$_4$Bi$_2$I$_{10}$, and Figure 16 for (*Rac*-MBA)$_4$Bi$_2$I$_{10}$.

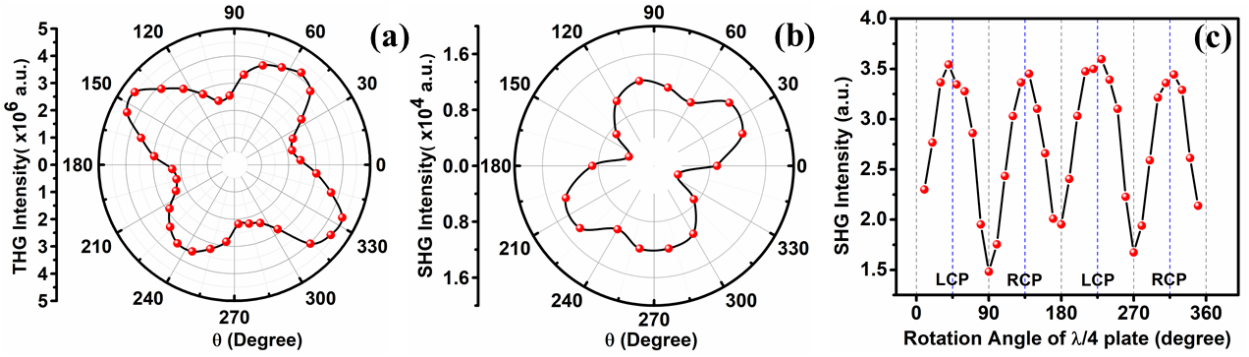

Figure 14. (a) THG and **(b)** SHG signal intensity of (*R*-MBA)$_4$Bi$_2$I$_{10}$ as a function of linear polarization angle of the incident light as tuned by λ/2 plate (pump excitation power of 0.75 mW at 1510 nm) **(c)** Change in SHG intensity of (*R*-MBA)$_4$Bi$_2$I$_{10}$ as a function of the rotation angle of the λ/4 plate.

The SHG and THG intensities were plotted as functions of θ, the polarization angle of the incident light relative to vertical polarization. This was achieved by rotating the half-wave plate by 180°, enabling a full 360° rotation of the pump light's polarization plane. Due to their intrinsic structural asymmetry, chiral perovskite crystals exhibited anisotropic SHG and THG responses. The SHG polar plots for both chiral samples, (*R*-/*S*-MBA)$_4$Bi$_2$I$_{10}$, displayed a distorted dipole-like profile, differing slightly from other SHG-active hybrid halide perovskites. However, a similar pattern, resembling a four-leaf clover shape, was recently reported by Kezheng Tao et al. in tin-based chiral hybrid halides.

For (*R*-/*S*-MBA)$_4$Bi$_2$I$_{10}$ the polarization-dependent SHG plots exhibit four maxima and minima. The two directions of maximum SHG intensity are perpendicular to each other, while the two minimal-intensity directions are offset by 45°. The polarization ratio ($\rho = (I_{max} - I_{min})/ (I_{max} + I_{min})$), provides insights into the anisotropy of the SHG/THG signals, which are influenced by the crystal structure and dipole moment orientation. The obtained ρ values for SHG were 59.58% for (*R*-MBA)$_4$Bi$_2$I$_{10}$ and 65.85% for (*S*-MBA)$_4$Bi$_2$I$_{10}$. Ideally, both chiral samples should exhibit identical ρ values, given their similar crystal structures. The slight difference observed could be attributed to subtle variations in the crystals or their orientation in the two samples. Although all experiments were conducted carefully, with all other parameters kept constant, a more precise comparison of the polarization ratio would be possible if measurements were performed on single crystals. This would enable a systematic variation of the polarization angle relative to a specific crystal axis.

In contrast, the THG responses of all three samples exhibited four-lobed patterns, with the highest polarization ratio of 51.83% observed for (*Rac*-MBA)$_4$Bi$_2$I$_{10}$, compared to 35.02% for (*R*-MBA)$_4$Bi$_2$I$_{10}$ and 33.02% for (*S*-MBA)$_4$Bi$_2$I$_{10}$. This difference is likely due to the more symmetrical structure of (*Rac*-MBA)$_4$Bi$_2$I$_{10}$ compared to its chiral counterparts.

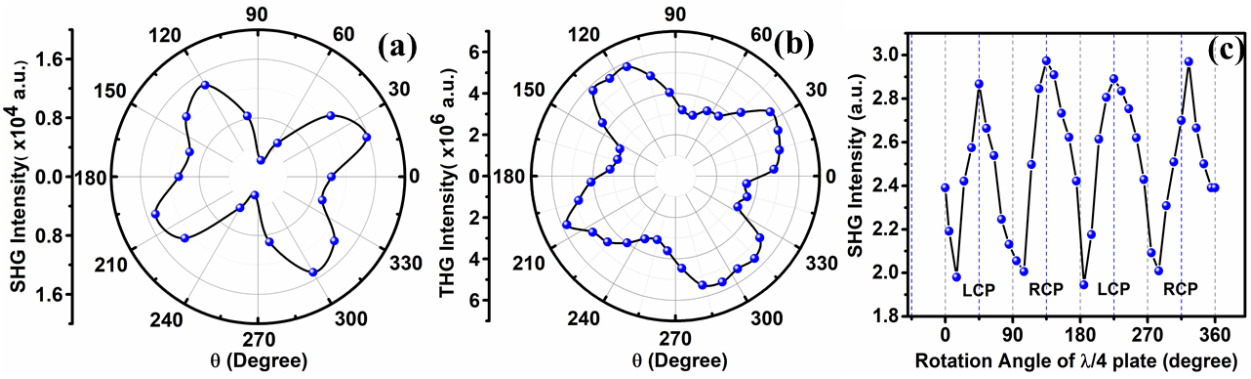

Figure 15. (a) SHG and **(b)** THG signal intensity of (*S*-MBA)$_4$Bi$_2$I$_{10}$ as a function of linear polarization angle of the incident light as tuned by λ/2 plate (pump excitation power of 0.75 mW at 1510 nm) **(c)** Change in SHG intensity as a function of the rotation angle of the λ/4 plate.

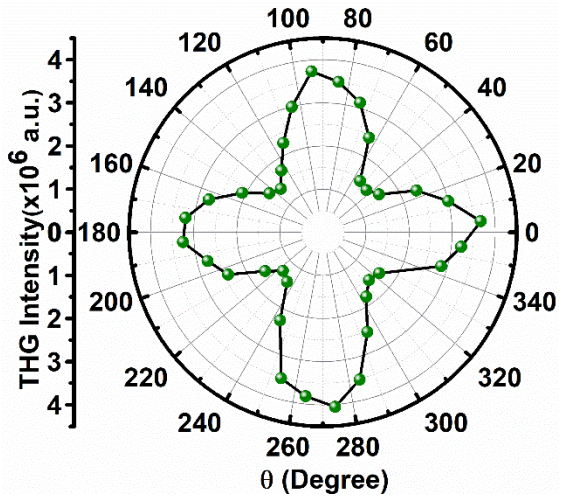

Figure 16. THG signal intensity of (*Rac*-MBA)$_4$Bi$_2$I$_{10}$ as a function of linear polarization angle of the incident light as tuned by λ/2 plate (pump excitation power of 0.75 mW at 1530 nm).

The inherent chirality of (*R-/S*-MBA)$_4$Bi$_2$I$_{10}$ inspired us to explore their nonlinear optical (NLO) chiroptical effects and evaluate their potential for circularly polarized light (CPL) detection in the near-infrared (NIR) region. To investigate this, circular polarization-dependent SHG measurements were conducted on (*R*-MBA)$_4$Bi$_2$I$_{10}$ and (*S*-MBA)$_4$Bi$_2$I$_{10}$. For these experiments, the λ/2 plate in the setup was replaced with a λ/4 plate to produce circularly polarized excitation pump light. The λ/4 plate was continuously rotated from 0° to 360°, which provided the fundamental pump polarization change from linear to left- and right-handed circular polarization (LCP and RCP).

The results for (*R*-MBA)$_4$Bi$_2$I$_{10}$ and (*S*-MBA)$_4$Bi$_2$I$_{10}$ are shown in Figure 14c and Figure 15c, respectively. The intensity profiles exhibit clear differences between the responses to LCP and RCP excitation under identical intensity conditions, demonstrating the material's sensitivity to the handedness of circular polarization. Furthermore, no mirror symmetry is observed with respect to a 180° rotation of the λ/4 plate, providing a definitive indication of the material's chirality.

To quantitatively evaluate the circular polarization sensitivity of SHG in (*R*-MBA)$_4$Bi$_2$I$_{10}$ and (*S*-MBA)$_4$Bi$_2$I$_{10}$, we calculated the anisotropy factor g_{SHG-CD}, as previously defined in the literature.[27]

$$g_{SHG-CD} = 2\frac{I^L_{SHG} - I^R_{SHG}}{I^L_{SHG+} I^R_{SHG}} \quad (7)$$

where I^L_{SHG} and I^R_{SHG} represent the intensity of detected SHG under LCP and RCP illumination, respectively. The calculated g_{SHG-CD} values were 0.088 for (*R*-MBA)$_4$Bi$_2$I$_{10}$ and 0.076 for (*R*-MBA)$_4$Bi$_2$I$_{10}$ at 1510 nm. However, these values are lower than the g_{SHG-CD} of 0.58 reported for (S-MBA)$_4$Bi$_2$Br$_{10}$ microplates in a recent study, [32] yet these results highlight the potential of these materials as innovative CPL detectors in the NIR region. This finding is particularly noteworthy because most current CPL detectors are designed for visible light detection. The demonstrated performance of (*R*-MBA)$_4$Bi$_2$I$_{10}$ in the NIR range highlights their innovative potential to broaden the scope of CPL detection, opening new possibilities for NIR applications.[27, 32]

5.4. Z-Scan measurements of (*R*-/*S*-/*Rac*-MBA)$_4$Bi$_2$I$_{10}$ thin films

Inspired by the pronounced THG response exhibited by the (*R*-/*S*-/*Rac*-MBA)$_4$Bi$_2$I$_{10}$ crystals, we extended our investigation to evaluate their third-order nonlinear optical properties governed by $\chi^{(3)}$. To achieve this, open- and closed-aperture Z-scan experiments were performed on thin films of all three samples under nonresonant excitation at 800 nm. These measurements provided insights into their nonlinear absorption and refractive indices, showcasing the materials' potential for advanced optical applications. The details of the Z-scan setup and data analysis are provided in Chapter 2. Briefly, the Z-scan experiments were conducted using a custom-built setup featuring a Ti: sapphire regenerative amplifier (Spitfire Pro XP, 35 fs, 800 nm, 1 kHz repetition rate) as the light source. Neutral density filters were used to fine-tune the laser power for the measurements. The laser beam was split into two components: one directed to an autocorrelator for pulse width measurement (pulse width before the setup was measured as 65 fs), and the other split further for the main experiment. A portion of the beam was sent to a reference photodiode, while the rest was focused onto the sample mounted on a translational stage (PI M414.3PD), achieving a focal spot size of approximately 70 μm. The transmitted beam was subsequently split and directed to two photodiodes—one with an aperture for closed-aperture measurements and the other without an aperture for open-aperture measurements. Data acquisition was done using a lock-in amplifier synchronized with an optical chopper in the beam path. The collected data was processed and analyzed through a custom LabVIEW interface.

5.4.1. Open aperture Z-Scan measurements

Figures 17, 18, and 19 depict the normalized transmittance versus sample position obtained from open-aperture Z-scan measurements for thin films of (*R*-MBA)$_4$Bi$_2$I$_{10}$, (*S*-MBA)$_4$Bi$_2$I$_{10}$ and (*Rac*-MBA)$_4$Bi$_2$I$_{10}$ at different input intensities. As the sample moves closer to the focal point, the normalized transmittance decreases, indicating the occurrence of reverse saturable absorption (RSA). Since the excitation energy (1.55 eV) is lower than the bandgap energy (2.48 eV) of (*R*-/*S*-/*Rac*-MBA)$_4$Bi$_2$I$_{10}$, direct single-photon transitions to the conduction band are not possible. The absorption spectrum of the (*R*-/*S*-/*Rac*-MBA)$_4$Bi$_2$I$_{10}$ films (Figure 8b) confirms the absence of one-photon absorption at 800 nm. Therefore, the observed decrease in transmittance near the focal point can be attributed to two-photon absorption (TPA), where electrons are excited to the conduction band through the simultaneous absorption of two photons. Therefore, the observed nonlinear absorption in the material under nonresonant excitation at 800 nm can be attributed to the generation of bound or free carriers through two-photon absorption (TPA) processes.

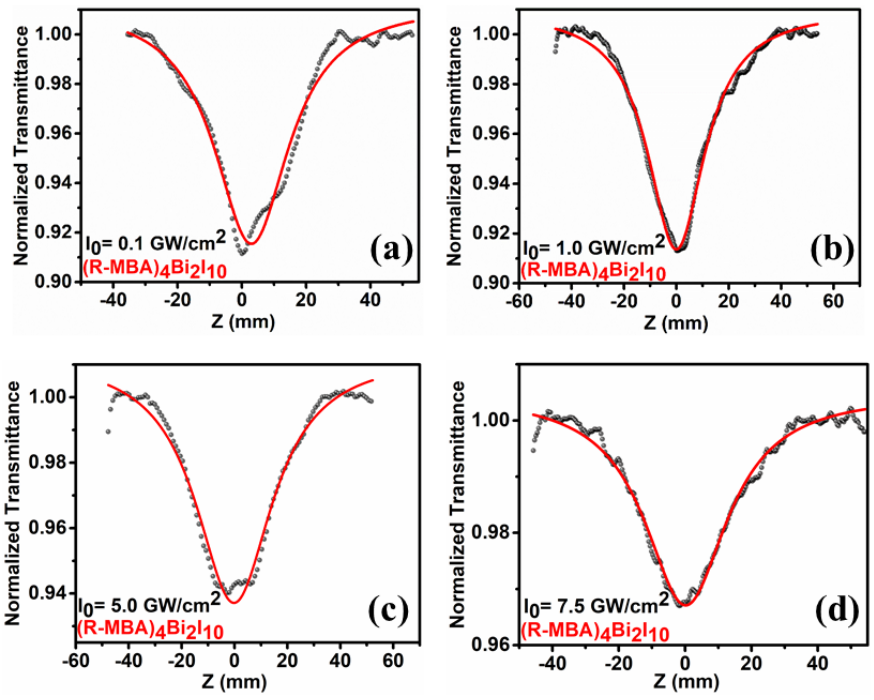

Figure 17. Open aperture (OA) Z-scan curves obtained for (*R*-MBA)$_4$Bi$_2$I$_{10}$ film at different intensities **(a)** 0.1 GW/cm^2, **(b)** 1.0 GW/cm^2, **(c)** 5.0 GW/cm^2, and **(d)** 7.5 GW/cm^2 with fs laser excitation at 800 nm. The red curves are the fits to the Equation 8.

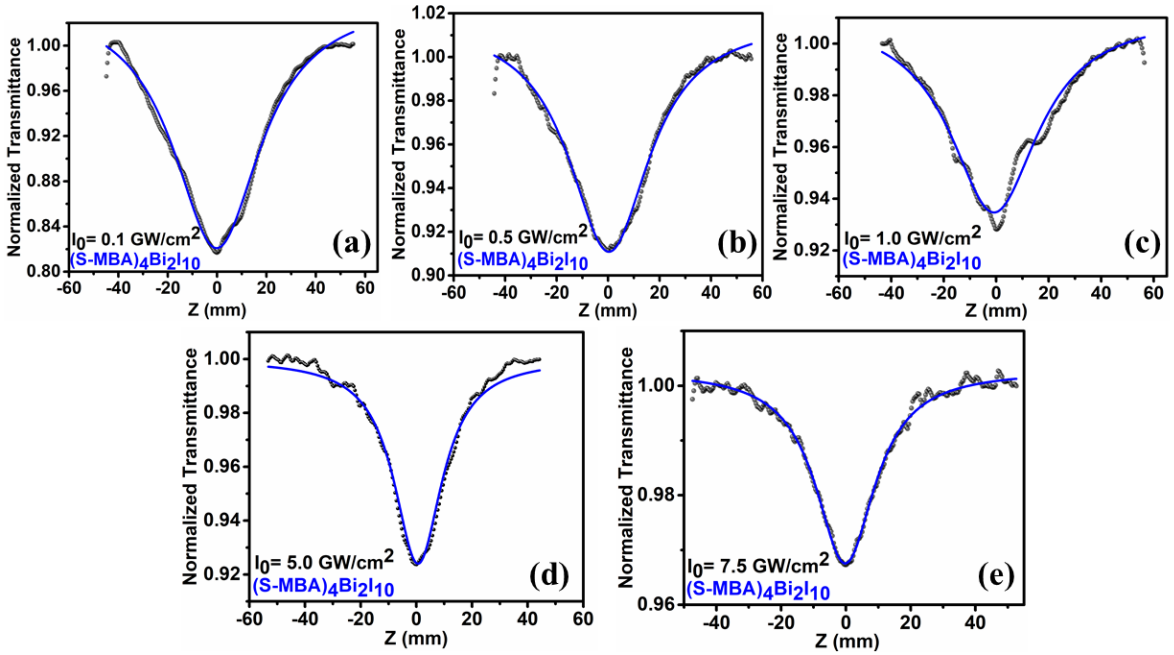

Figure 18. Open aperture (OA) Z-scan curves obtained for (*S*-MBA)$_4$Bi$_2$I$_{10}$ film at different intensities **(a)** 0.1 GW/cm^2, **(b)** 0.5 GW/cm^2, **(c)** 1.0 GW/cm^2, **(d)** 5.0 GW/cm^2 and **(e)** 7.5 GW/cm^2 with fs laser excitation at 800 nm. The blue curves are the fits to the Equation 8.

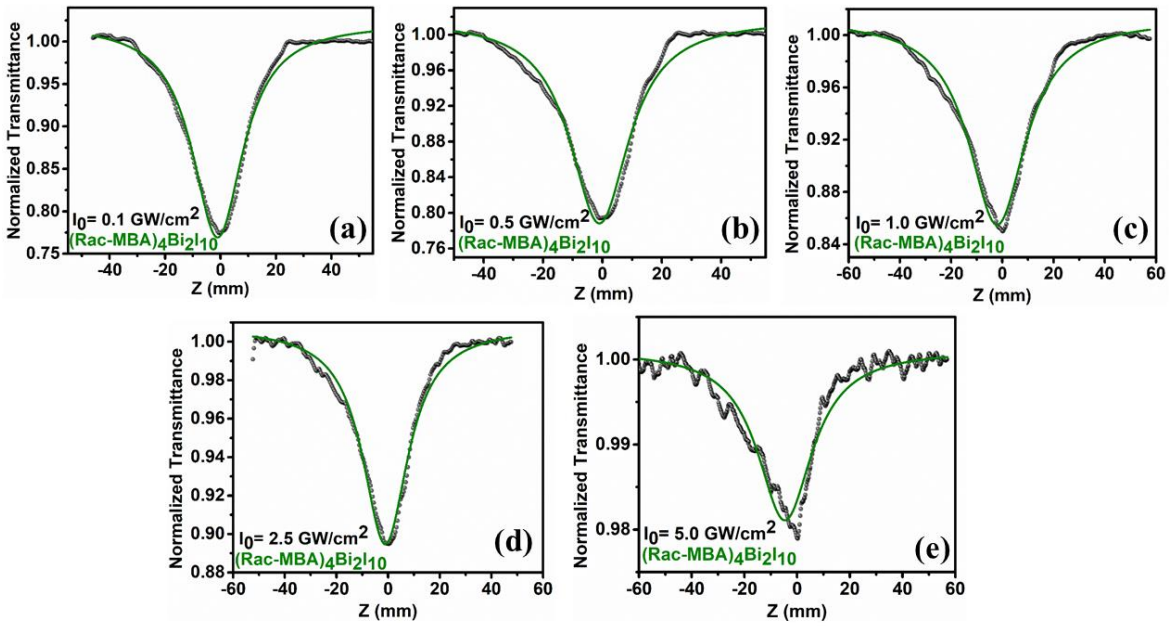

Figure 19. Open aperture (OA) Z-scan curves obtained for (*Rac*-MBA)$_4$Bi$_2$I$_{10}$ film at different intensities **(a)** 0.1 GW/cm^2, **(b)** 0.5 GW/cm^2, **(c)** 1.0 GW/cm^2, **(d)** 2.5 GW/cm^2 and **(e)** 5.0 GW/cm^2 with fs laser excitation at 800 nm. The green curves are the fits to the Equation 8.

Careful control of the incident light intensity ensured the avoidance of supercontinuum generation during the experiments. The scans were repeated multiple times to obtain a good signal-to-noise ratio. Additionally, with the use of ultrashort pulses with a 1 kHz repetition rate, nonlinear scattering and thermal effects were minimal.

We have extracted the TPA coefficient for (*R*-/*S*-/*Rac*-MBA)$_4$Bi$_2$I$_{10}$ films by fitting their obtained open aperture Z-scan transmittance data to Equation (8).[45]

$$T(z) = 1 - \frac{1}{2\sqrt{2}}\left(\frac{Q}{1+{(z-z_0)^2}/{z_r^2}}\right) \quad (8)$$

where, $Q = \beta I_0 L_{eff}$

and, $L_{eff} = {1 - e^{-\alpha_0}L}/{\alpha_0}$

Q is the nonlinear absorption parameter, z_0 is the focal point, β is the TPA coefficient, L_{eff} is the effective sample length, and I_0 is the peak irradiance.

The Rayleigh length, z_r is defined as $z_r = \pi w_0^2/\lambda$ and in this experiment it is determined to be 5.8 mm. Here w_0 (70.14 μm) is the beam width at the focus. The effective path length, 120 nm, is significantly smaller than the Rayleigh range (z_r), fulfilling the thin film approximation condition $L_{eff} << z_r$.

5.4.2 Close aperture Z-Scan measurements

Figures 20, Figure 21, and Figure 22 represent the closed-aperture (CA) Z-scan traces obtained for thin films of (*R*-MBA)$_4$Bi$_2$I$_{10}$, (*S*-MBA)$_4$Bi$_2$I$_{10}$, and (*Rac*-MBA)$_4$Bi$_2$I$_{10}$ respectively at different input intensities. For (*R*-MBA)$_4$Bi$_2$I$_{10}$, the CA curves reveal a valley-peak configuration, with a pre-focal transmission dip (valley) followed by a post-focal transmission rise (peak). This behavior indicates positive refractive nonlinearity, characterized by a nonlinear refractive index ($n_2>0$). Conversely, (*S*-MBA)$_4$Bi$_2$I$_{10}$ shows a reversed peak-valley structure, indicating negative refractive nonlinearity ($n_2<0$). A similar trend is observed for (*Rac*-MBA)$_4$Bi$_2$I$_{10}$.

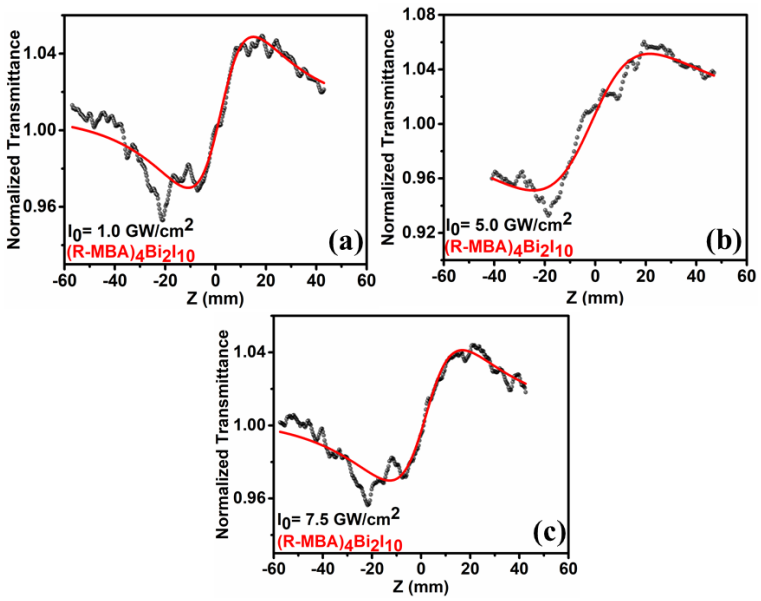

Figure 20. Closed-aperture (CA) Z-scan curves obtained for (*S*-MBA)$_4$Bi$_2$I$_{10}$ film at different intensities **(a)** 1.0 GW/cm^2, **(b)** 5.0 GW/cm^2, and **(c)** 7.5 GW/cm^2 with fs laser excitation at 800 nm. The blue curves are the fits to the Equation 9.

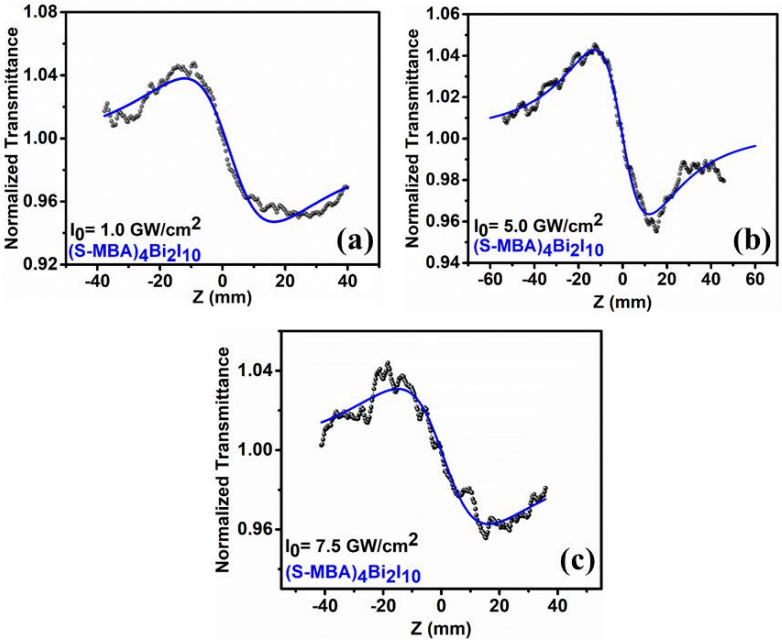

Figure 21. Closed-aperture (CA) Z-scan curves obtained for (*S*-MBA)$_4$Bi$_2$I$_{10}$ film at different intensities **(a)** 1.0 GW/cm^2, **(b)** 5.0 GW/cm^2, and **(c)** 7.5 GW/cm^2 with fs laser excitation at 800 nm. The blue curves are the fits to the Equation 9.

We determined the values of n_2 by fitting the CA traces to the following equation (Equation 9).[46]

$$T(z)_{close} = 1 - \frac{4x}{(1+x^2)(9+x^2)}\Delta\phi_0 \quad (9)$$

$x = {}^{z}/_{z_r}$

$\Delta\phi_0 = k\, n_2 I_0 L_{eff}$

Here $\Delta\phi_0$is on axis nonlinear phase shift with the sample at focus (z=0), n_2 is the third-order nonlinear refractive index, and $k = {}^{2\pi}/_{\lambda}$ is the wave vector.

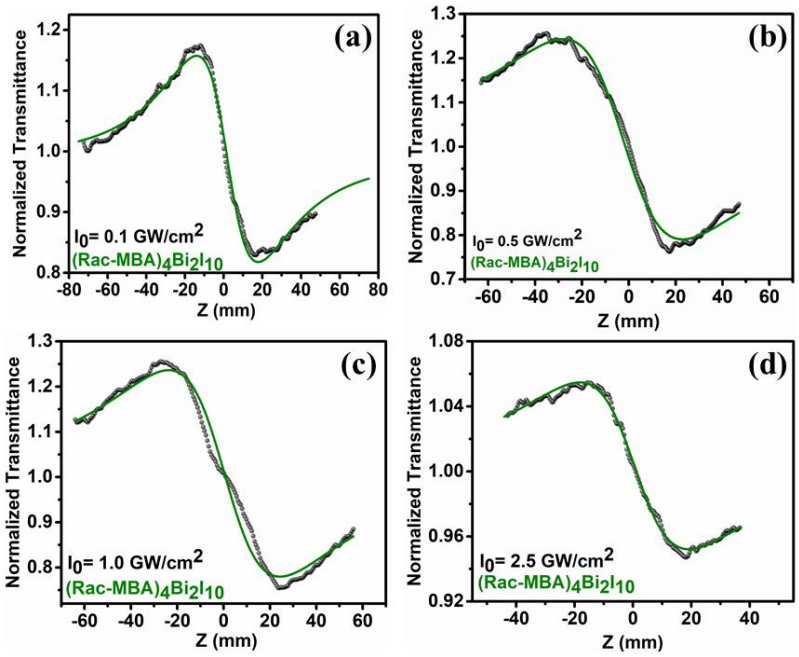

Figure 22. Closed-aperture (CA) Z-scan curves obtained for (*Rac*-MBA)$_4$Bi$_2$I$_{10}$ film at different intensities **(a)** 0.1 GW/cm^2, **(b)** 0.5 GW/cm^2, **(c)** 1.0 GW/cm^2, and **(d)** 2.5 GW/cm^2 with fs laser excitation at 800 nm. The green curves are the fits to the Equation 9.

We determined the values of β and n_2 for (*R*-/*S*-/*Rac*-MBA)$_4$Bi$_2$I$_{10}$ films across a range of peak intensities from 0.1 GW/cm² to 7.5 GW/cm², as shown in Table 4. The THG response driven by $\chi^{(3)}$ was particularly strong for (*R*-/*S*-/*Rac*-MBA)$_4$Bi$_2$I$_{10}$, which was also reflected in these $\chi^{(3)}$-related third-order nonlinear parameters, i.e. the TPA coefficient β and the nonlinear refractive index n_2, obtained from Z-scan measurements. The highest β value, measured at 0.1 GW/cm², was

5.3×10^5 cm/GW for (*Rac*-MBA)$_4$Bi$_2$I$_{10}$, which is exceptionally high compared to other perovskite-derived materials (refer to Table 5). Furthermore, (*Rac*-MBA)$_4$Bi$_2$I$_{10}$ exhibited a nonlinear refractive index at significantly lower peak intensities than its chiral counterparts, (*R*-/*S*-MBA)$_4$Bi$_2$I$_{10}$. The maximum n_2 value recorded for (*Rac*-MBA)$_4$Bi$_2$I$_{10}$ at 0.1 GW/cm² was 8.81 cm²/GW. Both (*R*-MBA)$_4$Bi$_2$I$_{10}$ and (*S*-MBA)$_4$Bi$_2$I$_{10}$ also demonstrated high β values, comparable to that of (*Rac*-MBA)$_4$Bi$_2$I$_{10}$, as shown in Table 4.

Table 4. Third Order NLO coefficients β and n_2 for (*R*-/*S*-/*Rac*-MBA)$_4$Bi$_2$I$_{10}$ thin films.

I_0 (GW/cm^2)	β (cm/GW)			n_2 (cm²/GW)		
	R	*S*	*Rac*	*R*	*S*	*Rac*
0.1	2.3×10^5 (±8010)	2.6×10^5 (±8086)	5.3×10^5 (±15244)	-	-	- 8.81 (±0.25)
0.5	-	5.4×10^4 (±1744)	1.1×10^5 (±3122)	-	-	- 2.35 (±0.06)
1.0	2.2×10^4 (±793)	1.8×10^4 (±624)	2.6×10^4 (±756)	0.20 (±0.003)	- 0.19 (±0.007)	- 0.47 (±0.01)
2.5	-	-	1.4×10^4 (±423)	-	-	- 0.26 (±0.007)
5.0	3.5×10^3 (±137)	3.9×10^3 (±117)	9.3×10^3 (±275)	0.05 (±0.001)	- 0.04 (±0.001)	-
7.5	1.1×10^3 (±43.2)	1.2×10^3 (±36.9)	-	0.02 (±0.0008)	- 0.02 (±0.001)	-

Interestingly, (*R*-MBA)$_4$Bi$_2$I$_{10}$ and (*S*-MBA)$_4$Bi$_2$I$_{10}$ exhibit opposite signs for n_2. This difference in the sign of n_2 may be attributed to structural or symmetry variations between the two, which could differentially affect their nonlinear optical responses. The high values of nonlinear parameters observed in (*R*-/*S*-/*Rac*-MBA)$_4$Bi$_2$I$_{10}$ thin films are likely a result of their 0D structural configuration. This unique structure provides strong quantum and dielectric confinement, significantly enhancing their nonlinear optical properties.[47-48] Furthermore, these materials exhibit a high exciton binding energy of approximately 150 meV, indicating substantial confinement of

electrons and holes within the inorganic $[Bi_2I_{10}]^{4-}$dimers.[33] This characteristic of the 0D perovskite derivative structure is likely a key factor contributing to the enhanced nonlinear optical responses observed.

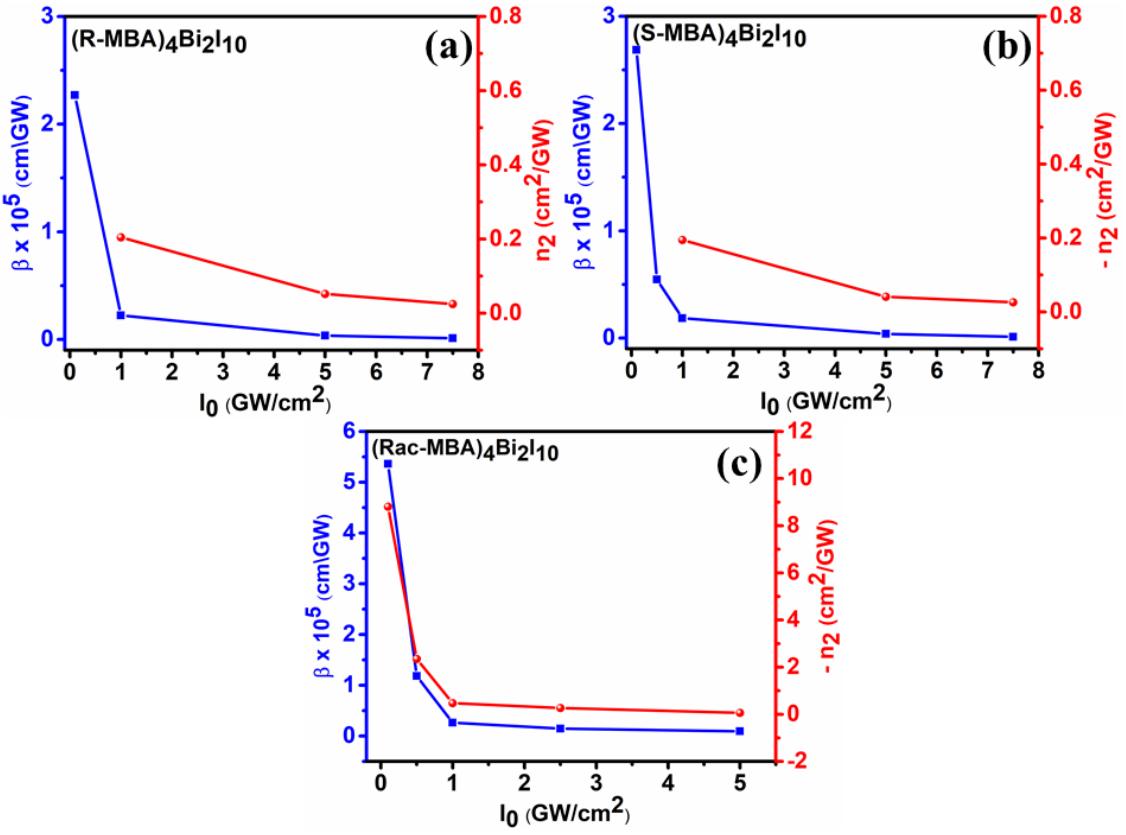

Figure 23. Variation of two-photon absorption (TPA) coefficient (β) and nonlinear refractive index (n_2) as a function of input intensity for **(a)** (*R*-MBA)$_4$Bi$_2$I$_{10}$, **(b)** (*S*-MBA)$_4$Bi$_2$I$_{10}$ and **(c)** (*Rac*-MBA)$_4$Bi$_2$I$_{10}$.

Figure 23 shows the variation of β and n_2 as a function of input intensity for (*R*-/*S*-/*Rac*-MBA)$_4$Bi$_2$I$_{10}$. In all three samples, both β and n_2 were decreasing with increasing input intensity and eventually saturating at higher intensities. The reduction in n_2 with rising intensity can be attributed to an increase in charge carrier density at higher intensities. The effective nonlinear refractive index, n_2^*, can be expressed using the following relation.[49]

$$n_2^* = n_2 + \frac{\xi_\gamma n(t)}{I} \tag{10}$$

Here, $n(t)$ is the photoexcited carrier density, ξ_γ is the change in refractive index per unit density of conduction band electrons, and I is the input intensity.

Free carriers can influence the refractive index due to their ability to absorb light.[50] Under nonresonant excitation, free carriers are primarily generated through multiphoton absorption, whereas under resonant conditions, they arise from linear absorption. During nonresonant femtosecond excitation at low intensities, the primary contribution to nonlinearity originates from bound charge carriers, as TPA is relatively weak in this regime. However, as the intensity increases, the nonlinearity becomes dominated by free carriers, which accumulate during the pulse.

Table 5. Comparison of two-photon absorption (TPA) coefficient (β) and nonlinear refractive index (n_2) of halide perovskites thin films.

Material	Excitation	β (cm/W)	n_2 (cm²/W)	Ref.
$CsPbBr_3$ NC thin film	600-800 nm, 1kHz, 70 fs	1.8×10^{-9}	$\sim 10^{-9}$	54
$CH_3NH_3Pb_{0.75}Sn_{0.25}I_3$ thin film	1535 nm, 400 fs, 43 MHz	1.15×10^{-3}	-	55
Cs_4PbBr_6 0D thin film	500-1500 nm, 70 fs, 1kHz,	$\sim 10^{-7}$	$\sim 10^{-9}$	45
$(BA)_2PbI_4$ thin film	550 nm	1.01×10^{-5}	7.1×10^{-11}	56
$CH_3NH_3PbBr_3$ thin film	1028 nm, 40 ns, 1 kHz	2.72×10^{-4}	1.9×10^{-11}	52
(*R*-MBA)$_4Bi_2I_{10}$ thin film	800 nm, 65 fs, 1kHz	2.3×10^{-4}	2.0×10^{-10}	this work
(*S*-MBA)$_4Bi_2I_{10}$ thin film	800 nm, 65 fs, 1kHz	2.6×10^{-4}	1.9×10^{-10}	this work
(*Rac*-MBA)$_4Bi_2I_{10}$ thin film	800 nm, 65 fs, 1kHz	5.3×10^{-4}	-8.81×10^{-9}	this work

In the low-intensity regime, TPA remains minimal, and n(t) remains nearly constant, causing the effective nonlinear refractive index, n_2^*, to decrease as the excitation power increases, following Equation 10. At higher intensities, the growth of n(t) becomes progressively counterbalanced by the rising excitation intensity, resulting in the saturation of n_2^* at elevated intensities.[51]

All three samples, (*R*-/*S*-/*Rac*-MBA)$_4$Bi$_2$I$_{10}$, exhibit a similar trend in their β values too, which decrease and eventually saturate as input intensity increases. This behavior is likely due to the direct dependence of β on the charge carrier density.[52] Similar reductions in optical nonlinearities have been reported for other materials, including graphene, and [53] methylammonium lead halide thin films.[52]

Additionally, an increase in transmission near the focal point is observed in the Z-scan measurements as input intensity rises. This phenomenon can be attributed to ground-state saturation, resulting from an elevated charge carrier density at higher intensities. However, a complete transition from reverse saturable absorption (RSA) to saturable absorption (SA) was not observed. Consequently, the observed variations in refractive index and nonlinear absorption are attributed to changes in free charge carrier density induced by indirect two-photon optical transitions.

5.5. Conclusions

We have explored the second- and third-order nonlinear optical (NLO) properties of (*R*-/*S*-/*Rac*-MBA)$_4$Bi$_2$I$_{10}$ and determined their corresponding nonlinear coefficients. The chiral crystals (*R*-/*S*-MBA)$_4$Bi$_2$I$_{10}$ exhibit second-harmonic generation (SHG) responses, alongside significantly stronger third-harmonic generation (THG) responses when excited with femtosecond near-infrared (NIR) pulses in the 1360–1590 nm range. The achiral counterpart, (*Rac*-MBA)$_4$Bi$_2$I$_{10}$, demonstrates the highest THG intensity among the samples. All crystals exhibit excellent optical stability, as evidenced by their high laser-induced damage threshold (LIDT) values.

Both chiral and achiral samples show resonance enhancement of the THG response, corresponding to their excitonic absorption peak around 510 nm. The chiral crystals also display circularly polarized SHG with a polarization ratio of approximately 8%. Z-scan measurements on thin films of these 0D perovskitoids, under femtosecond laser excitation at 800 nm, reveal exceptionally high values for the nonlinear absorption coefficient (β) and the nonlinear refractive index (n_2), with the

achiral (*Rac*-MBA)$_4$Bi$_2$I$_{10}$ showing the highest values. Both β and n_2 exhibit an inverse relationship with input intensity, with saturation effects becoming evident at higher intensities. At these elevated intensities, third-order nonlinearity is predominantly governed by free carriers generated through two-photon absorption. These findings highlight the potential of hybrid chiral metal halides as efficient and optically stable materials for NLO applications. Their strong THG response, large β and n_2 values, and excellent optical stability make them promising candidates for technologies such as optical switching and upconverted lasing.

5.6. References

1. Boyd, R. W., Chapter 1 - The Nonlinear Optical Susceptibility. In *Nonlinear Optics (Third Edition)*, Boyd, R. W., Ed. Academic Press: Burlington, 2008; pp 1-67.

2. Zhang, R.; Fan, J.; Zhang, X.; Yu, H.; Zhang, H.; Mai, Y.; Xu, T.; Wang, J.; Snaith, H. J., Nonlinear Optical Response of Organic–Inorganic Halide Perovskites. *ACS Photonics* **2016,** *3* (3), 371-377.

3. Song, Y.; Chen, Y.; Jiang, X.; Ge, Y.; Wang, Y.; You, K.; Wang, K.; Zheng, J.; Ji, J.; Zhang, Y.; Li, J.; Zhang, H., Nonlinear Few-Layer MXene-Assisted All-Optical Wavelength Conversion at Telecommunication Band. *Advanced Optical Materials* **2019,** *7* (18), 1801777.

4. Nayak, A.; Park, J.; De Mey, K.; Hu, X.; Duncan, T. V.; Beratan, D. N.; Clays, K.; Therien, M. J., Large Hyperpolarizabilities at Telecommunication-Relevant Wavelengths in Donor–Acceptor–Donor Nonlinear Optical Chromophores. *ACS Central Science* **2016,** *2* (12), 954-966.

5. Ye, W.; Zeuner, F.; Li, X.; Reineke, B.; He, S.; Qiu, C.-W.; Liu, J.; Wang, Y.; Zhang, S.; Zentgraf, T., Spin and wavelength multiplexed nonlinear metasurface holography. *Nature Communications* **2016,** *7* (1), 11930.

6. Xu, J.; Li, X.; Xiong, J.; Yuan, C.; Semin, S.; Rasing, T.; Bu, X.-H., Halide Perovskites for Nonlinear Optics. *Advanced Materials* **2020,** *32* (3), 1806736.

7. Braune, M.; Maiwald, M.; Eppich, B.; Brox, O.; Ginolas, A.; Sumpf, B.; Trankle, G., Design and Realization of a Miniaturized DFB Diode Laser-Based SHG Light Source With a 2-nm Tunable Emission at 488should be a spacenm. *IEEE Transactions on Components, Packaging and Manufacturing Technology* **2017,** *PP*, 1-6.

8. Li, G.; Chen, Y.; Jiang, H.; Chen, X., Broadband sum-frequency generation using d33 in periodically poled LiNbO3 thin film in the telecommunications band. *Opt. Lett.* **2017,** *42* (5), 939-942.

9. Yao, L.; Zeng, Z.; Cai, C.; Xu, P.; Gu, H.; Gao, L.; Han, J.; Zhang, X.; Wang, X.; Wang, X.; Pan, A.; Wang, J.; Liang, W.; Liu, S.; Chen, C.; Tang, J., Strong Second- and Third-Harmonic Generation in 1D Chiral Hybrid Bismuth Halides. *Journal of the American Chemical Society* **2021,** *143* (39), 16095-16104.

10. Ravindran, S.; Datta, A.; Alameh, K.; Lee, Y. T., GaAs based long-wavelength microring resonator optical switches utilising bias assisted carrier-injection induced refractive index change. *Opt. Express* **2012,** *20* (14), 15610-15627.

11. Geldenhuys, R.; Merwe, J. S. V. D.; Thakulsukanant, K.; Wang, Z.; Chi, N.; Yu, S., Contention resolution and variable length optical packet switching using the active vertical-coupler-based optical Crosspoint switch. *Opt. Switch. Netw.* **2011,** *8* (2), 86–92.

12. Connelly, M. J., Theoretical calculations of the carrier induced refractive index change in tensile-strained InGaAsP for use in 1550 nm semiconductor optical amplifiers. *Applied Physics Letters* **2008,** *93* (18).

13. Shin, S.; Su, C. B., Strong increase of the derivative of the carrier-induced index change of semiconductor lasers at low injected carrier density. *IEEE Photonics Technology Letters* **1993,** *5*, 981-983.

14. Shen, W.; Chen, J.; Wu, J.; Li, X.; Zeng, H., Nonlinear Optics in Lead Halide Perovskites: Mechanisms and Applications. *ACS Photonics* **2021,** *8* (1), 113-124.

15. Baikie, T.; Fang, Y.; Kadro, J. M.; Schreyer, M.; Wei, F.; Mhaisalkar, S. G.; Graetzel, M.; White, T. J., Synthesis and crystal chemistry of the hybrid perovskite (CH3NH3)PbI3 for solid-state sensitised solar cell applications. *Journal of Materials Chemistry A* **2013,** *1* (18), 5628-5641.

16. Ma, J.; Wang, H.; Li, D., Recent Progress of Chiral Perovskites: Materials, Synthesis, and Properties. *Advanced Materials* **2021,** *33* (26), 2008785.

17. Billing, D. G.; Lemmerer, A., Synthesis and crystal structures of inorganic–organic hybrids incorporating an aromatic amine with a chiral functional group. *CrystEngComm* **2006,** *8* (9), 686-695.

18. Ahn, J.; Lee, E.; Tan, J.; Yang, W.; Kim, B.; Moon, J., A new class of chiral semiconductors: chiral-organic-molecule-incorporating organic–inorganic hybrid perovskites. *Materials Horizons* **2017,** *4* (5), 851-856.

19. Jana, M. K.; Song, R.; Liu, H.; Khanal, D. R.; Janke, S. M.; Zhao, R.; Liu, C.; Valy Vardeny, Z.; Blum, V.; Mitzi, D. B., Organic-to-inorganic structural chirality transfer in a 2D hybrid perovskite and impact on Rashba-Dresselhaus spin-orbit coupling. *Nature Communications* **2020,** *11* (1), 4699.

20. Ma, J.; Fang, C.; Chen, C.; Jin, L.; Wang, J.; Wang, S.; Tang, J.; Li, D., Chiral 2D Perovskites with a High Degree of Circularly Polarized Photoluminescence. *ACS Nano* **2019,** *13* (3), 3659-3665.

21. Yuan, C.; Li, X.; Semin, S.; Feng, Y.; Rasing, T.; Xu, J., Chiral Lead Halide Perovskite Nanowires for Second-Order Nonlinear Optics. *Nano Letters* **2018,** *18* (9), 5411-5417.

22. Ahn, J.; Ma, S.; Kim, J.-Y.; Kyhm, J.; Yang, W.; Lim, J. A.; Kotov, N. A.; Moon, J., Chiral 2D Organic Inorganic Hybrid Perovskite with Circular Dichroism Tunable Over Wide Wavelength Range. *Journal of the American Chemical Society* **2020,** *142* (9), 4206-4212.

23. Long, G.; Sabatini, R.; Saidaminov, M. I.; Lakhwani, G.; Rasmita, A.; Liu, X.; Sargent, E. H.; Gao, W., Chiral-perovskite optoelectronics. *Nature Reviews Materials* **2020,** *5* (6), 423-439.

24. Dong, Y.; Zhang, Y.; Li, X.; Feng, Y.; Zhang, H.; Xu, J., Chiral Perovskites: Promising Materials toward Next-Generation Optoelectronics. *Small* **2019,** *15* (39), 1902237.

25. Sheikh, T.; Maqbool, S.; Rajput, P. K.; Mandal, P.; Nag, A., Effect of chirality on the optical properties of layered hybrid perovskite R- and S-α-methylbenzylammonium lead iodide. *Chemical Communications* **2022,** *58* (55), 7650-7653.

26. Zheng, Y.; Xu, J.; Bu, X.-H., 1D Chiral Lead Halide Perovskites with Superior Second-Order Optical Nonlinearity. *Advanced Optical Materials* **2022,** *10* (1), 2101545.

27. Fu, D.; Xin, J.; He, Y.; Wu, S.; Zhang, X.; Zhang, X.-M.; Luo, J., Chirality-Dependent Second-Order Nonlinear Optical Effect in 1D Organic–Inorganic Hybrid Perovskite Bulk Single Crystal. *Angewandte Chemie International Edition* **2021,** *60* (36), 20021-20026.

28. Coccia, C.; Moroni, M.; Malavasi, L., Chiral Metal Halide Perovskites: Focus on Lead-Free Materials and Structure-Property Correlations. *Molecules* **2023,** *28* (16), 6166.

29. Jiang, S.; Zhao, P.; Xing, G.; Kang, H.; Li, X.; Zhao, T.; Li, B.; Zhang, T., Bismuth-Based Chiral Perovskite with Different Dimensions for Second-Order Nonlinear Optical Properties. *Advanced Optical Materials* **2023,** *11* (18), 2203078.

30. Tao, K.; Li, Q.; Yan, Q., 1D Tin(II)-Based Chiral Hybrid Perovskite Single Crystals with Extremely Distorted Inorganic Chains for Second Harmonic Generation. *Advanced Optical Materials* **2024,** *12* (17), 2400018.

31. Zhao, L.; Han, X.; Zheng, Y.; Yu, M.-H.; Xu, J., Tin-Based Chiral Perovskites with Second-Order Nonlinear Optical Properties. *Advanced Photonics Research* **2021,** *2* (11), 2100056.

32. Fu, X.; Zeng, Z.; Jiao, S.; Wang, X.; Wang, J.; Jiang, Y.; Zheng, W.; Zhang, D.; Tian, Z.; Li, Q.; Pan, A., Highly Anisotropic Second-Order Nonlinear Optical Effects in the Chiral Lead-Free Perovskite Spiral Microplates. *Nano Letters* **2023,** *23* (2), 606-613.

33. Rajput, P. K.; Poonia, A. K.; Mukherjee, S.; Sheikh, T.; Shrivastava, M.; Adarsh, K. V.; Nag, A., Chiral Methylbenzylammonium Bismuth Iodide with Zero-Dimensional Perovskite Derivative Structure. *The Journal of Physical Chemistry C* **2022,** *126* (23), 9889-9897.

34. Kim, Y.-H.; Zhai, Y.; Lu, H.; Pan, X.; Xiao, C.; Gaulding, E. A.; Harvey, S. P.; Berry, J. J.; Vardeny, Z. V.; Luther, J. M.; Beard, M. C., Chiral-induced spin selectivity enables a room-temperature spin light-emitting diode. *Science* **2021,** *371* (6534), 1129-1133.

35. Ben-Moshe, A.; Teitelboim, A.; Oron, D.; Markovich, G., Probing the Interaction of Quantum Dots with Chiral Capping Molecules Using Circular Dichroism Spectroscopy. *Nano Letters* **2016,** *16* (12), 7467-7473.

36. Abdelwahab, I.; Grinblat, G.; Leng, K.; Li, Y.; Chi, X.; Rusydi, A.; Maier, S. A.; Loh, K. P., Highly Enhanced Third-Harmonic Generation in 2D Perovskites at Excitonic Resonances. *ACS Nano* **2018,** *12* (1), 644-650.

37. Kuk, Y.; Kee, J.; Ok, K. M., Chiral Ligand-Driven Systematic Synthesis of Coordination Polymers with Non-centrosymmetric Structures. *Chemistry – A European Journal* **2022,** *28* (19), e202200007.

38. Maqbool, S.; Thekkayil, Z.; Mandal, P., 1D Diisopropylammonium Lead Iodide Perovskite Shows Exceptional Optical Stability and Third-Order Nonlinearity. *Advanced Optical Materials* **2023,** *11* (15), 2202942.

39. Youngblood, N.; Peng, R.; Nemilentsau, A.; Low, T.; Li, M., Layer-Tunable Third-Harmonic Generation in Multilayer Black Phosphorus. *ACS Photonics* **2017,** *4* (1), 8-14.

40. Morris, C. D.; Chung, I.; Park, S.; Harrison, C. M.; Clark, D. J.; Jang, J. I.; Kanatzidis, M. G., Molecular Germanium Selenophosphate Salts: Phase-Change Properties and Strong Second Harmonic Generation. *Journal of the American Chemical Society* **2012,** *134* (51), 20733-20744.

41. Maqbool, S.; Sheikh, T.; Thekkayil, Z.; Deswal, S.; Boomishankar, R.; Nag, A.; Mandal, P., Third Harmonic Upconversion and Self-Trapped Excitonic Emission in 1D Pyridinium Lead Iodide. *The Journal of Physical Chemistry C* **2021,** *125* (41), 22674-22683.

42. Feutmba, G. F.; Hermans, A.; George, J. P.; Rijckaert, H.; Ansari, I.; Van Thourhout, D.; Beeckman, J., Reversible and Tunable Second-Order Nonlinear Optical Susceptibility in PZT Thin Films for Integrated Optics. *Advanced Optical Materials* **2021,** *9* (16), 2100149.

43. Fehn, T.; Vogtmann, T.; Hübner, J.; Schwoerer, M., Anisotropy of the nonlinear optical susceptibility χ(3) in polydiacetylene single crystals. *Applied Physics B* **1994,** *59* (2), 203-209.

44. Duan, Y.; Ju, C.; Yang, G.; Fron, E.; Coutino-Gonzalez, E.; Semin, S.; Fan, C.; Balok, R. S.; Cremers, J.; Tinnemans, P.; Feng, Y.; Li, Y.; Hofkens, J.; Rowan, A. E.; Rasing, T.; Xu, J., Aggregation Induced Enhancement of Linear and Nonlinear Optical Emission from a Hexaphenylene Derivative. *Advanced Functional Materials* **2016,** *26* (48), 8968-8977.

45. Krishnakanth, K. N.; Seth, S.; Samanta, A.; Venugopal Rao, S., Broadband ultrafast nonlinear optical studies revealing exciting multi-photon absorption coefficients in phase pure zero-dimensional Cs4PbBr6 perovskite films. *Nanoscale* **2019,** *11* (3), 945-954.

46. Sheik-Bahae, M.; Said, A. A.; Van Stryland, E. W., High-sensitivity, single-beam n2 measurements. *Opt. Lett.* **1989,** *14* (17), 955-957.

47. Edet, C. O.; Al, E. B.; Ungan, F.; Ali, N.; Ramli, M. M.; Asjad, M., Effects of the confinement potential parameters and optical intensity on the linear and nonlinear optical properties of spherical quantum dots. *Results in Physics* **2023,** *44*, 106182.

48. Saouma, F. O.; Stoumpos, C. C.; Wong, J.; Kanatzidis, M. G.; Jang, J. I., Selective enhancement of optical nonlinearity in two-dimensional organic-inorganic lead iodide perovskites. *Nature Communications* **2017,** *8* (1), 742.

49. Zheng, X.; Zhang, Y.; Chen, R.; Cheng, X. a.; Xu, Z.; Jiang, T., Z-scan measurement of the nonlinear refractive index of monolayer WS2. *Opt. Express* **2015,** *23* (12), 15616-15623.

50. Bulutay, C.; Turgut, C. M.; Zakhleniuk, N. A., Carrier-induced refractive index change and optical absorption in wurtzite InN and GaN: Full-band approach. *Physical Review B* **2010,** *81* (15), 155206.

51. Mushtaq, A.; Pradhan, B.; Kushavah, D.; Zhang, Y.; Wolf, M.; Schrenker, N.; Fron, E.; Bals, S.; Hofkens, J.; Debroye, E.; Pal, S. K., Third-Order Nonlinear Optical Properties and Saturation of Two-Photon Absorption in Lead-Free Double Perovskite Nanocrystals under Femtosecond Excitation. *ACS Photonics* **2021,** *8* (11), 3365-3374.

52. Kalanoor, B. S.; Gouda, L.; Gottesman, R.; Tirosh, S.; Haltzi, E.; Zaban, A.; Tischler, Y. R., Third-Order Optical Nonlinearities in Organometallic Methylammonium Lead Iodide Perovskite Thin Films. *ACS Photonics* **2016,** *3* (3), 361-370.

53. Zhao, M.; Peng, R.; Zheng, Q.; Wang, Q.; Chang, M.-J.; Liu, Y.; Song, Y.-L.; Zhang, H.-L., Broadband optical limiting response of a graphene–PbS nanohybrid. *Nanoscale* **2015,** *7* (20), 9268-9274.

54. Krishnakanth, K. N.; Seth, S.; Samanta, A.; Rao, S. V., Broadband femtosecond nonlinear optical properties of CsPbBr 3 perovskite nanocrystals. *Opt. Lett.* **2018,** *43* (3), 603-606.

55. Xie, Y.; Fan, J.; Liu, C.; Chi, S.; Wang, Z.; Yu, H.; Zhang, H.; Mai, Y.; Wang, J., Giant Two-Photon Absorption in Mixed Halide Perovskite CH3NH3Pb0. 75Sn0. 25I3 Thin Films and Application to Photodetection at Optical Communication Wavelengths. *Advanced Optical Materials* **2018,** *6* (3), 1700819.

56. Liang, W.-Y.; Liu, F.; Lu, Y.-J.; Popović, J.; Djurišić, A.; Ahn, H., High optical nonlinearity in low-dimensional halide perovskite polycrystalline films. *Opt. Express* **2020,** *28* (17), 24919-24927.

57. Haynes, A. S.; Saouma, F. O.; Otieno, C. O.; Clark, D. J.; Shoemaker, D. P.; Jang, J. I.; Kanatzidis, M. G., Phase-Change Behavior and Nonlinear Optical Second and Third Harmonic Generation of the One-Dimensional K(1–x)CsxPSe6 and Metastable β-CsPSe6. *Chemistry of Materials* **2015,** *27* (5), 1837-1846.

Chapter 6
Thesis Summary and Future Outlook

In this thesis, we investigated the charge carrier dynamics in $CsPbBr_3$ nanocrystals (NCs) integrated with two copper-based inorganic hole-transporting layers (HTLs). In photovoltaic devices, charge-transporting layers play a pivotal role. Following photon generation, these layers ensure efficient and irreversible charge separation, a critical factor for enhancing device performance. Focusing on hole-transporting layers, inorganic HTMs offer distinct advantages over their organic counterparts. These include exceptional stability under humid and high-temperature conditions, favorable band alignment, UV-visible transparency, and high hole mobility, making them highly promising for advanced photovoltaic applications.

Using time-resolved terahertz spectroscopy (TRTS) and transient absorption spectroscopy, we successfully monitored ultrafast hole injection from $CsPbBr_3$ NC films into CuI and Cu_2O HTLs. The hole transfer occurs on a sub-picosecond timescale, including the transfer of hot carriers. A quenching observed in the initial THz peak conductivity indicates that hole transfer occurs even faster than the instrument response time (~300 fs). The combination of excellent stability, solution processability, cost-effectiveness, and superior hole extraction efficiency establishes Cu_2O as a standout candidate for HTL applications. These results provide valuable insights into the underlying mechanisms of device operation and will definitely aid in developing innovative design strategies for more efficient photovoltaic devices.

We explored the mechanism behind the sharp increase in LSPR Q-factor with Cr co-doping in Sn-doped In_2O_3 NCs. We successfully monitored changes in the complex dielectric function of co-doped NCs, observing that the sample with the highest Cr doping concentration exhibited the highest dielectric constant. This enhancement is likely responsible for reducing ionic impurity scattering, as a higher dielectric constant weakens the Coulombic interaction between ionic dopants and free carriers.

Kerr nonlinearity measurements showed that increasing Cr doping concentration resulted in slower Kerr nonlinearity decay. The sample with the highest Cr doping exhibited the longest relaxation time, highlighting the ability to tailor Kerr nonlinearity by modulating doping levels and, consequently, the carrier density. Remarkably, all samples demonstrated optical Kerr effect (OKE) recovery times of less than one picosecond, making these materials highly suitable for ultrafast optical switching applications. OKE experiments also provided valuable insights into the vibrational dynamics of the material. A clear shift of vibrational modes toward lower frequencies

was observed with increasing Cr doping. Additionally, a low-energy optical phonon mode emerged with high Cr doping levels. The changes in vibrational dynamics, particularly the introduction of low-energy optical phonon modes, are expected to have a direct impact on the localized surface plasmon resonance (LSPR) properties of the material.

Chiral halide perovskites have garnered significant attention in recent years due to their remarkable nonlinear optical (NLO) properties. Studies have demonstrated wavelength-tunable and polarization-dependent second-harmonic generation (SHG) in low-dimensional chiral hybrid perovskites. However, the prevalent use of toxic lead (Pb) in these materials raises environmental concerns, prompting the development of lead-free alternatives.

We investigated the wavelength-tunable and polarization-dependent SHG and third-harmonic generation (THG) in a 0D chiral, lead-free hybrid perovskite derivative, ((*R*-/*S*-/*Rac*-MBA)$_4$Bi$_2$I$_{10,}$ where MBA represents methyl benzyl ammonium. Unlike previously reported bismuth-based chiral perovskites, this material exhibits both SHG and a significant THG response, coupled with excellent thermal stability.

The third-order nonlinear optical properties of these materials were examined using open-aperture (OA) and closed-aperture (CA) Z-scan techniques in the femtosecond (fs) regime. Z-scan measurements on thin films under 800 nm fs laser excitation revealed exceptionally high values for the nonlinear absorption coefficient (β) and nonlinear refractive index (n_2). Among the samples, the achiral (*R*-/*S*-MBA)$_4$Bi$_2$I$_{10}$ demonstrated the highest β and n_2 values. Both parameters showed an inverse relationship with input intensity, with saturation effects becoming evident at higher intensities. At elevated intensities, third-order nonlinearity was primarily dominated by free carriers generated through two-photon absorption.

The unique 0D structure of these materials provides strong quantum and dielectric confinement, significantly enhancing their NLO properties. Their strong THG response, large β and n_2 values, and outstanding optical stability position these hybrid chiral metal halides as promising candidates for advanced photonic applications, including optical switching and upconverted lasing.

While significant research efforts focus on developing new materials and improving device architectures to enhance efficiency, the study of charge carrier dynamics remains relatively underexplored. Ultrafast charge carrier dynamics in complete devices, involving the perovskite

absorber layer and charge transport layers, can provide critical insights into interfacial charge transfer efficiency and recombination mechanisms. Understanding these dynamics, especially in devices with alternative HTLs like NiO, CuSCN, and carbon-based materials such as graphene, paired with various perovskites, could pave the way to develop new device theories required to make efficient photovoltaics.

Chiral perovskites have demonstrated exceptional promise in nonlinear optical applications. There is still a high demand for efficient circularly polarized light (CPL) detectors and emitters across different regions of the electromagnetic spectrum. Techniques like Z-scan with circularly polarized light offer exciting opportunities to investigate third-order nonlinear optical properties in these chiral systems.

A particularly intriguing development arises from the interaction of chirality with electron spin. Chiral molecules have the unique ability to selectively filter electrons based on their spin properties, a phenomenon known as the spin filtering effect. This interplay between chirality and spin opens new pathways for applications in spintronics and quantum information systems.

List of Publications

1. Souvik Roy, Aman Chaturvedi, Sanjit Dey, DRG Koppalu Puneeth Kumar, Saikat Pahan, Souvik Panda Mahapatra, Pankaj Mandal, and Hosahudya Gopi*. Anion Tuned Structural Modulation and Nonlinear Optical Effects of Metal-Ion Directed 310-Helix Networks. *Chem. Eur. J., 2023, 29, 72, 0947-6539*.
2. Aman Chaturvedi, Parikshit Kumar Rajput, Shabnum Maqbool, Angshuman Nag, Pankaj Mandal*. Nonlinear Optical Properties of 0D Chiral Hybrid Bismuth Iodides. *(Accepted, Advanced Materials, DOI:10.1002/adma.202501022).*
3. Indra Narayan Chakraborty, Adhra S. Sury, Aman Chaturvedi, Ankit Dhankhar, Pankaj Mandal, and Pramod P. Pillai*. Quantum Dot-Sensitized Photon Upconversion Enables Chemical Synthesis with Visible-Light. *(Submitted)*
4. Aman Chaturvedi, Parikshit Kumar Rajput, Angshuman Nag, Pankaj Mandal. Bismuth based Chiral Hybrid Halides with Strong Second and Third Order Nonlinear Optical Properties. *(Manuscript under preparation)*
5. Aman Chaturvedi, Gurpreet Kaur, H.N. Ghosh, Pankaj Mandal*. Ultrafast Hole Injection Dynamics in $CsPbBr_3$ NCs with solution-processed CuI and Cu_2O as Hole Transporting Layers. *(Manuscript under preparation)*
6. Aman Chaturvedi, Bharat Tandon, Angshuman Nag, Pankaj Mandal*. Probing change in dielectric constant and Kerr nonlinearity with Cr doping in Sn-doped In_2O_3 nanocrystals. *(Manuscript under preparation)*
7. Souvik Roy, Aman Chaturvedi, Pankaj Mandal, H.N. Gopi*. Metal induced β-turns in the short Tripeptides. *(Manuscript under preparation).*

Copyrights and Permissions

IISER PUNE

Aman Chaturvedi <chaturvedi.aman@students.iiserpune.ac.in>

Case CSCSI0224804 solution proposed: PLEASE DO NOT REPLY

1 message

ACS Publications <acs@service-now.com>
Reply-To: ACS Publications <acs@service-now.com>
To: chaturvedi.aman@students.iiserpune.ac.in

Wed, Jul 24, 2024 at 12:15 PM

ACS Chemistry for Life®

Solution proposed to your case.

Short Description: Request for Permission to Use Figure in Thesis
Priority: 3 - Moderate

If you feel your case is not completely resolved, please select the button below and select "Reject Solution" from the portal.

Leave a comment as to what is still causing the issue to your case.

Reopen Case

Comments:

07-24-2024 02:45:18 AM EDT - Ranjith Alexander Additional comments

Dear Dr. Chaturvedi,

I hope you're doing well, and thank you for contacting ACS Publications Support.

Your permission requested is granted as long as your thesis won't be sold, and there is no fee for this reuse. In your planned reuse, you must cite the ACS article as the source, add this direct link https://doi.org/10.1021/acsenergylett.7b00926

If you need any more help, please don't hesitate to let me know.

Best regards,
Ranjith Alexander
~~~~~~~~~~~~~~~~~~~~~~~~~~~~~~~~
Ranjith Alexander
ACS Publications Support
Customer Services & Information
Website: https://acs.service-now.com/acs
Email: support@services.acs.org
Phone: 800-227-9919 | 202-872-(HELP) 4357
~~~~~~~~~~~~~~~~~~~~~~~~~~~~~~~~

IISER PUNE

Aman Chaturvedi <chaturvedi.aman@students.iiserpune.ac.in>

Request for Permission to Use Figure in Thesis

1 message

ACS Publications <acs@service-now.com> Wed, Jul 24, 2024 at 12:14 PM
Reply-To: support@services.acs.org
To: chaturvedi.aman@students.iiserpune.ac.in

Dear Dr. Chaturvedi,

I hope you're doing well, and thank you for contacting ACS Publications Support.

Your permission requested is granted as long as your thesis won't be sold, and there is no fee for this reuse. In your planned reuse, you must cite the ACS article as the source, add this direct link https://doi.org/10.1021/acsenergylett.7b00926

If you need any more help, please don't hesitate to let me know.

Best regards,
Ranjith Alexander
~~~~~~~~~~~~~~~~~~~~~~~~~~~~~~~~
Ranjith Alexander
ACS Publications Support
Customer Services & Information
Website: https://acs.service-now.com/acs
Email: support@services.acs.org
Phone: 800-227-9919 | 202-872-(HELP) 4357

Case Info:

Case Number : CSCSI0224804

Created On: 07-24-2024 02:24:35 AM EDT

Short Description: Request for Permission to Use Figure in Thesis

Description: My name is Aman Chaturvedi, and I am a graduate student in the Department of Chemistry at Indian Institute of Science Education and Research Pune. I am currently working on my thesis, titled Ultrafast Dynamics and Non Linear Photonics of Perovskites and Doped Semiconductor NCs which focuses on Ultrafast Charge Carrier Dynamics and Nonlinear Optical Properties of Perovskites.
I am writing to seek your permission to use a figure from your publication,*Low-Dimensional Organometal Halide Perovskites*, published in ACS Energy Letters <https://pubs.acs.org/journal/aelccp>in 2017. The figure I am interested in is Figure 1.
https://doi.org/10.1021/acsenergylett.7b00926
The figure is particularly relevant to my research, and I believe it would significantly enhance the quality and clarity of my work. Proper credit will be given to the original source, and the figure will be cited.
If there are any specific conditions or permission forms that I need to complete, please let me know, and I will be happy to comply.

Thank you for considering my request. I look forward to your positive response.

Best regards,
Aman Chaturvedi
Research Fellow,
THz Spectroscopy Group,
Lab C-129, Main Building,
Indian Institute of Science Education and Research Pune,
~~~~~~~~~~~~~~~~~~~~~~~~~~~~~~~~

Dr. Homi Bhabha Road, Pashan, Pune 411008.
Contact : 7249423210, 02025908675.

Ref:MSG1773177_i6WLZSFb5YRI7Mv4BJ7h